NASA Technical Memorandum 82478

Space and Planetary Environment Criteria Guidelines for Use in Space Vehicle Development, 1982 Revision (Volume 1)

JANUARY 1983

NASA

NASA Technical Memorandum 82478

Space and Planetary Environment Criteria Guidelines for Use in Space Vehicle Development, 1982 Revision (Volume 1)

Robert E. Smith and George S. West, *Compilers*
George C. Marshall Space Flight Center
Marshall Space Flight Center, Alabama

National Aeronautics
and Space Administration

Scientific and Technical
Information Branch

1983

TABLE OF CONTENTS

TABLE OF CONTENTS (Continued)

TABLE OF CONTENTS (Continued)

TABLE OF CONTENTS (Continued)

TABLE OF CONTENTS (Concluded)

Page intentionally left blank

FOREWORD

NASA TM-82478 and NASA TM-82501 (Volumes 1 and 2) entitled, "Space and Planetary Environment Criteria Guidelines for Use in Space Vehicle Development, 1982 Revision," provide information relative to the natural environment for altitudes greater than 90 km above the surface. (NASA TM-82473 entitled, "Terrestrial Environment (Climatic) Criteria Guidelines for Use in Aerospace Vehicle Development, 1982 Rivision," provides natural environmental information for altitudes below 90 km.) NASA TM-82478 and NASA TM-82501 are a compendium of up-to-date information on the physical characteristics of bodies in the solar system and a guide to recent scientific literature. They are intended for NASA engineers, for scientists who design spacecraft and space experiments, and for teachers and others interested in the space program.

Figures and tables reprinted from copyrighted material are included with permission of the copyright holder.

These volumes are a follow-on to NASA TM-78119, 1977. However, NASA TM-78119 is still considered to be of use and of interest to scientists and engineers in some areas, but any conflict in the data will be resolved by using the values in the new documents. Furthermore, there is no intent to automatically change any references to previous documents in contract Scopes of Work by the issuance and acquisition of either TM-82473, TM-82478, or TM-82501.

These guidelines are recommended as a tool for use in the development of space vehicles and associated equipment, and the information presented is based on data and models currently considered to be accurate. However, an environment specialist should be consulted in critical design interface applications for the most current information and scientific interpretation.

Sections on the Sun, Terrestrial Space, the Moon, Mercury, Venus, and Mars constitute Volume I. Volume II contains chapters on Jupiter, Saturn, Uranus, Neptune, Pluto, Comets, Asteroids, and Interplanetary Dust.

Various programs of NASA's Office for Space Transportation Systems, Office for Aeronautics and Space Technology, Office for Space Science and Applications, and Office for Space Transportation Operations provided resources required for the preparation of this document.

ACKNOWLEDGEMENTS

Many individuals participated in the project compiling information, writing, and reviewing. Overall project director was M. H. Davis, Universities Space Research Association, who also contributed to the writing and editing. Special recognition is due Duncan Steel of the Department of Astrogeophysics, University of Colorado, and Chris McKay, University of Colorado.

The following assembled information and wrote sections of the document (institutional affiliations are given for purpose of identification only):

INTRODUCTION - William W. Vaughan, NASA, Marshall Space Flight Center
- Robert E. Smith, NASA, Marshall Space Flight Center
- George S. West, NASA, Marshall Space Flight Center

SUMMARY - Robert E. Smith, Marshall Space Flight Center

		PRINCIPAL AUTHOR	REVISIONS AND SUPPLEMENTARY MATERIAL
SECTION 1.	THE SUN	Oran R. White, Independent Robert E. Smith, NASA, MSFC	James Klimchuck, High Altitude Observatory
SECTION 2.	TERRESTRIAL SPACE	Hugh Anderson, SAI, Bellevue, WA.	
SECTION 3.	THE MOON	Eric Christiansen, U.S. Geolo. Survey	M. H. Davis, USRA
SECTION 4.	MERCURY	Duncan Steel, Univ. of Colo.	
SECTION 5.	VENUS	Duncan Steel	M. H. Davis
SECTION 6.	MARS	Chris McKay, Univ. of Colo.	
APPENDIX A.	NEUTRAL ATMOSPHERE MODELS	Robert E. Smith, NASA, Marshall Space Flight Center	

Others who contributed comments and corrections included:

Ronald Greeley, Arizona State University
Richard Hodges, University of Texas/Dallas
Michael Carr, USGS
Donald Hunten, University of Arizona
Robert Strom, University of Arizona
T. Neil Divine, Jet Propulsion Laboratory
George West, NASA, Marshall Space Flight Center
Robert E. Smith, NASA, Marshall Space Flight Center

Editorial and bibliographis services were provided by

Steven Carroll, Document Control, Inc.
Sheri Harms, Document Control, Inc.
Sylvia Pigors
Margaret Rothermel
Judy Maples
Connie Webb
Melanie A. Cook, USRA
Carter Emmart
Melanie deMuth, USRA
Vicki Littlefield
Dianne Johnson, RDD Consultants

SUMMARY

This document provides a consolidated presentation of space and planetary natural environment data for use as design criteria guidelines in space vehicle development programs.

Specifically, information is provided in the disciplinary areas of atmospheric and ionospheric properties, radiation, geomagnetic field, astrodynamic constants, and meteoroids for the Earth's atmosphere above 90 km, interplanetary space, and the atmospheres and surfaces (when available) of the Moon and the planets (other than Earth) of this solar system. The current Marshall Space Flight Center (MSFC) upper atmosphere model is described in detail.

INTRODUCTION

A knowledge of environment parameters is necessary for the establishment of design requirements for space vehicles and associated equipment. Such data are required to define the design condition for fabrication, storage, transportation, test, preflight, in-flight, and on-orbit design conditions and should be considered for both the whole system and the components which make up the system. The purpose of this document is to provide guideline data on space and planetary environmental conditions relative to various disciplinary areas which are applicable to the design of space vehicles and associated equipment for NASA.

Good engineering judgment must be exercised in the application of the environment data to space vehicle design analysis. Consideration must be given to the overall vehicle mission and performance requirements. Knowledge still is lacking on the relationships between some of the environment variates which are required as inputs to the design of space vehicles. Also, interrelationships between space vehicle parameters and environment variables cannot always be clearly defined. Therefore, a close working relationship and team philosophy should exist between the design/operational engineer and the respective organization's environment scientists. Although a space vehicle design should accommodate all expected operational environment conditions, it is neither economically nor technically feasible to design space vehicles to withstand all extremes. For this reason, consideration should be given to protection of space vehicles or critical subsystem for some extremes. This document does not specify how the designer should use the data in regard to a specific space vehicle design. Such specifications may be established only through analysis and study of a particular design problem.

Assessment of the natural environment in early stages of a space vehicle development program will be advantageous in developing a space vehicle with a minimum operational sensitivity to the environment. For those areas of the environment that need to be monitored prior to and during tests and operations, this early planning will permit development of the required measuring and communication systems for accurate and timely monitoring of the environment.

The environment criteria data presented in this document were formulated based on discussions and requests from engineers involved in space vehicle development and operations; therefore, they represent responses to actual engineering problems and are not just a general compilation of environmental data. This report is used extensively by various government and private space vehicle development organizations in design and operational studies. Inquiries may be directed through appropriate organizational channels for subsequent communications to the Atmospheric Sciences Division, Marshall Space Flight Center, Alabama 35812.

Based on known and projected user requirements, it was decided that it is more advantageous to present the natural environment parameters grouped according to spatial regions rather than scientific disciplinary areas. These spatial areas are interplanetary space and those surrounding the individual planets and the Earth's Moon. The outer limits depend upon the component of the environment being discussed. For clarity in discussion, limits have been arbitrarily taken to be 10 radii above the surface of the planet or Moon. In the discussion of the meteoroid environment, however, the limits extend to a point where the gravitational attraction of the planet or Moon becomes negligible.

Some of the space and planetary environmental data available today are speculative and will remain so until additional satellites, planetary probes, and manned space flights provide more information. Therefore, care must be used in the interpretation and use of available space environment data for a specific design decision. Although the data in this document provide valuable guides for preliminary design studies and analyses, their use for final program decisions depends upon the specific design problem involved. This report was prepared primarily for use in NASA space vehicle development and advanced study projects. The data contained in this document are reviewed on a continuing basis, and revision or amendments will be published as necessary. The numbers given in brackets refer to references given at the end of each section.

This document does not include the subject of environmental test procedures. Reference should be made to Department of Defense MIL-STD-810C Environmental Test Methods (1975)* available from the National Technical Information Service, Springfield, Virginia, 22161. This document covers procedures for: Low Pressure (Altitude), High and Low Temperature, Temperature Shock, Temperature Altitude, Solar Radiation, and Space Simulations (Unmanned Test). An excellent comparison of the various international environmental testing standards may be found in the Journal of Environmental Sciences, Vol. XXIV, Number 2, March/April 1981.

---

*Revision being considered by DOD.

TECHNICAL MEMORANDUM 82478

SPACE AND PLANETARY ENVIRONMENT CRITERIA GUIDELINES FOR USE IN SPACE VEHICLE DEVELOPMENT, 1982 REVISION

(VOLUME I)

SECTION 1. THE SUN

1.1 INTRODUCTION

The Sun is the star about which all bodies in our solar system revolve. It provides the light and heat upon which we depend for life, and its gravity field determines the movement of the planets and other bodies in their orbits. It is a main sequence star of type G-2. In any other place in the universe, it would scarcely be worthy of special study, but its central role in our solar system makes it a unique object for research.

Short and long wavelengths of solar electromagnetic radiation along with energetic particles emitted by the Sun are absorbed by the Earth's atmosphere. Moreover, the extremely bright central solar disk interferes with observation of the corona except at times of solar eclipse or, less effectively, when the coronagraph is used to block the central image artificially. Much new information has been learned in the past several decades through observations from platforms above the atmosphere: balloons, high-flying aircraft, rockets, satellites, and spacecraft. Besides observations of electromagnetic radiation at all wavelengths, such platforms have permitted direct measurements of solar particle emissions that had previously been inferred from geomagnetic and other effects observable at the surface.

Like all main sequence stars, the Sun's energy output derives from the nuclear fusion conversion of hydrogen to helium and heavier nuclei in its core. Photons diffuse outward until, after several thousand years, they reach the convective envelope (Fig. 1-1). Another byproduct of the fusion reaction is a flux of neutrinos which freely escape the Sun. (Reference 1-1 discusses attempts to detect the neutrino flux and interpretations of the puzzling results.)

1.2 BRIEF QUALITATIVE DESCRIPTION

At the center of the Sun is the core, where energy is produced by nuclear reactions. Surrounding the core are concentric shells: the radiative zone; the convective envelope at about 0.8 R_S; the photosphere, the layer from which visible radiation emerges; the chromosphere; and the corona, the Sun's outer atmosphere. Energy is transported outward through the convective envelope by convective motions which are organized into cells. The Sun's "lower atmosphere" or photosphere is the region from which energy is radiated directly into space. This radiation approximates the Planck distribution at 5800°K; most of the energy falls within the visible part of the spectrum (Fig. 1-2).

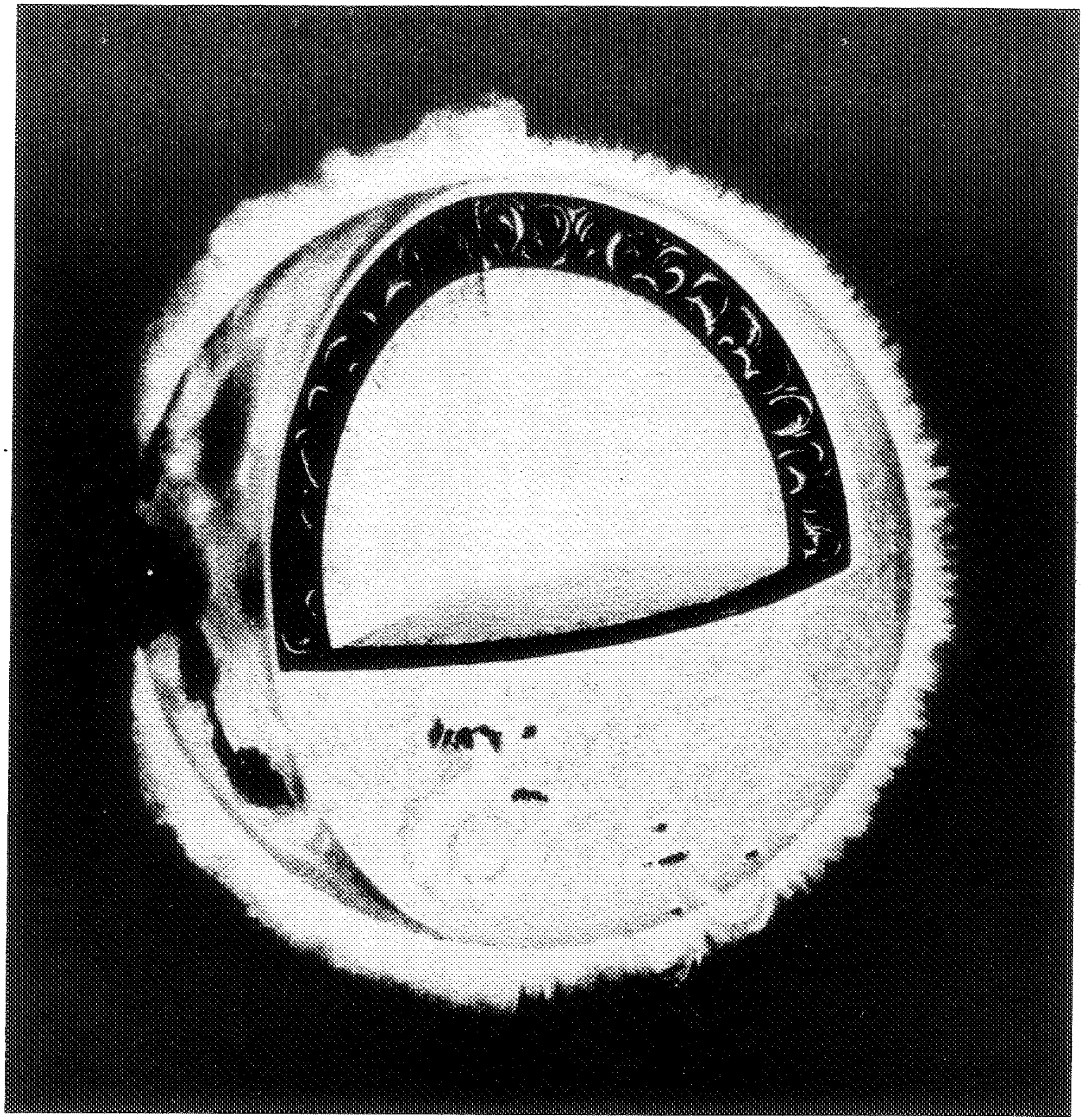

Figure 1-1. A cross section of the Sun indicates the inner energy-generating core (0.2 R_o in radius), the radiative envelope which extends out to 0.8 R_o, and the outer convective shell [1-12].

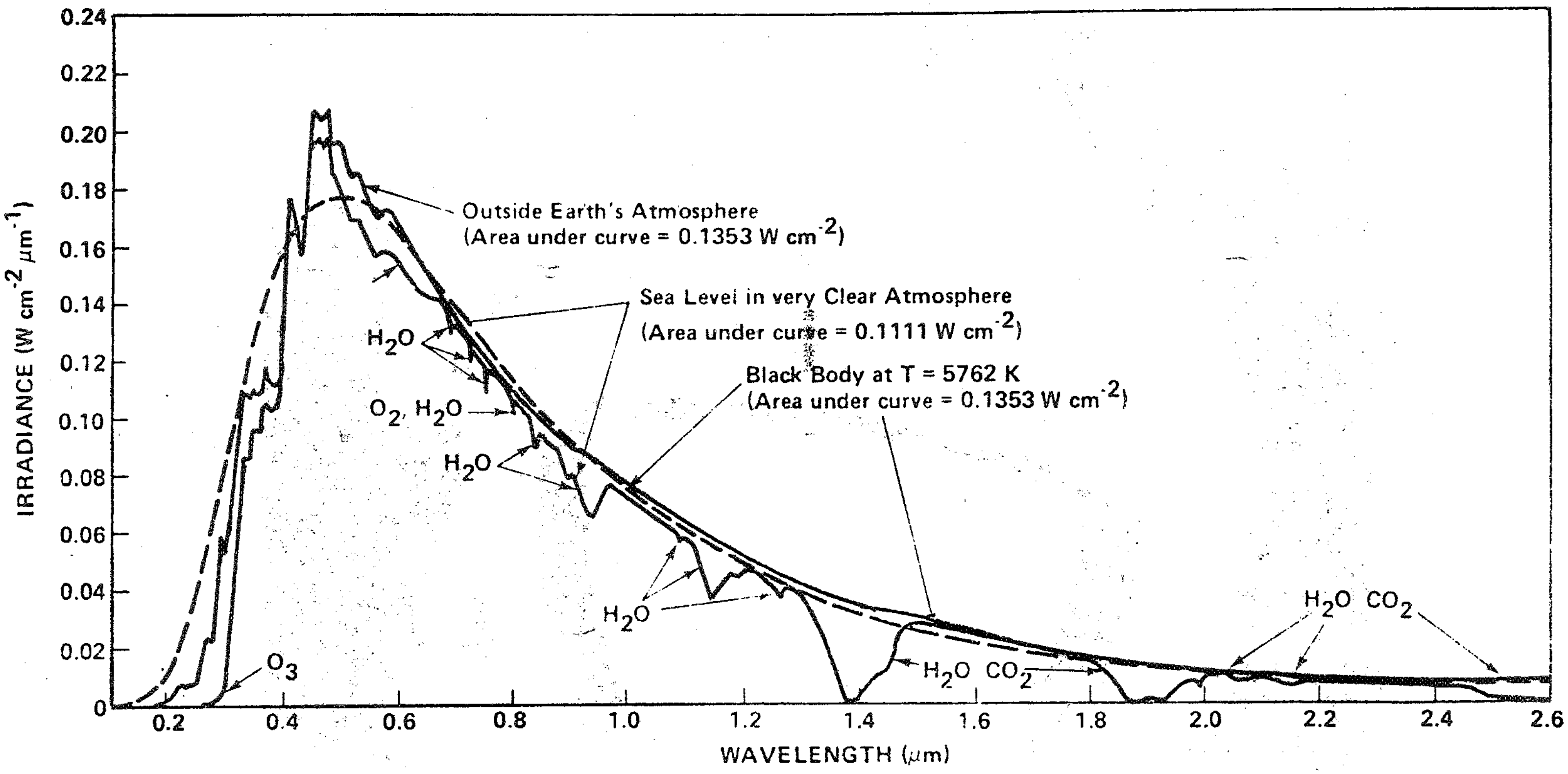

Figure 1-2. Normally incident solar radiation at sea level on very clear days, solar spectral irradiance outside the Earth's atmosphere at 1 AU, and blackbody spectral irradiance curve at T = 5762°K (normalized to 1 AU) [1-2].

The chromosphere, extending for a few thousand kilometers above the photosphere, has a maximum temperature of around 10^4°K. The corona, which extends several solar radii above the chromosphere, has temperatures of some 2×10^6°K. These regions emit electromagnetic radiation in the UV, EUV, and X-ray spectral regions. This radiation, though of relatively small total energy, is the major factor in forming ionospheres and in planetary upper atmosphere photochemistry.

A consequence of the heating of the Sun's outer atmosphere is its expansion into the surrounding interplanetary space. This continuous outward flow of plasma is called the solar wind. It consists of protons, electrons, and alpha particles, as well as small fluxes of heavier ions. Typical velocities are 300 to 400 km/sec, but its velocity may be as high as 1000 km/sec.

Although the total energy output of the Sun is remarkably steady, the surface of the Sun exhibits many types of irregularities, including sunspots, faculae, plages (bright areas), filaments, prominences, and flares. All are believed to be ultimately the result of interactions between ionized gases in the solar atmosphere and the Sun's magnetic fields. Most solar activity follows the sunspot cycle. The appearances of individual sunspots on the solar disk cannot be predicted, but they statistically follow a fairly regular periodic pattern (Fig. 1-3). Sunspots are discussed in greater detail in the next section.

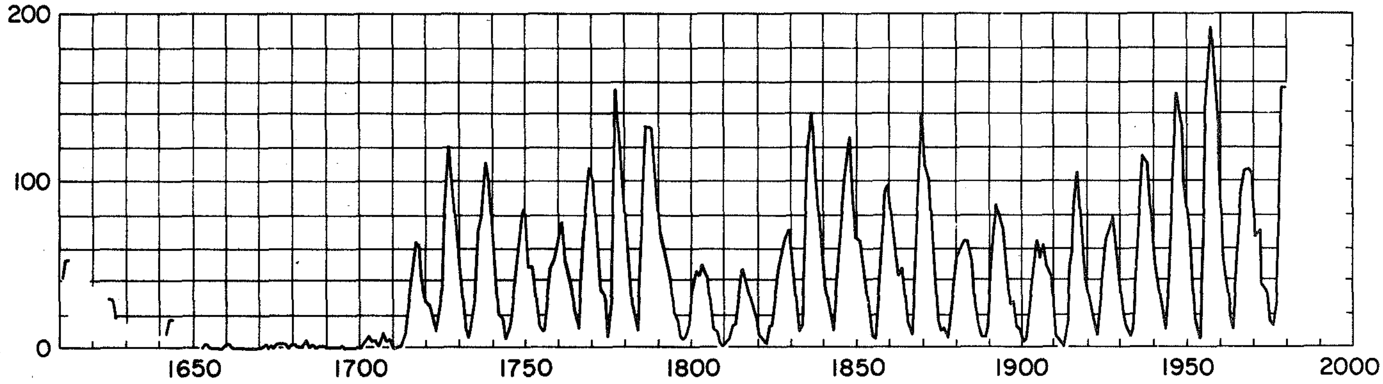

Figure 1-3. The Sunspot Number Chronology as derived from direct measurements and historical documents. (Figure courtesy of Dr. J. A. Eddy, High Altitude Observatory.)

1.3 PHYSICAL PROPERTIES

Table 1-1 lists the physical properties of the Sun.

TABLE 1-1. PHYSICAL PROPERTIES[a]

Quantity	Value	Comments
Distance from the Earth	1.496×10^8 km	1 AU
Mass	1.991×10^{30} kg	
Radius	6.960×10^5 km	$109 \times R_{Earth}$
Angular Diameter at Earth	1919 arc sec	
Luminosity	3.86×10^{33} erg/sec	
Equivalent Blackbody Temperature	5780°K	
Gravity at Visible Surface	2.74×10^4 cm/sec^2	$27 \times g_{Earth}$
Rotation Period[b]	Approximately 27 d	
General Magnetic Field	Approximately 1 gauss at surface (local fields can be much greater)	
Magnetic Period	Overall reversal approximately every 11 years (22-year period)	
Tilt of Solar Equator to Ecliptic	7 deg	

a. The information presented is based primarily on Reference 1-3.

b. Note there is differential rotation between different latitude zones: a 26.9-day period at the equator and a 29.5-day period at 45 deg latitude (paragraph 1.4.3).

1.4 SOLAR EMANATIONS – DESCRIPTIVE

1.4.1 The Nature of the Sun's Output

The end result of the energy-producing fusion reaction in the solar core is the emission of energy and mass from the Sun into the solar system and beyond into interstellar space. This solar output occurs in the form of electromagnetic radiation, plasma, and energetic particles. Table 1-2 [1-4] provides a summary.

The bulk of the energy export occurs in the form of electromagnetic radiation. Although neutrino flux is potentially the second largest mode of energy loss from the Sun, the theoretically predicted neutrino flux has not been confirmed experimentally. The discrepancy has not been resolved, since, as Bahcall and Davis [1-1] emphasize, experimental errors are sufficiently large to allow measured neutrino fluxes from zero to one-third of the predicted values. Neutrinos interact very weakly with all

TABLE 1-2. TOTAL ENERGY FLUX OF SUN

(erg cm^{-2} sec^{-1} at 1 AU)

Radiant Energy	solar constant $S = 1.37 \times 10^6$
Neutrinos	predicted flux = 5×10^4
Solar Wind	1
Magnetic Field	0.01

materials, and they can be ignored in spacecraft design. In terms of sensible solar outputs, solar radiation at visible wavelengths and the solar wind plasma are the most important energetically.

Values for the fluxes of the solar outputs will be stated at one astronomical unit (AU), because the most reliable measurements have come from spacecraft near the Earth. Electromagnetic radiative fluxes are easily scaled for other positions in the solar system by using the inverse square law, but scaling plasma and particle fluxes is difficult because of interactions that occur in interplanetary space. These mapping problems will be discussed later

1.4.2 The Solar Cycle

The solar magnetic cycle is the basic underlying cause of all the observed fluctuations over long (years) and short (days to even minutes and seconds) time scales. The solar cycle was first seen in the systematic rise and fall of the number of visible sunspots. The apparent cyclic nature of solar activity with an 11-year period can be seen in the sunspot number record (Fig. 1-3) extending back to the beginning of the 18th century.

Figures 1-4a and 1-4b show more detailed variations in sunspot number for solar cycles 18, 19, 20, and 21 (now only about halfway completed). One-year running averages of the monthly mean of the Zurich sunspot number:

$$R_z = K\ (10\ g + f)$$

are given, where g is the number of spot groups observed on the solar disk at one time, f is the number of individual spots, and K is a normalization constant which varies from observing site to observing site.

The model of the Earth's upper atmosphere described in Appendix A requires inputs of the level of solar activity expected to prevail at the time the thermodynamic properties of the upper atmosphere need to be known. These inputs are the 162-day means of the 10.7-cm solar radio noise flux, $\bar{F}_{10.7}$, and the 3-hourly values of the geomagnetic, $K_p(a_p)$, index. Since the measured $\bar{F}_{10.7}$ data base is relatively short (1947 to date), the data base was extended back to 1749 using the following equation to convert recorded smoothed (R_Z) data to smoothed solar flux ($\bar{F}_{10.7}$) data:

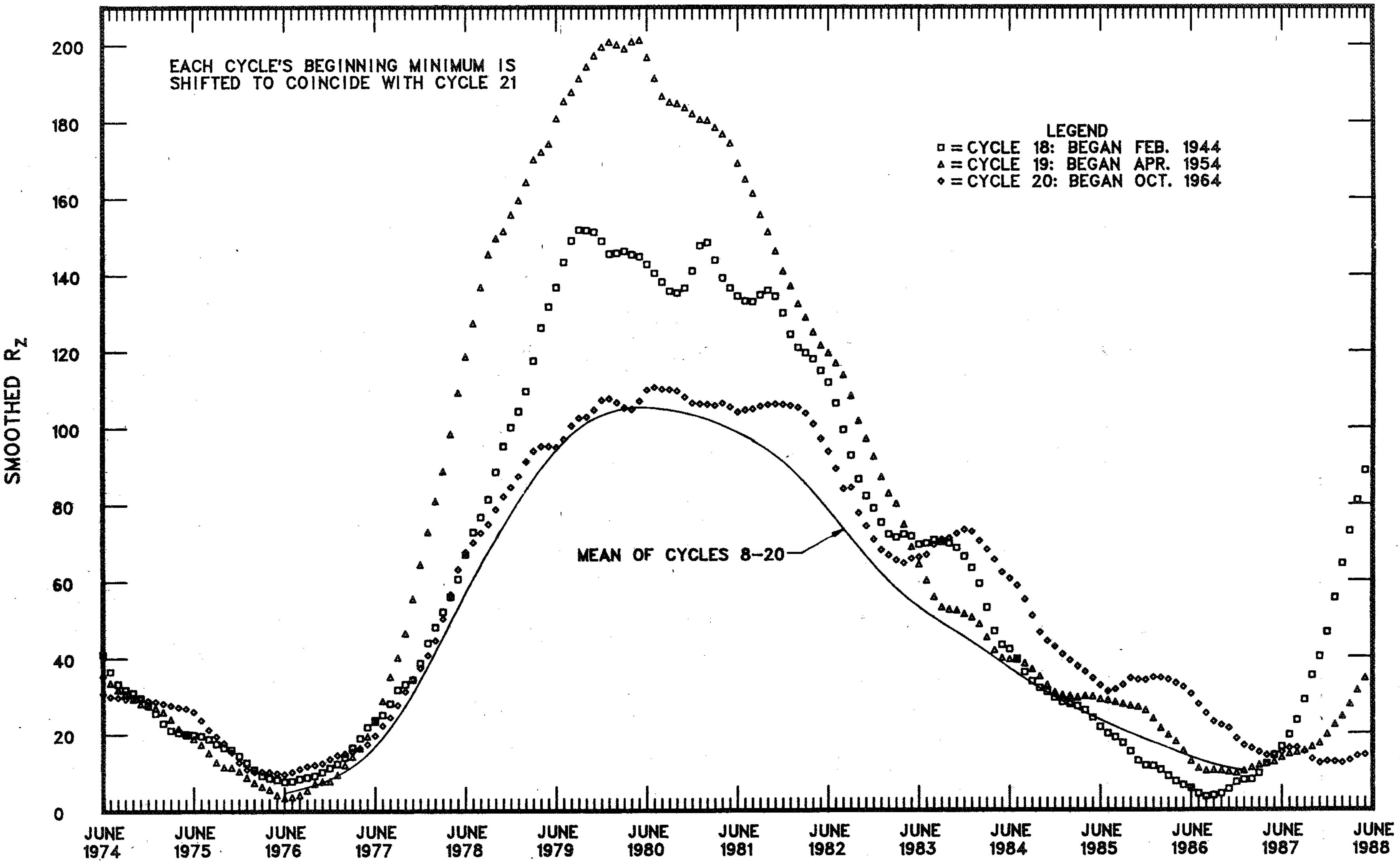

Figure 1-4a. Superposition of cycles 18, 19, and 20 [1-5].

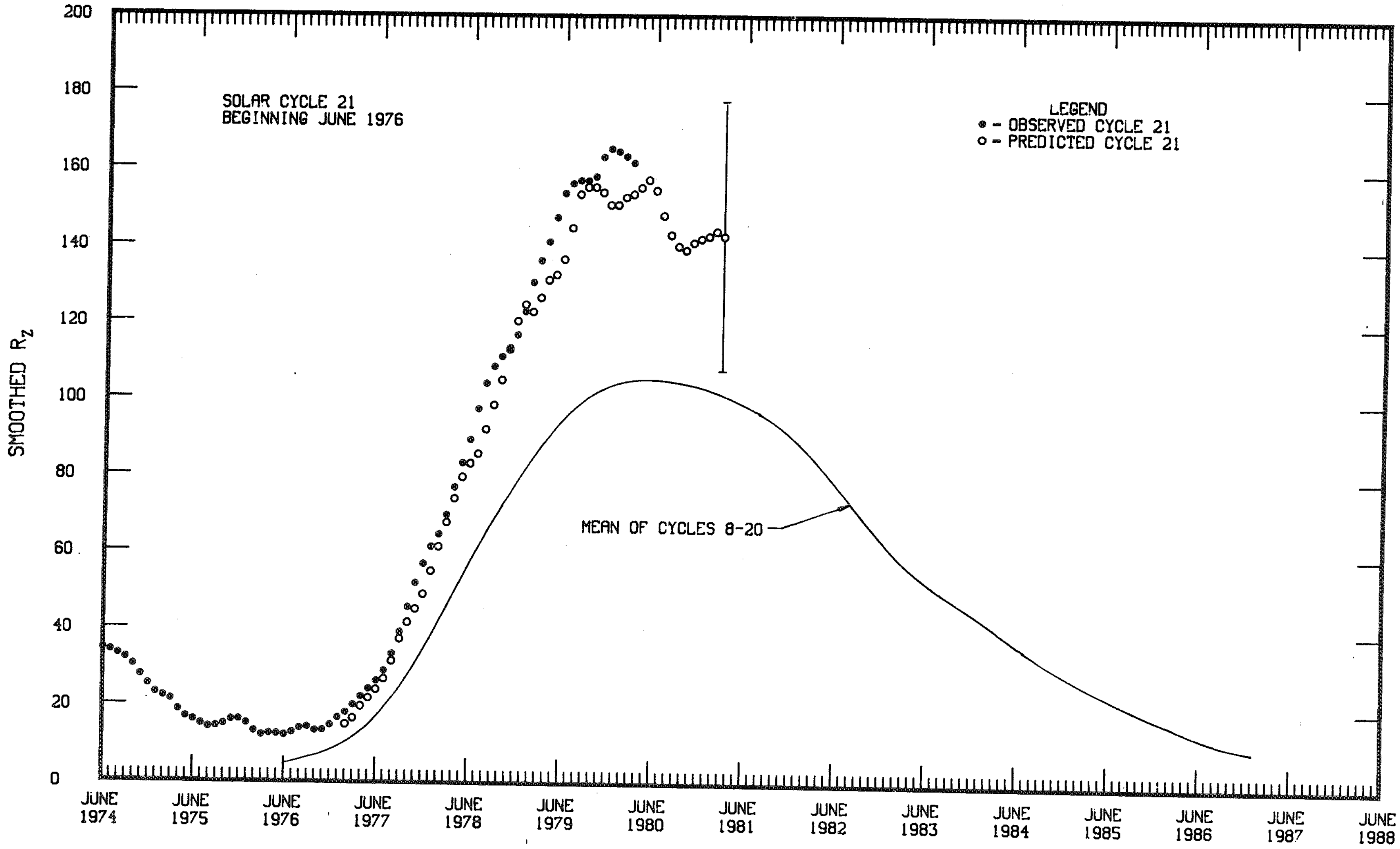

Figure 1-4b. Observed and one-year-ahead predicted smoothed sunspot numbers [1-5].

$$\bar{F}_{10.7} = 49.4 + 0.97\, R_Z + 17.6 \exp(-0.035\, R_Z)$$

The recorded data for $\bar{F}_{10.7}$ and R_Z from 1947 to the present were used to derive the equation which has a linear correlation coefficient of 0.98. This equation was used to construct smoothed solar flux $\bar{F}_{10.7}$ data for the period 1749 to 1946. After 1946, the measured values of $F_{10.7}$ are used to compute the $\bar{F}_{10.7}$.

Figure 1-4c shows the 97.7, 50.0, and 2.3 percentile values of this $\bar{F}_{10.7}$ data base arranged in a monthly sequence beginning at solar cycle minimum and extending through a mean solar cycle period, 11.08 yr. The values on the figure are the extreme and median values of the data set for each month since extreme value statistics has shown that they are most representative of the quoted percentile values for small data sets.

Hale's pioneering experiments at Mt. Wilson to measure solar magnetic fields in sunspots at the beginning of this century established the regular reversal of field polarities in sunspot pairs every 11 years. Later, in the 1950s, Babcock working at Mt. Wilson further established the fundamental character of the magnetic cycle through his discovery that the Sun's general dipole field as measured at the solar poles also reversed near the maximum of solar activity every 11 years. Therefore, the most fundamental process appears to be the 22-year periodicity in magnetic fields produced by dynamo action deep in the solar interior, but this in turn results in an 11-year periodicity in the degree of solar activity and intensities of those solar outputs originating in active regions surrounding sunspots.

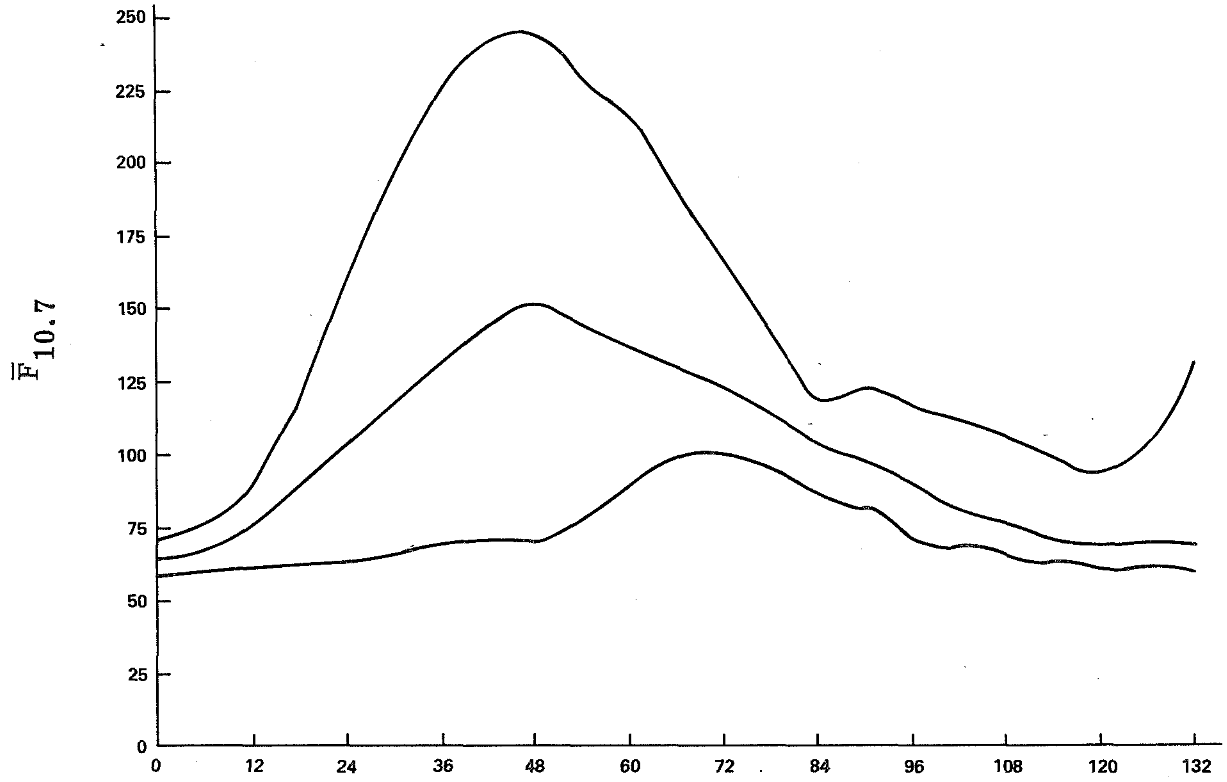

Figure 1-4c. Solar cycle variations of $\bar{F}_{10.7}$, superposition of cycles 1-21.

1.4.3 Variation in the Sun's Output

Both radiation and particle fluxes vary over times much shorter than 11 years. The Sun rotates with a period of approximately 27 days; consequently, any emission from, for example, a bright active region will be visible to a stationary observer for 13.5 days and then be invisible while the emitting region traverses the far side of the Sun. The pure square wave rotational modulation is smoothed by the systematic darkening of the active region near the two edges of the solar disk (i.e., limb darkening effects), and also by the slow evolution of active regions. Active regions where sunspots form have lifetimes of up to ten solar rotations, and during this time the emission shows the effects of both slow morphological change in the local magnetic field structure and the much faster fluctuations (seconds to minutes) caused by the occurrence of solar flares. We typically see more than one active region on the disk at a time; therefore, the observed waveform for the solar emission seen from a single point in the solar system may appear to be quite complicated and even aperiodic at times. The observed fluctuations are further complicated by the differential rotation of the Sun; i.e., equatorial regions of the Sun rotate faster than regions near the poles. Sunspot observations give the rotational period as 26.9 days for the equator and 29.5 days for 45 deg solar latitude. Nevertheless, autocorrelation analyses of such signals over spans of several rotations show the 27-day recurrence effects very clearly. Flares occur randomly in time and have a wide range in emission strength, but the large flares produce very large excursions in the Sun's radiation at wavelengths below 100 nm.

In considering variation of solar electromagnetic radiation caused by solar activity, we usually identify the active region effects with increases in emission strength, but quite a different situation exists for sunspots and the solar wind. Dark sunspots are obviously locales where visible radiation is reduced substantially; as discussed in the next section, the large sunspots appear to decrease the solar constant slightly as they cross the visible solar hemisphere. Similarly, times of increased solar wind speed are associated with the so-called "coronal holes," which appear dark in X-ray images of the Sun and which do not contain active regions. These explanations of variation in solar output levels became possible only through measurements made from space platforms over the last two decades. The most frequent cause of variation is the rotation of different types of solar regions across the visible disk, already described, together with the occurrence of solar flares and coronal transients.

1.5 SOLAR ELECTROMAGNETIC RADIATION

In presenting the data for the Sun's electromagnetic radiation, it is necessary to discuss the spectral distribution of this energy and the total amount of energy under the curve. The latter integral quantity measured at 1 AU is the Solar Constant (units of watts m^{-2} sec^{-1}). Measurements of the spectral distribution yield values for the Sun's spectral irradiance (units of energy flux in a spectral band of specified width).

The spectral energy distribution for the Sun resembles a Planck curve with an effective temperature of 5800°K, which means that the bulk of the solar energy lies between 150 nm and 10 μm with a maximum near 450 nm. This portion of the solar spectrum is emitted primarily by the solar photosphere, the deepest level observable. There are, however, striking and variable solar emissions outside this wavelength band that originate in the chromosphere and corona as well as in transient events such as flares. When we study the solar constant then, we study primarily the photosphere, which is dominated by convective motions in an ionized medium with

$$T_e = 5800°K \text{ and } N_e = 10^{15} \text{ electrons cm}^{-2}.$$

The state of the art in the measurement of the Sun's electromagnetic spectrum is given in considerable detail in White's [1-6] compendium on the solar output and its variation. The following discussion draws heavily on the individual review chapters [1-6], but new material from more recent measurements will be emphasized.

1.5.1 Measurements of the Solar Constant

Adopted value: 1371 ± 5 W m^{-2}

Some of the most intriguing recent results in solar physics have come from spacecraft measurements of the solar constant with cavity radiometers capable of precisions of one part in 10^4. This type of radiometer was developed at the Jet Propulsion Laboratory during the 1970s [1-7]. These devices are simple and rugged enough for flight outside the Earth's atmosphere onboard rockets and orbiting spacecraft.

To appreciate the impact of the new measurements, consider that Frolich [1-8] derived a consensus value of 1373 ± 20 W m^{-2} from all solar constant measurements made between 1965 and 1975. Willson and Hickey [1-9] immediately challenged this value on the grounds that it did not take into account the much higher precision of the very recent measurements. Their weighted mean from all credible aircraft, balloon, and space experiments conducted is 1371 ± 1 W m^{-2}. New measurements continue to come from the Nimbus 7 spacecraft [1-10] and the Solar Maximum Mission (SMM) satellite [1-11]. The Nimbus 7 experiment began on November 16, 1978, and Hickey et al. [1-12] report a mean solar irradiance value of 1371 ± 5 W m^{-2} from the Earth Radiation Budget (ERB) radiometer. Willson's experiment on SMM began operation in February 1980, and Willson et al. [1-11] report a total irradiance value of 1368 ± 6 W m^{-2}. Comparison of these four values for the solar constant shows the state of the art in the absolute determination of the total irradiance. Using these data it is difficult to make a case for a secular change in this solar output, but the prevailing trend in the measurements has been downward since 1966 [1-13].

1.5.2 Short-Term Fluctuations in the Solar Constant

The Nimbus 7 and SMM experiments mentioned in the previous paragraph give the first credible empirical evidence for variation in the total solar irradiance. Both experiments [1-10,1-11] show maximum downward excursions of 0.2 percent in the solar flux level, and the larger amplitude decreases are well correlated with the passage of large sunspots across the solar disk. These excursions have durations of approximately 10 days. Although these variations are quite small, they are important in solar physics because we are now forced to accept the idea of a net radiative loss in a sunspot; i.e., the missing sunspot flux is not made up by a slight increase in the brightness of the quiet photosphere surrounding the spot. Since the sunspot geometries and positions are known, this effect can be modeled by using mean sunspot brightnesses. Preliminary attempts at simulation account for only about half of the variance in the solar constant data. Nevertheless, the first-order effect appears to be the disk passage of dark sunspots, which is the simplest explanation possible.

1.5.3 The Solar Spectral Irradiance

Because the solar constant is so heavily weighted by the photospheric emission, its solar cycle variation is probably quite small (less than 0.5 percent), but the situation is quite different for the long and short wavelength ends of the Sun's spectral energy distribution. These extremes of the solar spectrum and strong absorption lines show effects of the solar activity cycle very clearly. This apparent different sensitivity to solar activity occurs because the emission in these bands originates in higher layers of the Sun's atmosphere, i.e., the chromosphere and corona, or in very energetic transient phenomena such as solar flares.

Absolute measurement of the solar spectrum is a difficult photometric task; consequently, our present picture of the spectral energy distribution is not completely satisfactory. Chapter IV in White's [1-6] compendium summarizes the situation as of 1976, but since that time new experiments have been started to measure the absolute flux levels from the time of solar minimum in 1976 to the maximum of solar cycle 21 in 1979. Heath [1-14] summarizes many of the new results which are just now being published. Table 1-3 defines several bands in the spectrum and lists typical flux levels and their variability. Figure 1-5 shows the solar spectral energy curve as constructed from measurements available in 1976.

TABLE 1-3. FLUX LEVELS IN THE SOLAR SPECTRUM

Spectral Region	Wavelength Band	Flux Level[a] Across Band	Variability in Cycle
Radio	$\lambda > 1$ mm	$10^{-8} - 10^{-14}$	100X
Far Infrared	1 mm $\geq \lambda > 10$ μm	10^{-2}	?
Infrared	10 μm $\geq \lambda > 0.75$ μm	$10 - 10^{5}$	?
Visible	0.75 μm $\geq \lambda > 0.3$ μm	10^{6}	<1 percent
Ultraviolet	0.3 μm $\geq \lambda > 0.12$ μm	$10^{2} - 10^{5}$	1 percent to 2X
Extreme UV	0.12 μm $\geq \lambda > 0.01$ μm	10^{2}	10X
Soft X-ray	0.01 μm $\geq \lambda >$ 1A	$10^{2} - 10^{-4}$	100X
Hard X-ray & Gamma ray	1 A $\geq \lambda$	$10^{-4} - 10^{-5}$	10 to 100X

a. In units of erg cm^{-2} sec^{-1} μ^{-1}.

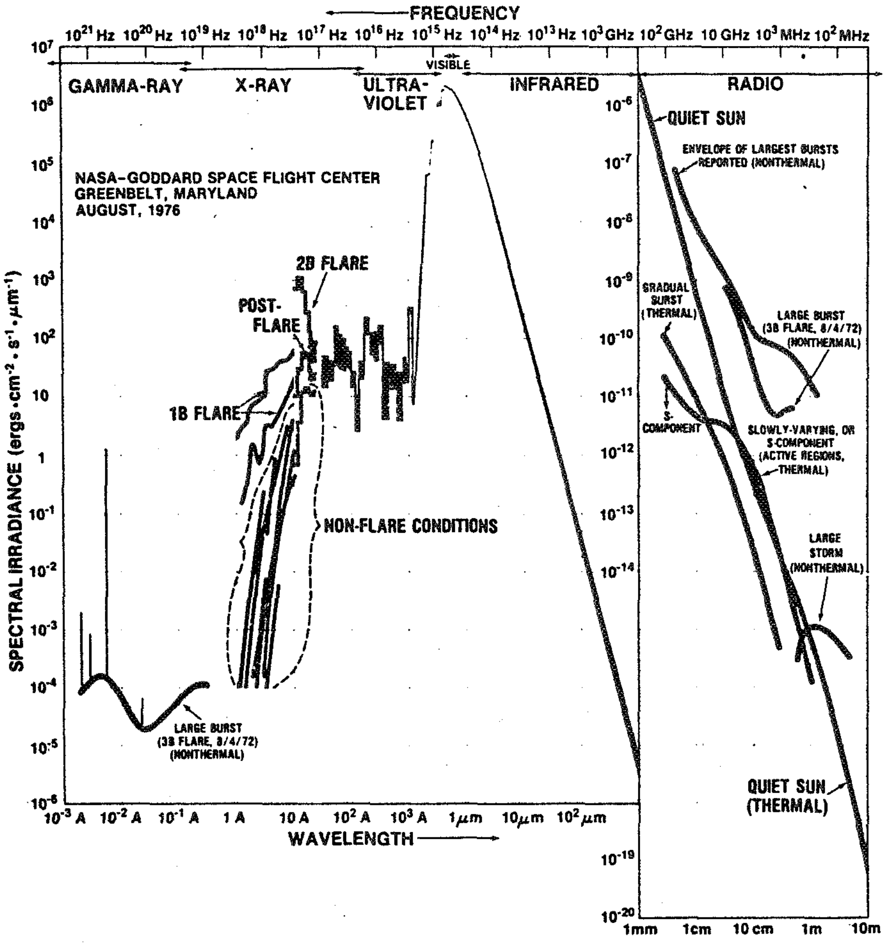

Figure 1-5. The Solar spectrum as derived from measurements available in 1976 [1-6].

The energetically dominant spectral region from 1200 Å to 10 μm (the ultraviolet, visible, and infrared bands in Table 1-3) contains 99.5 percent of the total radiant energy from the Sun and shows variations comparable to current measurement errors, except at short wavelengths near 1000 Å where the variability increases rapidly to 2X. This increased variability occurs because the blackbody radiation curve for the photosphere decreases rapidly to small flux values in the UV, and, as a result, the spectrum switches from a continuum-dominated spectrum to a pure emission line spectrum near 1400 Å. This emission line character continues all the way to the gamma ray region. The measured variability during a solar rotation and over the cycle increases because these emission lines originate in the corona, chromosphere, and flares rather than in the much brighter photosphere.

In the long wavelength region beyond 10 μm into the radio spectrum, we have a weak continuous spectrum again, showing increased variability as we go further from the visible spectrum. Once again, this increase arises from the increasing dominance of coronal emission as we go into the radio region. The low density ($N_e \sim 10^8$ cm^{-3}) and a high temperature ($T_e \sim 10^6$ K) solar corona displays large changes in its structure over a solar cycle as well as many short-lived transient events associated with individual active regions on the Sun.

Even though our picture of the solar spectrum is still incomplete in terms of absolute flux levels measured over one solar cycle, the situation is improving. Since many of the newer experiments began near solar minimum in 1976, by 1987 we should have our first continuous record of the variation of the spectrum over one solar activity cycle.

1.6 SOLAR PLASMA EMISSION

The Skylab epoch from 1972 to 1974 led to a significant improvement in our understanding of the solar corona and solar wind because for the first time the direct link between the solar atmosphere and the interplanetary medium was found in the so-called coronal holes. Hundhausen [1-15] summarizes the phenomenological description of the corona and its effect on the interplanetary medium. This early discovery epoch came in the declining phase of solar cycle 20; consequently, confirmation of the phenomenological model circa 1978 awaits measurements still to be made throughout the current cycle. Even though this description is not fully confirmed by observations over a full solar cycle yet, it succeeds in answering many long-standing questions about the origin of interplanetary disturbances and magnetic sector structure.

1.6.1 Properties of the Mean Solar Wind

The properties of the mean solar wind are summarized in Table 1-4.

TABLE 1-4. PROPERTIES OF THE MEAN SOLAR WIND AT 1 AU [1-16]

Radial Velocity = 468 ± 116 km sec^{-1}

Particle Density = 8.6 ± 6.6 cm^{-3}

Mean Field = $6.2 \pm 2.9 \times 10^{-6}$ gauss

Proton Temperature = $1.25 \pm 0.9 \times 10^{5}$ deg K

The uncertainties are 1-sigma limits. For comparison, note the properties of the four high-speed streams in Table 1-5.

TABLE 1-5. PROPERTIES OF HIGH-SPEED STREAMS (1973-1974) [1-15]

Radial Velocity = 600 - 700 km sec^{-1}

Proton Flux = 4×10^{8} proton cm^{-2} sec^{-1}

Energy Flux = 2 erg cm^{-2} sec^{-1}

Field = 4×10^{-5} gauss

1.6.2 The Solar Wind and the Interplanetary Magnetic Field

The mean solar wind is a flow of solar plasma past the Earth at a speed of approximately 450 km/sec. This flow was predicted by Parker [1-17] as the natural consequence of the outward pressure gradient in the high-temperature solar corona. It is not everywhere a simple radial flow because the Sun rotates and has magnetic fields extending into the corona. The Sun's weak dipole field of 1 to 10 gauss field strength emerges near its poles and extends out into space where it acts as a cage for the solar wind flow, but the solar wind pressure is sufficient to drag the field lines out radially at the solar equator and create an equatorial neutral sheet separating the regions of N and S magnetic polarity. Figure 1-6 shows this distortion of a dipole field as emanated from a simple axially symmetric model. These interplanetary fields of solar origin are stretched along spiral tracks because the solar wind carries the field lines outward while the Sun continues to rotate with its 27-day period. The ability of the solar wind to produce neutral sheets and flows along spiral tracks that extend outwards into the solar system is the reason for much of the structure observed in the solar wind plasma at 1 AU.

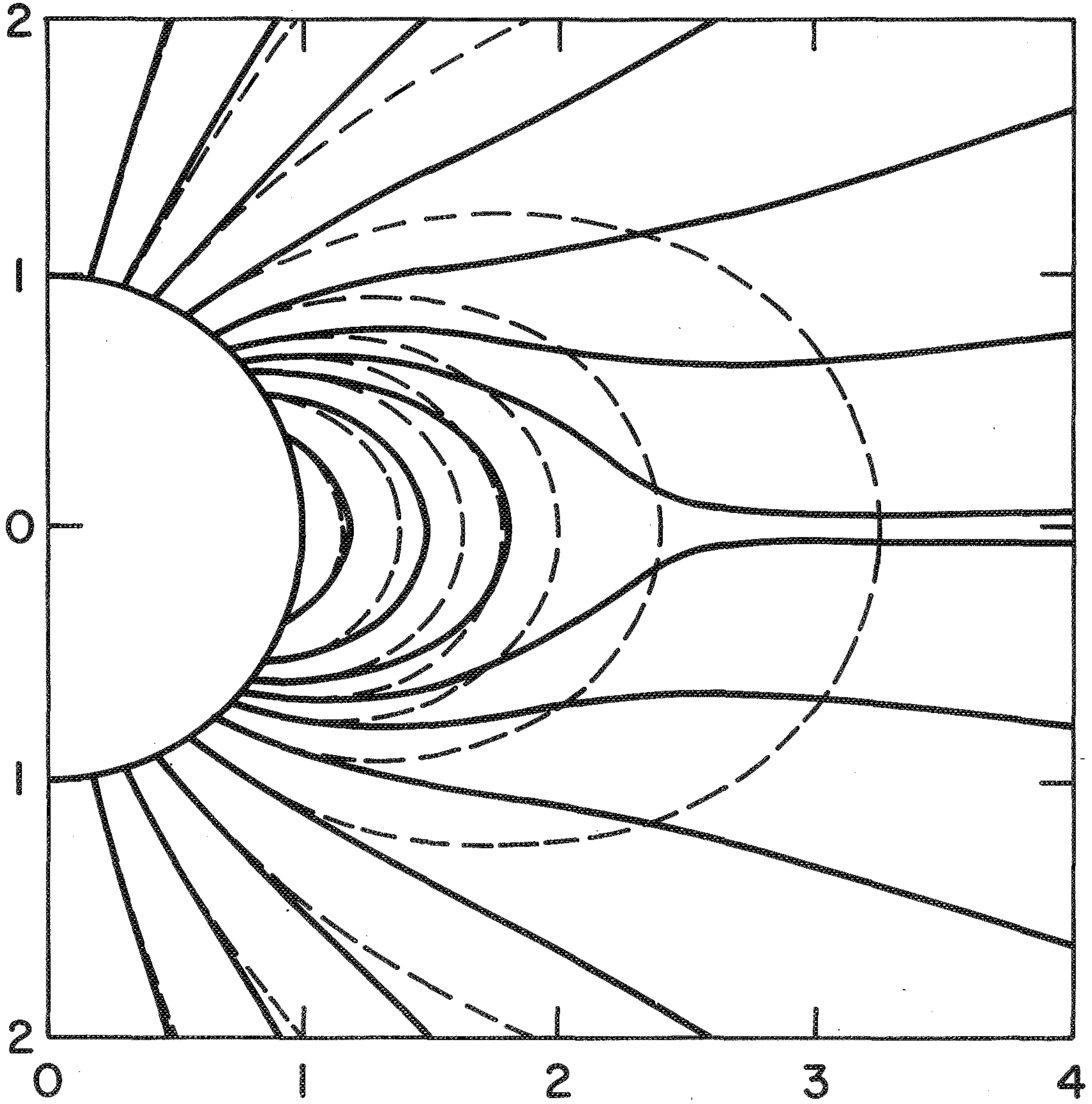

Figure 1-6. Distortion of a simple dipole field by a steady radial solar wind. Solid lines show field configuration resulting from flow, and dashed lines show the closed dipole field without flow [1-15].

The strong magnetic fields of solar active regions complicate this structure through large-scale topological changes in the solar field structure as it extends into the interplanetary medium. In these closed field regions, strong fields (>500 gauss) prevent flow of active-region plasma into the solar wind and thereby create zones in the solar wind where the plasma velocity is smaller. More important for interplanetary conditions, however, are the unipolar regions lying between the active regions and at the solar poles. The magnetic field lines from these quiet regions are open; i.e., they extend far out into space and provide an easy path for the solar wind flow (Figs. 1-6, 1-7, and 1-8). Such regions on the Sun are identified as the so-called coronal holes that appear to be the sources of high-speed solar wind streams with plasma velocities of up to 800 km/sec or more.

The properties of the interplanetary magnetic field are principally determined by separation of the N and S polarity regions, the equatorial neutral sheet, and the localized high-speed flow of plasma out of coronal holes. Measurements of the interplanetary field in the ecliptic show the abrupt polarity changes that define the interplanetary sector boundaries. These sectors of one dominant magnetic polarity arise because of the deviation of the neutral sheet from the plane of the ecliptic. In the idealized case of a perfect magnetic dipole, the neutral sheet would be planar and tilted relative to the ecliptic plane because of the 7 deg inclination of the Sun's rotation axis (Fig. 1-7). As the Sun rotates, this idealized neutral sheet would appear to wobble, and the field polarities observed at the Earth would change sign each time the intersection of the neutral sheet and the plane of the ecliptic sweeps across the observer. For the simple model shown in Figure 1-7, the observer would see two sector boundaries separated by 13.5 days in the interplanetary field. However, tightly closed magnetic fields from active regions warp the effective neutral sheet and produce additional intersections of the sheet with the plane of the ecliptic, which in turn leads to more frequent magnetic sector boundary crossings at the Earth (Fig. 1-8). An instrument flying well out of the ecliptic at heliographic latitudes greater than about 30 deg would probably never see a sector boundary; it would always see one magnetic polarity unless the sense of the global solar field changes. The mapping of the solar wind flow and interplanetary fields to high solar latitudes remains as an unfinished task in the exploration of the solar system.

Interplanetary magnetic field lines and, hence, sector boundaries, follow an Archimedes spiral pattern because the field lines are rooted in the solar surface and are carried outward by the radially flowing solar wind as the Sun rotates. To an observer located above the ecliptic plane, the pattern would resemble a slowly spinning pinwheel. This is indicated in Figure 1-9, which shows sector boundaries inferred from magnetic polarity data taken by spacecraft at 1 AU.

To gain some insight into the spiral structure, consider a stream with a 500 km/sec radial flow. A parcel of plasma in the stream takes 18 days to travel to Jupiter's orbit, and its trajectory will be a spiral of 0.7 of one turn. At Saturn's distance, the trajectory is wound 1.25 turns and increases to 5 turns at the orbit of of Pluto. Consequently,the spiral pattern is not tightly wound inside the orbit of Saturn.

1.6.3 High-Speed Streams

In addition to the large-scale effects of the neutral sheet, solar wind structure is strongly influenced by high-speed solar plasma streaming out of coronal holes. The solar surface field topology is such that a region with an open magnetic field can form

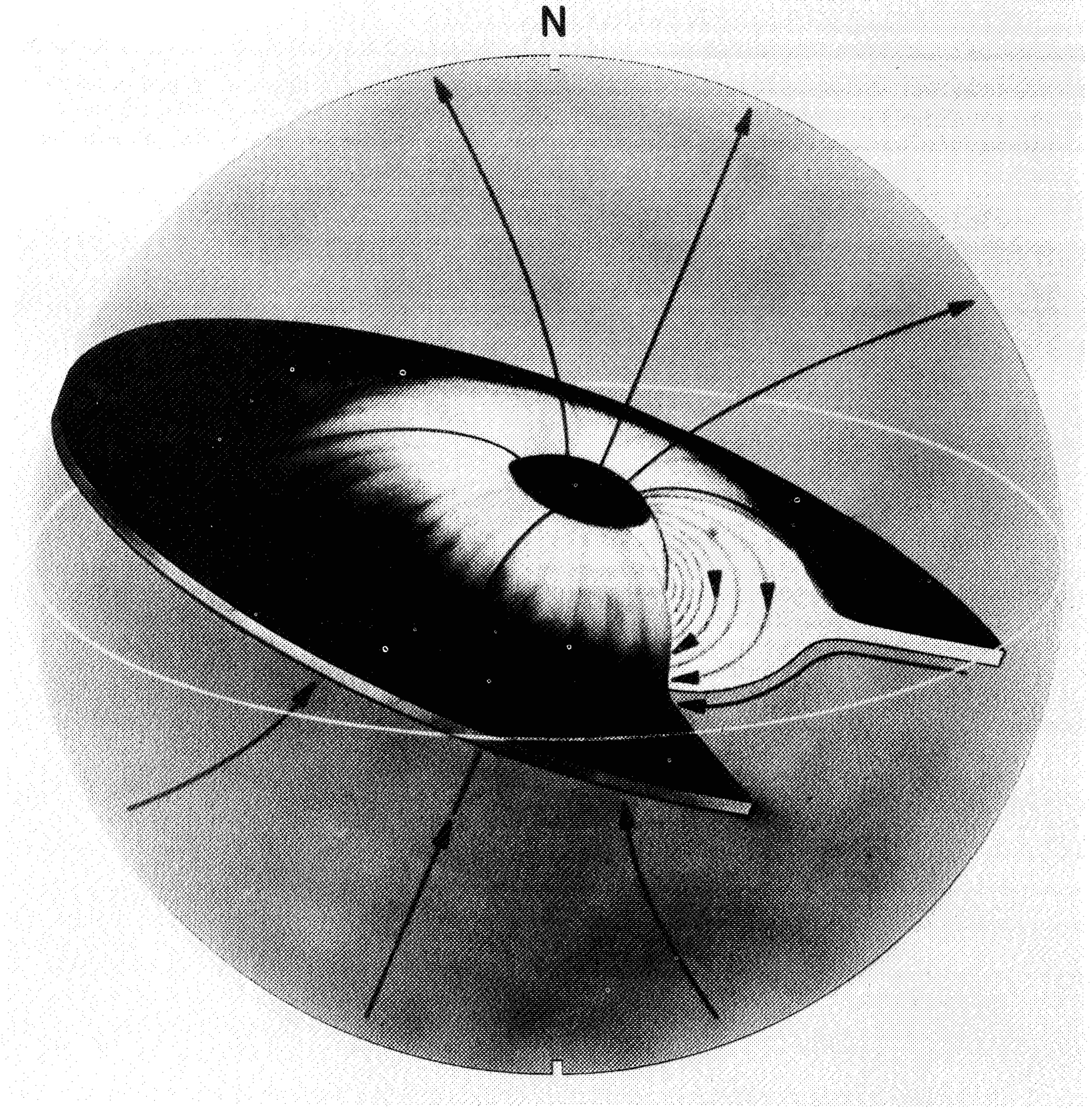

Figure 1-7. A schematic drawing of a simple solar wind and field configuration defining the Sun's equatorial neutral sheet and its tilt relative to the plane of the ecliptic [1-15].

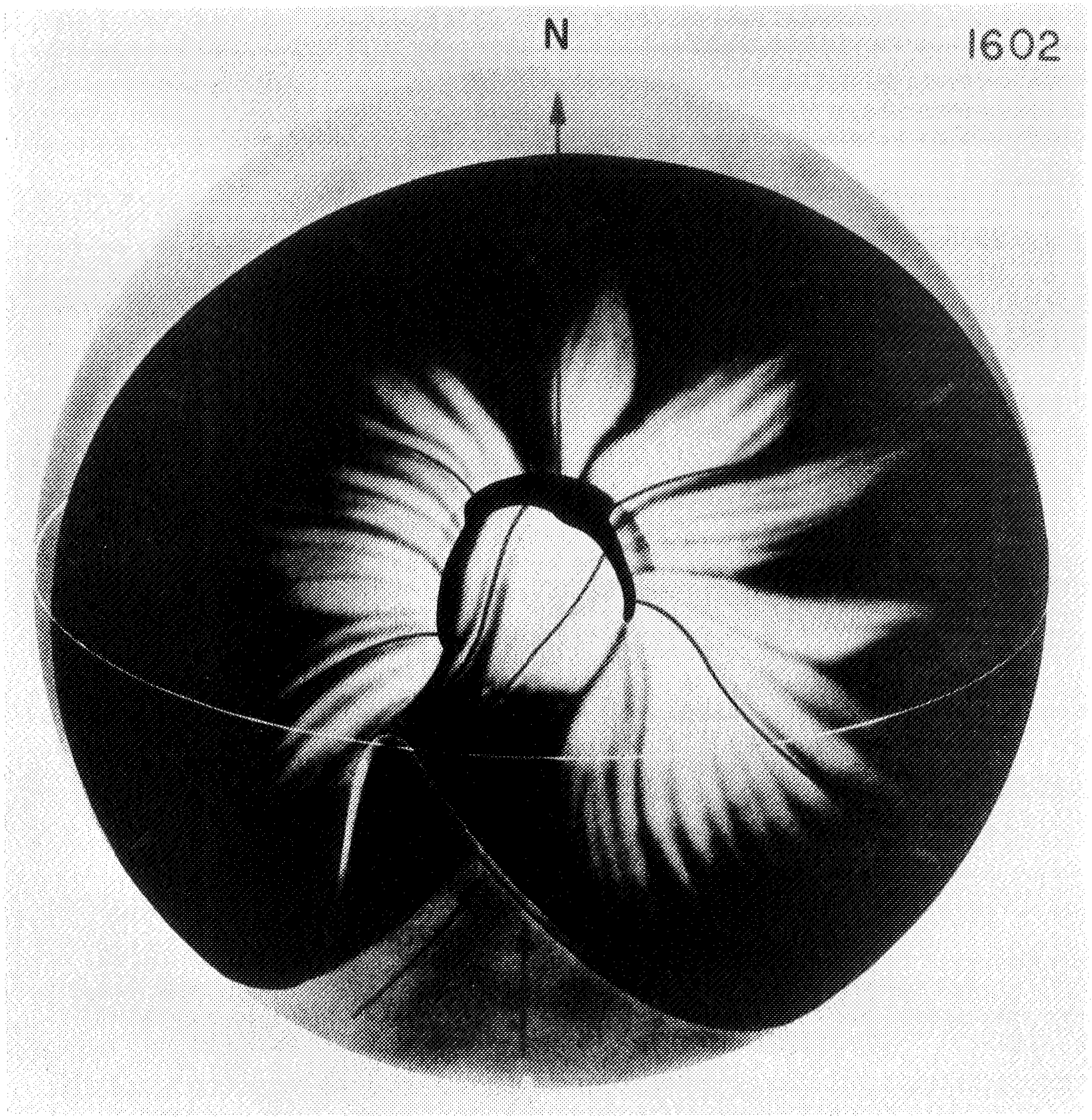

Figure 1-8. Schematic drawing of a realistic structure for the solar corona and neutral sheet, typical of the declining phase of the solar cycle. Note that the neutral sheet as shown crosses the ecliptic more than twice [1-15].

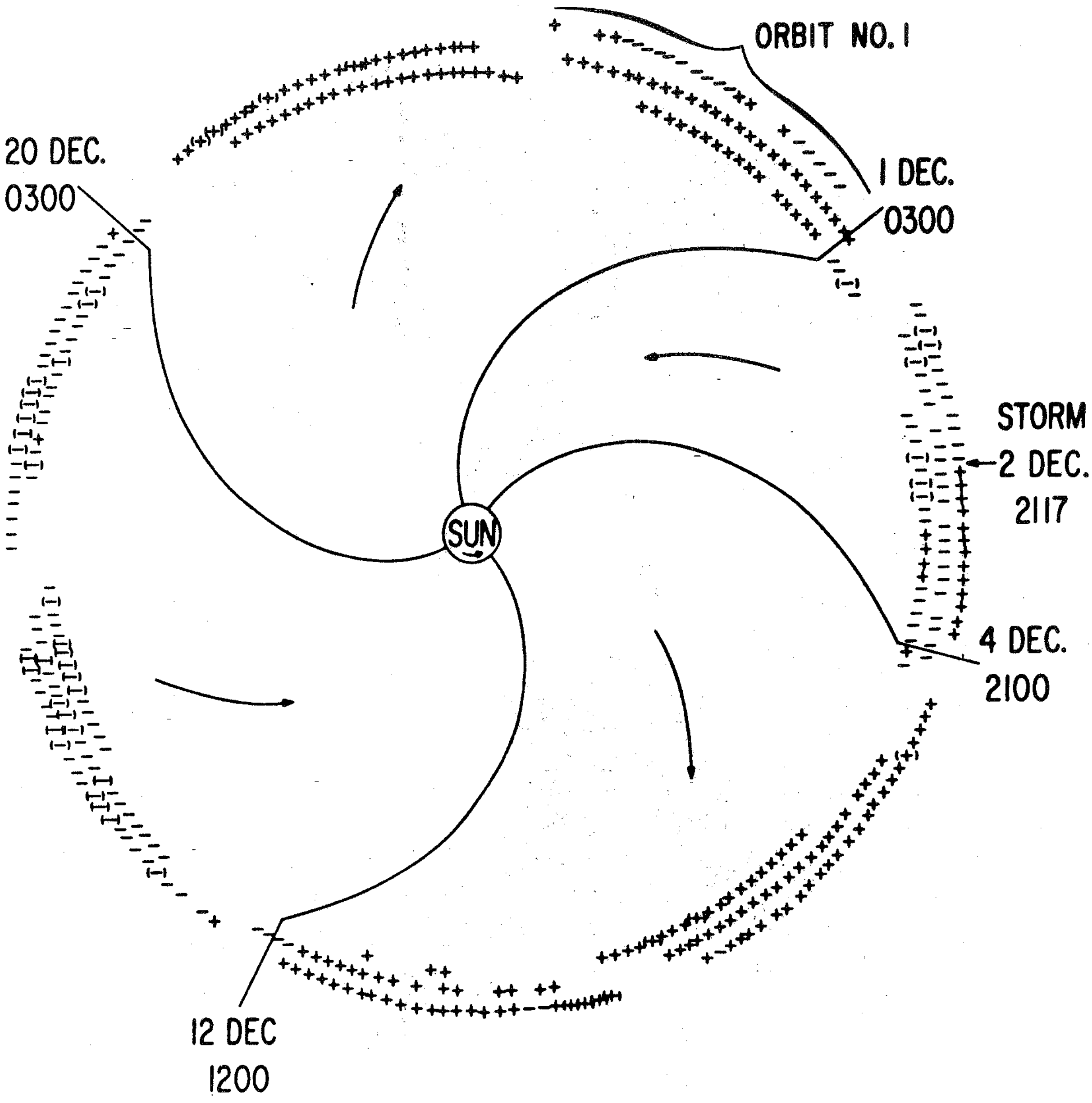

Figure 1-9. Observed polarity of the interplanetary magnetic field at 1 AU and the spiral-shaped magnetic sector boundaries inferred from field observations [1-18].

and allow hot coronal plasma to stream directly into interplanetary space. The streaming lowers the corona density to produce the so-called "hole" observed in coronal X-ray emission maps. These streams also have an Archimedes spiral shape but are less tightly wound than the ambient solar wind because of greater flow speed.

The overtaking of slower moving interplanetary material by a high-speed stream eventually produces a shock front along the leading edge of the stream (Fig. 1-10). At those times during the solar cycle when coronal holes and high-speed wind streams are present, the shocks and spiral tracks of the long-lived streams play an important role in particle acceleration and modulation of the flux of energetic particles in the outer regions of the heliosphere.

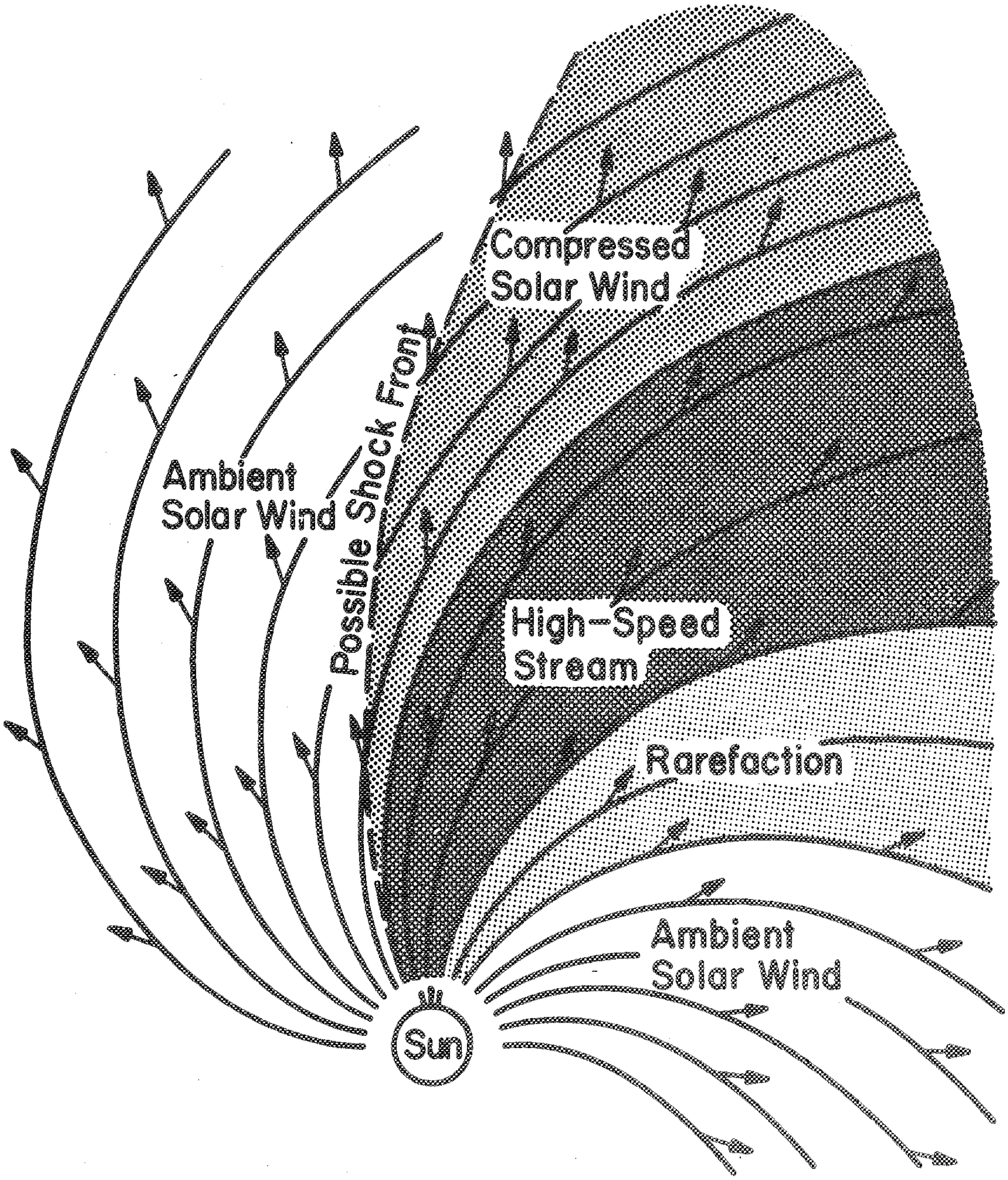

Figure 1-10. Schematic drawing showing how shock fronts are produced [1-19].

Hundhausen [1-15] summarized the properties of four high-speed streams in Table 1-5. Although the proton density in a high-speed stream is lower than for the mean solar wind, the velocity is higher and the particle flux remains about the same (a few × 10^8 protons cm^{-2} sec^{-1}). The magnetic field strength in streams is much higher than in the mean solar wind.

Figure 1-11 shows the observed variation of flow speed, density, and temperature with time as a high-speed stream passed by the Vela 3 spacecraft in 1966. Notice the shock front and rarefaction region trailing behind it.

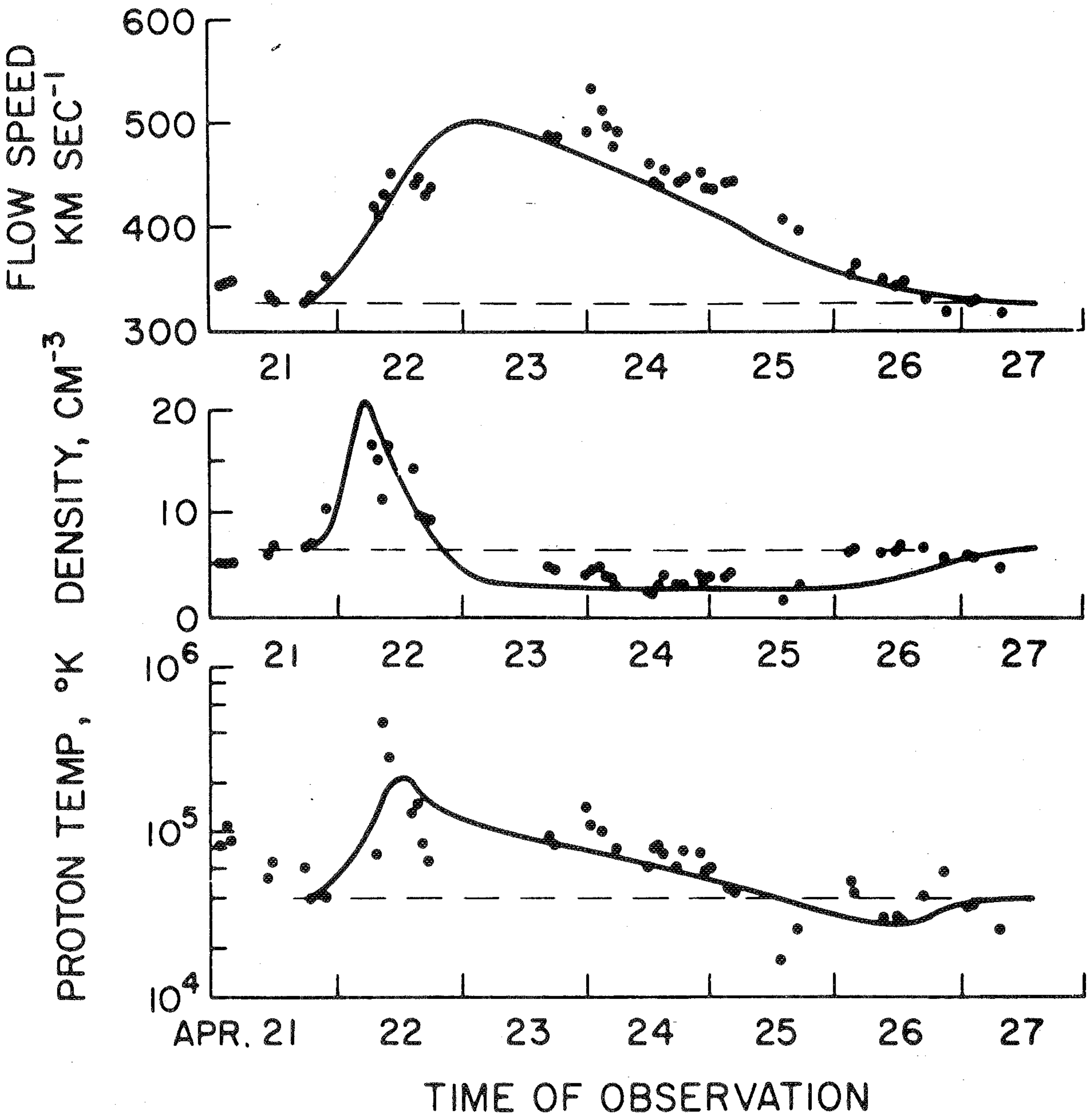

Figure 1-11. Seven-day time profiles of velocity, density, and temperature for a well-defined high-speed solar wind stream. Observations (dots) made by VELA-3 in April 1966. (The curves are from a theoretical model.) [1-19]

Hundhausen [1-15] suggests that the high-speed streams are at the high-speed limit, while the flow near a neutral sheet is the low-speed limit (300 km sec^{-1}). Since the solar poles have permanent coronal holes for most of the solar cycle, they may be the sites of long-lived, high-speed streams perpendicular to the ecliptic; the existence of such solar streams is only conjecture since all observations to date have been confined to ±30 deg of the ecliptic plane.

1.6.4 Coronal Transients

Solar material, at times, is suddenly ejected into space with velocities on the order of 1000 to 1500 km/sec, producing shock fronts as the fast material snow plows through the ambient wind, just as occurs for high-speed streams. In many cases such transients take place in the solar corona without the occurrence of a flare in the lower solar atmosphere. Many appear to be associated with the eruption of large, normally stable solar prominences. So, added to the picture of a wobbling neutral sheet and spiraling streams in the heliosphere are parcels of coronal plasma traveling at speeds of about 2X the solar wind which occur randomly in time. Models of the heliosphere with such parcels distributed along spiral tracks have been studied in the cosmic-ray modulation problem, but their role in the acceleration and diffusion of energetic particles is not yet understood. These transients are called coronal transients; they appear to be a true coronal phenomenon, possibly arising from large-scale topological rearrangement of the magnetic fields that extend into the outer solar atmosphere.

1.6.5 Spatial Variation of Solar Wind Properties

Our conception of the solar wind structure is strongly biased by the predominances of measurements in the plane of the ecliptic and near the Earth. However, estimates of the solar wind density at heliographic latitude up to 26 deg have been obtained from data taken on the Viking spacecraft during the last solar minimum in 1976 (Muhleman and Anderson [1-20]). They find the density to decrease according to a linear combination of two power laws with $r^{-2.7}$ and r^{-2} radial dependences, but the $r^{-2.7}$ term disappears at latitudes above 20 deg, leaving only the r^{-2} dependence. This behavior is expected from the simple models shown in Figures 1-6 and 1-7 where the plasma is confined in the equatorial region by the dipole field. At higher latitudes the flow straightens the field lines to allow the density to follow an r^{-2} dependence expected from number density conservation.

The mean solar wind speed increases with solar latitude, and the current estimates of the latitudinal gradient range from 2 km sec^{-1} deg^{-1} to 15 km sec^{-1} deg^{-1}. Stable plasma streams are believed to flow from the solar poles with velocities on the order of 700 km sec^{-1}.

1.6.6 Variation of the Solar Wind During the Solar Cycle

In situ measurements of the properties of the solar wind show variability at all time scales. Changes in averages over time periods of the order of the 11-year solar activity cycle have been attributed, at least in part, to the relatively greater number of high-speed streams that appear during the declining phase of the cycle. The magnitude of the interplanetary magnetic field remains relatively constant, though its components are extremely variable. The helium abundance appears to vary in phase with the solar cycle.

The spatial and temporal structure of the solar wind also varies during the solar cycle. The pattern of change is determined by the cyclic variation of the surface magnetic fields on the Sun. Hundhausen's picture of the variation begins with the reversal in the solar magnetic field polarity that occurs approximately 2 years after the maximum of solar activity. At this time the Sun's polar fields strengthen, and the two polar coronal holes reappear as stable structures lasting for the next 6 years or so. As the number of active regions declines, the solar magnetic field pattern at low latitudes evolves into larger and larger structures of the same magnetic polarity. This in turn leads to the appearance of small, short-lived coronal holes at latitudes below 45 deg. The solar wind now begins to show short-lived streams with moderate plasma flow speeds. This magnetic evolution to larger scale structures continues through the declining phase of the cycle until the low-latitude coronal holes connect with the polar holes and appear as low-latitude extensions of the magnetic polar caps. During this time the solar wind is dominated by high-speed solar wind streams lasting for several solar rotations. Empirically, these effects appear as the 27-day recurrence patterns commonly seen in geomagnetic activity and solar wind speed and magnetic sector structure.

Figure 1-12 shows the daily averaged polarity of the interplanetary magnetic field at 1 AU as inferred from ground-based observations of the geomagnetic field. The data are arranged into rows of 27 days so that recurrent sectors associated with long-lived features on the Sun appear as columns of predominantly one polarity.

Notice the bimodal nature of the display for the 2 or 3 years before the minimum of solar cycle 20 (early 1976). This has been clearly identified with two large and long-lived coronal holes which extended to the equator from the north and south polar holes at roughly opposite sides of the Sun. These holes and their associated high-speed wind streams are shown in Figure 1-13. Notice that the magnetic field polarities of the streams (indicated by + and - symbols and taken from the data of Fig. 1-12) agree with the polarities of the holes as inferred from measurements of the underlying photospheric fields (indicated similarly on the coronal maps).

As the active regions associated with the next solar cycle appear at heliographic latitudes of about 45 deg, the polar cap fields begin to weaken, and the scale of low-latitude coronal holes decreases. During the rising part of the 11-year cycle, high-speed streams occur less frequently. The surface field structure on the Sun becomes more chaotic, and the frequency of transients such as solar flares increases. This evolution toward a more chaotic condition continues until solar activity peaks, and the process begins to repeat itself.

1.7 HIGH-ENERGY PARTICLES IN THE HELIOSPHERE

At the beginning of the 20th century, experiments on the conductivity of air led to the discovery of a flux of high-energy particles at the Earth. These early studies established that the most energetic particles arrive at the Earth from all directions and, for this reason, they were called galactic cosmic rays. During the 1940s, however, lower energy particles observed at high altitudes were definitely identified as solar in origin. They are frequently associated with large solar flares.

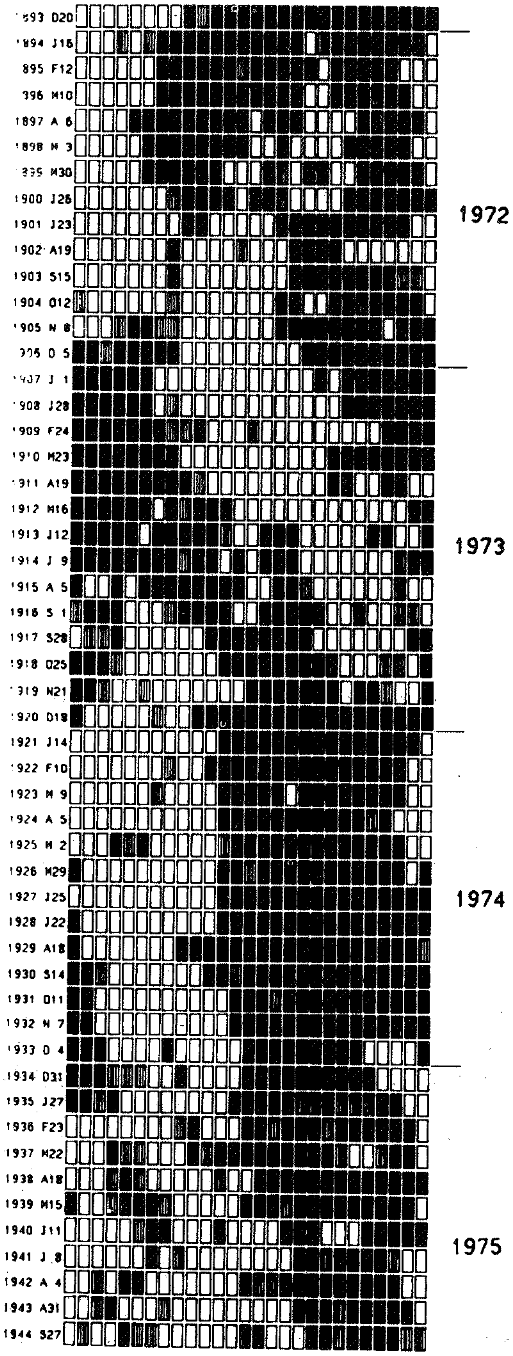

Figure 1-12. The daily averaged polarity of the interplanetary magnetic field at 1 AU, arranged in rows of 27 days to show the long-lived sectors [1-15].

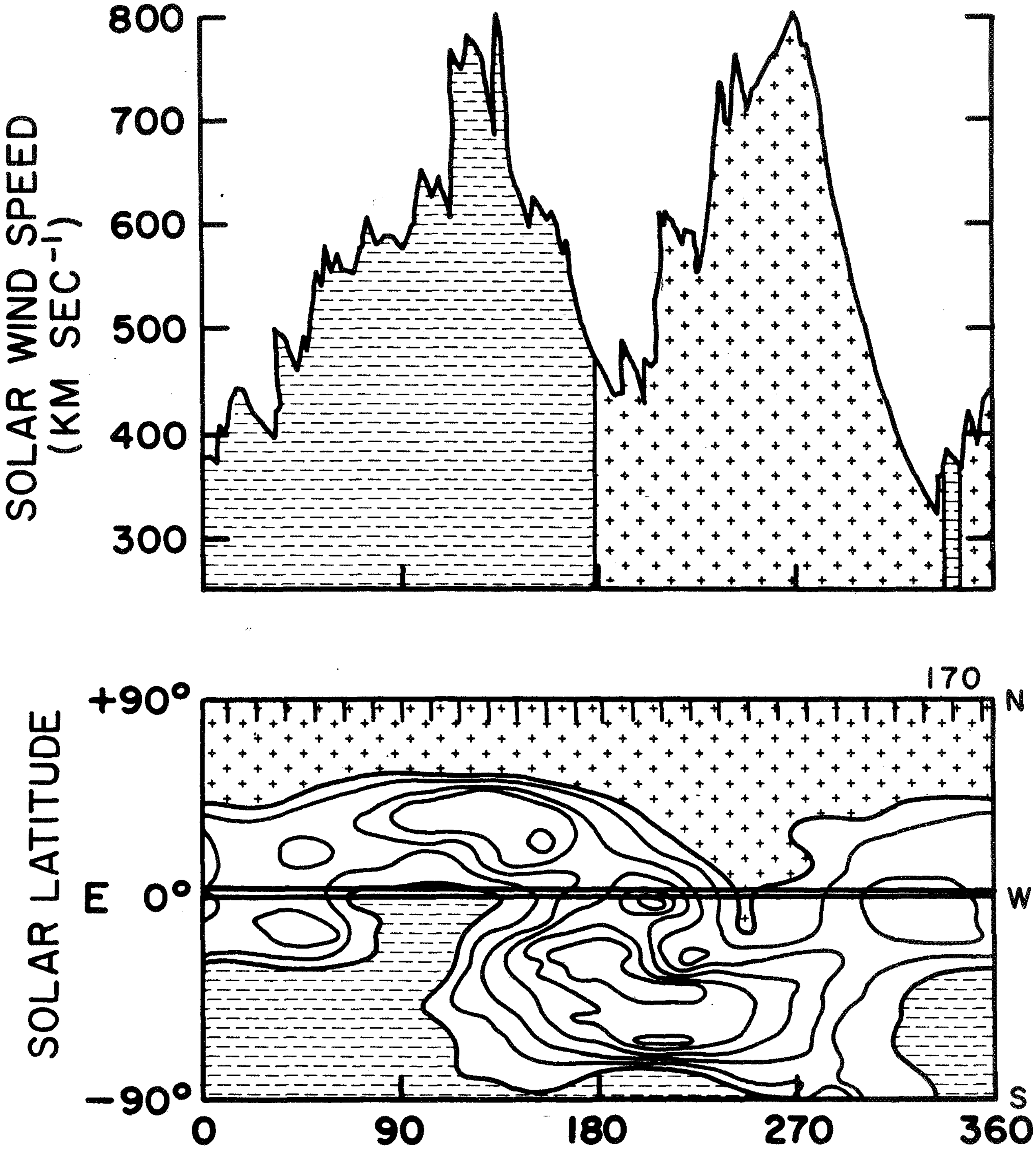

Figure 1-13. Top: Solar wind speed observed by spacecraft at 1 AU. + and - indicate magnetic polarity [1-15]. Bottom: Coronal brightness contour map showing the north and south polar coronal holes in 1974. (Carrington longitude refers to a coordinate system fixed on the Sun which rotates rigidly with a period of 27.14 days as seen from the Earth.)

The mean energy of the galactic component is on the order of 10 BeV, with energies as high as 10^9 BeV. Solar particle energies rarely exceed 1 BeV, and they have a mean energy on the order of 100 MeV.

All of the elements from hydrogen up to iron in the periodic table have been identified in cosmic rays, but their abundances depart substantially from the standard cosmic abundance; cosmic rays are abnormally rich in carbon and the heavier elements such as iron. This abnormal composition is attributed to the ultimate sources of the particles in the galaxy. Figure 1-14 shows the galactic cosmic-ray energy spectra for various species. Cosmic rays remain objects of research in cosmology, solar physics, high-energy physics, magnetohydrodynamics, and stellar structure.

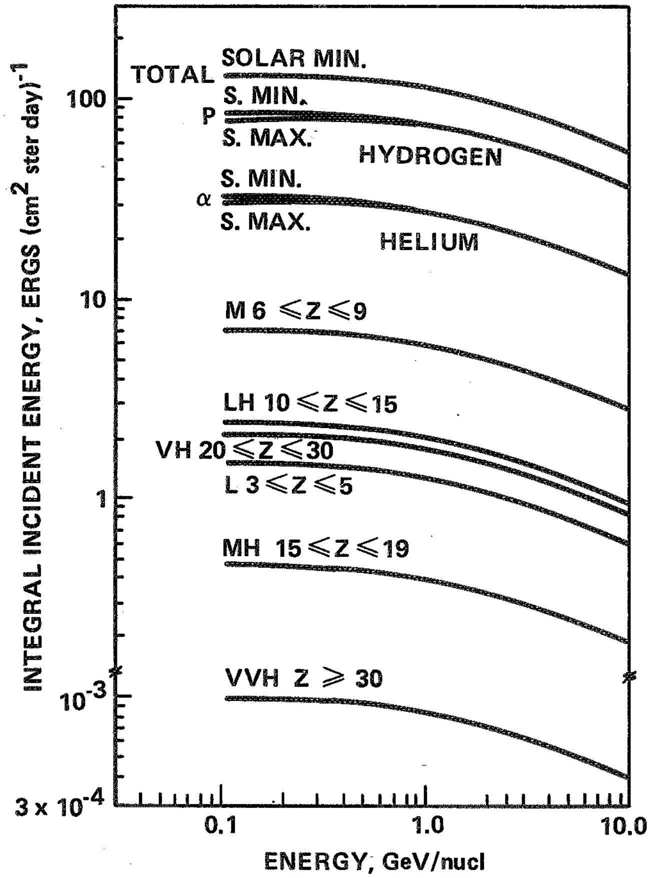

Figure 1-14. Integral energy intensities for galactic cosmic ray nuclei [1-21].

The most fascinating mystery about galactic cosmic rays is their origin. Local source conditions must be extreme to accelerate particles to BeV energies, and supernovae are prime candidates.

1.7.1 High-Energy Particles from the Sun

There are two classes of high-energy particles of solar origin, both closely associated with very large solar flares and eruptions often occurring in the declining phase of the 11-year solar cycle. The frequency of their occurrence tends to follow the degree of solar activity. The two components are distinguished by their arrival time at the Earth and, hence, their energies. The highest energy particles arrive at the Earth approximately 20 min after the occurrence of a large flare; they appear to be accelerated particles directly emitted from the flare volume. The second component is observed approximately 24 hr later in association with a magnetized plasma cloud passing by the Earth. These late arrivals appear to be trapped within the plasma cloud and carried to the Earth at speeds of about 1000 km/sec. They enter the Earth's atmosphere isotropically as the cloud envelopes the Earth, whereas the higher energy component is strongly directional, coming predominantly from the western hemisphere of the Sun. This east to west asymmetry for location of source regions on the Sun shows that the particles have spiral trajectories similar to the pattern of interplanetary magnetic field frozen into the radial solar wind flow, and this immediately establishes the ability of relatively weak magnetic fields (3×10^{-5} gauss) to influence the particle diffusion over long distances in the heliosphere.

Because of their close association with large flares, the energetic particle bursts are relatively infrequent. For example, only 34 events occurred with particle energies greater than 30 MeV in solar cycle 19 (1954 to 1965), while for cycle 20 (1965 to 1976) there were fewer than 20 such events. For this reason, such high-energy particle events are unimportant in total energy relative to the much slower but steady solar wind. Typical proton fluxes at 1 AU are 10 to 100 protons cm^{-2} $ster^{-1}$ sec^{-1} with energies above 10 MeV, but this falls to below 10 protons cm^{-2} $ster^{-1}$ sec^{-1} for particles above 30 MeV, illustrating the steepness of the energy spectra of particle bursts associated with flares [1-21]. The total number of protons associated with single events is 10^7 - 10^8 protons cm^{-2} on the average, but the particularly intense bursts deposit 10^{10} protons cm^{-2} at energies greater than 10 MeV.

The higher energy particles are easier to detect, and most of our experience to date is for energies above 10 MeV. Improved detectors for particles with energies less than 10 MeV show the existence of a fluctuating background. The Sun is apparently a continuous emitter of these lower energy particles. They appear to come from active regions, but the continuous fluctuation in flux level prevents association with particular events such as sub-flares.

Figure 1-15 shows energy spectra for protons and alpha particles for seven major events between 1967 and 1969.

Lanzerotti [1-21] discusses the solar cycle cosmic ray variation; his figure for variability of the solar component is shown as Figure 1-16. The solar component follows the activity cycle, with the largest number of events occurring near solar maximum when the flare production rate is the highest. For reasons not yet understood, the most intense particle events tend to occur approximately 2 years after the maximum.

1.7.2 Influence of Solar Activity on Energetic Particle Fluxes

Even though galactic cosmic rays themselves are not related to the Sun, their flux at the Earth is modulated by solar plasma effects. These very high-energy particles arrive at the Earth uniformly from all directions. Records made at the time of great solar flares show a decrease in the observed galactic flux level beginning 24 to 48 hr after the flare. These decreases, known as Forbush decreases, are on the order

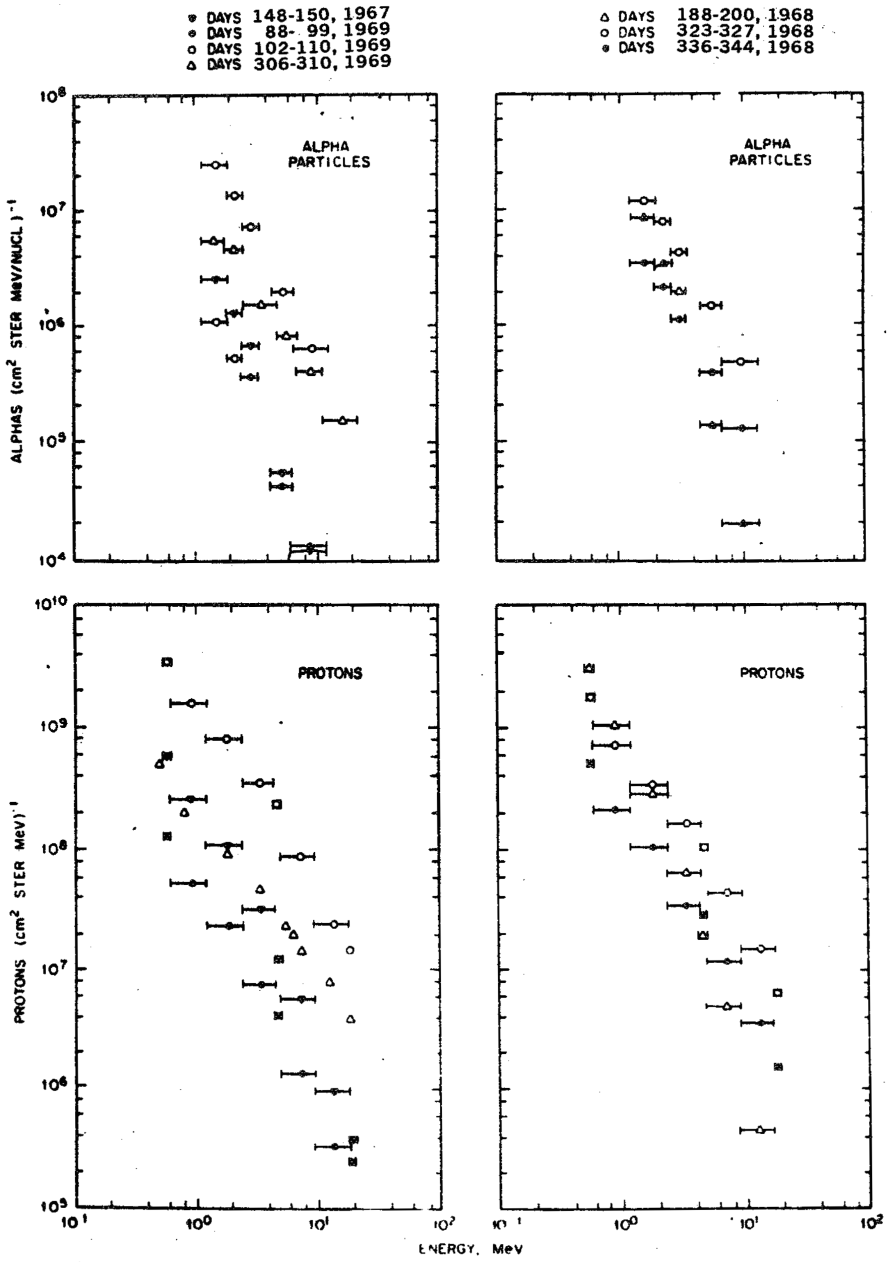

Figure 1-15. Event-integrated proton and α particle spectra for seven major events between 1967 and 1969 [1-21].

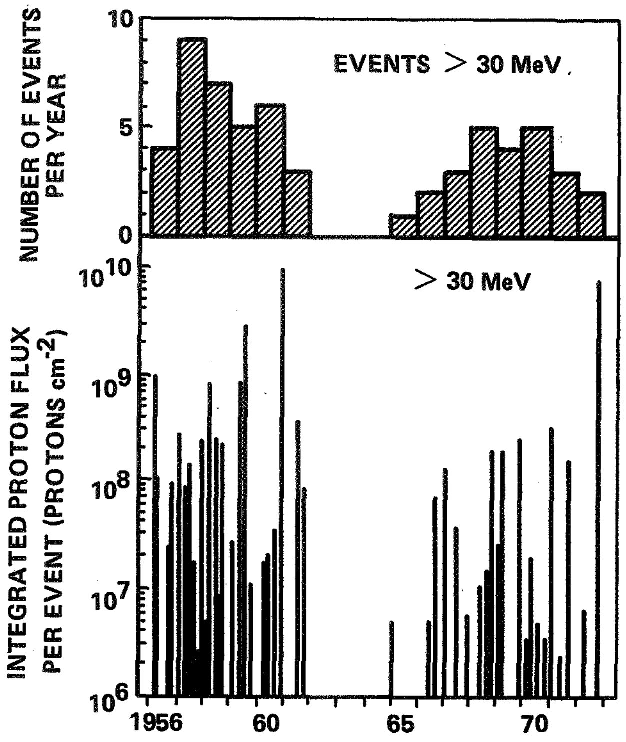

Figure 1-16. Variability of the solar component [1-4].

of 10 percent and may last for several days before the galactic intensity recovers its preflare level. This effect coincides with the passage of a cloud of solar plasma which disturbs the local conditions for diffusion and propagation of high energy particles.

Figure 1-17 shows galactic cosmic rays plotted together with the Zurich sunspot number [1-22]. The galactic component is strongest at solar minimum and weakest at solar maximum. This modulation is almost 100 percent for energies below 500 MeV, according to Lanzerotti [1-21], but drops to a few percent at energies of 100 BeV. It is believed to arise from the interaction of the high-energy particles with high-speed plasma clouds and shocks produced by transients on the Sun. The modulation effect is the subject of intense study and controversy at the present time.

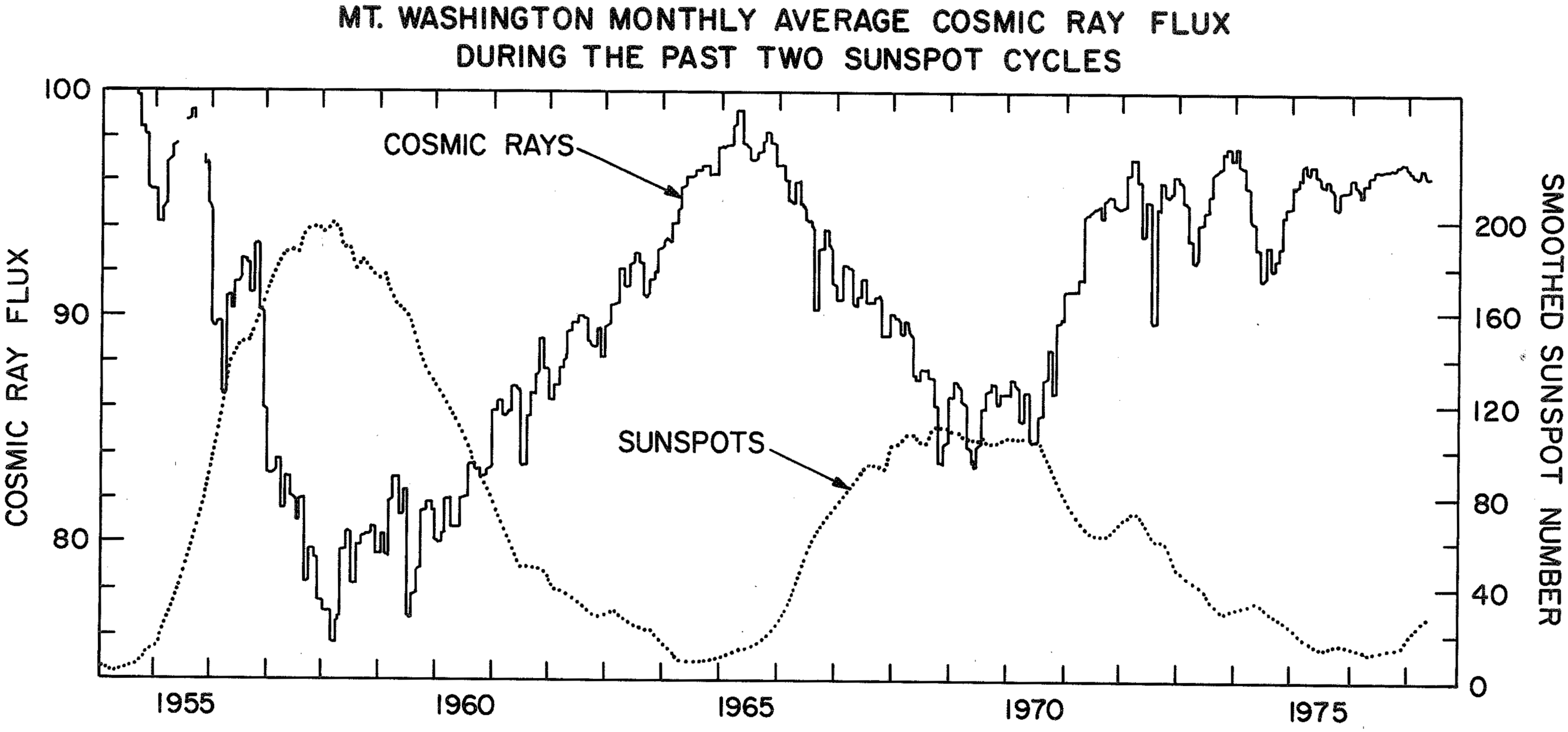

Figure 1-17. Galactic cosmic rays reaching the inner solar system and the Earth are modulated by the solar cycle.

REFERENCES

1-1. Bahcall, J. N. and Davis, R.: An Account of the Development of the Solar Neutrino Problem. Essays in Nuclear Astrophysics, Chapter 12; edited by C. A. Barnes, D. D. Clayton, and D. N. Schramm; Cambridge University Press, to be published (early 1982).

1-2. Newkirk, G. (editor): Study of the Solar Cycle from Space: Solar Cycle and Dynamics Mission. NASA SCADM-3, 1980.

1-3. Gibson, E. G.: The Quiet Sun. NASA, Washington, D.C., 1973.

1-4. Livingston, W. C.: Solar-Terrestrial Influences on Weather and Climate. Ohio State Symposium, B. M. McCormack and T. A. Seliza (editors), D. Reidel Publ. Co., Boston, 1979.

1-5. NOAA: Solar-Geophysical Data. U.S. Department of Commerce, 1981.

1-6. White, O. R. (editor): The Solar Output and Its Variation. Colo. Assoc. Univ. Press, Boulder, 1977.

1-7. Willson, R. C.: Active Cavity Radiometer Type IV. Appl. Opt., vol. 18, pp. 179-188, 1979.

1-8. Frolich, C.: Contemporary Measures of the Solar Constant. The Solar Output and Its Variation, Chapter 3, Colo. Assoc. Univ. Press, Boulder, 1977.

1-9. Willson, R. C. and Hickey, J. R.: 1976 Rocket Measurements of the Solar Constant and Their Implications for Variation in the Solar Output in Cycle 20. The Solar Output and Its Variation, Chapter 3, Colo. Assoc. Univ. Press, Boulder, 1977.

1-10. Hickey, J. R., Stowe, L. L., Jacobowitz, H., Pellegrino, P., Maschoff, R. H., House, F., and VonderHaar, T. H.: Initial Solar Irradiance Determinations from Nimbus 7 Cavity Radiometer Measurements. Science, vol. 208, pp. 700-702, 1981.

1-11. Willson, R. C., Gulkis, S., Janssen, M., Hudson, H. S., and Chapman, G. A.: Observations of Solar Irradiance Variability. Science, vol. 211, pp. 700-702, 1981.

1-12. Hickey, J. R., Alton, B. M., Griffin, F. J., Jacobiwitz, H., Pellegrino, P., and Smith, E. A.: Proc. Symp. on the Solar Constant and the Spectral Distribution of Solar Irradiance. Hamburg, 1981.

1-13. Foukal, P. V.: in Proceedings of the International Conference on Sun and Climate. Toulouse, CNES, 1981.

1-14. Heath, D. F.: in Proceedings of the International Conference on Sun and Climate. Toulouse, CNES, 1981.

1-15. Hundhausen, A. J.: Coronal Holes and High Speed Wind Streams. Chapter 7, J. B. Zirker (editor), Colorado Assoc. Univ. Press, Boulder, 1977.

1-16. Feldman, W. D., Asbridge, J. R., Bame, S. J., and Gosling, J. T.: Plasma and Magnetic Fields from the Sun. The Solar Output and Its Variation, Chapter 5, Colo. Assoc. Univ. Press, Boulder, 1977.

1-17. Parker, E. N.: Dynamics of the Interplanetary Gas and Magnetic Fields. Astrophys. J., vol. 128, pp. 664-676, 1958.

1-18. Hundhausen, A. J.: Corona Expansion and the Solar Wind. Springer-Verlag, New York, 1972.

1-19. Holzer, J. R.: Solar System Plasma Physics. Vol. 1, North Holland Publishing Co., 1979.

1-20. Muhleman, D. O. and Anderson, J. D.: Solar Wind Electron Densities from Viking Dual-Frequency Radio Measurements. Astrophys. J., vol. 247, pp. 1093-1101, 1981.

1-21. Lanzerotti, L. J.: Measures of Energetic Particles from the Sun. The Solar Output and Its Variation, Chapter 5, Colo. Assoc. Univ. Press, Boulder, 1977.

1-22. Morall, H.: Observations of the Eleven-Year Cosmic-Ray Modulation Cycle. Sp. Sci. Rev., vol. 19, pp. 845-920, 1976.

SECTION 2. TERRESTRIAL SPACE (THE EARTH)

2.1 INTRODUCTION

The region of space discussed in this chapter extends from approximately 80-km altitude above Earth's surface, the lower boundary of the ionosphere, to the boundary of the Earth's magnetosphere, where the unperturbed interplanetary medium is reached. Thus it extends to the bow shock approximately 100,000-km radial distance (16 Earth radii, R_e) in the sunward direction, and down the magnetospheric tail in the anti-sunward direction, to a larger distance whose actual value depends on the effect of interest. This distance may extend beyond the lunar orbit at 60 R_e (approximately 385,000 km). "Terrestrial Space" includes the orbits of lower artificial Earth satellites to beyond the geostationary orbit (approximately 7 R_e).

A spacecraft operating in this volume is affected by the following:

Environmental factors	Effects
Earth's gravity	Acceleration, torque
Neutral atmosphere	Heating and drag, torque
Sunlight and albedo light	Heating and power, drag, torque
Magnetic field	Torque, surface charges, induced electrical potential
Electric field	Electric potential
Thermal plasma	Charging, change of refractive index for em waves
Fast charged particles	Ionization, radiation damage
Meteoroids	Mechanical damage

It is not possible in a single chapter to explain all the interactions which influence the Earth's atmosphere, ionosphere, and magnetosphere. Indeed, the detailed quantitative understanding of Terrestrial Space in terms of fundamental physics is still on the frontier of research. However, much useful information has been gained from ground-based and space measurements and partial theoretical understanding has been achieved.

The following paragraphs briefly describe the physical relationships between different parts of Terrestrial Space. Succeeding paragraphs describe the most important factors quantitatively using empirical or parametric models. For an excellent general reference review the AFCRL Handbook of Geophysics [2-1].

2.2 GENERAL DISCUSSION

The gravitational field results from the mass of the solid Earth and reflects the distribution of that mass. It traps the neutral atmosphere.

Above approximately 90-km altitude the ion-electron pairs, formed in sunlight by photoionization and, to a lesser extent, collisional ionization by cosmic rays and auroral particles, recombine so slowly that in quasi-equilibrium an appreciable plasma density forms. While the plasma density remains less than the neutral density below an altitude of 10^3 km, electrical forces dominate the behavior of the plasma above approximately 90 km where the electron cyclotron and plasma frequencies (1 to 3 MHz) exceed the collision frequency of electrons with neutrals. The ionospheric plasma is most dense at 200 to 400 km and supplies plasma to higher altitudes by bulk flow. At the 100 to 200-km level the ionosphere has some electrical conductivity perpendicular to the magnetic field, $\underset{\sim}{B}$, because of collisions with neutrals. (At higher and lower altitudes this conductivity is very small.) Parallel conductivity is larger than the perpendicular at all altitudes.

The magnetic field has two sources: currents inside the Earth and currents in the magnetosphere. At the surface approximately 99 percent of the field is due to internal currents. Without the solar wind flowing past the Earth, this intrinsic geomagnetic field would decrease with distance with the dominant dipole term giving a $1/r^3$ dependence. It would have approximate cylindrical symmetry about the dipole axis, inclined approximately 11 deg to the Earth's rotation axis. In fact, the solar wind plasma cannot penetrate the geomagnetic field freely. It compresses the field to about 10 R_e distance at the subsolar point and flows around the volume in which the field is thus confined. The magnetic field lines from the polar regions of Earth, which would have reached an equatorial distance greater than 10 R_e, are dragged along by the solar wind to form a tail. Figure 2-1 shows the resulting shape of the magnetosphere. Another way to describe this phenomenon is to note that the solar wind plasma in flowing around the magnetosphere produces electric currents which, when added to the Earth's internal currents, produce the field of Figure 2-1. Figure 2-2 shows the bow shock, approximately 4 R_e sunward of the magnetopause. The supersonic solar wind, flaring back around it, is slowed down and partially thermalized.

Although most impinging solar wind flows around the magnetosphere, some flows in at the cusps, as magnetic flux is peeled off the sunward side and laid back along the tail. More plasma, energy, and momentum diffuse in along the flanks of the tail. (Details of these mechanisms are not established.) Thus there is general anti-sunward flow of plasma and magnetic flux over the polar caps and along the tail in the magnetopause boundary region. The plasma and magnetic flux diffuse inward, coupled with migration of the field lines tied to the rotating Earth. Moving within the plasma sheet, they convect sunward (toward Earth) to approximately 4 R_e, where positive and negative particles then move in opposite directions around the Earth and out through the sunward magnetopause where they join the westward flowing ring current.

Inside the plasmapause, at approximately 4 R_e in the equatorial plane on the antisunward side, the magnetic field is dipole-like and co-rotates with the Earth. The particle density in the plasmasphere, which is filled with ions and electrons drawn up from the ionosphere, is relatively greater than in the convection region outside.

At any point where the plasma convection velocity is $\underset{\sim}{v}$ and the magnetic field $\underset{\sim}{B}$ there is an electric field $\underset{\sim}{E} = \underset{\sim}{v} \times \underset{\sim}{B}$ normal to $\underset{\sim}{B}$. Because the conductivity is very high along $\underset{\sim}{B}$ and very low perpendicular to it (with certain local exceptions), the

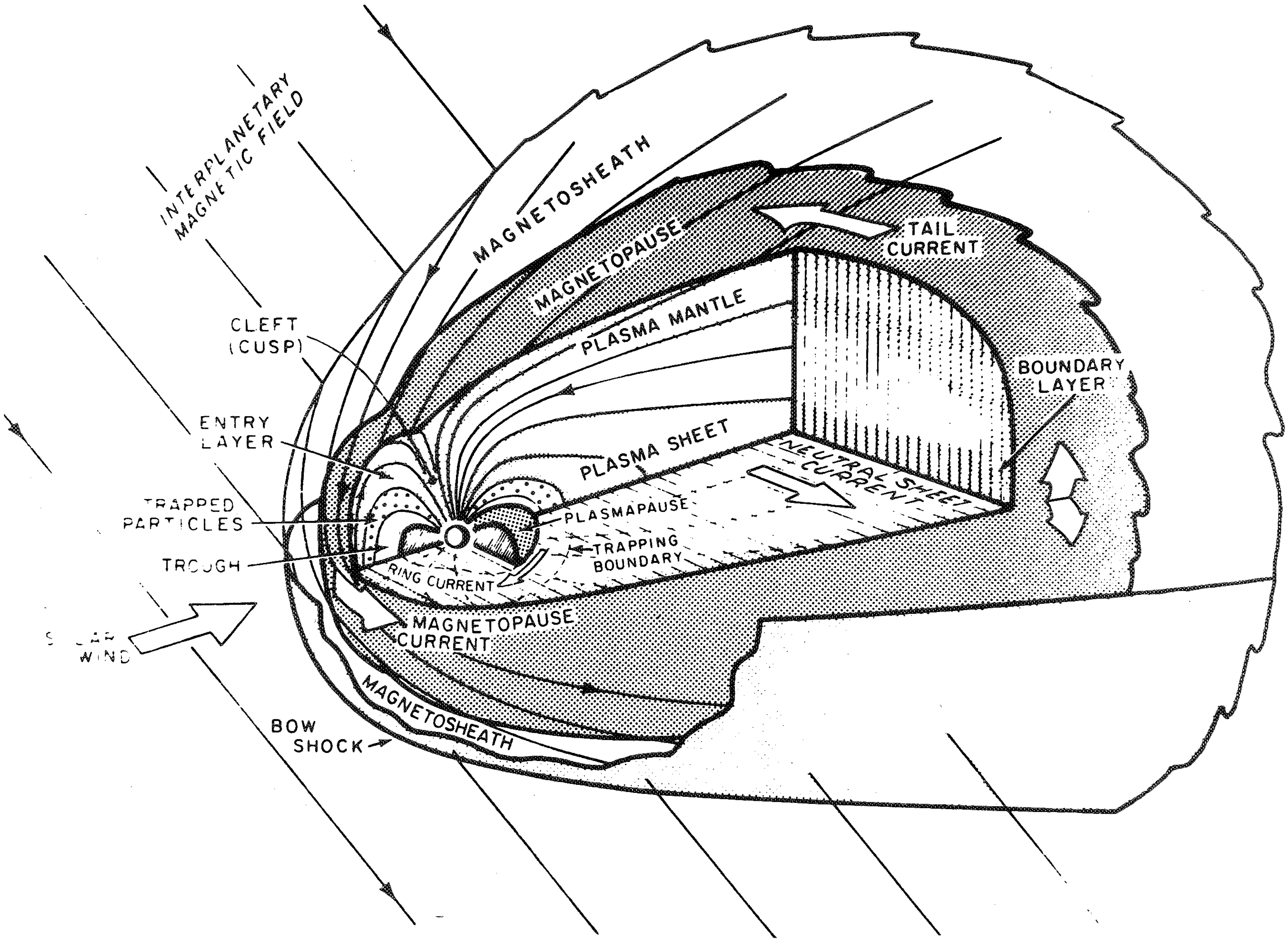

Figure 2-1. Schematic view of the magnetosphere (courtesy of W. Heikkila) [2-2].

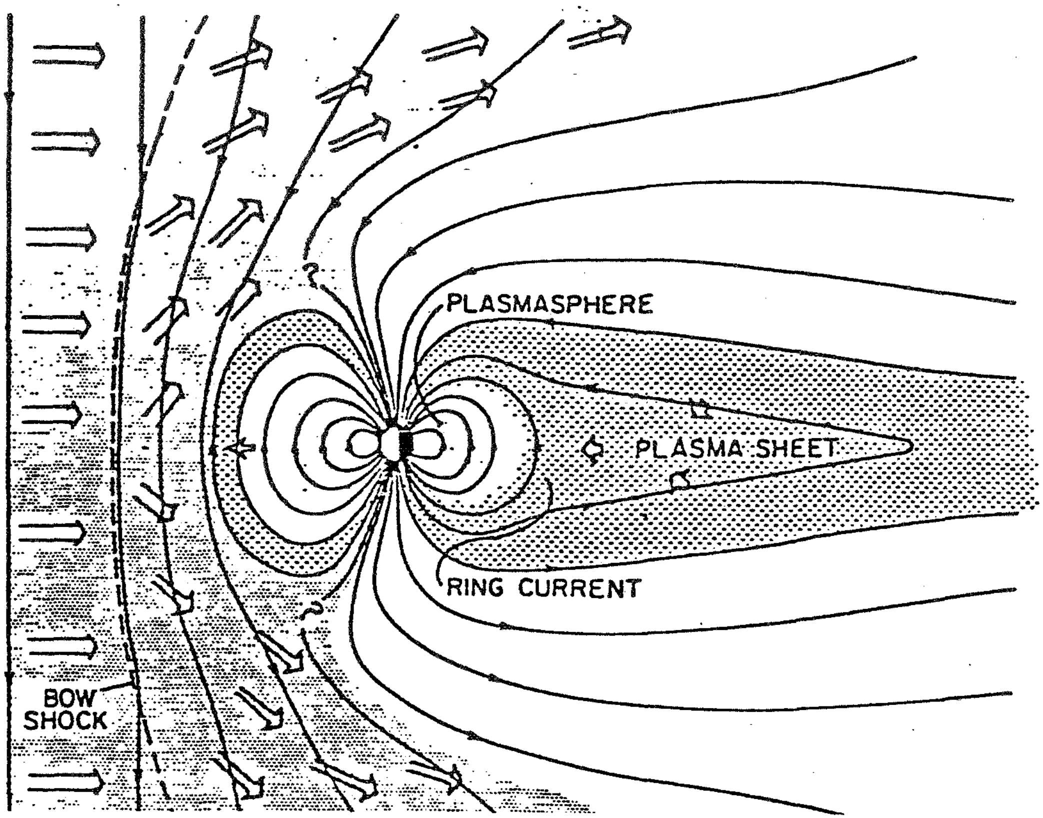

Figure 2-2. Plasma convection through the magnetosphere. (Question marks designate the assumed connection of geomagnetic and interplanetary field lines. Hollow arrows represent flow directions. The view is of a north-south meridional plane, with the Sun to the left; the dawn side of the Earth is in back, dusk side is above the page [2-3].)

electrical potential difference between any two magnetic field lines is constant so that electric fields generated by convective flow in one region are mapped along $\underset{\sim}{B}$ to other regions, including the ionosphere. The ionospheric conductivity across $\underset{\sim}{B}$ is relatively high so that currents flow there and dissipate energy by Joule heating. The ionospheric currents are supplied from the generating region of convection by field-aligned (Birkeland) currents.

Another important manifestation of the extraction of energy from the solar wind is the acceleration of ions and electrons to high, even relativistic, energies. Some portion of these charged particles precipitate into the atmosphere to form the aurorae, which are centered at approximately 65 deg magnetic latitude around each polar cap. The rest escape the magnetosphere, and some are trapped for a time as the Van Allen radiation.

The processes described above fluctuate substantially. Fluctuations are produced by variations in solar wind speed and density and changes in the imbedded interplanetary magnetic field (IMF). Enhanced solar wind flow, compressing the magnetosphere, may lead to a world-wide magnetic storm, which gives rise to changes in the magnetic field at Earth's surface and in the size of the various magnetospheric regions. Another source of fluctuations is sudden release of magnetic energy stored in the tail producing enhanced polar ionospheric currents and auroral particle precipitation. This latter set of phenomena is called the polar magnetic substorm. The role of interplanetary medium fluctuations in triggering this particular mode of release of the stored energy is the subject of much controversy. That external effects, such as a southward turning IMF, can trigger the release is clear. However, it is likely that the energy buildup and rapid release is an intrinsic property of the magnetospheric system and would proceed even if external conditions were unchanging.

To summarize, the solar wind and IMF streaming past the magnetic field of the the Earth produce the structure shown in Figures 2-1 and 2-2. About 1.4×10^{13} W from the solar wind impinges on the front of the magnetosphere of which 2 to 3 percent is absorbed [2-4]. Of this $1\text{-}3 \times 10^{11}$ W reaches the ionosphere, 85 percent dissipates and Joule heating and 15 percent as aurorae. Incidentally, the radiant energy input of sunlight onto the top of the atmosphere is 1.75×10^{16} W.

In the succeeding pages we give brief descriptions of each environmental factor and some numerical data. Reference 2-5 gives a general discussion of magnetospheric modeling.

2.3 THE SOLID EARTH AND ITS GRAVITY

The Earth as a planet in the solar system is described by the constants in Table 2-1.

TABLE 2-1. EARTH CONSTANTS (Epoch 1960.0) [2-6, 2-7, 2-8, 2-9]

Distance from sun (average)	1.496×10^{8} km (1.0 AU by definition)
Eccentricity of orbit	0.0167295
Orbital period (sidereal)	365.25636 days
Radius (equatorial)	6378.140 km
Mass	5.977×10^{27} g
Flattening (dynamic)	1:298.256
Average density	5.517 g/cm^3
Rotation rate $\dot{\theta}$	0.72921×10^{-4} sec^{-1}
Gravitational constant, GM	3.986012×10^{5} km^3/sec^2
Inclination of equator	23.45 deg
Period of rotation (sidereal)	23.934 hr

2.3.1 The Earth's Gravitational Field

The gravitational acceleration $\underset{\sim}{g}$ can be written as the gradient of a scalar potential U,

$$\underset{\sim}{g} = \underset{\sim}{\nabla U} \quad .$$

It is convenient to write U in a spherical coordinate system as

$$U = \frac{GM}{r}\left[1 - \sum_{n=2}^{\infty} (a_e/r)^n J_n P_n(\sin \phi') + \sum_{n=2}^{\infty} \sum_{m=1}^{n} (a_e/r)^n P_{nm}(\sin \phi') \right.$$
$$\left. (C_{nm}\cos m\lambda + S_{nm}\sin m\lambda)\right]$$

where

r = radius from center of the Earth, km

ϕ' = geographic latitude

λ = geographic longitude

P_n = Legendre function

P_{nm} = associated Legendre function

GM = gravitational constant of Earth

a_e = equatorial radius of the Earth, km .

Values for the zonal harmonics (J_n) are as follows:

$J_2 = (1082.7 \pm 0.1) \times 10^{-6}$

$J_3 = (-2.56 \pm 0.1) \times 10^{-6}$

$J_4 = (-1.58 \pm 0.2) \times 10^{-6}$

$J_5 = (-0.15 \pm 0.2) \times 10^{-6}$

$J_6 = (0.59 \pm 0.2) \times 10^{-6}$

$J_7 = (-0.44 \pm 0.2) \times 10^{-6}$

Values for the tesseral harmonics (C_{nm}, S_{nm}) are as follows:

n	m	C_{nm}	S_{nm}
2	2	1.57×10^{-6}	-0.897×10^{-6}
3	1	2.10×10^{-6}	0.16×10^{-6}
3	2	0.25×10^{-6}	-0.27×10^{-6}
3	3	0.077×10^{-6}	0.173×10^{-6}
4	1	-0.58×10^{-6}	-0.46×10^{-6}
4	2	0.074×10^{-6}	0.16×10^{-6}
4	3	0.053×10^{-6}	0.004×10^{-6}
4	4	-0.0065×10^{-6}	0.0023×10^{-6}

($C_{21} = S_{21} = 0$)

These coefficients have been determined from surface gravity measurements and satellite orbit observations [2-7,2-8]. The zonal harmonics (J_2, J_3, J_4 ...) have a greater effect on the orbit of a satellite than the tesseral harmonics. The tesseral harmonics cause oscillatory disturbances that change sign rapidly, but the effect of zonal harmonics is cumulative. The even coefficients, J_2, J_4 ..., can be determined from the regression of an artificial Earth satellite orbit's node and the rotation of its perigee. Reliable gravitational coefficients have been obtained from low-altitude artificial satellites.

A significant geodetic result thus obtained is the reliable determination of J_2 and, hence, the flattening f. Presently accepted values of 1/f range from 298.2 to 298.3. This flattening of the Earth causes the largest deviation of the gravitational field of the Earth from that of a homogeneous sphere.

Numerous higher-order spherical harmonic expansions have been derived from analyses of artificial satellite motions, but because they yield divergent results, only the first few terms are tabulated here. They make the largest contribution, with additional terms giving diminishing returns.

2.3.2 An Approximate Geopotential Field

The gravitational field can be well approximated using the first three zonal harmonic coefficients (J_2, J_3, and J_4) and the main tesseral harmonic coefficients (C_{22} and S_{22}). The following expression for the gravitational potential function of the Earth is recommended for space vehicle design studies.

$$U = \frac{GM}{r}\left[1 - \frac{J_2}{2}(a_e/r)^2(3\sin^2\phi' - 1) - \frac{J_3}{2}(a_e/r)^3(5\sin^3\phi' - 3\sin\phi')\right.$$
$$- \frac{J_4}{8}(a_e/r)^4(35\sin^4\phi' - 30\sin^2\phi' + 3)$$
$$\left. + 3(C_{22}\cos 2\lambda + S_{22}\sin 2\lambda)(a_e/r)^2\cos^2\phi')\right]$$

2.4 NEUTRAL ATMOSPHERE AND WINDS

2.4.1 Neutral Atmosphere Structure

Atmospheric conditions affect Earth satellites at 90 to 1000 km altitude by producing drag and, at the lower altitudes, frictional heating. Mass density and winds are the important factors and only neutral density need be considered. Near the lower limit of the range, where atmospheric density is greatest, an unpowered spacecraft will de-orbit in a very short time; near the upper limit, the drag effect on orbital lifetime is almost negligible.

Most of the density values for the atmosphere between 90 and 2500 km have been derived from analyses of changes in the periods of orbiting satellites. Figures 2-3 and 2-4 show mass and number density of the 1976 Standard Atmosphere; Figure 2-5 shows temperature [2-10]. It should be noted that as the collision rate decreases with height a point is reached where atmospheric constituents are not completely mixed; each tends to assume its own scale height, kT/mg, with m the molecular weight. When the mean free path for collisions exceeds the scale height, individual molecules must be regarded as in orbit around the Earth, though subject to collisions [2-11].

2.4.1.1 Variations

Density and other parameters vary with solar activity as the absorbed solar energy changes. Note that solar radiant flux at extreme ultra-violet (EUV) and other short wavelengths (absorbed above 100 km) varies much more than solar flux in the visible.

Geomagnetic activity (indirectly related to solar activity) also affects the neutral atmosphere through the Joule heating caused by ionospheric currents and by precipitation of particles whose energy is absorbed in the 90- to 200-km range.

2.4.2 Neutral Atmosphere: Chemical Composition

In the Earth's homosphere, which extends from the surface to an altitude of 90 to 100 km, the atmospheric gases mix thoroughly. However, above 90 km, and particularly near 105 km, EUV solar radiation causes molecular oxygen to dissociate. The atomic oxygen thus produced, together with diffusive transport processes, results in a changing atmosphere. Accordingly, the atmospheric chemical composition above the homopause at 90 to 100 km is a function of the variable amounts of EUV radiation received from the Sun.

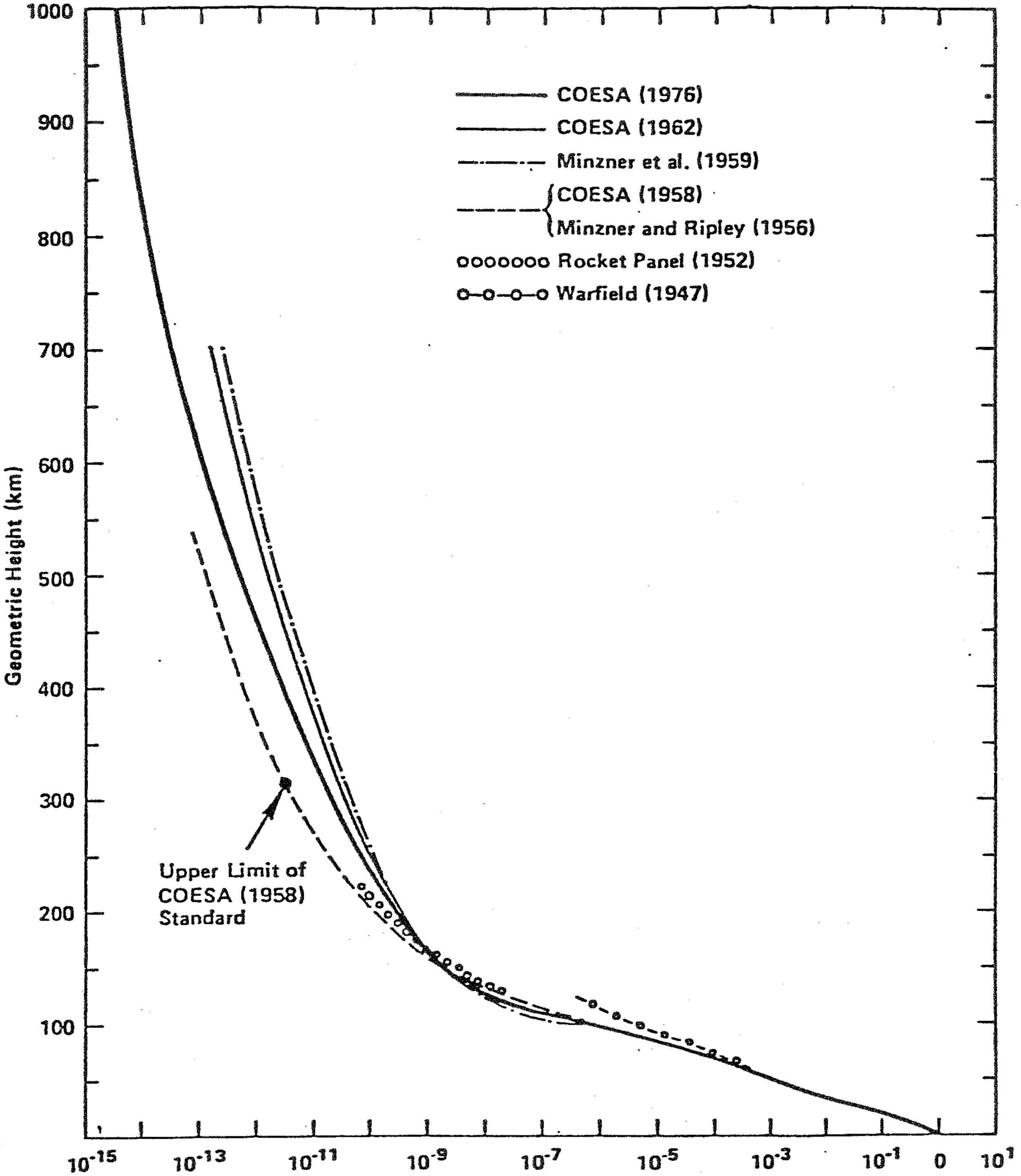

Figure 2-3. Atmospheric density versus geometric height for the 1976 U.S. Standard Atmosphere and for four earlier U.S. Standard and model atmospheres [2-10]. (For references, see original article.)

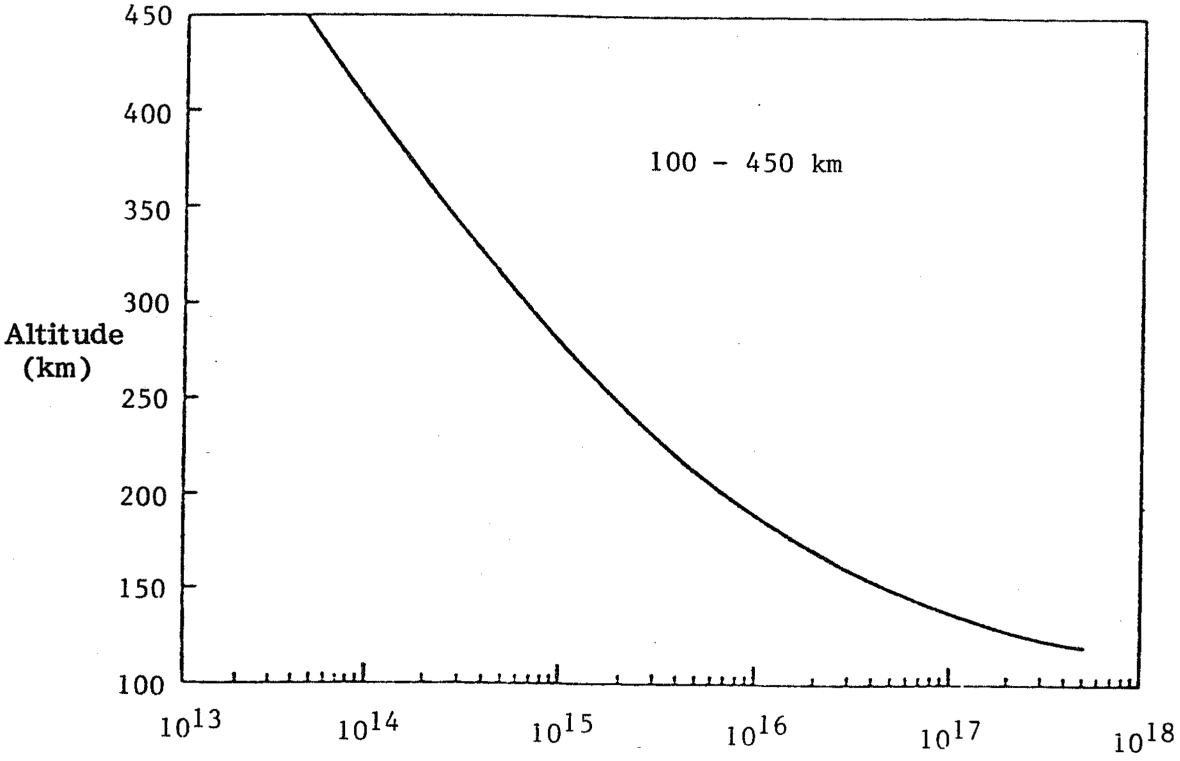

Total number density (m^{-3}) versus altitude (km).

(a)

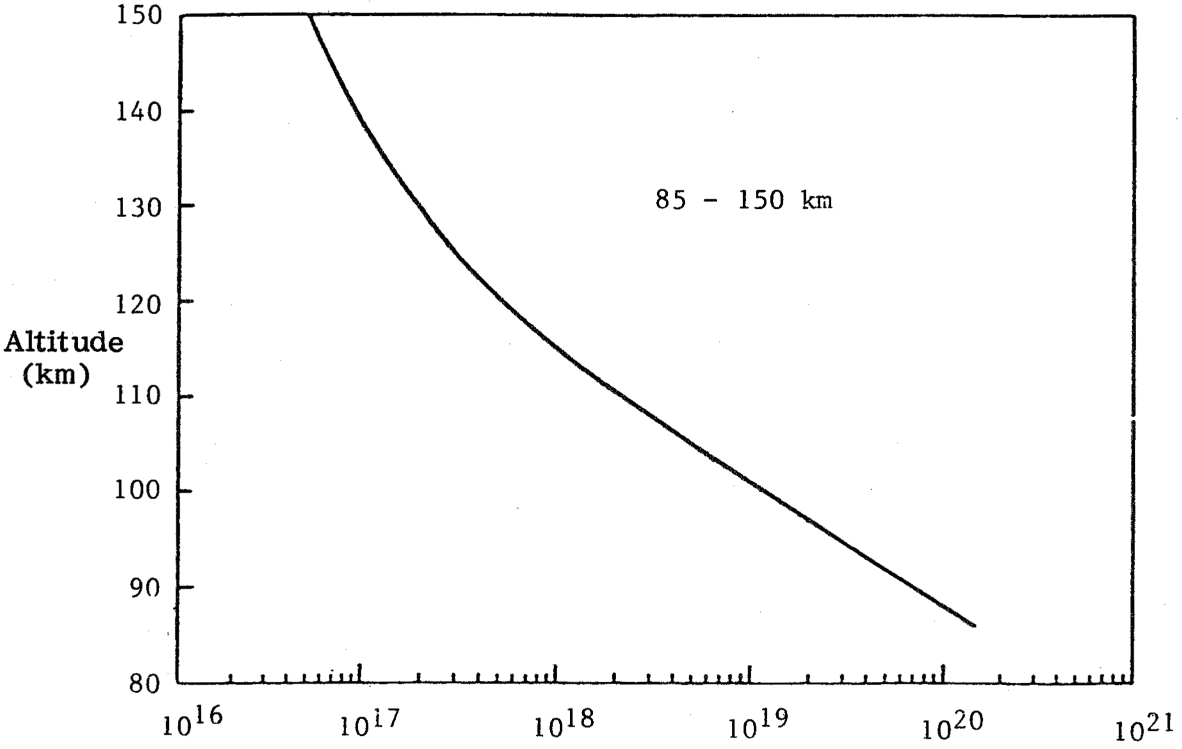

Total number density (m^{-3}) versus altitude (km).

(b)

Figure 2-4. Atmospheric density [2-10].

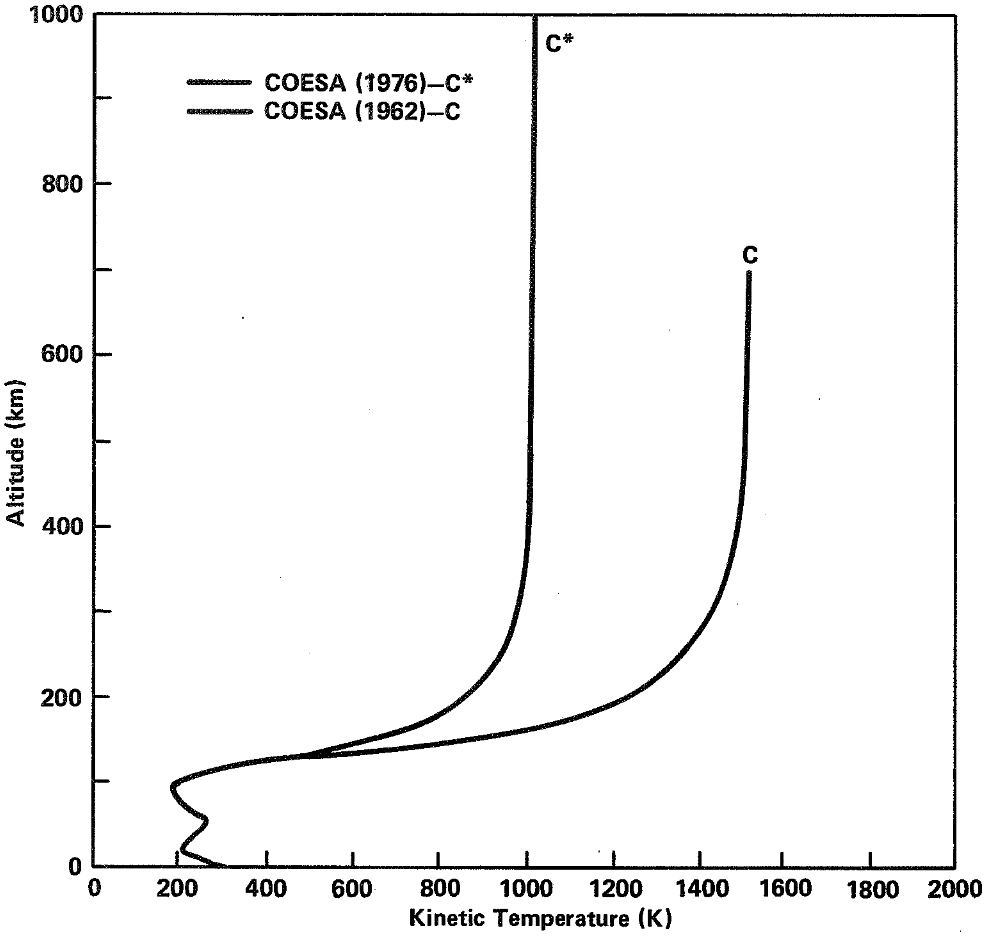

Figure 2-5. Kinetic temperature versus altitude [2-10].

2.4.3 Neutral Atmosphere: Temperature

The temperature lapse rate is influenced by solar radiation. In the lower thermosphere (100 to 300 km), solar radiation in the EUV band (40 to 2000 Å) is absorbed, causing the temperature to increase steadily with altitude. Above 300 km, where little or no solar radiation is absorbed, the temperature becomes isothermal as shown in Figure 2-5. The isothermal temperature, which is designated as the "exospheric temperature," varies diurnally, seasonally, and with solar and geomagnetic activity, from about 650 to 2100°K.

2.4.4 Neutral Atmosphere: Density Variations

Variation in density above the homopause is closely related to the amount of EUV received from the Sun. Since EUV cannot be measured at the Earth's surface, early investigators made use of the approximate correlation between solar activity and radio radiation at 10.7 cm, which is received at the surface. The mean daily solar flux at 10.7 cm measured by the National Research Council, Ottawa, Canada, has been adopted as an indicator of the amount of EUV radiation reaching the top of the Earth's atmosphere.

The principal periodic variability found in the solar flux at 10.7 cm occurs with a cycle of 27 days, corresponding to the 27-day solar rotation. The same periodicity is reflected in atmospheric density. Semiannual, diurnal, and solar cycle variations have also been identified in the upper atmospheric temperature.

Upper atmosphere density variations also can be correlated with fluctuations in the magnetic field at the Earth's surface, since geomagnetic variations are strongly correlated with precipitating electrons and protons in the polar regions, and precipitating particles heat the lower thermosphere in the polar regions with resulting changes in the global thermospheric temperature and density. This correlation between changes in the geomagnetic field and atmospheric density variations is useful in predicting density variations. Figures 2-6 and 2-7 show typical density profiles under various conditions.

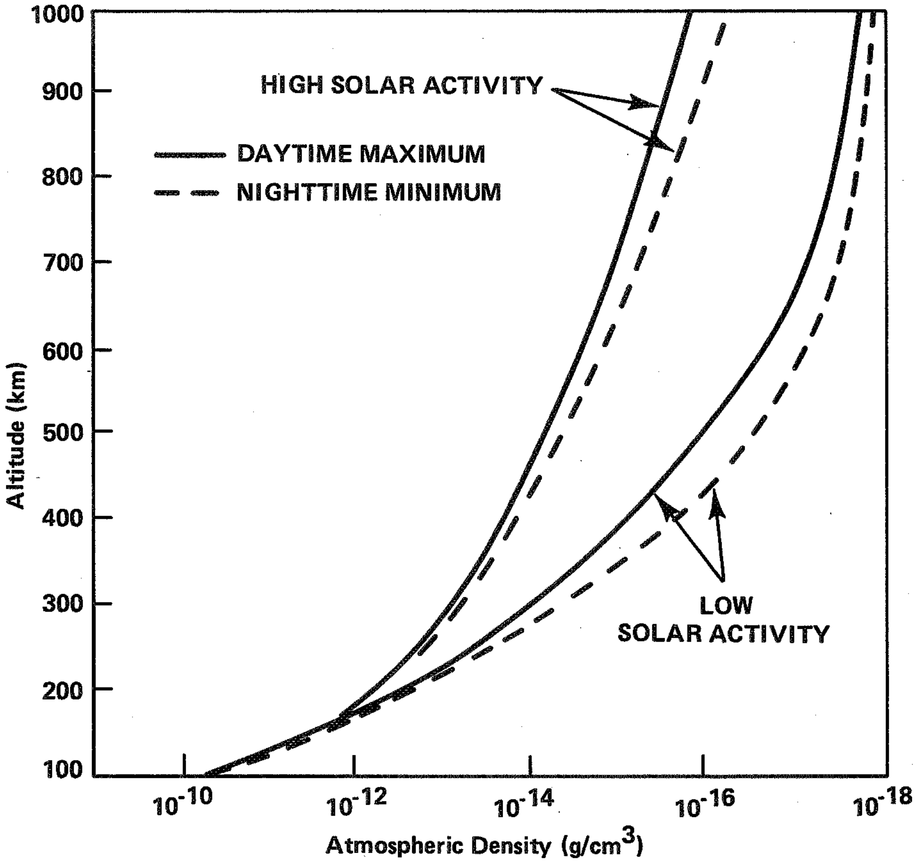

Figure 2-6. Typical daytime maximum and nighttime minimum atmospheric density profiles for high and low solar activity [2-14].

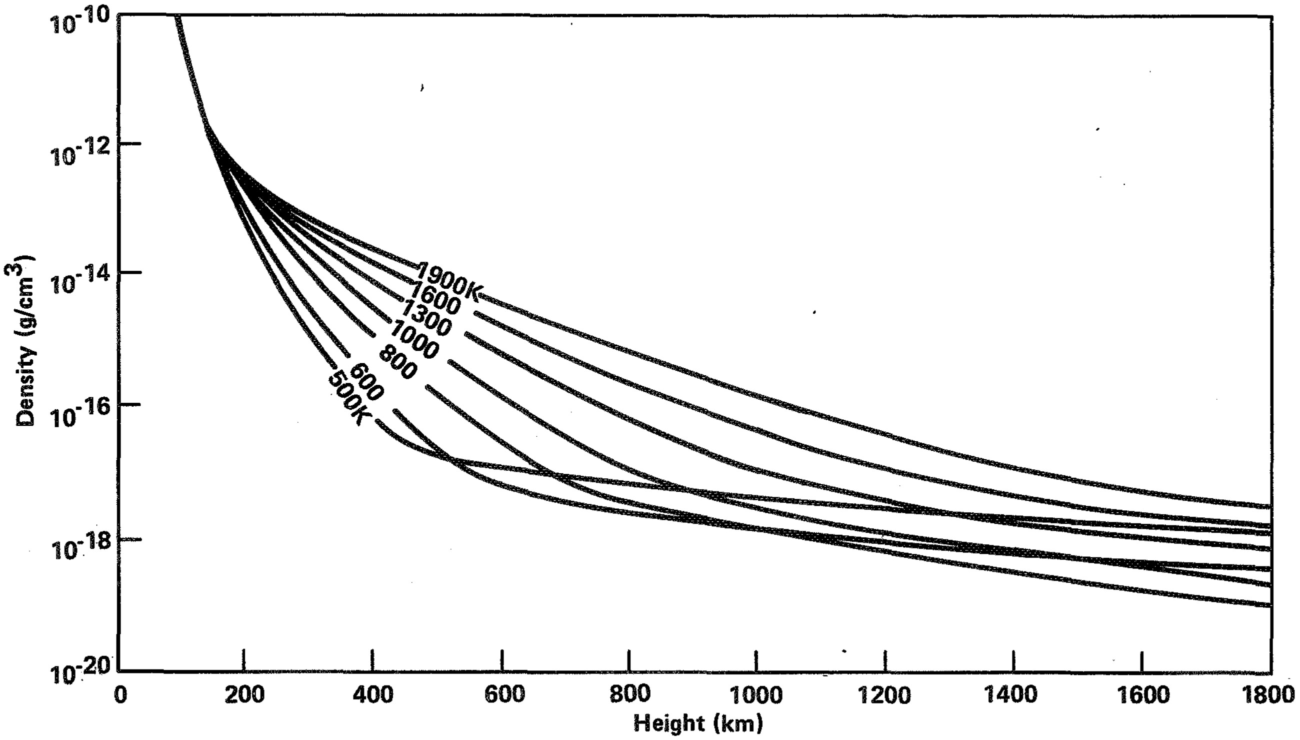

Figure 2-7. Density profiles for seven values of exospheric temperature [2-14].

Atmospheric density also varies between the winter and summer hemispheres in the 60 to 80 deg latitude range. Some investigators attribute the observed higher upper atmosphere density in the winter hemisphere to an increased concentration of helium.

For engineering applications an upper atmosphere computer model is needed to predict the neutral gas properties of the atmosphere between 90- and 2500-km altitude for orbital dynamics, lifetime, and control and guidance analyses. Only nominal atmospheric density data is needed below approximately 90 km. The Global Reference Atmosphere Model is used with the MSFC Lifetime Prediction Computer Routine at MSFC for calculating orbital lifetime. This model is a combination of the 4-D Model Atmosphere, the Groves Model, and the Jacchia 1970 Atmosphere Model [2-12]. Solar activity, either observed or predicted, is an input. Reference 2-13 provides for one of the many techniques for predicting future levels of solar activity for inputs to the atmospheric model.

2.4.5 Neutral Atmosphere: 2,500 to 65,000-km Altitude

Gas pressure decreases exponentially with increasing altitude above 2,500 km until it reaches the interplanetary value of 10^{-15} N/cm^2 (10^{-13} mb) near 20,000 km. It then remains relatively constant with increasing altitude.

Gas density decreases exponentially above 2,500 km to the interplanetary value of approximately 10^{-23} g/cm^3 near 20,000 km and then remains relatively constant with altitude.

Kinetic temperature increases above 2,500 km to the interplanetary value of about 2×10^5 °K at 20,000 km and then remains relatively constant.

Additional information on the structure and variability of the very high thermosphere is given in References 2-15 and 2-16.

2.4.6 Winds in the Neutral Atmosphere

Information about upper atmosphere winds is derived from satellite drag data and ground-based optical and incoherent-scatter-radar data. These are fit into a theory based on the following considerations: the upper atmosphere is heated by absorbed solar ultraviolet energy and, in the auroral zone, by particle fluxes plus the Joule heating of the auroral electrojet. Some heating also results from waves in the lower atmosphere [2-17]. Heated air rises and flows towards cooler regions where it descends, just as in the troposphere. Above 300-km viscosity tends to make the motion uniform, i.e., slablike. Collisions with ions tend to reduce the velocity difference between ions and neutrals; the effect is strongest in the sunlight ionosphere where the ion density is highest. The ions are tied to the geomagnetic field or drift where there are electric fields, as in the polar regions.

Based on these ideas, Geisler [2-18] and Kohl and King [2-19] have computed wind fields from Jacchia's [2-20] static diffusion model, J64, of the thermosphere, and Geisler [2-21] has computed winds using Jacchia and Slowey's [2-22] modifications to J64. In these studies, the temperature, density, and mean molecular weight fields are used to derive pressure gradients. These are combined with ion drag forces to generate wind fields. Figures 2-8 and 2-9 depict the distribution of winds as a function of time and latitude, respectively, assuming only solar heating. The predicted meridional winds become large at night, approaching 225 m/sec above 300 km at 0200 LT, and then decrease to about 100 m/sec above 300 km at 1400 LT because of the increase in ion drag.

Analyses of satellite drag data show that, at least in some cases, winds in equinox blow towards the equator, not away. Calculations by Dickinson et al. show that during geomagnetically active times, auroral heating at high latitudes dominates the solar heating and forces circulation from pole to equator [2-23]. In geomagnetically quiet times the flow is away from the sunlit regions. Figures 2-10 and 2-11 show calculated zonally averaged flow. Wind speeds at 300-km altitude and 40-deg latitude average 50, 20, and 5 m/sec equatorward at summer solstice, equinox, and winter solstice.

2.4.6.1 Super-Rotation

King-Hele deduced from an analysis of satellite orbits that the atmosphere is rotating faster than the Earth above 140 km to approximately 450 km [2-24, 2-25]. The average eastward winds are inferred to increase from about 40 m/sec at 200 km to 160 m/sec at 350 km at 30 deg latitude. Above 450 km, the wind direction appears to reverse. Challinor believes that this apparent mean rotation of the upper atmosphere is caused by an eastward daytime motion which is primarily confined to equatorial latitudes and notes that the satellite observations are weighted toward low latitude and daytime conditions [2-26]. A number of other explanations have been offered for the inferred super-rotation of the upper atmosphere, and it may even be that the phenomenon is spurious.

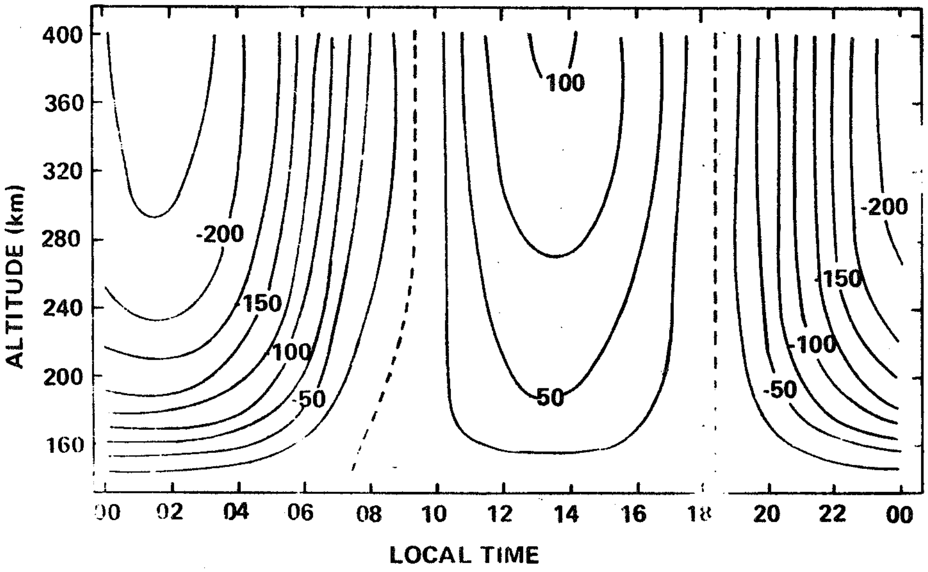

Figure 2-8. Contours of meridional wind speed at 45 deg N latitude (m/sec) positive values directed toward the north [2-22].

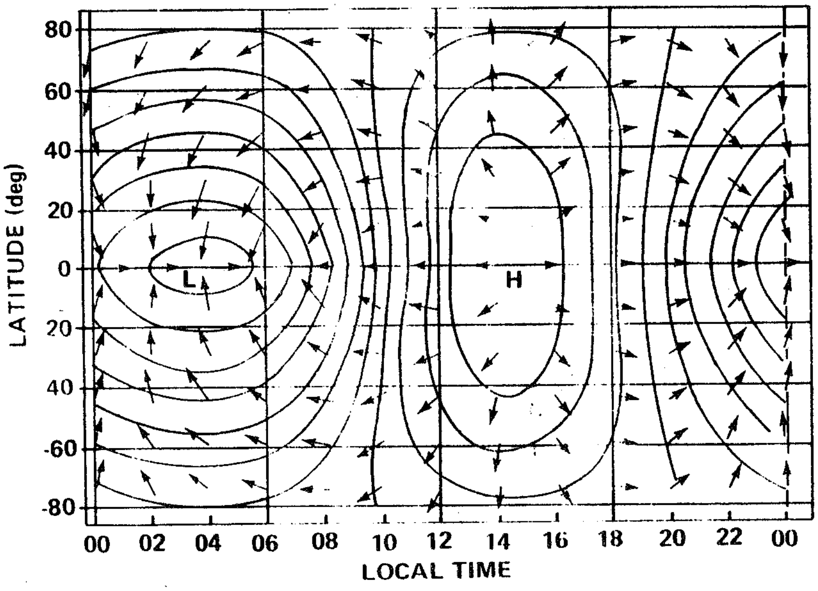

Figure 2-9. Wind vectors at the 300-km level. (Largest arrow represents wind speed at 225 msec^{-1} [2-22].)

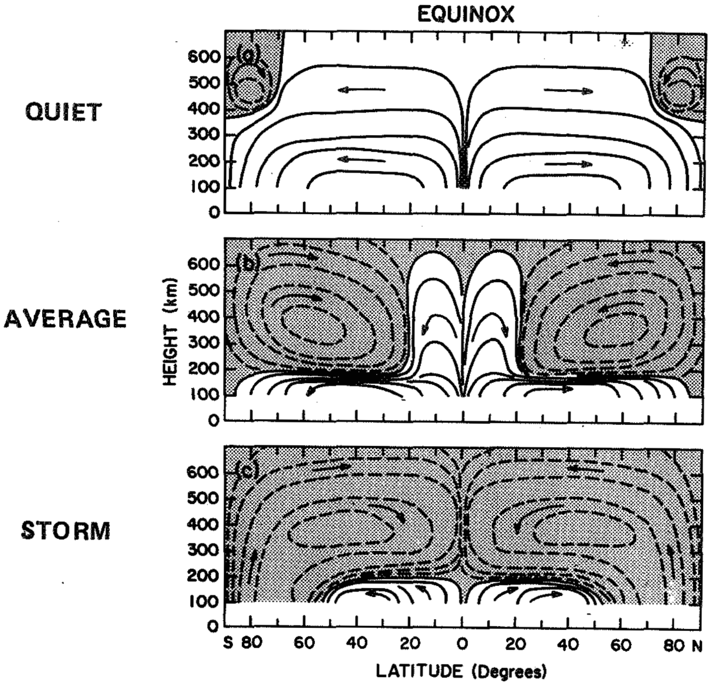

Figure 2-10. Schematic diagram of the zonal mean meridional circulation in the thermosphere during equinox for various levels of auroral activity. Contours illustrate mass flow.

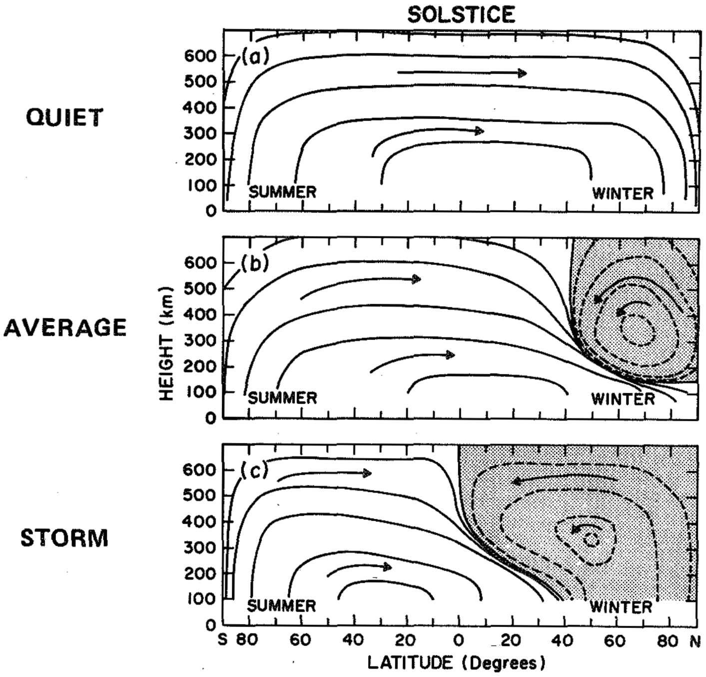

Figure 2-11. Same as Figure 2-10, but at solstice [2-23].

2.4.6.2 Anomalous Strong Winds Associated with Geomagnetic Storms

Increases in winds as well as atmospheric density in the upper atmosphere during geomagnetic storms have been observed many times. On one occasion near the auroral oval, a horizontal wind speed on the order of 1.5 km sec^{-1} was observed to occur at approximately 150-km altitude simultaneously with a large increase in the ambient density during a very large geomagnetic storm. Theoretical calculations suggest the possibility of associated vertical wind speeds on the order of 50 to 75 m sec^{-1}. Large changes in the composition of the neutral upper atmosphere have also been observed during geomagnetic storms.

2.5 SUNLIGHT AND EARTHSHINE

A satellite in Earth's orbit is illuminated by sunlight and earthshine. Solar radiation is treated elsewhere (Section 1.0). Earthshine consists of reflected sunlight and thermal radiation from the Earth and its atmosphere.

Thermal radiation can be expressed by blackbody times the emissivity of the radiating surface. At wavelengths for which the atmosphere is transparent, radiation at orbital altitude coming from the Earth's surface is that of a blackbody at approximately 288°K. Where the atmosphere is opaque, radiation is received from the colder upper atmosphere as shown in Figure 2-12 [2-27,2-28].

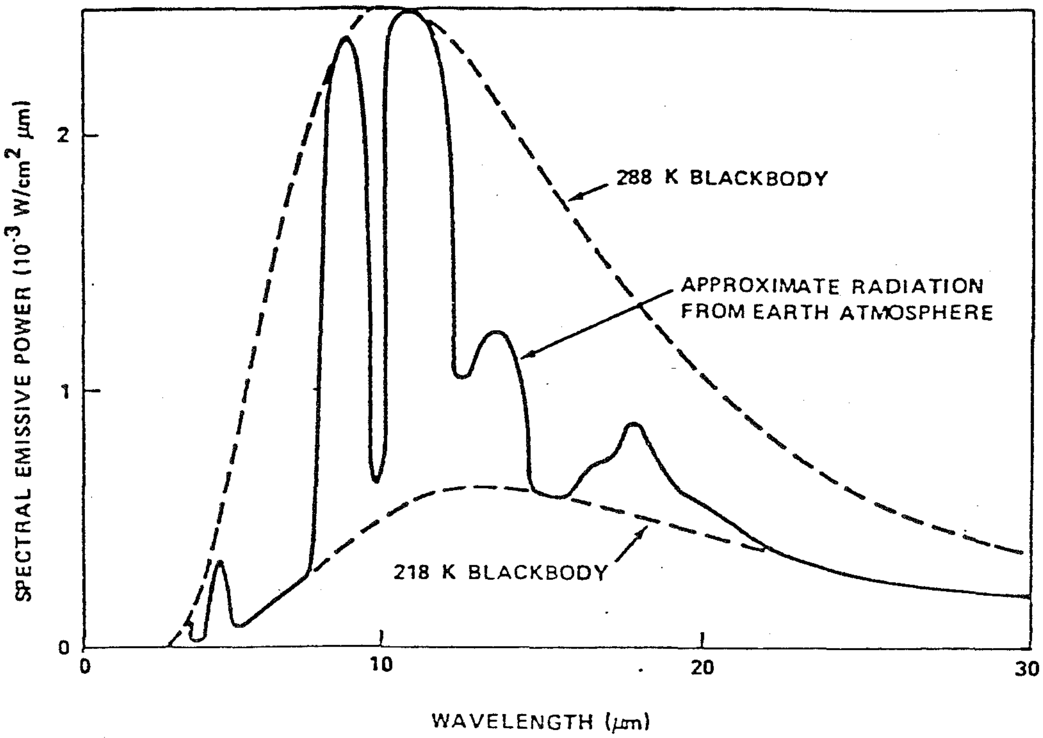

NOTE: The 288°K blackbody curve approximates the radiation from the Earth's surface, and the 218°K blackbody curve approximates the radiation from the atmosphere in those spectral regions where the atmosphere is opaque.

Figure 2-12. A typical spectral emissive power curve for the thermal radiation leaving the Earth [2-27,2-28].

The spectral distribution of sunlight is approximately blackbody at 5760°K, and so peaks in the visible, 0.4 to 0.7 μm wavelength. The energy flux at the Earth (the solar constant outside the atmosphere) is

$$1.97\ \mathrm{cal/(cm^2\ min)} = 1371 \pm 5\ \mathrm{W\ m^{-2}} = \pi F\ .$$

The ratio of total energy reflected to the total incident, called global albedo, equals 0.39. If we assume that the Earth is a uniform, gray, diffusive reflector, having reflectance independent of incident angle, then the spectral radiant flux reflected from an element of Earth's sunlit surface is

$$L_r^\lambda = 0.39 \cos\theta\, F_\lambda\ \mathrm{ergs/(cm^2\ sec\ ster\ wavelength)}\ \text{if}\ \cos\theta > 0\ ,$$

$$= 0\ \text{if}\ \cos\theta < 0\ ,$$

where

θ = solar zenith angle at element of surface

F_λ = erg/(cm^2 wavelength) from Sun .

Obviously, $\pi F_\lambda \cos\theta$ is the incident energy per unit surface area and πL_r^λ is the energy reflected per unit area into a hemisphere.

Actually L_r^λ depends in a complicated way on the angles of incidence and reflection and upon the nature of the surface. We may define the local albedo as the ratio of the energy reflected at all wavelengths in all directions from a unit area to the incident energy at all wavelengths. Some values are

0.10 to 0.80 clouds

0.05 to 0.45 land

0.03 to 0.20 water.

Table 2-2 shows some typical variations of local albedo and thermal emission encountered in Earth orbit over various time periods.

2.6 METEOROIDS

The solid objects encompassed by the term "meteoroids" range in size from microns to kilometers and in mass range from $\leq 10^{-12}$ g to $\geq 10^{+16}$ g. Those less than 1 gram are often called "micrometeoroids." If objects of more than approximately

TABLE 2-2. VARIATION OF THE TIME AVERAGE EFFECTIVE VALUES ABOUT THEIR GLOBAL VALUES (2-27)

Time Increment	Earth Emitted Thermal Radiation Variation Albedo Variation	W/m^2
$\Delta t < 0.3$ hr	$+0.30^{+0.30}_{-0.15}$	237^{+28}_{-97}
$0.3 < \Delta t < 3$ hr	0.30 ± 0.10	237^{+24}_{-48}
$\Delta t > 3$ hr	0.30 ± 0.05	237 ± 21

10^{-6} g mass reach Earth's atmosphere they are heated to incandescence, producing the visible effect called a "meteor." If the initial mass and composition permits some of the original meteoroid to reach Earth's surface unvaporized, the object is called a "meteorite."

Meteoroids are thought to derive primarily from comets and asteroids with perihelia near or inside Earth's orbit. The original objects were supposedly broken down into a distribution of smaller bodies by collisions. Meteoroids recently formed still tend to be concentrated near the orbital path of their parent body. These "stream meteoroids" produce the well known meteor showers which occur at certain dates and from particular directions (Table 2-3).

Meteoroids may be classified by composition: stony, iron, and, perhaps, icy. From their composition the type of parent body can be inferred.

Meteoroids are attracted by the Earth's gravity field so that the flux from allowed directions in near-Earth orbit is increased by approximately 1.7 over the interplanetary value. The Earth also shields certain arrival directions.

The total mass infall to Earth is estimated to be approximately 10^{10} g/year. Figure 2-13 shows the distribution of number with mass, where $N (\geq m)$ is the number flux with mass $\geq m$ [2-29]. The flux is low and, therefore, difficult to measure. Evidence includes: spherules on the sea floor and the polar icecaps, impacts detected with special sensors on satellites, meteor trails in the atmosphere observed visually and by radar, lunar crater counts, and zodiacal light.

The fluxes of Figure 2-13 are probably uncertain by a factor of 10. The units may be converted to particles/m^2 sec by division by 3.155×10^{13} = antilog 13.499. (To convert to interplanetary intensity, particles/m^2 sec ster, multiply by 2 to correct for Earth shielding, divide by 2 to correct for gravitational focusing, and divide by π.) The data are of the form $N (\geq m) = \text{const}/m^{\alpha}$, with α slowly changing. There is some evidence that the flux in Earth-lunar space is greater than the general level along the Earth's orbit by a factor between 1 and 2. The interplanetary flux is higher in the asteroid belt than at 1 AU.

TABLE 2-3. MAJOR METEOROID STREAMS [2-14]

Name	Period of Activity	Date of Activity	F_{max} Maximum	Geocentric Velocity (km/sec)
Quadrantids	January 2 to 4	January 3	8.0	42
Lyrids	April 19 to 22	April 21	0.85	48
η-Aquarids	May 1 to 8	May 4 to 6	2.2	64
O-Cetids	May 14 to 23	May 14 to 23	2.0	37
Arietids	May 29 to June 19	June 6	4.5	38
ζ-Perseids	June 1 to 16	June 6	3.0	29
β-Taurids	June 24 to July 5	June 28	2.0	31
δ-Aquarids	July 26 to August 5	July 8	1.5	40
Perseids	July 15 to August 18	August 10 to 14	5.0	60
Orionids	October 15 to 25	October 20 to 23	1.2	66
Arietids, southern	October through November	November 5	1.1	28
Taurids, northern	October 26 to November 22	November 10	0.4	29
Taurids, night	November		1.0	37
Taurids, southern	October 26 to November 22	November 5	0.9	28
Leonids, southern	November 15 to 20	November 16 to 17	0.9	72
Bielids	November 12 to 16	November 14	0.4	16
Geminids	November 25 to December 17	December 12 to 13	4.0	35
Ursids	December 20 to 24	December 22	2.5	37

F_{max} is the ratio of average maximum cumulative stream to average sporadic flux for a mass of 1 g and a velocity of 20 km/sec.

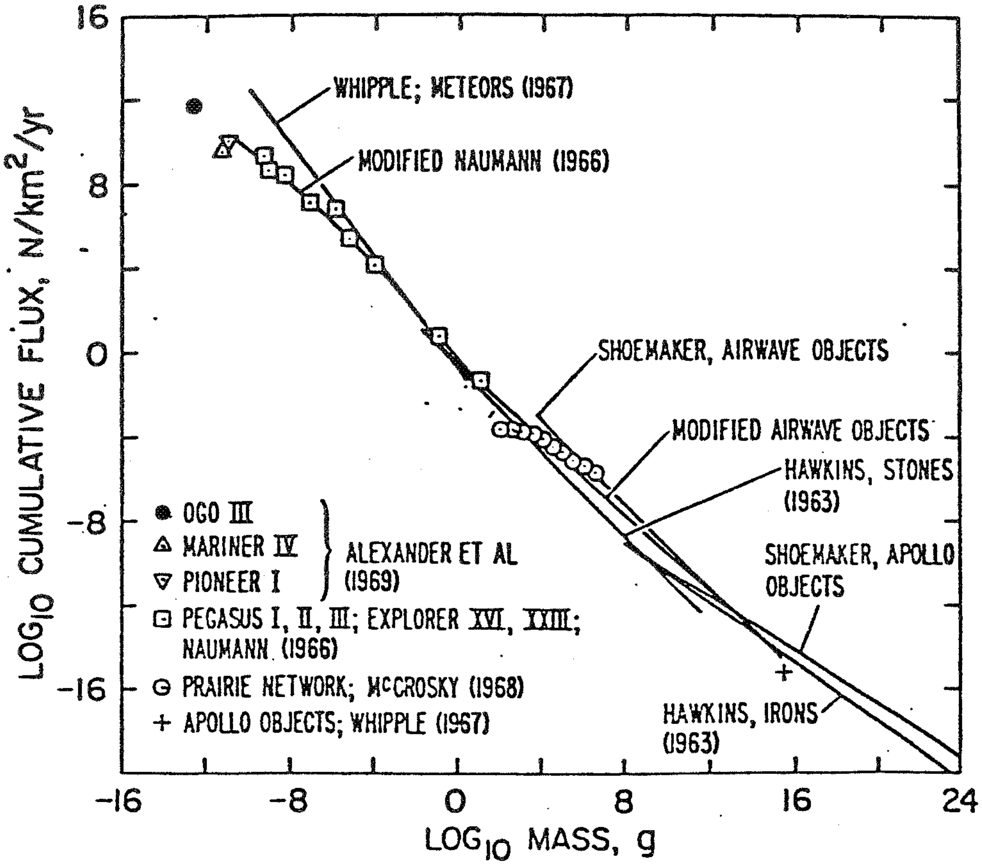

Figure 2-13. Terrestrial mass-influx rates of meteoroids. N is the flux of particles with mass greater than m [2-29].

Figure 2-14 shows a recent compilation of data for near-Earth space derived by various means, over a more restricted mass range than Figure 2-13. (The fluxes shown in Figures 2-13 and 2-14 are 1-year averages.) The flux for $m < 10^{-12}$ g is rather uncertain. There have been other recent estimates of micrometeoroid flux a factor of 10 higher than those shown in Figure 2-13 [2-30]. This appears to represent a real uncertainty.

2.7 PLASMA AND ELECTROMAGNETIC FIELDS

2.7.1 Magnetic Field

The Earth's internal field is measured on the surface and by low-altitude satellites. It changes measurably over a period of a few years and its strength and rate of change have been remeasured several times in the past 15 years. Precision, as well as temporal and spatial resolution, have improved as field mapping finds increasing application in geophysical prospecting and other areas.

For the present purpose the internal field from the surface to approximately 2000-km altitude may be represented by the gradient of a scalar magnetic potential (because the field has zero curl in this region of space).

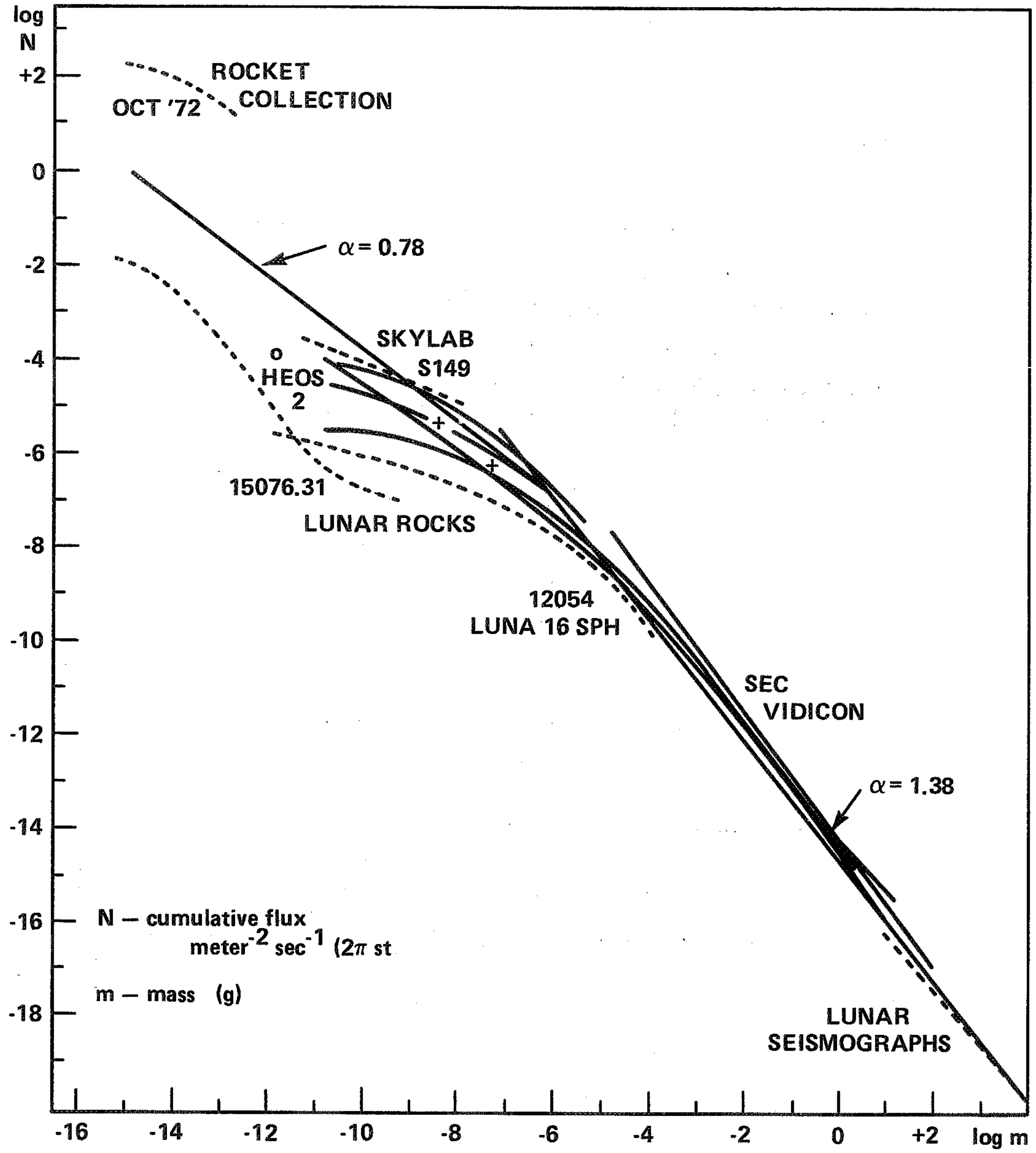

Figure 2-14. Cumulative particle fluxes from various data sources [2-31].

$$\underset{\sim}{B}_{int} = - \underset{\sim}{\Delta} \phi$$

and in geocentric spherical coordinates.

$$\Phi = R_e \sum_{n=1}^{\infty} \sum_{m=0}^{n} P_n^m(\cos \theta) \left[\frac{R_e}{r}\right]^{n+1} [g_n^m \cos m \phi + h_n^m \sin m \phi]$$

r = radial distance

θ = co-latitude

ϕ = longitude east .

The strength of the multipoles is given by the Schmidt coefficients, g_n^m, h_n^m. Detailed discussions, values of the coefficients up to n = 10, their time derivatives, and computer programs for numerical evaluation of $\mathbf{B}$ are given in References 2-32, 2-33, 2-34, and 2-35. The residuals between the field so calculated and the measured surface field are approximately 180 γ ($1\ \gamma = 10^{-5}$ gauss) and 0.15 deg of inclination and declination [2-36]. Values of the first few coefficients in gammas according to the 1965 IGRF fit are

n	m	g_n^m	h_n^m
1	0	-30339	---
1	1	-2123	5758
2	0	-1664	---
2	1	2995	-2086
2	2	1567	130

The dipole terms dominate even at $r = R_e$.

Note that these coefficients are written for use with P_n^m, the Schmidt functions, which have a different normalization than the usual Legendre polynomials P_{nm}. The relationship is

$$P_n^m = \left[\varepsilon_m \frac{(n-m)!}{(n+m)!}\right]^{\frac{1}{2}} P_{nm}$$

$$\begin{aligned} \varepsilon_m &= 2 \quad \text{for} \quad m \neq 0 \\ &= 1 \quad \text{if} \quad m = 0 \ . \end{aligned}$$

The mean square value of P_n^m integrated on a sphere is $[2n + 1]^{-\frac{1}{2}}$.

The components of the field are:

$$B_{north} = \frac{1}{r} \frac{\partial \phi}{\partial \theta}$$

$$B_{east} = \frac{1}{r \sin \theta} \frac{\partial \Phi}{\partial \phi}$$

$$B_{\text{vert down}} = \frac{\partial \Phi}{\partial r}$$

Also the major dipole term is $P_1^o = \cos\theta$.

To visualize the field, it is convenient to choose a new spherical coordinate system as follows:

> The geographic system is rotated, so that the new polar axis coincides with the "dipole axis" making $g_1' = h_1' = 0$ in the new system.
>
> The system is translated to minimize the $n = 2$ term, leaving $n = 1$ unchanged. (Higher order terms are altered, however.)

This is called the eccentric dipole coordinate system. The rotation carries the pole 11.5 deg from the rotation axis in the meridian of 69 deg W longitude. The translation carries the origin 342 km in the direction of 6.5 deg N latitude, 161.8 deg E longitude. The dipole strength is approximately 8.1×10^{25} gauss cm^3.

In describing the magnetosphere it is convenient to label the field lines with their equatorial crossing distance in units of Earth radii; this is called the "L value," and it may be defined to take account of the real internal field including the higher order multipoles. It is also useful to define the invariant latitude, Λ, at which a field line reaches Earth's surface. Using its real L value and the dipole relationship

$$\cos\Lambda = \frac{1}{\sqrt{L}}$$

Beyond an altitude some fraction of an R_e it is necessary to include the effects of the external currents: magnetopause surface currents, the distributed ring currents, and tail currents. Attempts to calculate these in a self-consistent manner including plasma convection are of great research interest at present [2-3,2-21]. Various mathematical formalisms have been devised for representing the external field analytically. (Like the scalar potential for the internal field they can represent the field but do not specify the source currents uniquely.)

A useful procedure has been given by Olson for calculating the quiet-time field inside the magnetopause on the dayside and inside the tail out to approximately 200 R_e [2-37]. Updated models allowing for dipole tilt have since been derived [2-5]. A computer program to calculate B can also be provided by Olson.[1] Figure 2-15 shows the strength of this external field.

An abbreviated form of the representation is

$$B_x = 0.8535z - 0.00507\,xz + (2.1143z - 5.246\,xz)\exp(-0.06\,r^2)$$

---

[1] Dr. W. P. Olson, McDonnell-Douglas Aeronautics Co., Code A-3-208-13-3, 5301 Bolsa Avenue, Huntington Beach, CA 92647.

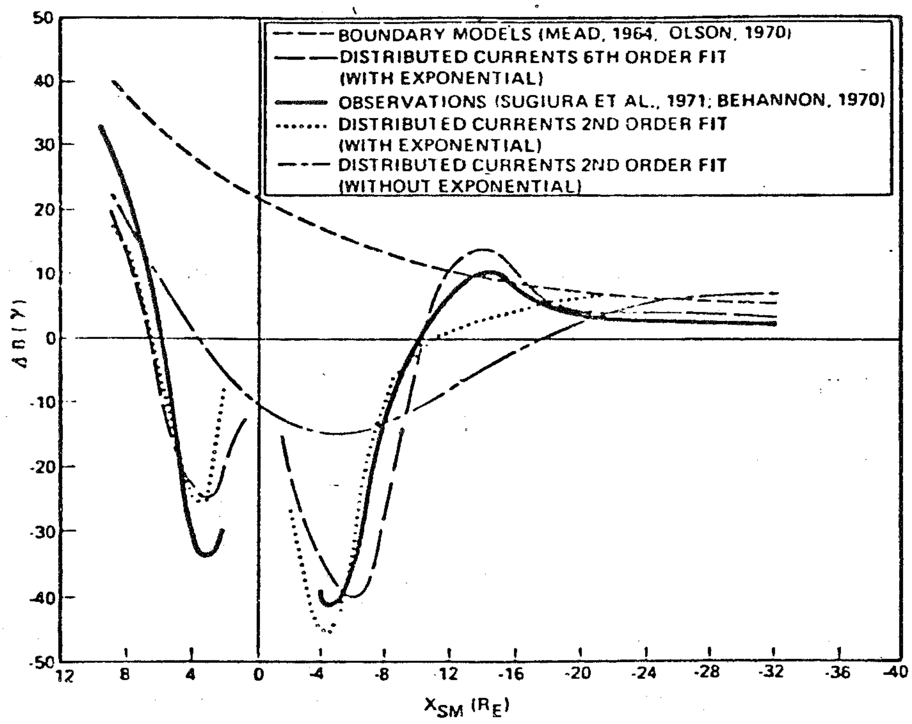

Figure 2-15. The ΔB along the Sun-Earth line [2-37].

$$B_y = -[0.01382 + 67.7682 \exp(-0.06\, r^2)]yz$$

$$B_z = 8.196 + 1.363x - 0.01524z^3 + 0.0088y^2 + 0.0609x^2$$

$$+ [-8.803 + 3.578x - 1.7927z^2 - 6.0491y^2 - 6.8595x^2] \exp(-0.06r^2) \quad .$$

To this must be added the internal field for which a dipole antiparallel to the z axis is adequate. The coordinates are

x toward the Sun

z toward the north ecliptic pole

y toward dusk meridian.

The origin is at Earth's center and the units are R_e.

2.7.2 Electric Field

In the presence of a magnetic field the electric field that is observed depends upon the frame of reference in which the field is measured. If $\underset{\sim}{E}_1$ and $\underset{\sim}{B}_1$ are observed in frame 1 and $\underset{\sim}{E}_2$, $\underset{\sim}{B}_2$ in a second frame moving with velocity $\underset{\sim}{v} \leq\leq c$ with respect to the first, then in cgs units

$$\underset{\sim}{E}_{2\perp} = \underset{\sim}{E}_{1\perp} + \frac{\underset{\sim}{v}}{c} \times \underset{\sim}{B}_1 \qquad \underset{\sim}{B}_2 = \underset{\sim}{B}_1$$

$$\underset{\sim}{E}_{2\parallel} = \underset{\sim}{E}_{1\parallel}$$

where $\parallel$ and $\perp$ are measured with respect to $\underset{\sim}{B}$. In more useful units the first equation becomes:

$$\underset{\sim}{E}_{2\perp}\ [\text{volts/m}] = \underset{\sim}{E}_{1\perp}\ [\text{volts/m}] + \frac{\underset{\sim}{v}\ [\text{m/sec}]}{10^4} \times \underset{\sim}{B}\ [\text{gauss}] \quad .$$

Since above a few hundred kilometers altitude the plasma is in most cases free to move, making $\underset{\sim}{E} = 0$ in its own rest frame, in any other frame with velocity $\underset{\sim}{v}$

$$\underset{\sim}{E}_{\perp} = \frac{\underset{\sim}{v}}{10^4} \times \underset{\sim}{B}$$

$$\underset{\sim}{E}_{\parallel} = 0 \quad .$$

Thus a spacecraft moving with $\underset{\sim}{v}$ develops a potential across it and may draw current from the plasma depending upon its resistance and the ability of the plasma to supply current (paragraph 2.9). Energy dissipated by the current is at the expense of the kinetic energy of the satellite. A satellite in low-Earth orbit would develop $(8 \times 10^3/10^4) \times 0.5 = 0.4$ V/m, for example.

In the lower ionosphere the high collision rate partly ties the plasma to the neutrals so that in the neutral frame of reference an electric field may exist. Then an electric current $\underset{\sim}{J}$ flows; given by

$$\underset{\sim}{J} = \sigma_p \underset{\sim}{E}_{\perp} - \sigma_H \frac{\underset{\sim}{E}_{\perp} \times \underset{\sim}{B}}{B} + \sigma_{\parallel} \underset{\sim}{E}_{\parallel} \quad ,$$

where σ_p and σ_H are the Pedersen and Hall conductivities and $\sigma_{\parallel}$ the intrinsic or parallel conductivity [2-38]. The perpendicular current occurs because the different ratios of cyclotron to collision frequency for ions and electrons makes the particles drift differently. Figure 2-16 shows typical values of conductivities.

Since $\underset{\sim}{E}_{\parallel} = 0$ (except perhaps in certain time-varying cases and above auroral arcs) the perpendicular field maps along $\underset{\sim}{B}$ so that the electric potential between two field lines is constant along their length, regardless of their separation. Thus, the electric field known in one plane, may be mapped elsewhere.

In an Earth-centered but non-rotating coordinate system it is convenient to regard the field as having three parts:

a) Dawn to dusk polar cap field. A few tens of millivolts per meter gives approximately 50 kV potential across the polar cap from dawn to dusk, driving the magnetosphere.

b) The plasma sheet convection field which maps into a dusk-dawn field tens of millivolts per meter just outside the polar cap and corresponds to Earthward convection of plasma. Field strengths are less than 1 mV/m.

c) The co-rotation field (small) inside L = 4 to 6 corresponding to the rigid rotation with the Earth of the plasma in this volume.

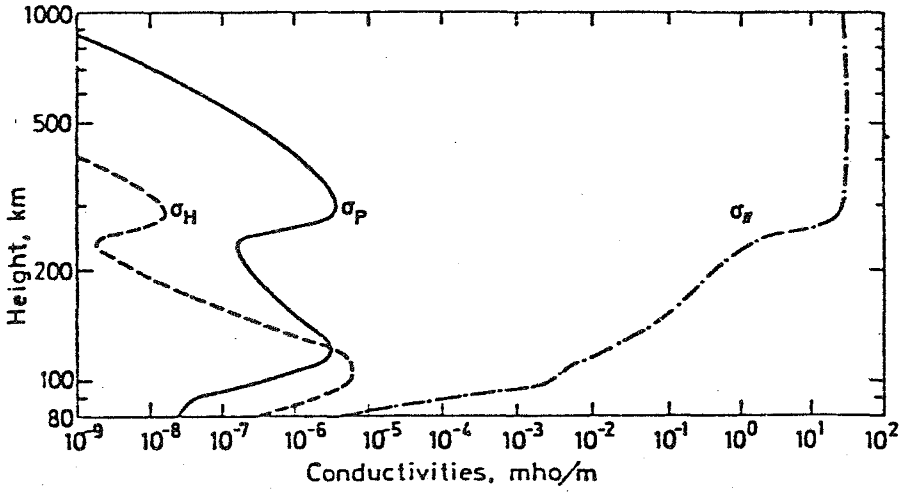

Figure 2-16. Typical variation of the ionospheric conductivities with height for a nighttime ionosphere [2-38].

The total field is highly variable during substorms. It is generally stronger in the polar cap and plasma sheet during storms. There are various analytic models of the field giving both spatial and temporal dependence [2-5]. Reference 2-3 shows schematic diagrams of the various components.

2.8 CHARGED PARTICLES

Ions and electrons occur in the magnetosphere with energies from approximately 1 eV to many MeV, and dividing them into groups is somewhat artificial. However, it is convenient to consider the lower energy particles that may be characterized by number density and temperature (sometimes several temperatures) separate from higher energy particles that have non-thermal distributions and are best characterized by intensity or flux.

The effects of particles on a spacecraft can be extremely complicated and extended discussion is beyond the scope of this handbook. They are given briefly as follows:

a) Energetic particles cause ionization to their penetration depth with damage a possible consequence.

b) Plasma density and temperature (average energy) determine the potential to which the spacecraft charges (typically kT negative), the current that may be drawn to or from a surface, and the sheath and wake dimensions (paragraph 2.9).

c) Electromagnetic waves with frequency near or less than the electron plasma frequency

$$\omega_{pe} = \left[\frac{4\pi N_e e^2}{\varepsilon_o m_e}\right]^{\frac{1}{2}} \quad \text{or} \quad f = 9000 \sqrt{N_e} \text{ Hz} \quad , \quad (N_e = \text{electrons/cm}^3)$$

will propagate only in certain modes and directions if at all.

2.8.1 Low Energy Plasma – Ionosphere

The ionosphere extends from some 60-km altitude out to the plasmapause, the boundary of the plasmasphere on the L = 4 to 6 shell. The ionization is created in the upper atmosphere as the result of solar radiation and cosmic rays interacting with the atmosphere to produce a plasma usually consisting of equal concentrations of positively and negatively charged particles. The plasma remains in a state of dynamic equilibrium because charged particles lost through recombination are balanced by newly-created particles. Variations from geographical anomalies in the Earth's magnetic field exist (Fig. 2-17). Because the prime source of energy for the ionosphere is the Sun, the parameters defining the ionosphere vary diurnally, seasonally, and with the solar cycle (Figs. 2-18 and 2-19). At high latitudes and in the plasmasphere, variations are caused by magnetic storms.

2.8.1.1 The Ionosphere Below 1000 km

Three regions are defined to describe prominent features of the lower ionosphere. In order of increasing altitude and increasing ion concentration they are the D, E, and F regions (Fig. 2-18). Large diurnal effects occur in the ionosphere. At nighttime, the D region virtually disappears, and a depression in electron concentration occurs between the E and F regions.

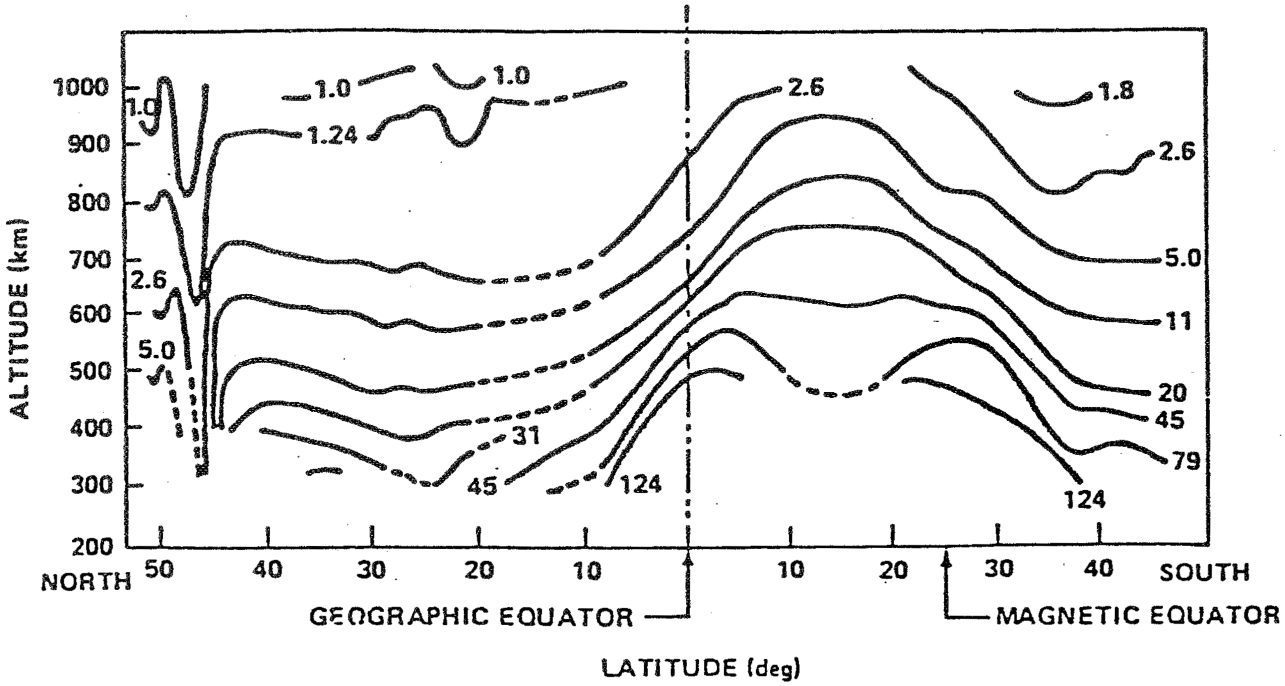

Figure 2-17. Daytime equal-electron-density contours (Units: $10^4/\text{cm}^3$) [2-39].

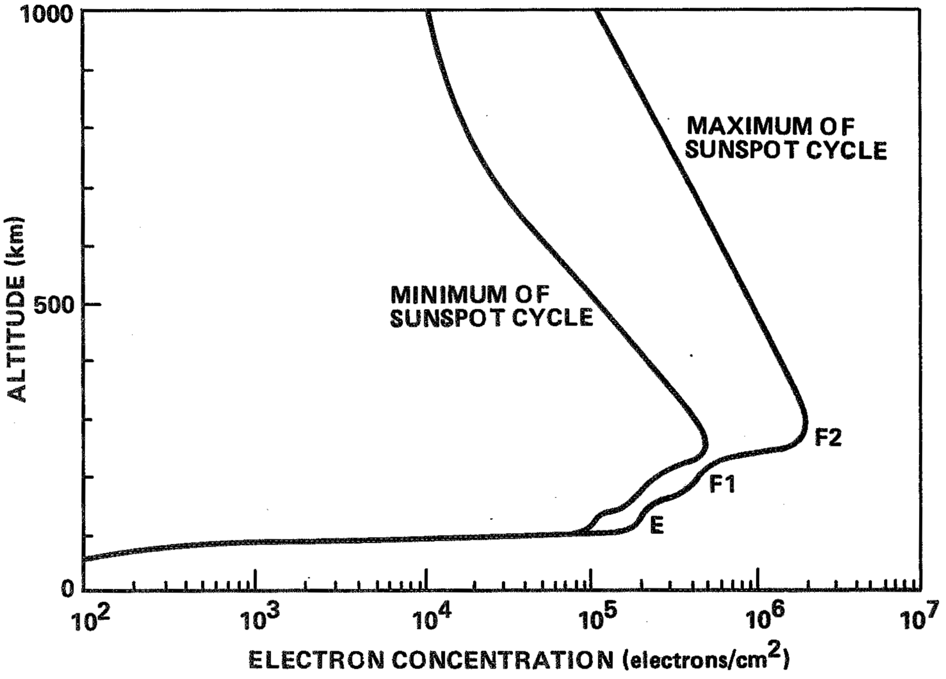

Figure 2-18. Normal electron distribution, daytime [2-40].

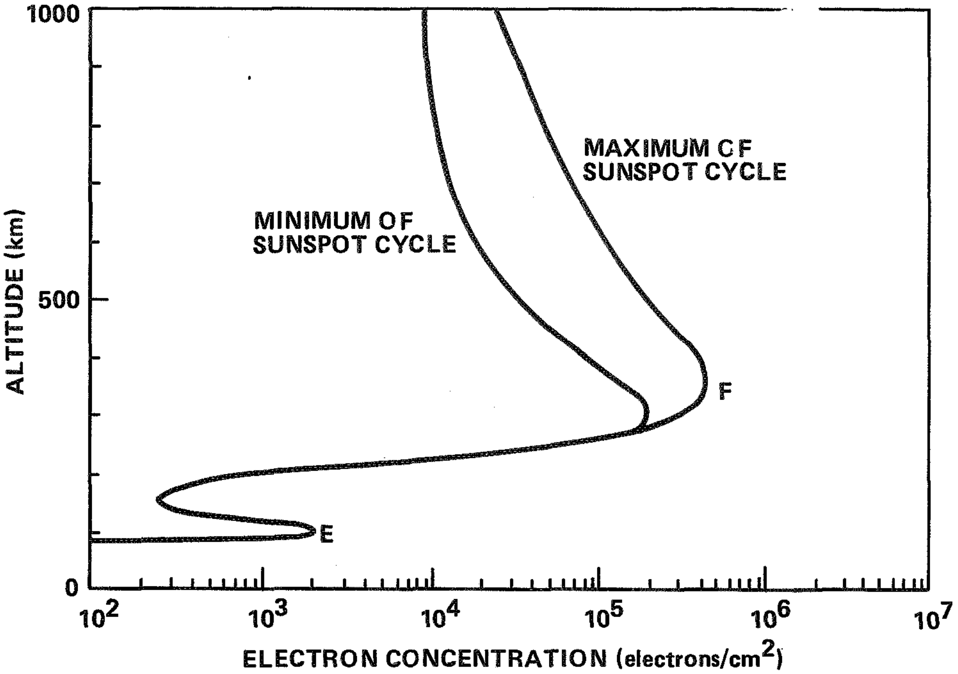

Figure 2-19. Normal electron distribution, nighttime [2-40].

The D region, the lowest ionospheric region, has an approximate altitude range from 60 to 85 km. The predominant ionizing agent is the Lyman alpha radiation of hydrogen (1216 Å) with cosmic rays contributing at lower altitudes. Nitric oxide (NO^+) and oxygen (O_2^+) are the principal ionic constituents, together with heavy ion complexes involving water vapor (Figs. 2-20 and 2-21). The D region has the lowest electron density concentration of the three regions with a maximum of 10^3 electrons/cm^3 near 80 km.

The approximate altitude range of the E region is from 85 to 140 km. Ultraviolet and soft X-radiation are the principal ionizing agents in this region. Precipitating auroral particles are important at high latitudes. The electron concentration in the E region ranges from approximately 10^5 electrons/cm^3 during solar minimum to a value approximately 50 percent larger during solar maximum.

The F region has an approximate altitude range from 140 to 1000 km and in daytime has two divisions, F_1 and F_2. The solar spectrum from 200 to 900 Å is the principal ionizing agent in this region. The two divisions occur because the degree of ionization and recombination falls off with decreasing altitude at different rates. The F_1 region is associated with the ion production peak occurring in the vicinity of 150 km. The F_1 region disappears at night as the concentration of electrons decreases above the E region. The F_2 region is associated with the peak in the electron density distribution which varies with time of day, season, solar cycle, and latitude. It usually lies within the region from 200 to 400 km. The predominant ions near the low-altitude boundary are NO^+ and O_2^+; a gradual transition occurs with increasing altitude, until O^+ becomes the principal ion at the upper boundary.

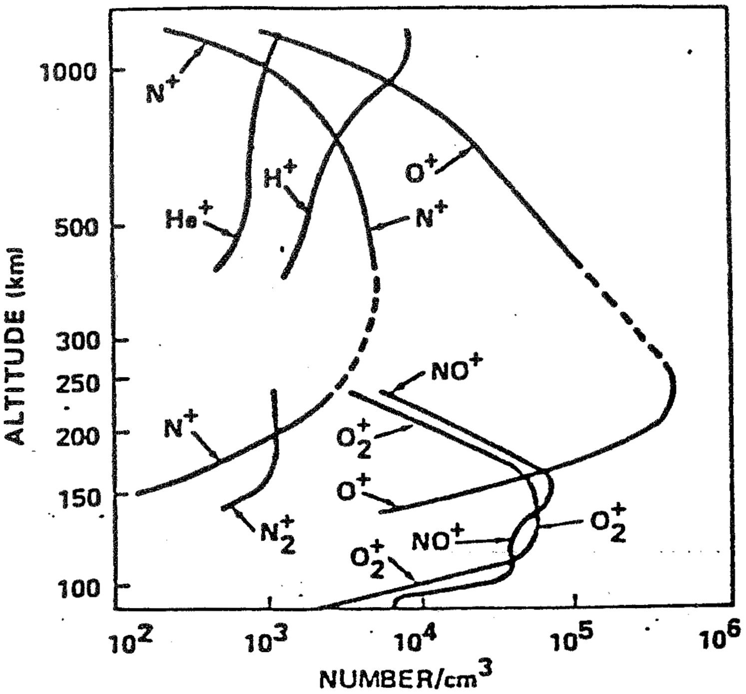

Figure 2-20. Ionic composition of the solar minimum daytime winter ionosphere [2-14].

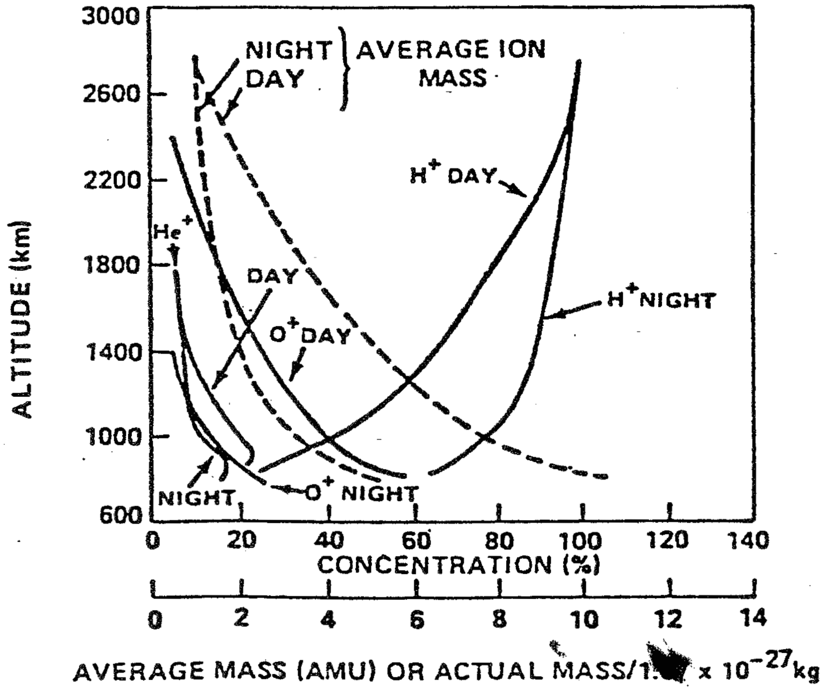

Figure 2-21. Relative concentration of ions for solar minimum and a quiet summertime. (Nighttime summer profiles are also appropriate for winter daytime.) [2-14]

The section of ionosphere above the peak of the F_2 region is commonly referred to as the topside ionosphere. Information on the topside ionosphere has been obtained mainly through satellite measurements and the incoherent backscatter radar technique [2-41].

2.8.1.2 The Ionosphere Above 1000 km

The ionosphere above 1000 km includes the upper portion of the topside ionosphere and the plasmasphere (or outer ionosphere) extending to altitudes of the order of 3 to 4.5 Earth radii. From this altitude to about 10 R_e is the region of transition to the interplanetary medium.

Most information on the outer ionosphere has come through experimental research with the aid of whistlers (RF electromagnetic signals generated by some lightning discharges in tropospheric thunderstorms) although in situ measurements by satellites have also provided useful results. The data indicate a steady decrease in electron concentration with increasing altitude, and a rapid and abrupt concentration decrease of three to four orders of magnitude at 15,000 to 25,000 km above the magnetic equator. This decrease in electron concentration is called the "knee" or plasmapause [2-42].

The predominant ions in the outer ionosphere vary with altitude. In the lowest part of the region, atomic oxygen (O^+) predominates, whereas atomic hydrogen (H^+) is the main constituent above 1000 km (Fig. 2-21). The electron and ion densities balance to give charge neutrality.

2.8.1.3 Ionospheric Temperature

The temperature profile of the ionosphere above the E region has been obtained by sounding rockets, satellites, and backscatter sounders. The temperature of the ionosphere depends on the balance between the various heating and cooling processes there and the diurnal and seasonal variation of this balance. The daytime temperature of the ionospheric electrons in the F_1 region is generally larger than the ambient gas temperature by a factor of two. This results from the relative efficiency of the ambient electrons in removing excess kinetic energy from the energetic photoelectrons that are continually released on the dayside and the relatively small number of electrons that share this energy. Below about 250 km the resulting hot electron gas is cooled mainly by collisions with neutral particles at lower altitudes and by collisions with ions at higher altitudes. The temperature of the ions approaches that of the electrons above 600 km; both exceed the neutral gas temperature.

The model presented herein is based on experimental results for altitudes below 1000 km.

Temperature measurements made by the IMP 1 Spacecraft in the region from 2 to 5 R_E show that the electron temperature, T_e, is approximately proportional to the square of the radial distance from the Earth. Here, a value of 2.4 for the power of the radial distance is used to join lower altitude daytime temperature to data obtained from the OGO-1 Satellite. A value of 1.90 was used as the power to match nighttime values of T_e with the low temperature readings. The electron temperature profiles for daytime summer solar minimum conditions at altitudes below 1000 km are presented in Figure 2-22; the ion temperature profiles are presented in Figure 2-23.

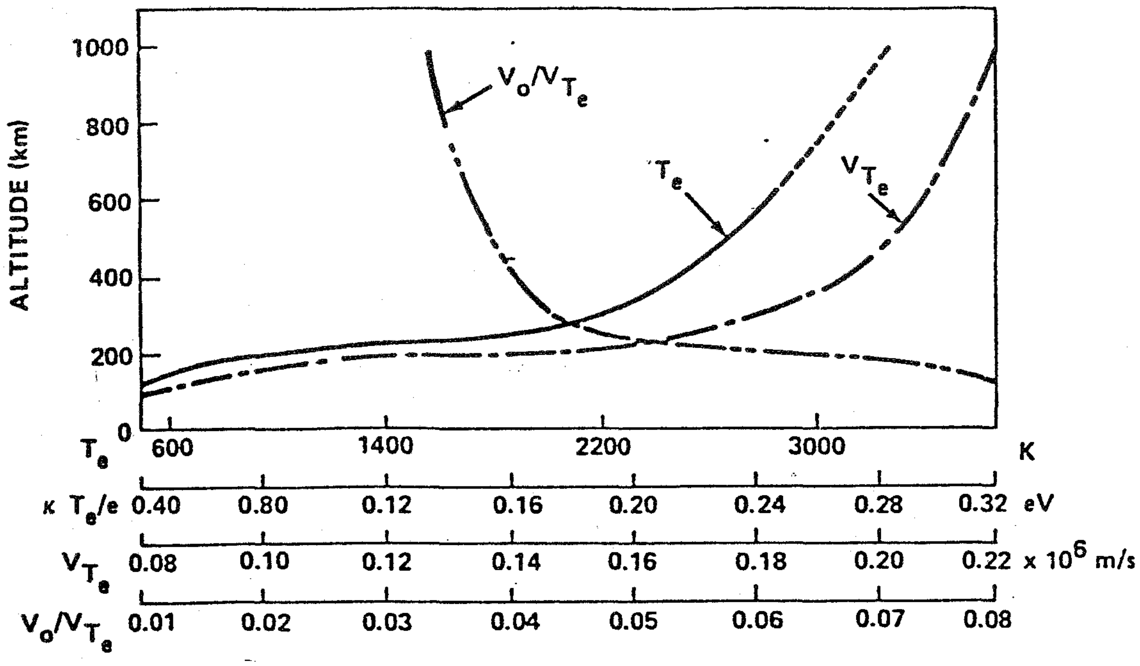

Figure 2-22. Electron temperature, thermal velocity, and satellite/thermal velocity ratio [2-14].

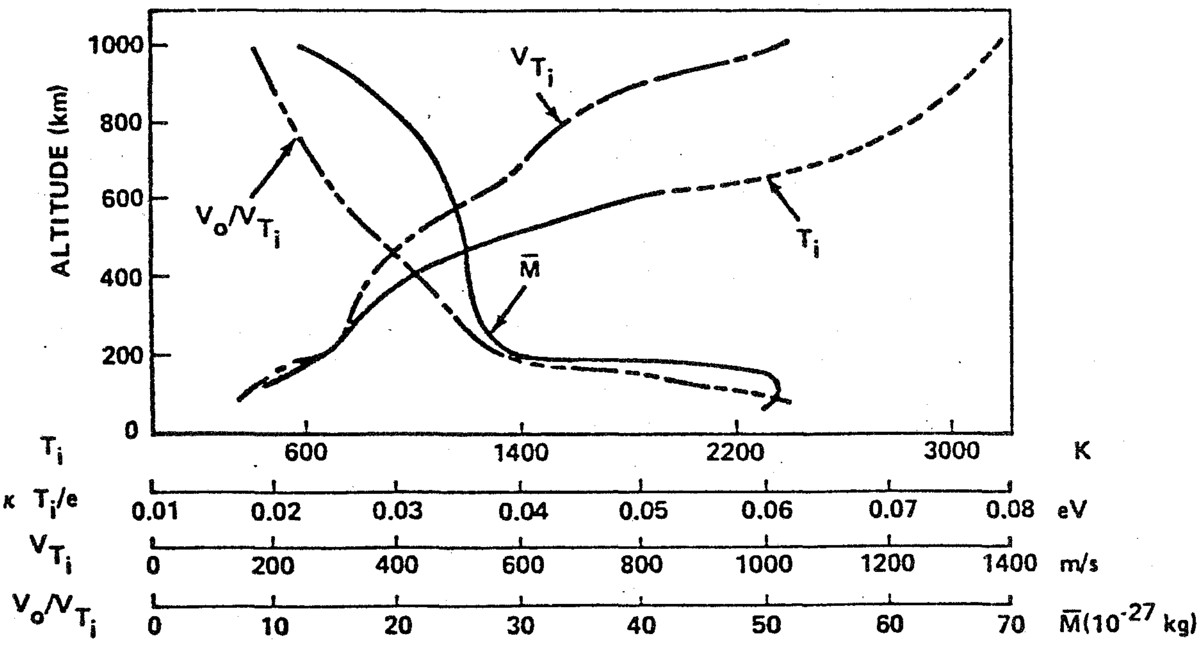

Figure 2-23. Ion temperature, thermal velocity, and satellite/thermal velocity ratio [2-14].

Above 1000 km, the ion temperature is taken as equal to the electron temperature because the ion temperatures theoretically approach the electron temperature values. Figure 2-24 gives the electron temperature profiles during periods of minimum and maximum solar activity.

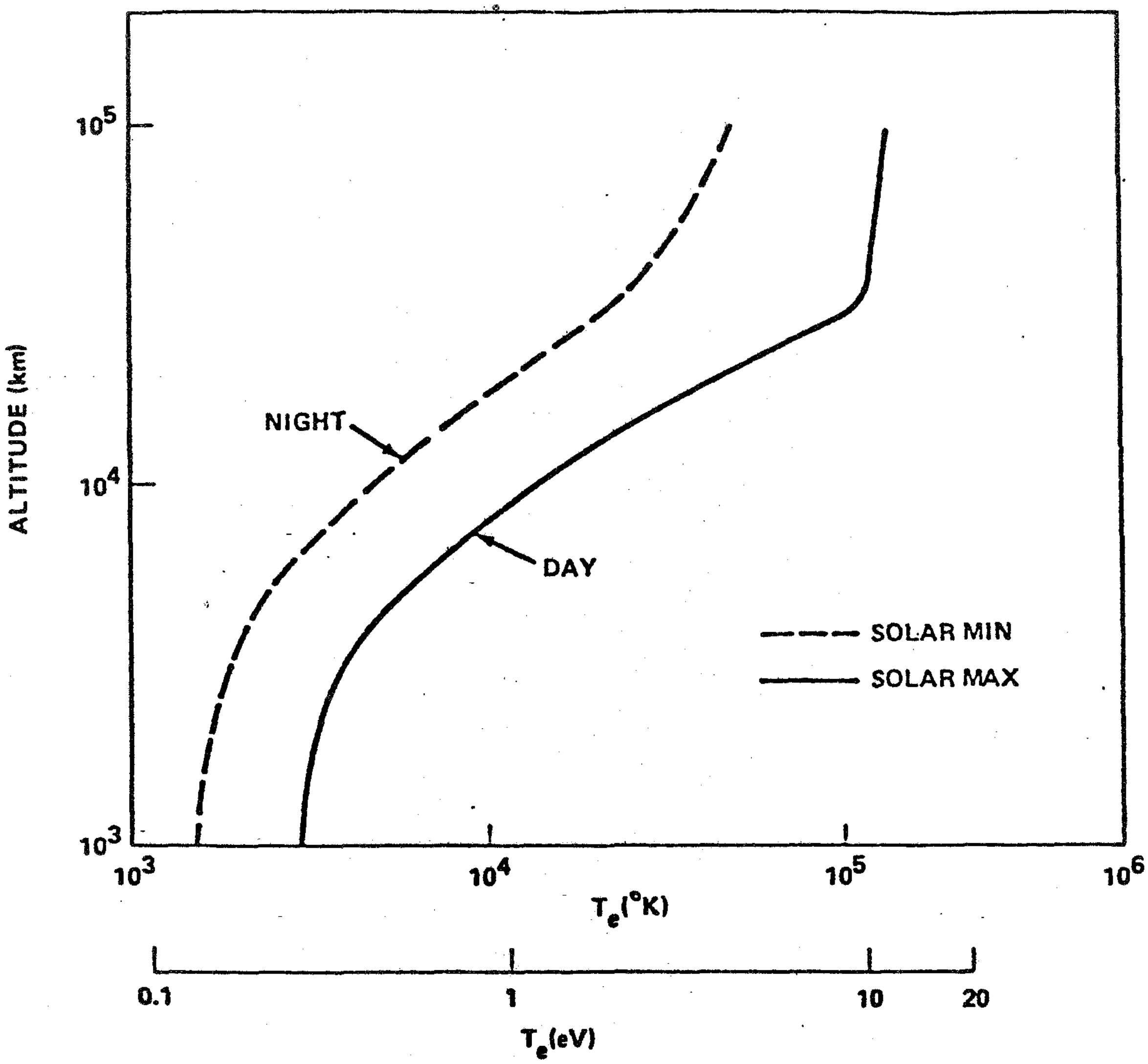

Figure 2-24. Model of electron temperature profiles [2-14].

The flux of the ionospheric particles to a spacecraft is important in calculating sheath and charging effects. The fluxes determine the maximum currents of either sign that may be drawn. An isolated body goes to a sufficiently negative potential to reduce the electron current to equal the ion current (paragraph 2.9). Particle fluxes for electrons and ions below 1000 km are presented in Figure 2-25 and fluxes above 1000 km are presented in Figure 2-26. For electrons, the number of particles flowing through a unit area is based on the electron thermal velocity, V_{T_e} ; for ions, the number is based on the satellite orbital velocity, V_o (circular orbit), because it is generally greater than the ion thermal velocity.

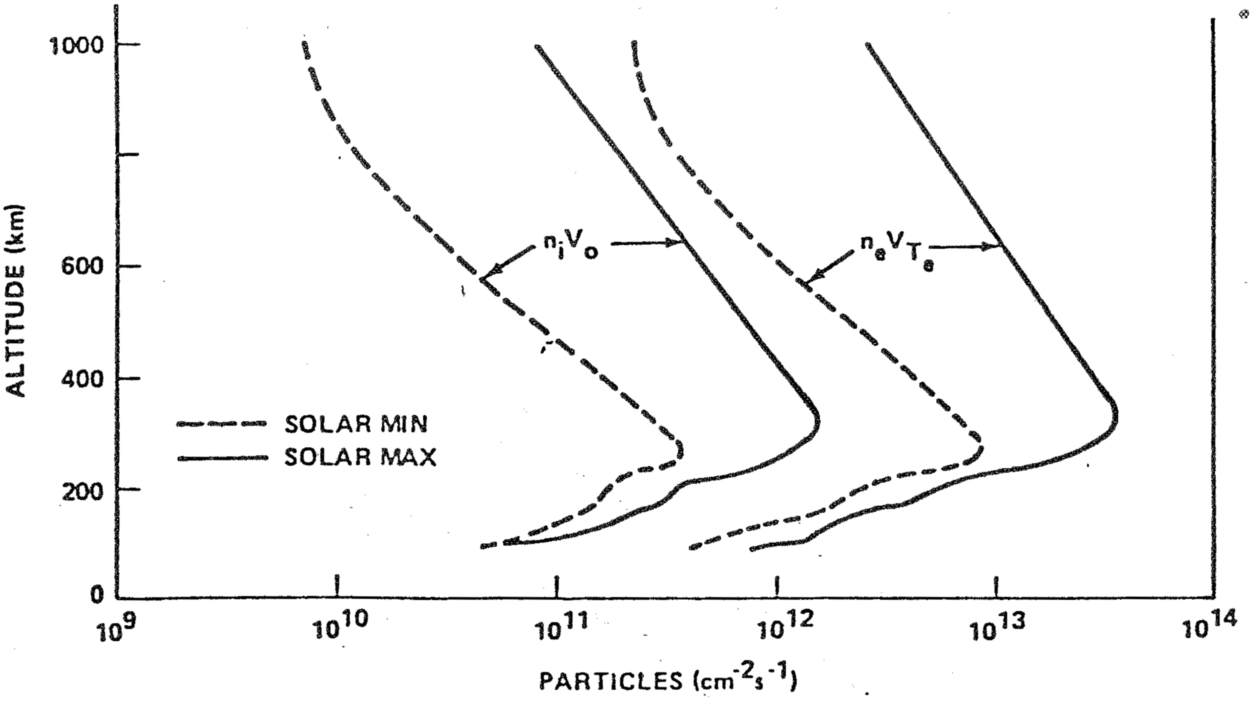

Figure 2-25. Thermal particle flux, daytime [2-14].

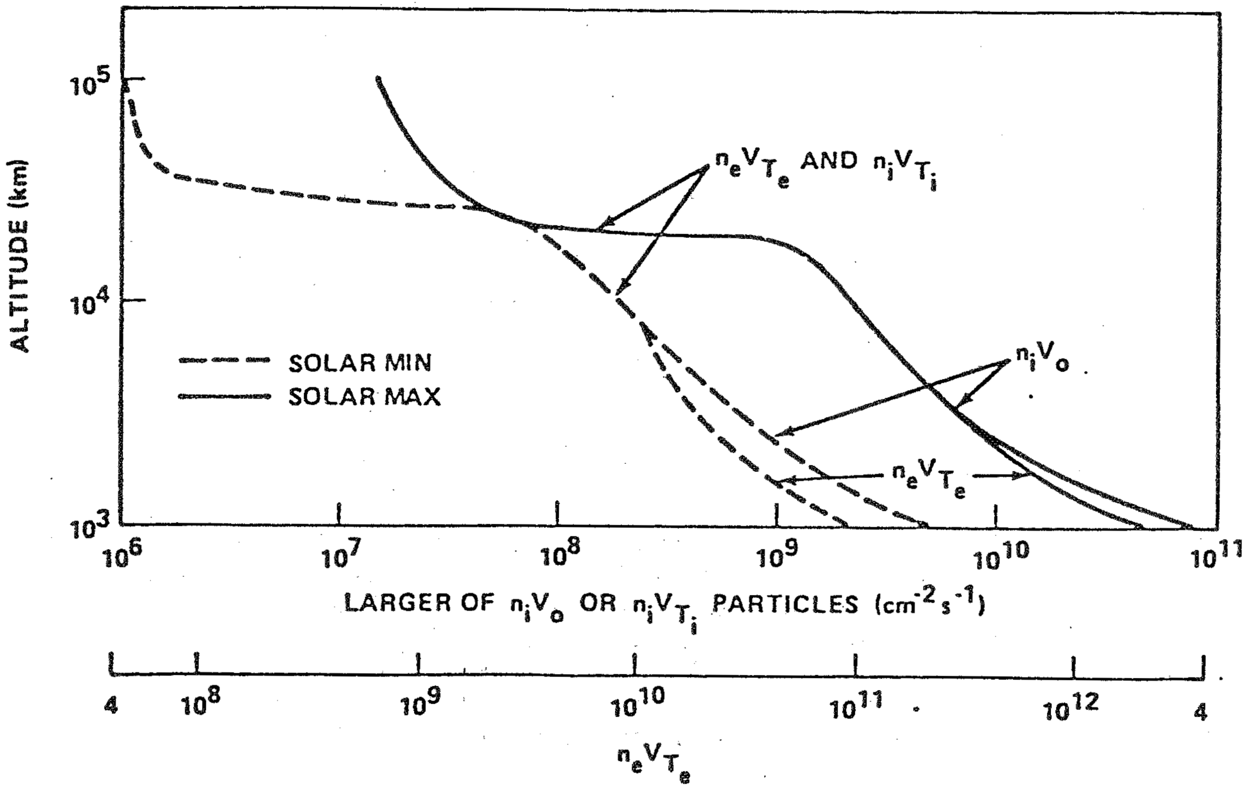

Figure 2-26. Thermal particle fluxes above 1000 km [2-14].

The topside ionosphere and plasmasphere are also populated by Van Allen belt particles (paragraph 2.8.2).

2.8.1.4 Plasma Sheet

Beyond the plasmapause lies the plasma sheet, sometimes called the auroral domain because it extends at high latitudes to the diffuse auroral zone (Figs. 2-1 and 2-2). The plasma density is low, but the average energy is higher than in the ionosphere-plasmasphere, so it is convenient to give the flux of particles as in Figure 2-27, instead of density.

The environment at geosynchronous orbit, 6.6 R_e radius, is of special interest because many satellite systems operate there. At this distance the environment varies with both local time and magnetic activity (substorm or world-wide storm), and a satellite may find itself on either side of the plasmapause or even outside the magnetopause on the day side as these boundary surfaces move.

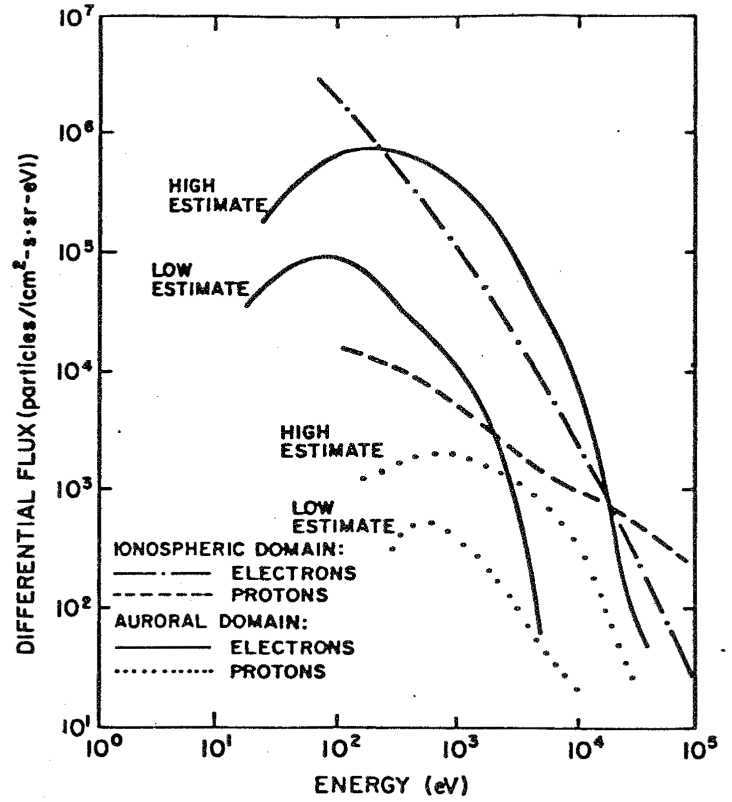

Figure 2-27. Composite electron and proton spectra in the inner magnetosphere and plasma sheet [2-43,2-44].

2.8.2 Energetic Particles

The energetic particles found in the magnetosphere are the geomagnetically trapped or Van Allen radiation, together with the still more energetic cosmic rays that enter from outside.

2.8.2.1 Trapped Particles

The trapped particles, accelerated within the magnetosphere, move as follows:

a) They rotate around the field at the cyclotron frequency,

$$\omega_{ce} = eB/mc \quad (f_{ce} \simeq 2.8 \text{ [MHz/Gauss]} \cdot B \text{ [gauss]})$$

b) The (guiding) center of gyration moves in latitude along the magnetic field lines until the mirror point is reached (the point of maximum $|B|$). The particle is reflected and drifts to the mirror point in the outer hemisphere. (If a mirror point were in the atmosphere the particle would be lost through collisions.)

c) The line on which the guiding center moves drifts in longitude, electrons east and positive particles west, always crossing the equator at the same distance (in the dipole approximation). Thus a particle's guiding center moves on a closed surface or L-shell. Similar motion occurs in the real geomagnetic field, with guiding centers following irregularities.

In this motion kinetic energy is conserved so long as $\underset{\sim}{B}$ is static. Temporal variations of the field accelerate and decelerate particles and also move them from one location to another. Another quantity rigorously conserved is directional intensity, (particles per cm^2 sec sterad keV). If we follow a group of particles along their trajectory, the directional intensity is constant wherever they go, in agreement with Liouville's theorem.

This motion may be described by the adiabatic invariants which are "almost constants" of the motion. The first invariant is

$$\frac{mv_{\perp}^2}{B} = \text{const} = mv^2 \left(\frac{\sin^2\alpha}{B}\right) \quad , \text{ since } v^2 = \text{const} \quad ,$$

with α the angle between velocity and field. Since α = 90 deg at the mirror points,

$$\frac{\sin^2 \alpha}{B} = \frac{1}{B_{mirror}}$$

gives the mirroring field. The second and third invariants constrain the longitudinal drift around the Earth [2-28].

Particle lifetime ranges from hours (even less than a full revolution around the Earth) to years. Radiation may be durably trapped, if of proper energy, inside L = 10. Beyond that, drift in longitude would carry it through the magnetopause on the day side. Because of the trapped particles' motion, the distribution of omnidirectional flux as a function of energy in a single meridian plane defines the omnidirectional flux at all longitudes. Similarly, the directional intensity as a function of energy and pitch angle along a single radius in the equatorial plane determines the intensity everywhere.

Models of the trapped radiation have been compiled by Vette and others at the National Space Science Data Center [2-10,2-43,2-45,2-46,2-47,2-48,2-49,2-50]. These models provide numerical and graphical data and computer programs which are available from the NSSDC, NASA/Goddard Space Flight Center to calculate flux at any position. The "fluence" (time integrated flux) for any orbit may be calculated from these data.

Some representative omnidirectional fluxes in a meridian plane, shown in Figures 2-28 through 2-31, are from these models. Figure 2-32 shows differential energy spectra.

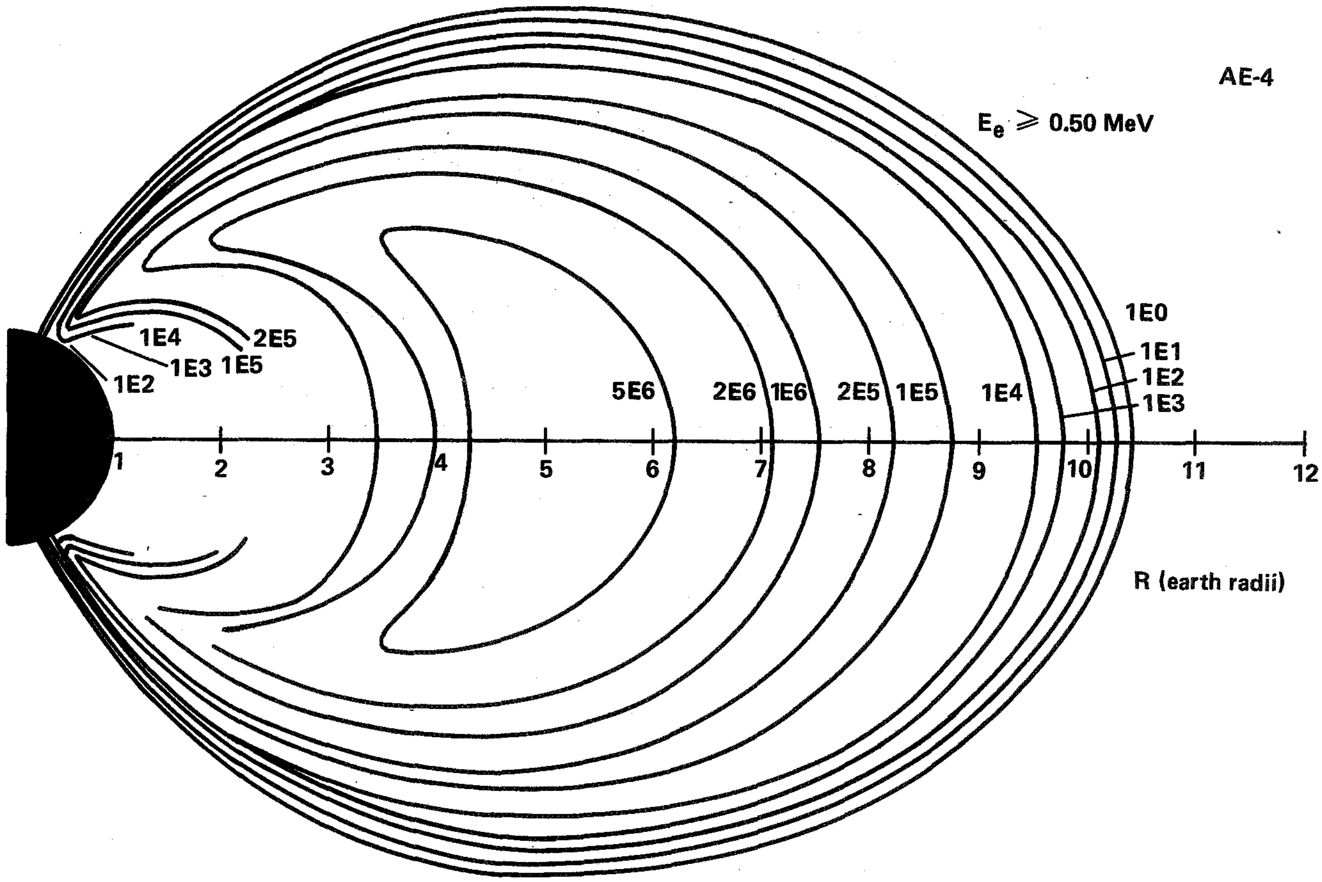

Figure 2-28. R-λ map of AE-4 electron fluxes for Epoch 1964, threshold energy 0.5 MeV. Solar minimum.

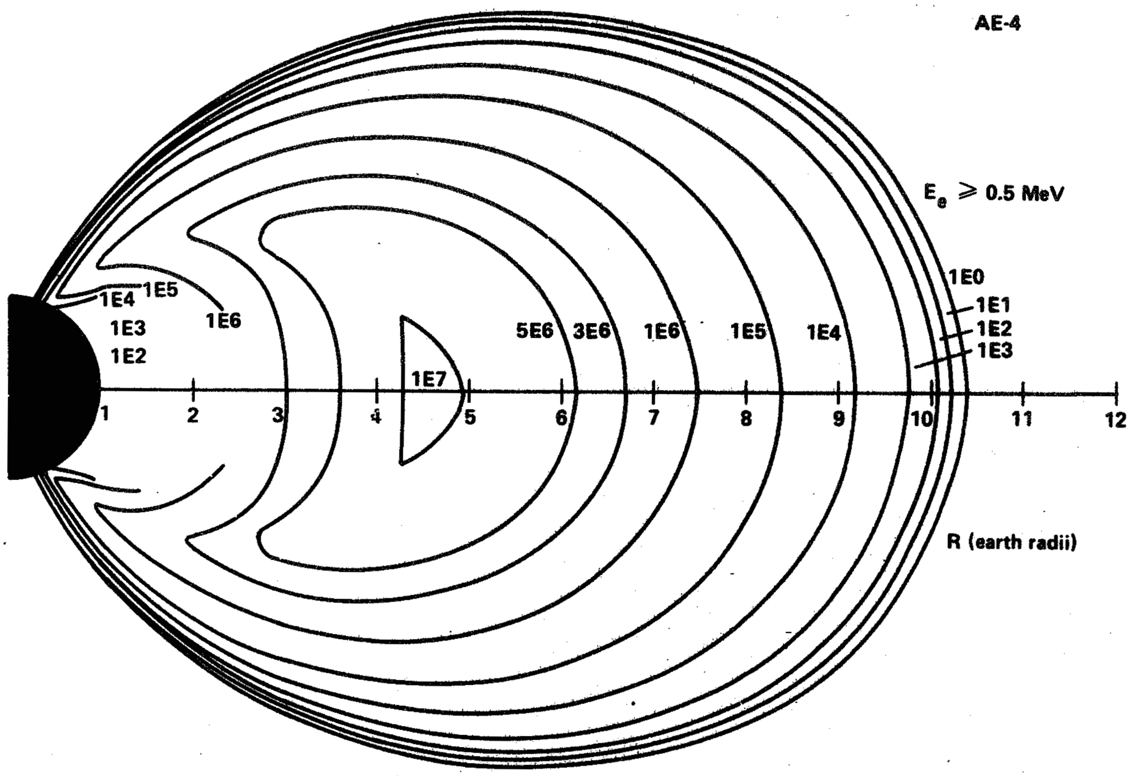

Figure 2-29. R-λ map of AE-4 electron fluxes for Epoch 1967, threshold energy 0.5 MeV. Solar maximum.

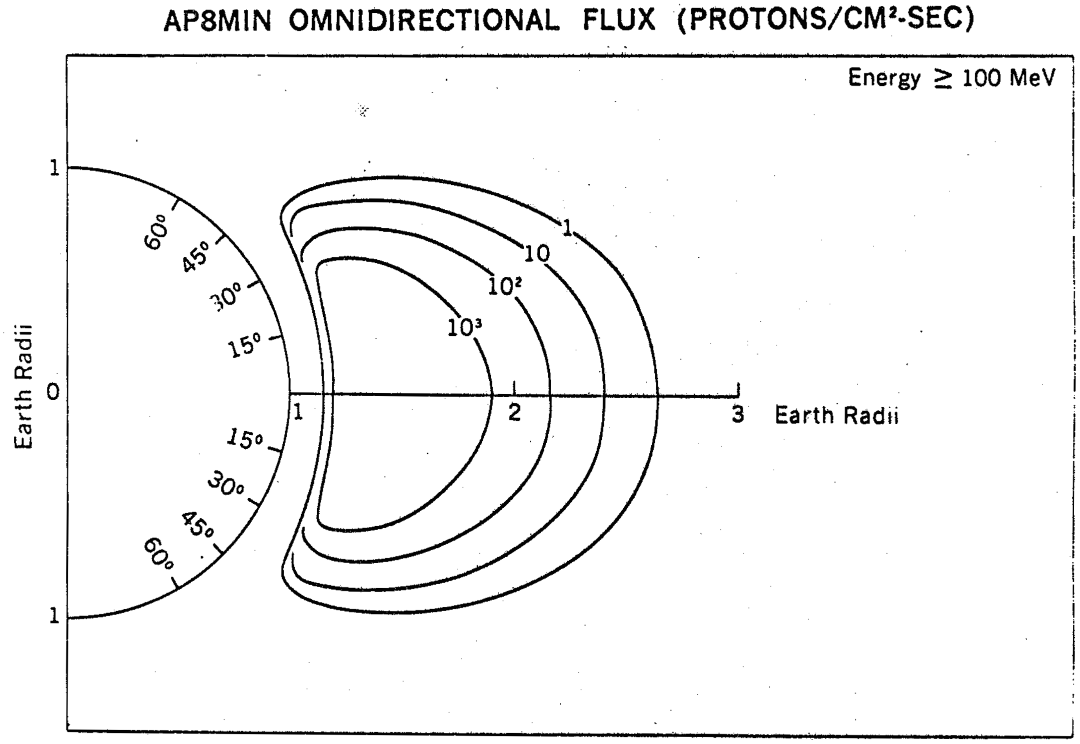

Figure 2-30. AP8MIN R-λ plot of constant intensity flux contours with an energy of ≥ 100 MeV [2-47].

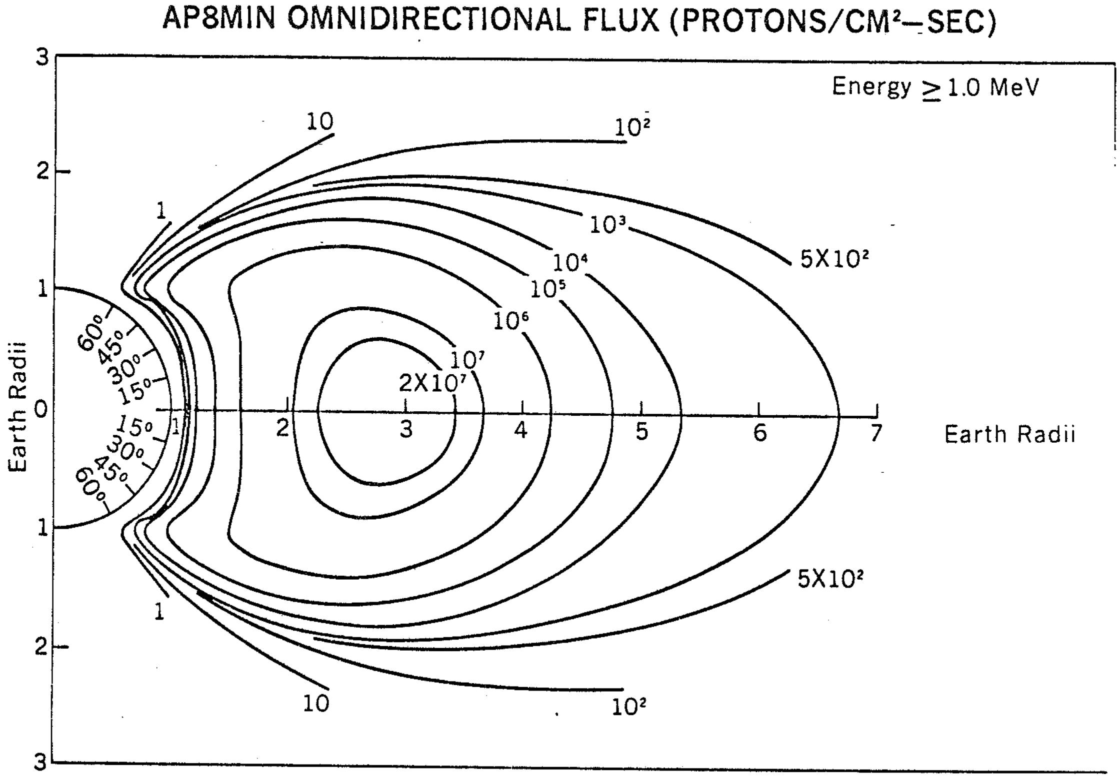

Figure 2-31. AP8MIN R-λ plot of constant intensity flux contours with an energy of ≥ 1.0 MeV.

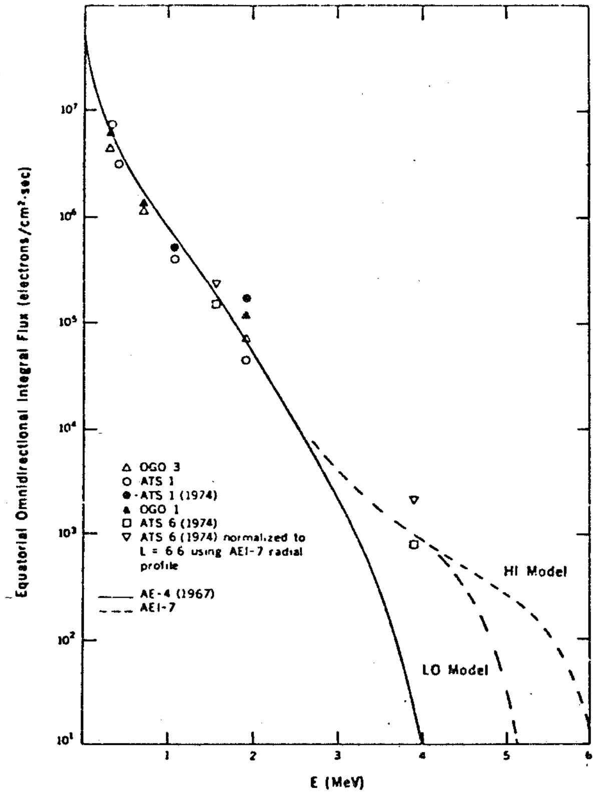

Figure 2-32. Model electron spectra together with experimental data for geosynchronous orbit [2-51].

Chan et al. [2-43] have calculated fluxes of electrons and protons with $E < 100$ keV encountered in five regions along the ISEE satellite orbit (21 R_e apogee, 280 km perigee, 28.5 deg inclination). Figures 2-33 and 2-34 show fluxes, spin averaged.

The intensity received along a satellite orbit may be integrated over an orbital period or other interval. Figure 2-35 shows the orbit averaged spectra for ISEE, and Figures 2-36 and 2-37 show the omnidirectional electron and proton fluxes received in low altitude orbits per day [2-46]. The asymmetry of the geomagnetic field brings the radiation belts lowest over the South Atlantic anomaly as illustrated in Figure 2-38. Vehicles at 100- to 400-km altitude will also encounter auroral radiation in the auroral zone at 60 to 70 deg geomagnetic latitude. The diffuse auroral radiation is an extension of the plasma sheet and has similar directional intensities. In the evening sector discrete arcs occur with electron spectra probably resulting from localized electric fields parallel to $\underset{\sim}{B}$. Figure 2-39 was based on rocket measurements in aurora at approximately 300-km altitude. Proton fluxes are less than 1 percent of the electron flux. These electrons produce locally enhanced electron density in the ionosphere as they collide with the neutral atmosphere. Figure 2-40 shows auroral electron density as measured by the Chatanika incoherent scatter radar.

At geosynchronous orbit fluxes are less energetic [2-52]. Figure 2-41 shows the flux there integrated over a day (Fig. 2-32).

2.8.3 Cosmic Radiation

Cosmic ray particles enter the magnetosphere from outside it and are of two types:

a) Galactic cosmic rays – steady mean flux intensity from outside the solar system

b) Solar cosmic rays – come in bursts from the Sun.

The particles move in the geomagnetic field without significant energy change, but a particle of given magnetic rigidity, R, (R = P/Z momentum per unit charge) is prevented from reaching certain locations. The minimum rigidity that can reach a given location depends on the direction of arrival at that location. In the dipole approximation to the field

$$R_{min} = \frac{60 \cos^4 \lambda}{r^2 \left[1 + (1 - \cos^3 \lambda \cos \gamma)^{\frac{1}{2}}\right]^2} \text{ GV}$$

where

r = radial distance in Earth radii

λ = latitude

γ = half angle of allowed cone of arrival direction about the normal to the meridian plane. (Directions closer to the normal are allowed.)

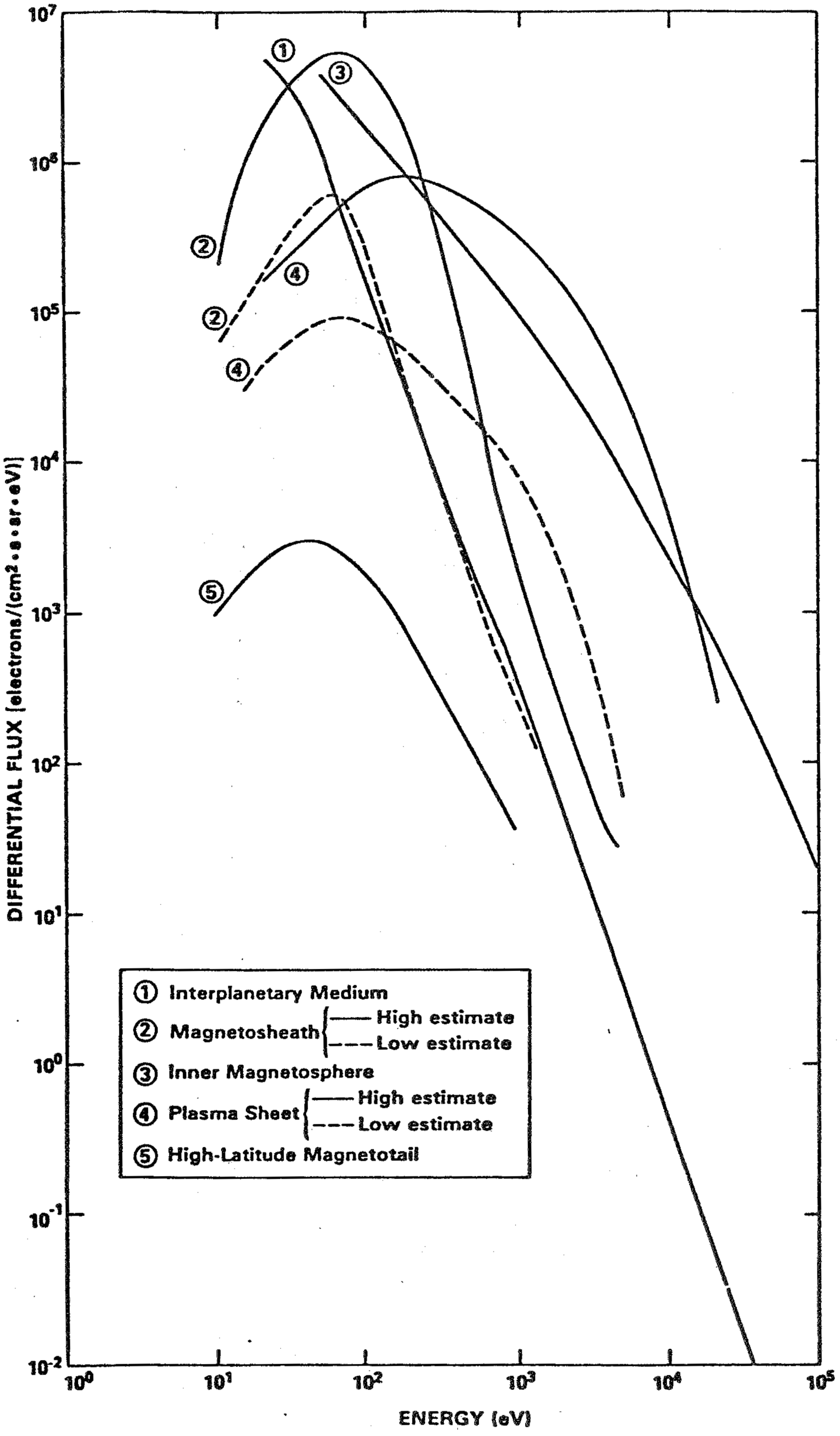

Figure 2-33. Composite electron spectra [2-43].

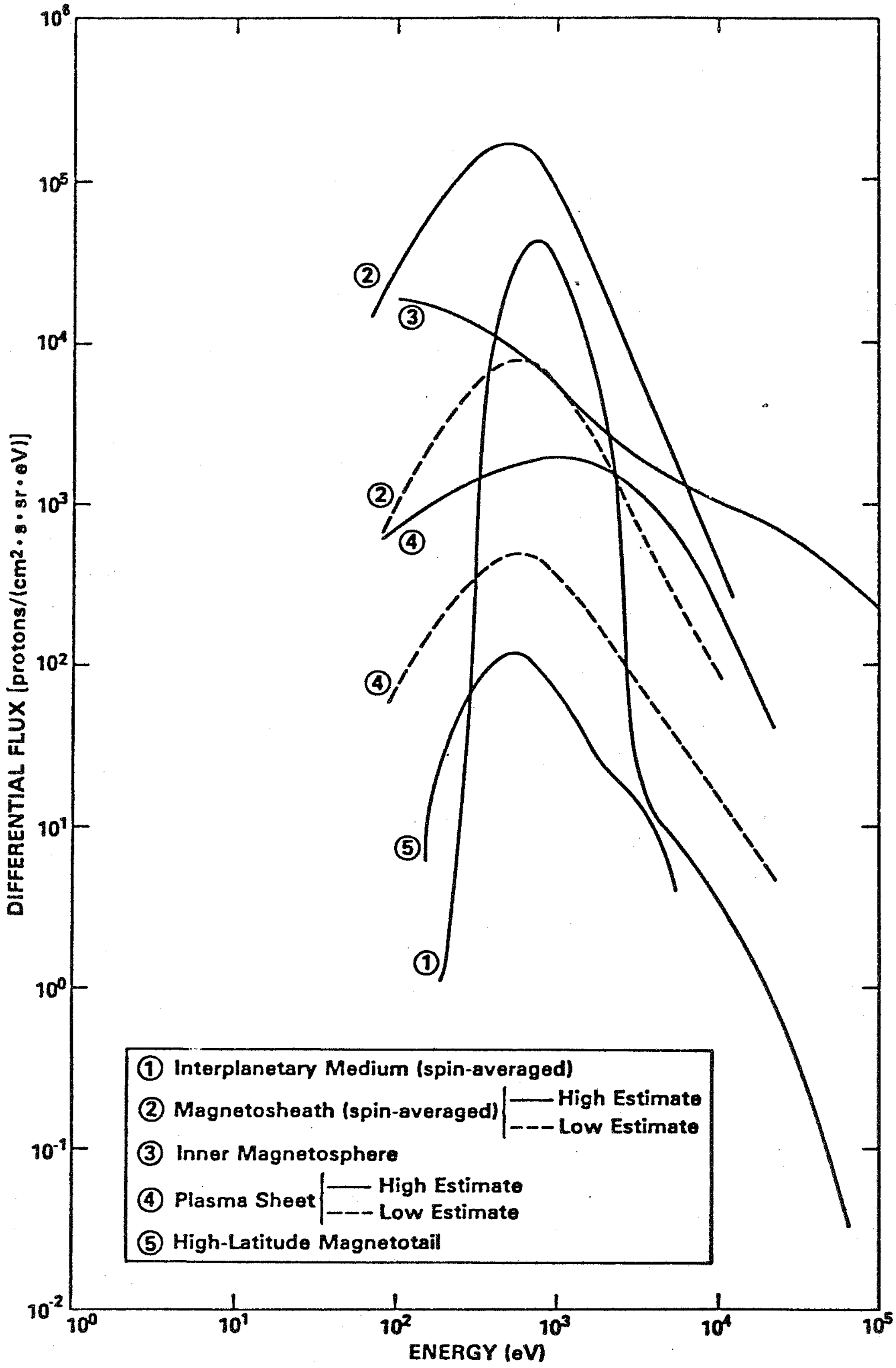

Figure 2-34. Composite proton spectra [2-43].

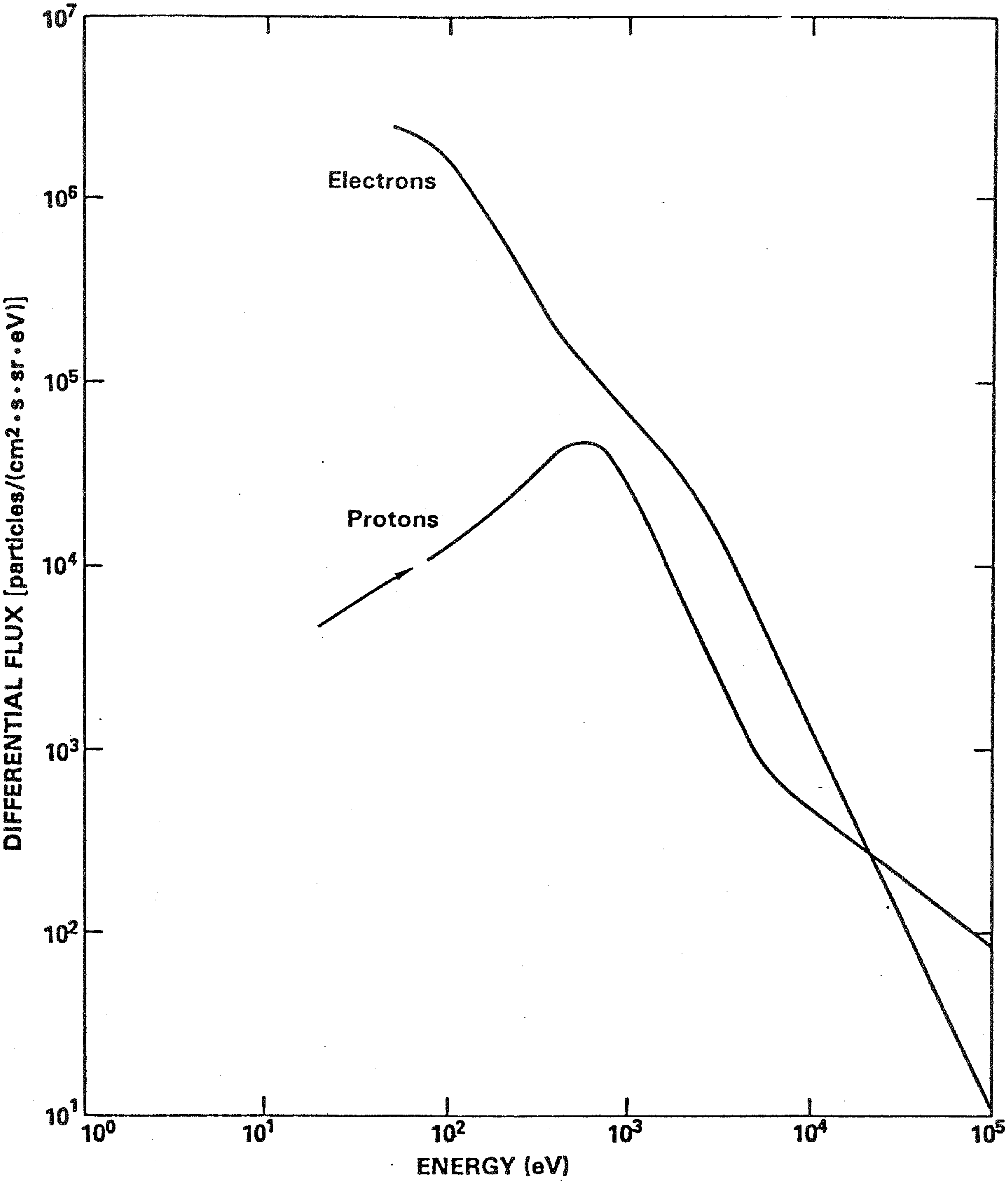

Figure 2-35. Orbit-averaged differential spectra, ISEE [2-14].

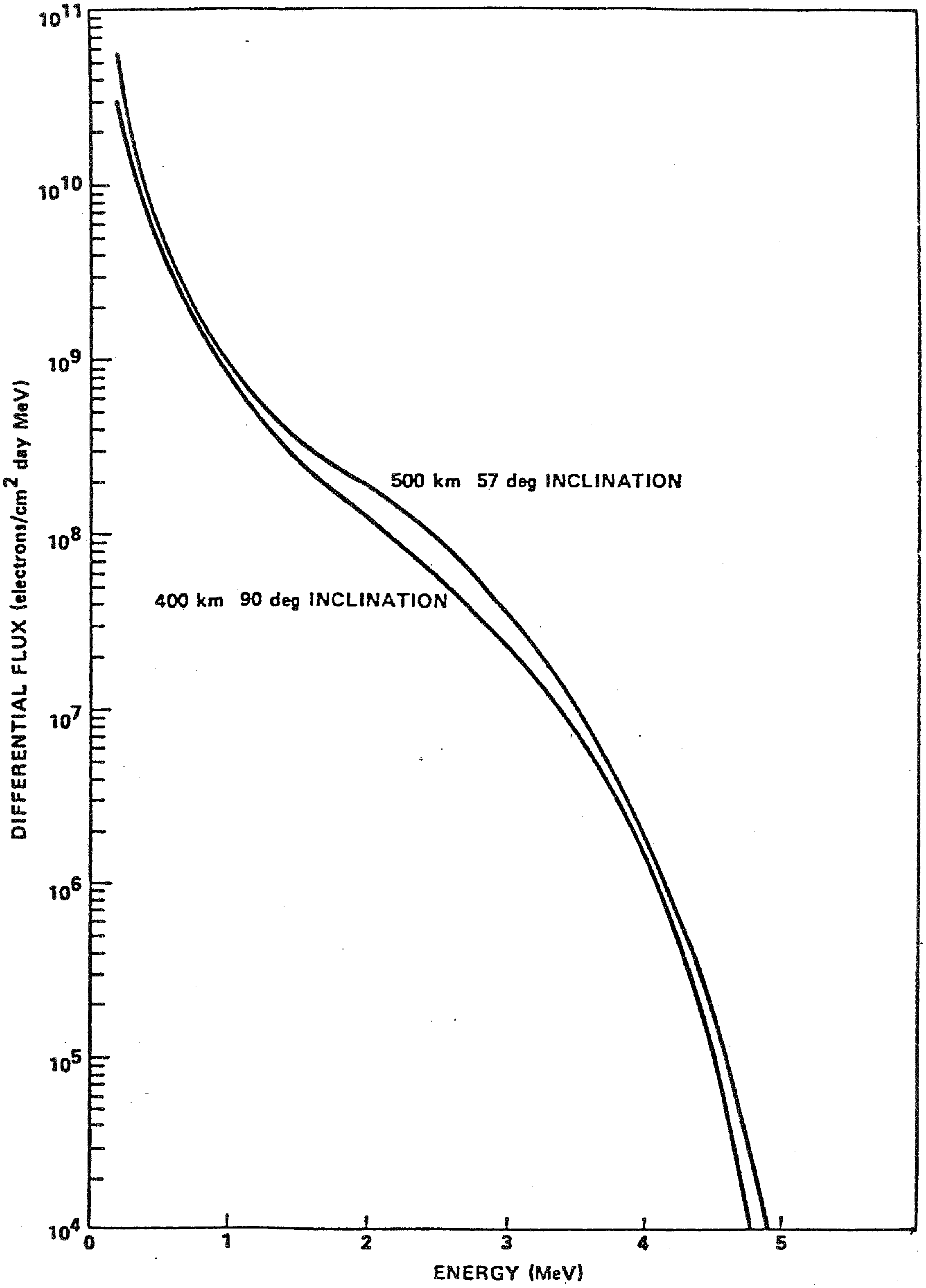

Figure 2-36. Electron differential energy spectra [2-14].

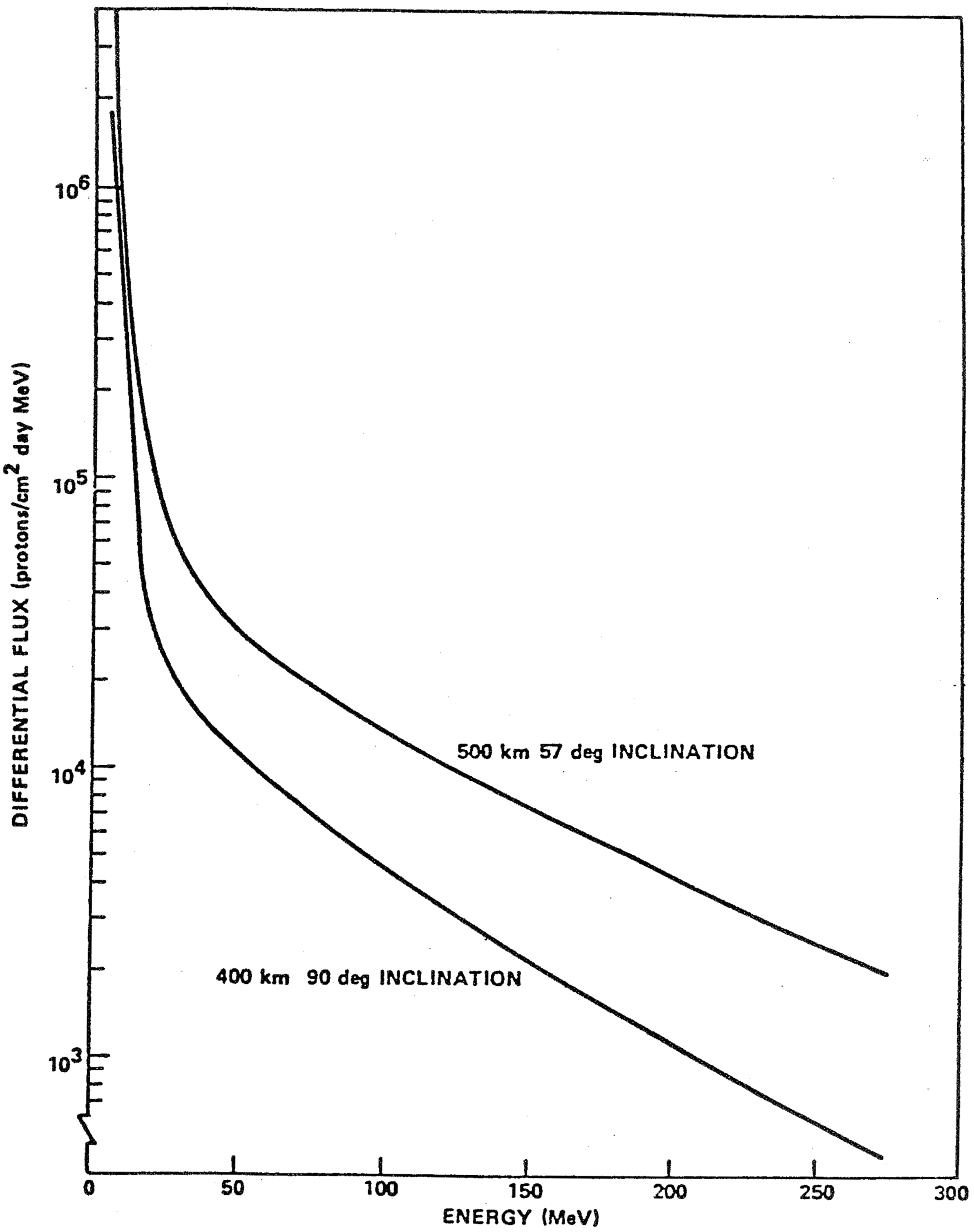

Figure 2-37. Proton differential energy spectra [2-14].

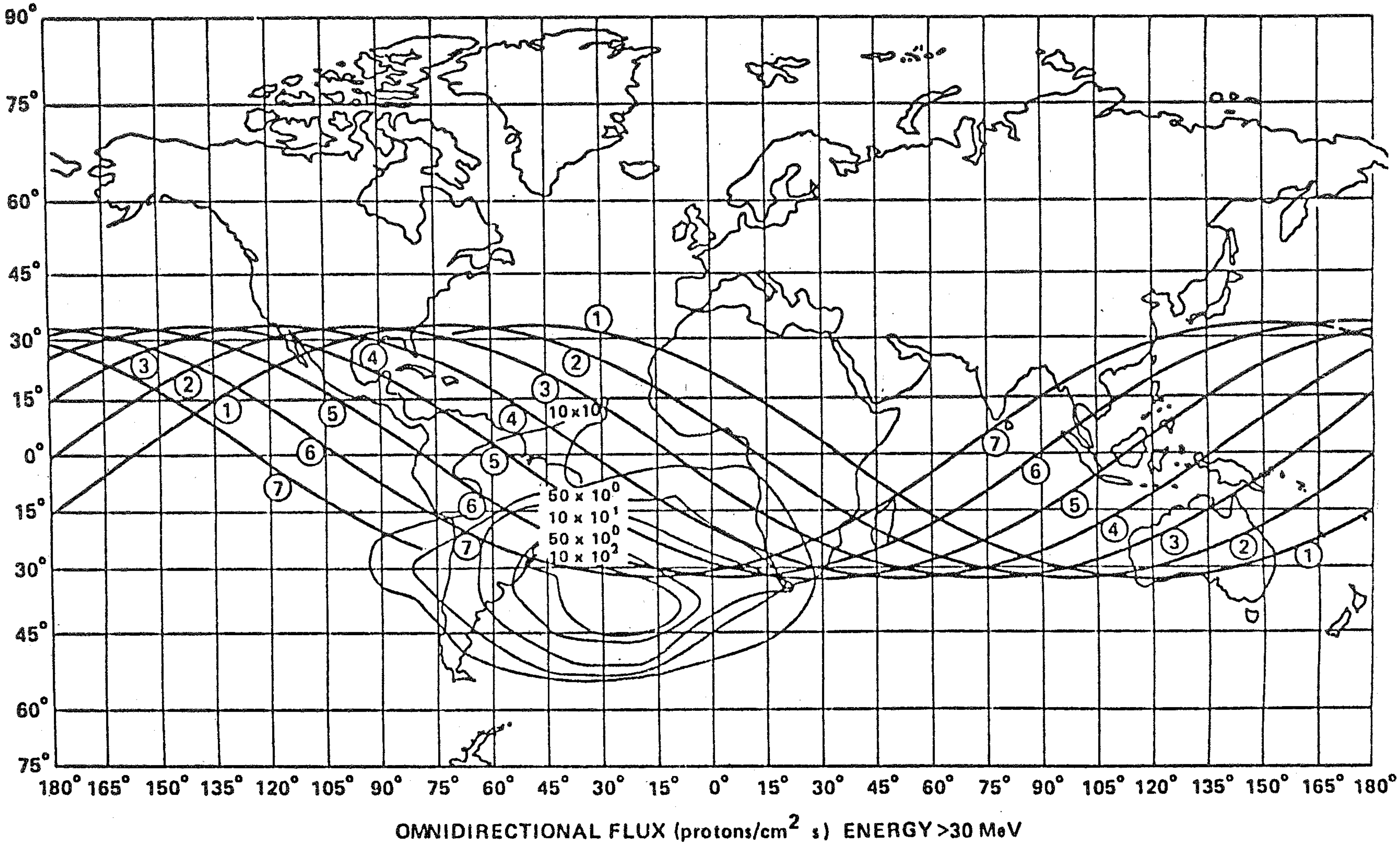

Figure 2-38. Proton flux densities at an altitude of 296 km.

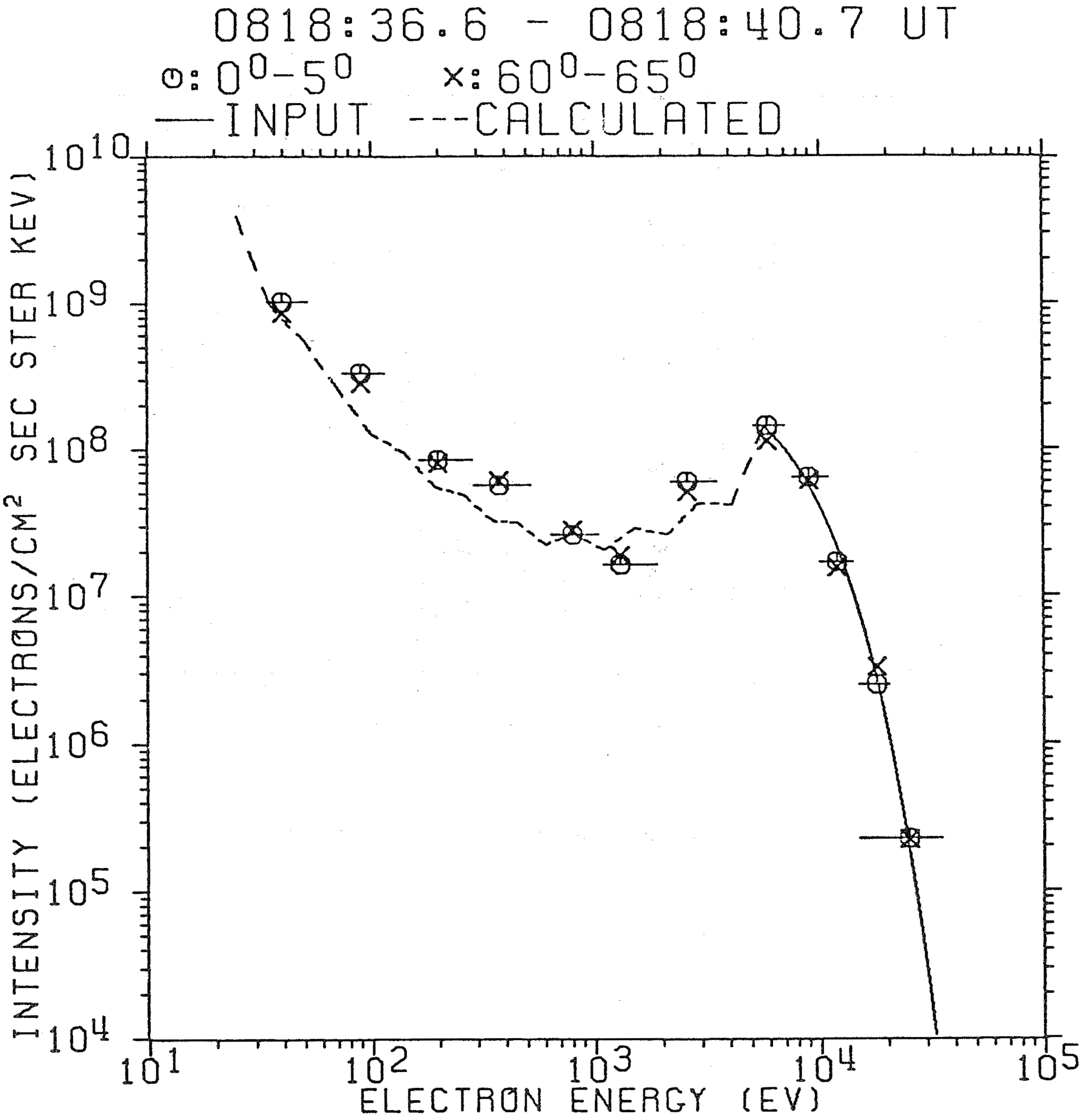

Figure 2-39. Auroral electron intensity (center of the arc) [2-53].

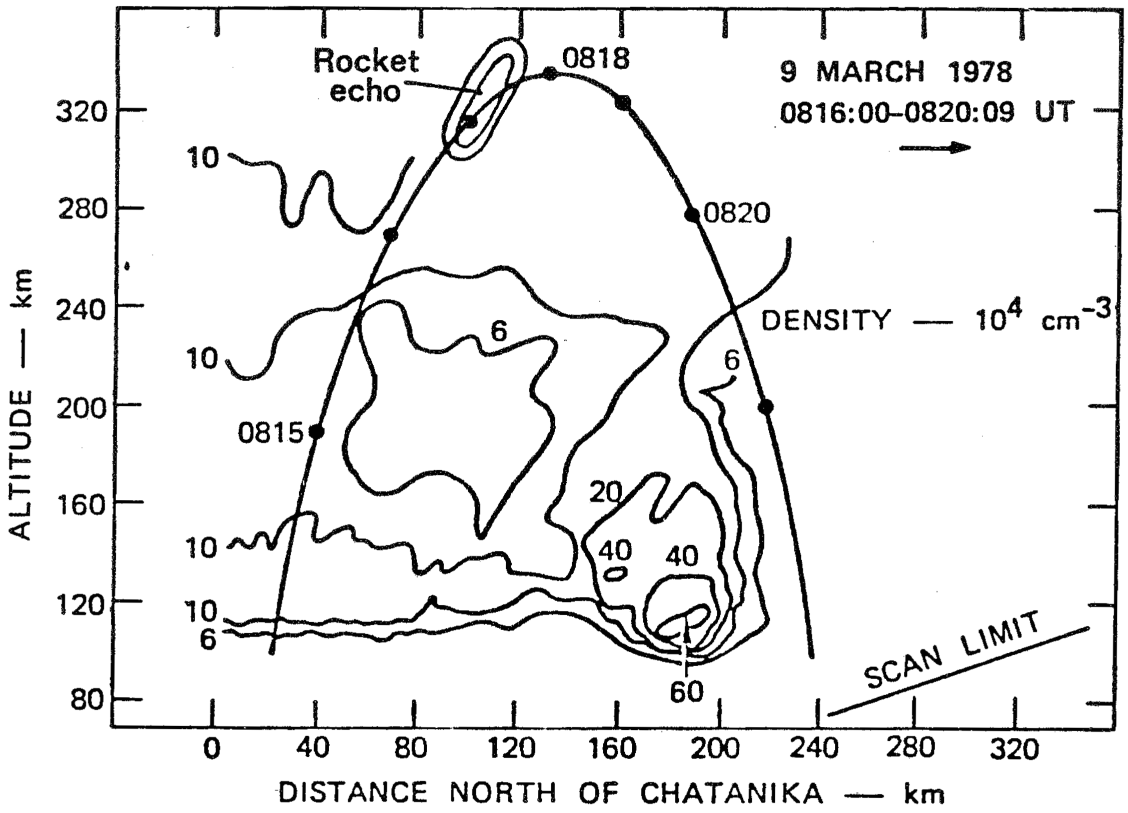

Figure 2-40. Ionospheric electron density in an aurora [2-54].

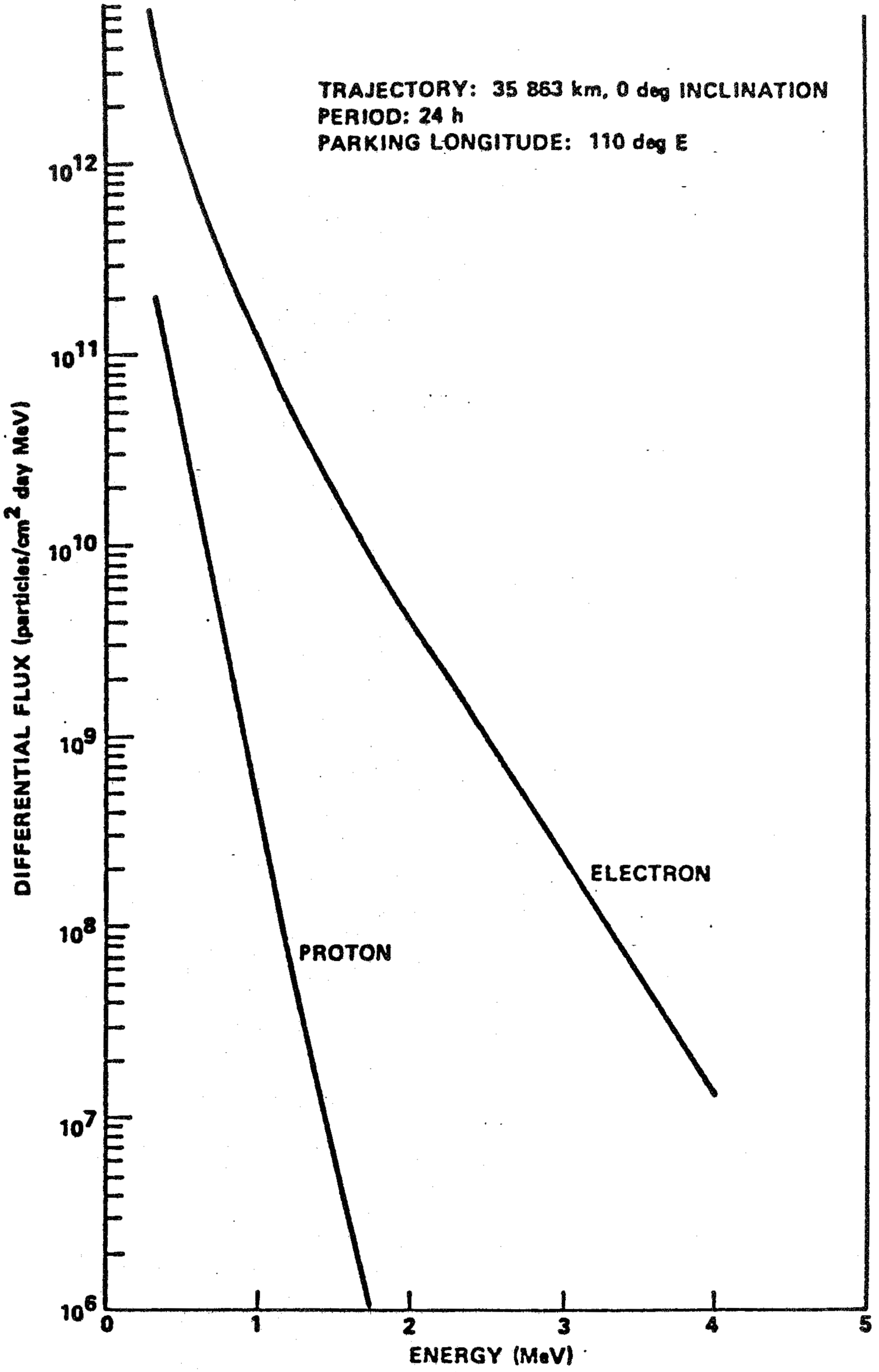

Figure 2-41. Electron and proton differential energy spectra [2-14].

One GV = 10^9 V; one GeV = 10^9 eV. For vertical arrival at Earth's surface $r = 1$, $\gamma = 90$ deg so

$$R_{min} = 15 \cos^4\lambda \ [GV]$$

The rigidity of a particle is related to its energy [2-55]

$$E = \sqrt{(RZ)^2 + (mc^2)^2} = \text{total energy, GeV}$$

where

mc^2 = rest mass energy in GeV

Z = atomic number

R = magnetic rigidity.

The external field alters R_{min} so that in the polar cap, above about 65 deg latitude, the cutoff is nearly zero.

2.8.4 Galactic Cosmic Rays

So far as we know these particles fill our portion of the galaxy uniformly and isotropically outside the solar system. They consist of approximately 85 percent protons, 14-percent alpha particles, and approximately 1-percent heavier nuclei. In addition, the electron and positron flux amounts to approximately 1 percent of the proton flux. Nuclei occur with energies at least up to 10^{20} eV. The differential energy spectrum of all particles above a few GeV is proportional to $1/E^\gamma$ with γ approximately 2.6 (Figs. 2-42 and 2-43).

2.8.4.1 Effect of Solar Activity on Galactic Cosmic Rays at the Earth

The intensity of particles with energy below approximately 10 GeV that reach Earth's orbit is reduced below the interstellar level by interaction with the solar wind and interplanetary magnetic field. It is thought that a cavity approximately 100 AU in radius from the Sun is affected. The result is that in the active part of the 11 year solar cycle the galactic cosmic ray intensity at Earth is reduced. The effect on the energy spectrum is shown in Figures 2-42 and 2-43.

Figure 2-44 shows the dose rate versus latitude. Note that lowest energy particles are reduced the most. One effect of this is that as cosmic rays penetrate the atmosphere, or a solid vehicle, the intensity and dose rate for particles of solar maximum increase up to approximately 40 g/cm^2 shielding thickness. This is because the high energy particles produce many secondaries of various kinds (Fig. 2-45) [2-56].

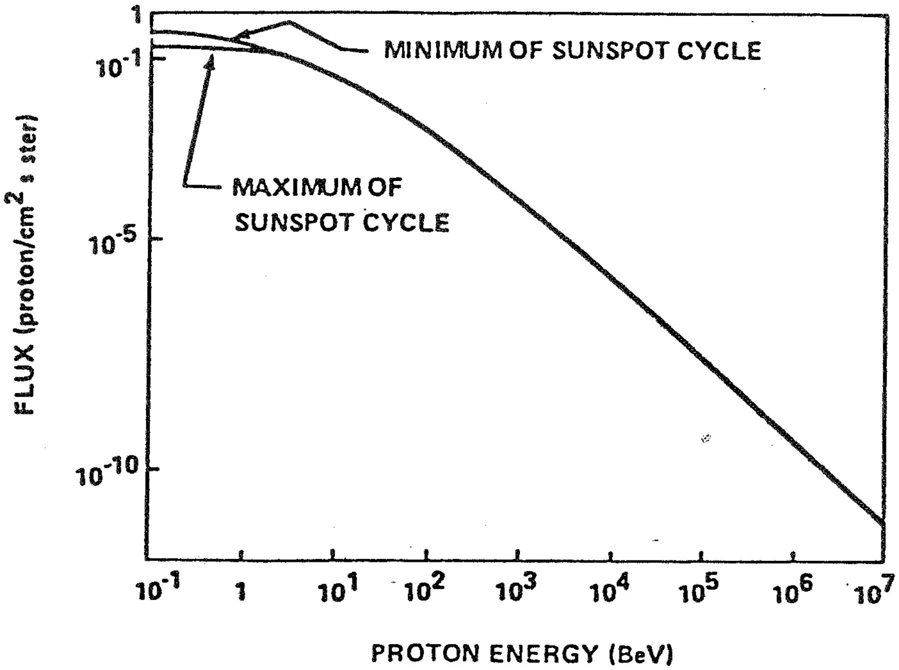

Figure 2-42. Galactic radiation integral energy spectrum. The flux is the number above the given energy [2-14].

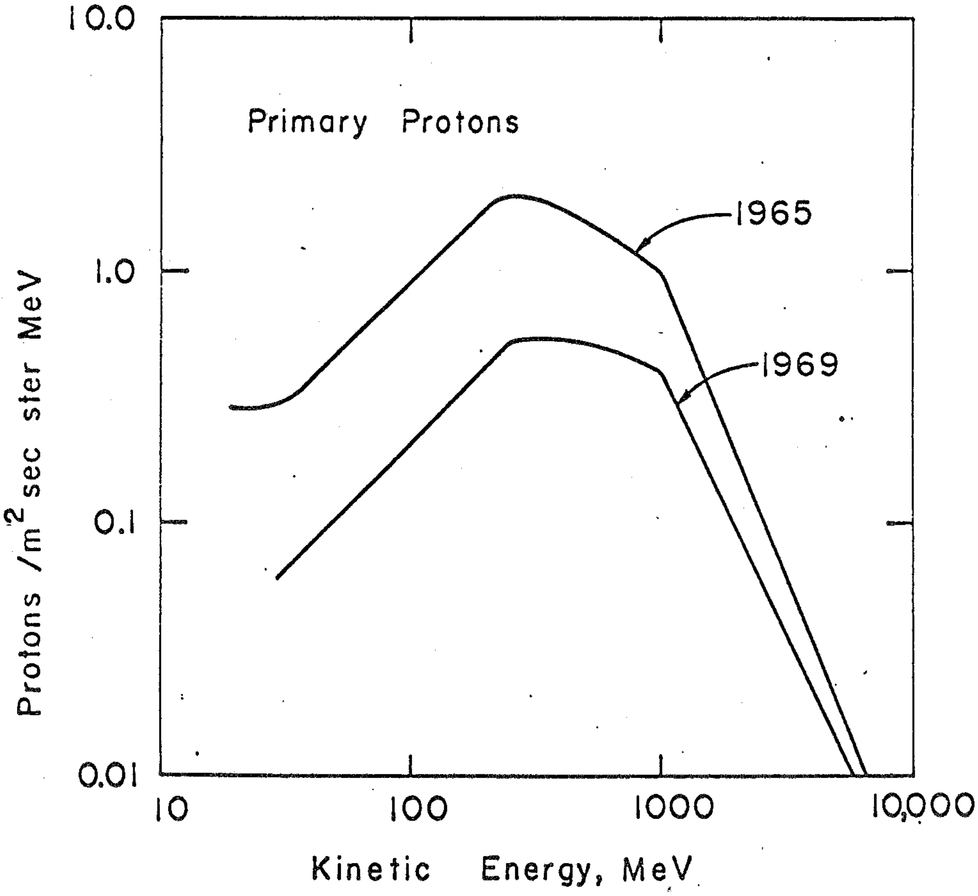

Figure 2-43. Differential flux of galactic cosmic ray protons at solar maximum (1969) and minimum (1965) [2-56].

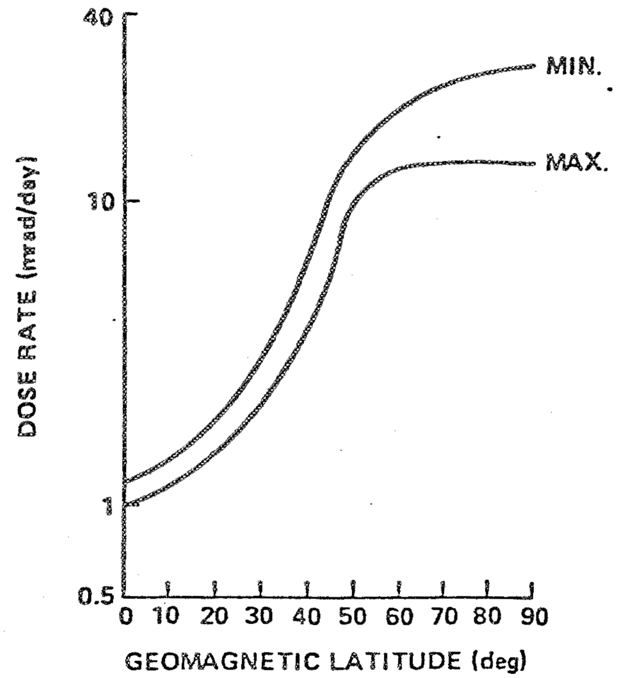

Figure 2-44. Cosmic ray dose rate as a function of latitude at solar minimum and solar maximum [2-14].

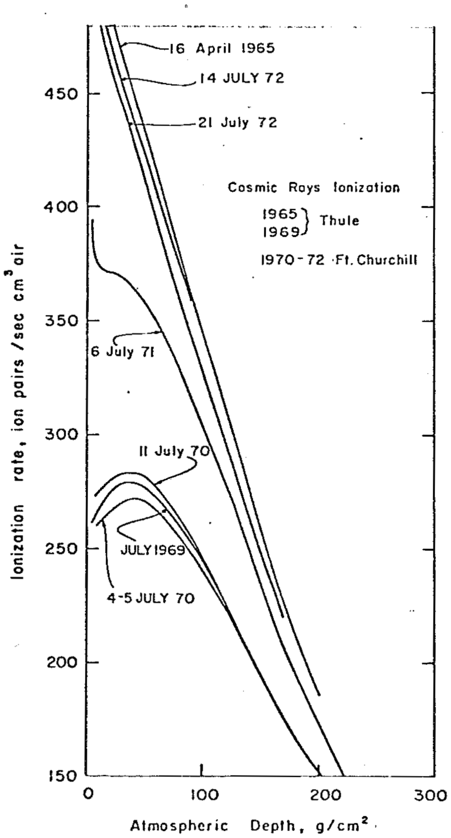

Figure 2-45. Ionization rate in the atmosphere versus depth [2-14].

2.8.5 Solar Cosmic Rays

Solar cosmic rays are ejected from the Sun in solar flare events and consist of protons, alphas, and electrons. They are generally of lower energy than galactic cosmic rays. Below 1 GeV kinetic energy and down to 1 MeV the integral flux of solar protons is 10^5 greater than galactic particles, but is less above a few GeV. Table 2-4 shows some model spectra.

TABLE 2-4. MODEL SOLAR COSMIC RAY SPECTRA [2-14]

Protons:	N_p (>T) =	$7.25 \times 10^{11}\ T^{-1.2}$;	1 MeV $\leq$ T $\leq$ 10 MeV
		$3.54 \times 10^{11}\ e^{-P(T)/67}$;	10 MeV $\leq$ T $\leq$ 30 MeV
		$2.64 \times 10^{11}\ e^{-P(T)/73}$;	T $\geq$ 30 MeV.
Alphas:	N_α (>T)	N_p (>T) ;	T < 30 MeV
		$7.07 \times 10^{12}\ T^{-2.14}$;	T $\geq$ 30 MeV.

T = kinetic energy = $E - m_0c^2$

$P = RZ$ = momentum

The stream of solar cosmic rays reaches and envelopes Earth minutes after a solar flare and reaches peak intensity in a few hours. It then decays in 1 to 2 days. Solar cosmic ray bursts are sporadic but are most frequent near solar maximum. Figure 2-46 shows dose rates from both solar and galactic particles [2-57]. Unshielded, the dose from solar particles is greater. However, a few tens of mg/cm^2 of shielding excludes the effects of solar cosmic rays and galactic cosmic rays dominate [2-58,2-59].

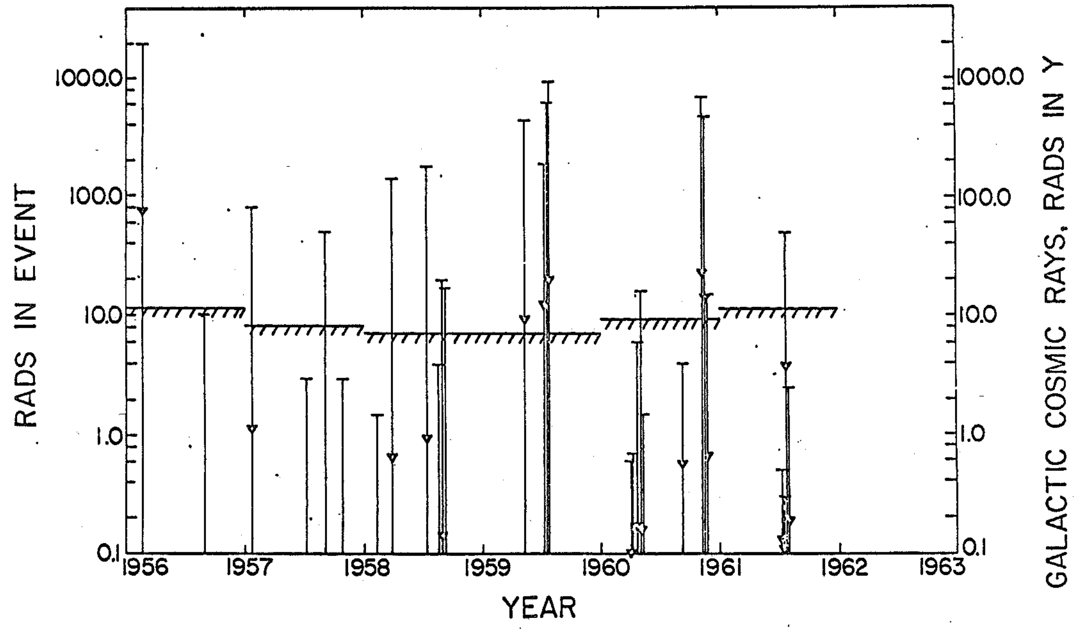

Figure 2-46. Dose from solar cosmic ray events (vertical lines) and from galactic cosmic rays (hatched horizontal lines). Tops of lines T 30 MeV, triangles, T 100 MeV [2-57].

2.9 SPACECRAFT CHARGING

In orbit, or in deep space, vehicles can develop an electric potential up to tens of thousands of volts relative to the ambient plasma, and large differential potentials can also occur. One of the consequences is electrical discharge or arcing which can damage surface structures and electronic systems [2-60]. Garrett recently published a comprehensive review [2-61].

Garrett's review paper [2-60] gives the basic spacecraft charging equation in terms of number or current densities:

$$J_E(V) - (J_I(V) + J_{SE}(V) + J_{BSE}(V) + J_{PH}(V) + J_B(V) + J_{SI}(V)$$
$$+ J_{RLC}(V) = J_T(V)$$

where

V = satellite potential

J_E = ambient electron flux to a point on satellite surface

J_I = ambient ion flux to a point on satellite surface

J_{SE} = secondary electron flux due to J_E

J_{SI} = secondary ion flux due to J_I

J_{BSE} = backscattered electrons due to J_E

J_{PH} = photoelectron flux

J_B = active current sources such as charged particle beams or ion thrusters

J_{RLC} = resistive, capacitive, and inductive coupling currents between a point and adjoining surface .

Analysis of each of these terms is complex and depends upon the spacecraft configuration and materials, whether it is in sunlight or shadow, its altitude, and variable factors such as the flux of high energy solar particles and magnetic storm activity.

Use of conducting surfaces where possible and adequate grounding techniques can significantly reduce differential charging, which is usually a more serious problem than is the development of a high satellite-to-space potential. Active techniques such as low-current electron and ion emitters have been used to clamp the satellite potential to the surrounding plasma.

REFERENCES

2-1. Valley, S. L. (ed.): AFGL Handbook of Geophysics and Space Environments. McGraw-Hill, New York (1965 and later supplements).

2-2. Heikkila, W. J.: EOS, vol. 54, 1973, p. 764.

2-3. Wolf, R. A.: Ionospheric-Magnetosphere Coupling. Space Sci. Rev., vol. 17, 1975, pp. 537-562.

2-4. Stern, D. P.: Energetics of the Magnetosphere. NASA GSFC TM-82039, November 1980.

2-5. Olson, W. P. (ed.): Quantitative Modelling of Magnetospheric Processes. Am. Geophys. Union, Washington, D.C., Geophysical Monograph 21, 1979.

2-6. Allen, C. W.: Astrophysical Quantities. Univ. of London Athlone Press, London, 1963.

2-7. Gaposchkin, E. M. (ed.): 1973 Smithsonian Standard Earth (III). Smithsonian Astrophysical Observatory Special Report 353, 1973.

2-8. Gaposchkin, E. M.: Gravity-Field Determination Using Laser Observations. Smithsonian Astrophysical Observatory, Center for Astrophysics, preprint series No. 548, February 1976.

2-9. The American Ephemeris and Nautical Almanac for the Year 1976. U. S. Government Printing Office, Washington, D.C.

2-10. Minzner, R. A. (ed.): The 1976 Standard Atmosphere Above 86 km Altitude. NASA SP-398, 1976.

2-11. Chamberlain, J. W.: The Theory of Planetary Atmospheres. Academic Press, New York, 1978.

2-12. Justus, C. G., Woodrum, A. W., Roper, R. G., and Smith, O. E.: Four-D Global Reference Atmosphere: Technical Description. Parts I and II, NASA TM X-64871 and 64872, September 1974.

2-13. Holland, R. L., Rhodes, C. A., and Euler, H. C., Jr.: Lagrangian Least-Squares Prediction of Solar Activity. MSFC TM X-82462, April 1982.

2-14. Space and Planetary Environment Criteria Guidelines for Use in Space Vehicle Development, 1977 Revision. NASA TM-78119.

2-15. Model of Earth's Atmosphere (90 to 2500 km). NASA SP-8021, March 1973.

2-16. Weidner, D. K. and Swenson, G. R.: Diurnal Variations in the Thermosphere from a Series of Marshall-University of Michigan Probes. J. Geophys. Res., vol. 74, 1969, pp. 4755-4763.

2-17. Roble, R. G.: The Thermosphere. In The Upper Atmosphere and Magnetosphere, National Academy of Science, Washington, D.C., 1977.

2-18. Geisler, J. E.: Atmospheric Wind in the Middle Latitude F-Region. J. Atmos. Terr. Phys., vol. 28, 1966, pp. 703-720.

2-19. Kohl, H. and King, J. W.: Atmospheric Winds Between 100 and 700 km and Their Effects on the Ionosphere. J. Atmos. Terr. Phys., vol. 29, 1967, pp. 1045-1062.

2-20. Jacchia, L. G.: The Temperature Above the Thermopause. Space Res., vol. 5, 1965, pp. 1152-1174.

2-21. Geisler, J. E.: A Numerical Study of the Wind System in the Middle Thermosphere. J. Atmos. Terr. Phys., vol. 29, 1967, pp. 1469-1482.

2-22. Jacchia, L. G. and Slowey, J.: The Shape and Location of the Diurnal Bulge in the Upper Atmosphere. Space Res., vol. 7, 1967, pp. 1077-1090.

2-23. Dickinson, R. F., Geisler, J. E., and Roble, R. G.: Meridional Circulation in the Thermosphere. I, Equinox Conditions. J. Atmos. Sci., vol. 32, 1975, pp. 1737-1754.

2-24. King-Hele, D. G.: Measurement of Upper-Atmospheric Rotational Speed from Changes in Satellite Orbits. Space Res. XII, COSPAR, 1971, pp. 847-855.

2-25. King-Hele, D. G. and Walker, D. M. C.: Upper-Atmosphere Zonal Winds: Variation with Height and Local Time. Planet. Space Sci., vol. 25, 1977, pp. 313-336.

2-26. Challinor, R. A.: The Apparent Rotation of the Upper Atmosphere. Planet Space Sci., vol. 16, 1968, pp. 557-566.

2-27. Earth Albedo and Emitted Radiation. NASA SP 8067, July 1971.

2-28. Raschke, E. and Bandeen, W. R.: The Radiation Balance of the Planet Earth from Radiation Measurements of the Satellite Nimbus II. J. Appl. Meteor., vol. 9, April 1970, pp. 215-238.

2-29. Gault, D. E.: Saturation and Equilibrium Conditions for Impact Cratering on the Lunar Surface: Criteria and Implications. Radio Sci., vol. 5, 1970, pp. 273-291.

2-30. McDonnell, J. A. M. (ed.): Cosmic Dust. John Wiley and Sons, New York, 1976. Chapter 3, "Meteors" by D. W. Hughes. Chapter 6, "Microparticle Studies by Space Instrumentation" by J. A. M. McDonnell.

2-31. Field, G. B. and Cameron, A. G. W. (eds.): The Dusty Universe: Proc. of a Symposium Honoring Fred Lawrence Whipple on his Retirement as Director of the Smithsonian Astrophysical Observatory, October 17-19, 1973. Neale Watson Academic Publ., Inc., New York, 1975, "Dust in the Solar System" by P. Millman.

2-32. Peddie, N. W.: International Geomagnetic Reference Field 1980. A report by IAGA Division I Working Group 1, Geophys. J. R. Astr. Soc., vol. 68, 1982, pp. 265-268.

2-33. IAGA Division 1, Study Group: International Geomagnetic Reference Field 1975, J. Geophys. Res., vol. 81, 1977, pp. 5163-5164.

2-34. Magnetic Fields Earth and Extraterrestrial. NASA SP-8017, March 1969.

2-35. Zmuda, A. J. (ed.): World Magnetic Survey 1957-1969. Bulletin 28, Int. Assn. Geomagn. and Aeron., 1971.

2-36. Stassinopoulos, E. G. and Mead, G D.: ALLMAG, GDALMG, LINTRA: Computer Programs for Geomagnetic Field and Field-Line Calculations. National Space Science Data Center, February 1972.

2-37. Olson, W. P. and Pfitzer, K. Q.: A Quantitative Model of the Magnetospheric Magnetic Field. J. Geophys. Res., vol. 79, 1974, p. 3739.

2-38. Egeland, A., Holter, O., and Omholt, A. (eds.): Cosmical Geophys. Universitetsforlaget, Oslo, 1973.

2-39. The Earth's Ionosphere. NASA SP-8049, March 1971.

2-40. Johnson, F. S. (ed.): Satellite Environment Handbook. 2nd ed., Stanford Univ. Press, 1965.

2-41. Chan, K. W. and Colin, L.: Global Electron Density Distribution from Topside Soundings. Proceedings of IEEE, vol. 57, No. 6, June 1969, pp. 990-1004.

2-42. Chappell, C. R., Harris, R. R., and Sharp, C. W.: The Morphology of the Bulge of the Plasmasphere. J. Geophys. Res., vol. 75, 1970, pp. 3848-3861.

2-43. Chan, K. W., Sawyer, D. M., and Vette, J. I.: Model of the Near-Earth Plasma Environment and Application to the ISEE-A and B Orbit. Rep. NSDC/WDC-A-R and S, 77-01, GSFC, 1977.

2-44. Garrett, H. B.: Review of Quantitative Models of the 0-100 KeV Near-Earth Plasma. Rev. Geophys. and Space Phys., vol. 17, 1979, pp. 397-417.

2-45. Burrell, M. O. and Wright, J. J.: Orbital Calculation and Trapped Radiation Mapping. NASA TM X-53406, March 8, 1966.

2-46. Charged Particle Radiation Environment for the Spacelab and Other Missions in Low Earth Orbit, Rev. A. NASA TMX-73358, 1977.

2-47. Sawyer, D. J. and Vette, J. I.: AP8 Trapped Proton Environment for Solar Maximum and Solar Minimum. INDC-A-RDS-76-06, National Space Science Data Center, December 1976.

2-48. Singley, G. W. and Vette, J. I.: The AE4 Model of the Outer Radiation Zone Electron Environment. NSSDC 72-06, NASA-GSFC, August 1972.

2-49. Teague, M. J., Chou, K. W., and Vette, J. I.: AE6: A Model Environment of Trapped Electrons for Solar Maximum. National Space Science Data Center 76-04, May 1976.

2-50. Teague, M. J. and Vette, J. I.: A Model of the Trapped Electron Population for Solar Minimum. NSSDC 74-03, NASA-GSFC, April 1974.

2-51. Chan, K. W., Teague, N. J., Schofield, N. J., and Vette, J. I.: Modeling of Electron Time Variations in the Radiation Belts. (In Reference 2-5.)

2-52. Stassinopoulos, E. G.: Radiation Hazards to Synchronous Satellites. NASA Report X-601-73-330, Goddard Space Flight Center, September 1973.

2-53. Pulliam, D. M., Anderson, H. R., Stammes, K., and Rees, M. H.: Auroral Electron Acceleration and Atmospheric Interactions, J. Geophys. Res., vol. 86, 1981, pp. 2397-2404.

2-54. Robinson, R. M.: Simultaneous Ground and Rocket-Based Measurements of Electric Fields and Currents in an Auroral Arc. Ph.D. Thesis, Rice University, Houston, Texas, 1980.

2-55. Störmer, C.: The Polar Aurora. Oxford Univ. Press, 1955.

2-56. Adams, J. A. S., Lowder, W., and Gessell, T. F. (eds.): The Natural Radiation Environment, II. USERDA Conf. 720805-P2, August 1972, Chapter 1 by H. R. Anderson.

2-57. Webber, W. R.: Time Variation of Low Rigidity Cosmic Rays During the Recent Sunspot Cycle. Prog. in Cosmic Ray Phys., vol. VI, N. Holland Publ. Co., Amsterdam, 1962.

2-58. Burrell, M. O.: The Calculation of Proton Penetration and Dose Rates. NASA TMX-53063, August 19, 1964.

2-59. Watts, J. W., Jr., and Burrell, M. O.: Electron and Bremstrahlung Penetration and Dose Calculation. NASA TN D-6385, June 1971.

2-60. Garrett, H. B. and Pike, C. P. (eds.): Space Systems and Their Interactions with Earth's Space Environment. Progress in Astronautics and Aeronautics, vol. 71, AIAA, New York, 1980.

2-61. Garrett, H. B.: The Charging of Spacecraft Surfaces. Rev. Geophys. Space Phys., vol. 19, 1981, pp. 577-616.

SECTION 3. THE MOON

3.1 INTRODUCTION

We on Earth often see ourselves as isolated and independent of our neighbors in the solar system. But our life is dominated, even made possible, by the Sun, and it is regulated by the periodicity of the Moon. The months of our year are measured by the regular motions of the Moon about the Earth; our tides rise and fall primarily as a result of a gravitational tug-of-war between the Moon and the Earth. The influence of the Moon on our cultural development is woven throughout our mythologies, art, and literature. Indeed, the Moon is our planetary companion.

Scientific interest in the Moon dates from the earliest recorded history (Reference 3-1 gives a review of early lunar studies), but it was not until the advent of the "space age" that we could examine the Moon firsthand. Nearly half of the Moon's surface had never been seen. In 1959, Luna 3, launched by the U.S.S.R., obtained the first photographs of the "far side." Our understanding of the Moon has changed radically during the last 20 years as a multitude of spacecraft have passed, orbited, impacted, and landed. Although the ultimate origin of the Moon is still elusive, we are familiar with the major processes and events which shaped its evolution over the past 4 billion years [3-2,3-3]. Because it has experienced little geologic activity for about 3 billion years, we may gain insight into the very early history of the Earth and other planets and the processes which shaped them by studying the ancient lunar surface.

This chapter is not intended to review exhaustively the history and development of the Moon but, rather, to summarize its major physical properties, to give engineering information for vehicle planning purposes, and to provide an entrance into the vast literature concerning the Moon. Taylor's 1975 review [3-4] is worthy of particular attention. Other recent reviews include References 3-1, 3-5, 3-6, and 3-7. Results of lunar studies are published annually in the Proceedings of the Lunar and Planetary Science Conference.

3.2 DYNAMIC PROPERTIES

The lunar dynamic properties are listed in Table 3-1.

TABLE 3-1. DYNAMIC PROPERTIES

Parameter	Value
Period: sidereal	27.322 days
synodic (new Moon to new Moon)	29.531 days
Eccentricity (geocentric orbit)	0.0549
Semi-major axis (mean Moon-Earth distance between body centers)	384,402 km
perigee distance	363,300 km
apogee distance	405,500 km
Mean orbital velocity	1.03 km sec^{-1}
Inclination of lunar orbit to ecliptic	5°7'
Inclination of lunar equator to ecliptic	1°32'

3.2.1 Comments

The values in Table 3-1 were taken from References 3-6, 3-8, and 3-9. A lunar ephemeris is published regularly in the American Ephemeris and Nautical Almanac [3-10]. The Earth and Moon make one revolution about their common center of mass in 27 days 7 hr 43 min 11.5 sec (the sidereal period). Tidal friction caused in part by the Earth's oceans is gradually slowing this revolution and causing the Moon to slowly spiral outward. The Moon is in synchronous rotation, keeping one face continually towards the Earth. Actually, nearly 60 percent of the lunar surface can be seen from the Earth because of the changing geometry between an observer and the Moon as it follows a slightly elliptic orbit inclined to the Earth's equator. In addition, there is a small physical libration of dynamical origin, a deviation from uniform rotation which is of the order of several minutes of arc [3-11]. Reviews of the orbital/tidal evolution of the Moon are contained in References 3-12 through 3-16. Recent laser ranging has permitted very refined orbital determination [3-17].

The large size of the Moon relative to its primary is unusual in our solar system and endows the Earth-Moon with the dynamic properties of a double-planet system. In addition, the Sun strongly perturbs the Moon's orbit. The solar perturbation results in significant departures from simple Keplerian motion. (Brown's classic text [3-18] gives a discussion of lunar orbit theory and Deprit [3-19] gives a recent review.)

3.3 PHYSICAL DATA

3.3.1 Mass, Figure, and Other Physical Properties

Table 3-2 summarizes the Moon's physical data.

TABLE 3-2. PHYSICAL DATA

Parameter	Value	Normalized (Earth = 1) or Comment
Mean radius (R)	1738 km (nominal)	0.272
Principal axes a	1738.6 km	
b	1738.2 km	
c	1738.5 km	
Mass (M)	7.353×10^{22} kg	0.0123
Mean density	3.342 g cm^{-3}	0.605
Surface area	37.9×10^{6} km^{2}	0.074
Volume	2.20×10^{10} km^{3}	0.02
Surface gravity	162.3 cm sec^{-2}	0.165
Escape velocity	2.37 km sec^{-1}	0.212
Gravitational parameter (GM)	4902 km^{3} sec^{-2}	0.0123
Moment of inertia factor (I/MR^2)	0.391 ± 0.002	(homogeneous = 0.4)
Bond Albedo	0.067	estimated [3-20]
Visual magnitude	-12.71 ± 0.06	full moon
Surface temperature	102°K - 384°K	[3-21]
Atmospheric density	2×10^{5} molecules/cm^{3}	surface, night [3-22]
Bulk conductivity	$< 10^{-5}$ ohm/m	

Striking among the Moon's bulk properties is its mean density (3.34 g/cm^3), which is lower than all of the inner rocky planets but greater than most other natural satellites. Phobos and Deimos, the moons of Mars, have densities less than 2 g/cm^3; the moons of Jupiter, except for Io, have densities less than about 3 g/cm^3. The density of the Moon implies that it is composed predominantly of silicate minerals, and an iron-rich core, if there is one, must be very small. This deduction is consistent with the coefficient of the moment of inertia for the Moon (approximately 0.395 [3-15]), which implies that the mass distribution within the Moon is nearly homogeneous. (For a homogeneous body the coefficient would have the value 0.4.)

3.3.1.1 Lunar Mapping Coordinate System

Map coordinates on the Moon are referred to the directions of the principal axes of inertia. Latitude is measured from the equator positive north (towards Mare Imbrium); longitude is measured positive eastward (towards Mare Crisium) (Fig. 3-1). A small crater, Mösting A, has traditionally been used as a reference point on the lunar surface, since there is no distinctive surface feature exactly at the point of intersection of the equator and the prime meridian. The coordinates of the center of Mösting A are [3-6]:

Longitude	-5° 9'50" ± 5"
Latitude	-3° 10'47" ± 4"

3.3.2 Gravity Field

The gravity field of the Moon has been extensively studied by lunar orbiters. The expansion for the gravitational potential in spherical harmonics is:

$$U = \frac{GM}{r}\left[1 + \sum_{n=2}^{\infty}\sum_{m=0}^{n}\left(\frac{R}{r}\right)^{n} P_n^m(\sin\phi)(C_{nm}\cos m\lambda + S_{nm}\sin m\lambda)\right]$$

where ϕ, λ, and r are Moon-centered spherical coordinates, latitude, longitude, and radial distance. The m=0 terms, zonal harmonics, are written J_n ($J_n = -C_{n0}$, by convention). The user of expansions of this type must be careful to note that both normalized and unnormalized functions appear in the literature. The coefficients differ by a normalizing factor. Table 3-3, adapted from Liu and Laing [3-24], gives unnormalized coefficients to order and degree (3,3). (For values to J(15), C(8,8), and S(8,8) review Reference 3-14. The table presented here is truncated.) Accuracy, estimated to be approximately 10 percent for J_2, declines markedly for coefficients of high order and degree.

For all but the most specialized purposes, only the J_2 and C_{22} terms need be included, giving the simplified expression:

$$U \simeq \frac{GM}{r}\left\{1 + \left(\frac{R}{r}\right)^{2}\left[\frac{J_2}{2}(1 - 3\sin^2\phi) + 3\,C_{22}\cos^2\phi\cos 2\lambda\right]\right\}$$

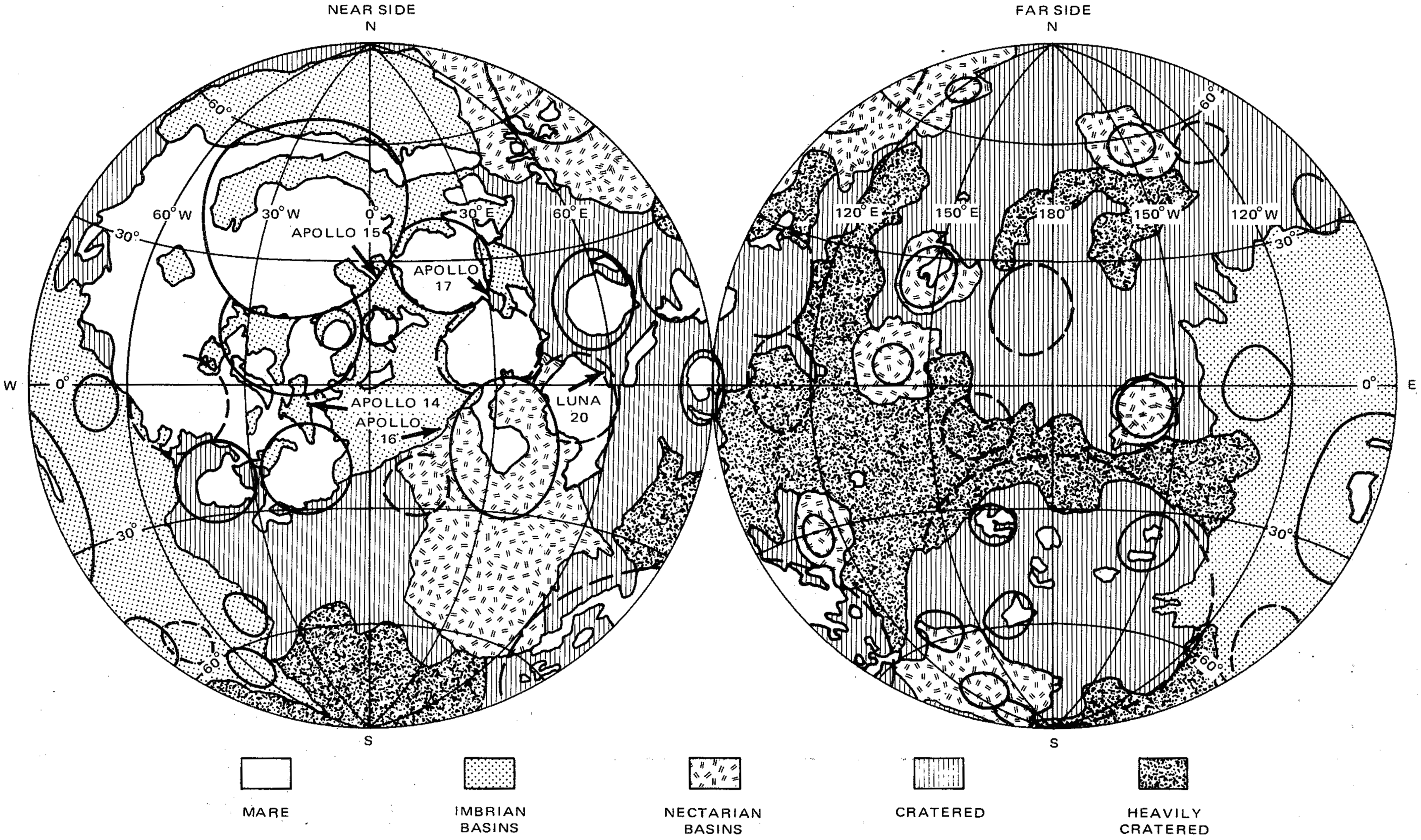

Figure 3-1. Simplified geologic map of the Moon showing the Apollo and Luna landing sites. The highland basins are divided into two groups based on their apparent ages - Imbrian (younger) and Nectarian (older). Mare basalts are shown in black, and a possible high-velocity zone at 50-km depth is indicated by stippling [3-23].

TABLE 3-3. SPHERICAL HARMONIC COEFFICIENTS OF LUNAR GRAVITY FIELD (TRUNCATED) [3-24]

Harmonic	Unnormalized Coefficient ±	Uncertainty
J(2)	0.1996×10^{-3}	0.20×10^{-5}
C(2,1)	0.8171×10^{-5}	0.24×10^{-5}
S(2,1)	-0.7213×10^{-5}	0.71×10^{-5}
C(2,2)	0.2359×10^{-4}	0.53×10^{-5}
S(2,2)	0.4538×10^{-5}	0.60×10^{-5}
J(3)	0.5878×10^{-5}	0.29×10^{-5}
C(3,1)	0.3001×10^{-4}	0.27×10^{-5}
S(3,1)	0.1421×10^{-5}	0.32×10^{-5}
C(3,2)	0.4698×10^{-5}	0.28×10^{-5}
S(3,2)	0.5748×10^{-6}	0.17×10^{-5}
C(3,3)	0.4847×10^{-5}	0.22×10^{-5}
S(3,3)	-0.2919×10^{-5}	0.13×10^{-5}
J(4)	-0.1195×10^{-4}	0.17×10^{-5}
J(5)	0.4544×10^{-5}	0.26×10^{-5}

Local variations in gravity have been detected that in many cases correlate with surface features [3-25]. Areas with anomalously high-gravitational acceleration have been called "mascons," short for mass concentrations, on the assumption that the variations result from high-density materials near the surface. Mascons generally occur at large impact basins filled with younger basaltic lavas. The high values of gravitational acceleration are ascribed to a superisostatic basalt fill and/or relief on the crust-mantle boundary [3-26]. Geophysical models of the Moon incorporating gravitational, as well as topographic, seismic, and librational data have been used by Bills and Ferrari [3-27] to estimate that the crustal thickness varies from 30 to 110 km.

3.3.3 Magnetic Field

The Moon does not at present possess an overall dipole magnetic field. However, surface magnetic fields of varying direction and amplitude have been detected and mapped. Strength of surface fields is in the range: 6 to 313 gammas

(1 gamma = 10^{-5} gauss = 10^{-9} tesla). Strongest fields are associated with the ancient highland areas (paragraph 3.5.1.2).

Since the Moon today has no dipolar magnetic field, the discovery of natural remnant magnetism (NRM) in samples returned from the Moon was unexpected. NRM is commonly acquired by rocks as they cool from high temperatures through a critical Curie temperature in the presence of an external magnetic field. Metallic iron, responsible for most of the lunar NRM, has a Curie temperature of about 750°C.

Lunar magnetism and its origin are discussed in References 3-28 through 3-33. If the primordial field was produced by a dynamo within a fluid metallic core, it apparently switched off as the Moon cooled and convection in the core slowed. Estimates of the strength of the primordial magnetic field necessary to create the observed NRM values vary widely – from 600 to 160,000 gammas. Other suggestions to explain the observed fossil magnetism include (1) close approach to the Earth and its magnetic field, (2) enhanced solar or solar wind magnetic fields, (3) permanent magnetization acquired during the period of accretion from a strong magnetic field in the solar nebula, and (4) short-lived magnetic fields during meteorite or comet impact.

3.4 INTERIOR

3.4.1 Structure

Studies of lunar rocks and experiments conducted by the Apollo science teams have given us a general idea of the structure of the lunar interior. The major units are (1) the crust (outer 30 to 110 km), (2) the mantle (extending to about 1000-km depth, and possibly (3) a central core (600 to 800 km in radius) (Fig. 3-2).

Many of the major geologic processes that modify the surface of a planet are driven by forces arising within the body. Volcanic activity, tectonic movements (folding and faulting), and a dipole magnetic field are examples of internally driven processes. Therefore, understanding the interior structure of the Moon would reveal much about its present and past geologic state.

A wide variety of observations and measurements demonstrate that the interior of the Moon possesses a layered internal structure. The average density of rocks at the surface is approximately 3.1 to 3.3 g/cm^3, while the bulk density of the Moon is 3.34 g/cm^3. Although the difference is slight, it does require some density increase with depth, which is consistent with the value noted for the moment of inertia coefficient [3-15]. (On Earth the density contrast is much larger; surface rocks have a density of near 2.7 g/cm^3, while the bulk density of the planet is 5.5 g/cm^3.)

3.4.2 The Core

The nature, or even the presence, of a distinct central core is still uncertain. However, a zone of 600 to 800 km in radius does not transmit seismic S-waves (shear waves), and it is known that S-waves cannot be transmitted through liquids [3-34]. So perhaps a zone of partial melt exists at this radius – the lunar equivalent of an asthenosphere. Temperatures, calculated from electrical conductivity measurements, indicate that 1600°C may be approached at this depth [3-35]. The moment of inertia data permit an Fe-FeS core of 700-km radius or an iron core of 400-km radius [3-15].

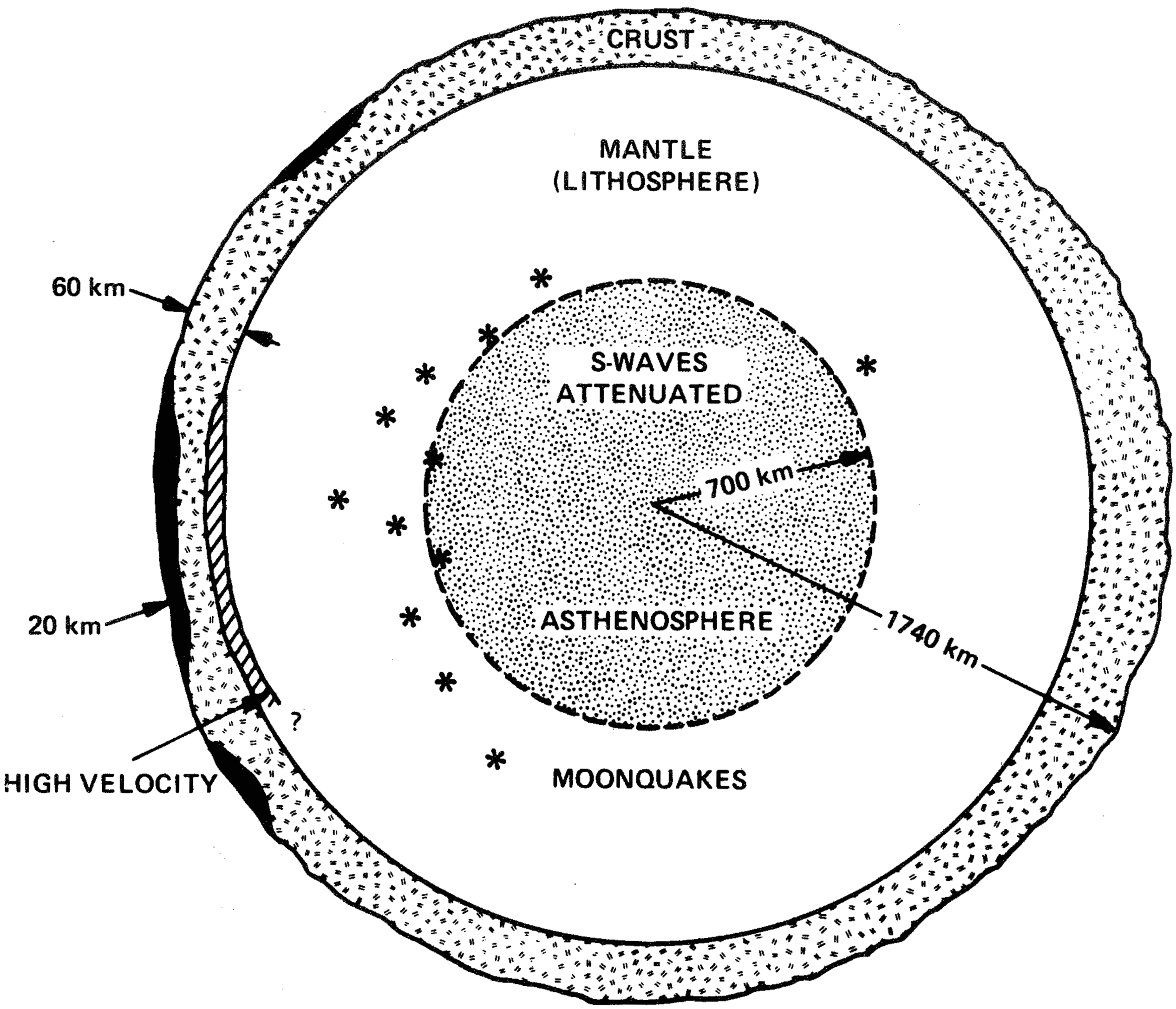

Figure 3-2. Major units of the lunar interior.

If the Moon has no core, the asthenosphere is probably primitive, undifferentiated material that is heated by radioactive decay of K, U, and Th.

3.4.3 The Mantle

A sharp increase in the velocity of seismic waves marks the crust-mantle boundary at a depth of approximately 60 km. Seismic velocities in the lunar mantle (approximately 8 km/sec) exceed terrestrial values and indicate a composition rich in olivine and pyroxene (Mg and Fe silicates) with a density of approximately 3.4 g/cm^3. Petrologic studies of the lunar basalts also indicate that they were generated from such rocks at mantle depth [3-4]. The lunar crust and mantle comprise a mechanically rigid outer shell, often called the lithosphere. The Moon's lithosphere is much thicker than Earth's (approximately 1000 km versus 100 km). At the base of the lithosphere a prominent zone of moonquake activity has been detected, though the periodicity of the quakes indicates that they are triggered by Earth-tides and are not the result of thermal convection as on the Earth [3-36]. Stress accumulation above a partially molten zone associated with the core may be responsible.

3.4.4 The Crust

The lunar seismic network established during the Apollo program provided detailed information about the crustal structure of the Moon in the Oceanus Procellarum region. Interpretations of seismic velocity profiles of the lunar crust indicate that it possesses a layered structure as well [3-35]. A relatively sharp discontinuity exists at a depth of approximately 25 km. The nature of the discontinuity is debated, but it appears to separate fragmented rock from underlying solid rock. Seismic velocities in the outer portions of the crust are low (2 to 4 km/sec) and gradually increase with depth. A layer of fine-grained breccia and broken rock fragments 1- to 2-km thick (the megaregolith) may be responsible for this part of the profile. The shattered rocks are probably bedrock smashed by repeated meteorite impact. The seismic velocities continue to increase to approximately 6 km/sec at 25 km. These are similar to velocities measured for lunar basalts; therefore, this may be the depth of basaltic lavas in Oceanus Procellarum [3-35]. Alternatively, and probably more consistent with the surface geology, the seismic profile could be the result of a thin (approximately 1 km) layer of basalt overlain by ejecta associated with large impact basins [3-37]. In either case, the increase in seismic velocity with depth can reasonably be attributed to the decreasing abundance of shock-induced microfractures [3-38]. From 25 to 60 km (the base of the crust in this region) seismic velocities are relatively uniform at approximately 7 km/sec and are similar to velocities determined for anorthosites (a calcium aluminum silicate feldspar) and gabbros (a ferro-magnesian mineral) like those exposed in the lunar highlands [3-35]. The uniformity of the seismic signals relative to the upper section of fractured crust suggests that shock-induced cracks were never formed below 25 km. Alternatively, cracks may have been annealed by a thermal event after their formation.

3.5 SURFACE OF THE MOON

The surface of the Moon has two major regions with distinctive geologic features and evolutionary histories (1) the relatively smooth, dark areas which Galileo first called "maria" and (2) the densely cratered rugged highlands (uplands), originally called "terrae." The highlands occupy about 83 percent of the Moon's surface and generally have a higher elevation, as much as 5 km above the mean radius. In places the maria lie about 5 km below the mean radius and are concentrated on the near side of the Moon (Fig. 3-1), a fact that still lacks an adequate explanation. Comprehensive reviews of the geology of the Moon's surface can be found in References 3-1 and 3-5. Much of the information regarding the lunar surface is the result of six manned landings on the Moon. Summaries of the geology of each of the Apollo landing sites are contained in a series of NASA Special Publications (Apollo 11, SP-214; Apollo 12, SP-235; Apollo 14, SP-272; Apollo 15, SP-289; Apollo 16, SP-315; and Apollo 17, SP-330). The Apollo missions were preceded by a series of unmanned Surveyor missions (NASA SP-184, 1969). Those missions, and the preceding Ranger program, returned considerable scientific information about the nature of the Moon's surface that is now often ignored because of the volume and quality of the information obtained by the Apollo missions.

3.5.1 Surface Morphology

3.5.1.1 Impact Craters

The main external geologic process modifying the surface of the Moon is meteorite impact. Craters range in size from minute pits only microns in diameter to gigantic basins hundreds of kilometers across which are the major land form on the Moon. Figures 3-3a through 3-3c show some of the variation in lunar craters.

An often used classification for craters distinguishes simple craters from complex craters and basins. Simple impact craters are the smallest, most abundant type and range from a few micrometers to approximately 15 km in diameter (Fig. 3-3a). They are generally bowl-shaped depressions. Fresh simple craters have bright rays and rubbly ejecta blankets composed of the material excavated by the impact and locally "churned" material. Simple craters may reach depths of 2 to 3 km. Complex craters, which are larger than 10 to 20 km in diameter, are relatively shallower (i.e., lower depth-to-diameter ratio) than small craters. Most complex craters have scalloped or terraced walls, central peaks, and broad, flat floors (Fig. 3-3b). The transition from simple to complex craters depends on several factors, including the impact energy and the strength of the material in which the crater was formed.

Larger complex craters have distinctive central peaks, and the still larger basins display multi-ring features such as those around an Orientale basin (Fig. 3-3c). Although these large basins are not as numerous as the smaller craters, their formation dramatically altered the appearance of the Moon, creating huge depressions where, in some cases, lavas accumulated later.

3.5.1.2 The Highlands

The lunar terrae, or highlands, are the high albedo or bright regions of the Moon. They are primarily old surfaces that became extensively cratered during early lunar history when the flux of meteorites was high; they may record the final stages of accretion.

The most abundant rocks in the highlands are anorthositic gabbros, composed principally of plagioclase, olivine, and pyroxene. Almost all the samples have been extensively brecciated, metamorphosed, and chemically contaminated by repeated meteorite impact, so that few, if any, pristine samples of the primordial crust appear in the lunar sample collection. Nevertheless, detailed studies of these ancient rocks have demonstrated the importance of magmatic differentiation in their formation. Apparently the Moon heated tremendously during accretion as the kinetic energy of impacting bodies was converted to heat. Additional heat may have been generated by radioactive decay within the Moon. Large parts of the Moon melted; perhaps even the outer several hundred kilometers became molten. As this "magma ocean" cooled, minerals crystallized and separated according to their densities. Dense minerals, rich in Fe and Mg, sank, adding to the bulk of the mantle; less dense minerals, like plagioclase, floated to the surface, forming anorthositic cumulates now exposed in the battered highlands [3-39,3-40]. The earliest known volcanic rocks – varieties of basalt – were erupted shortly after the crust formed.

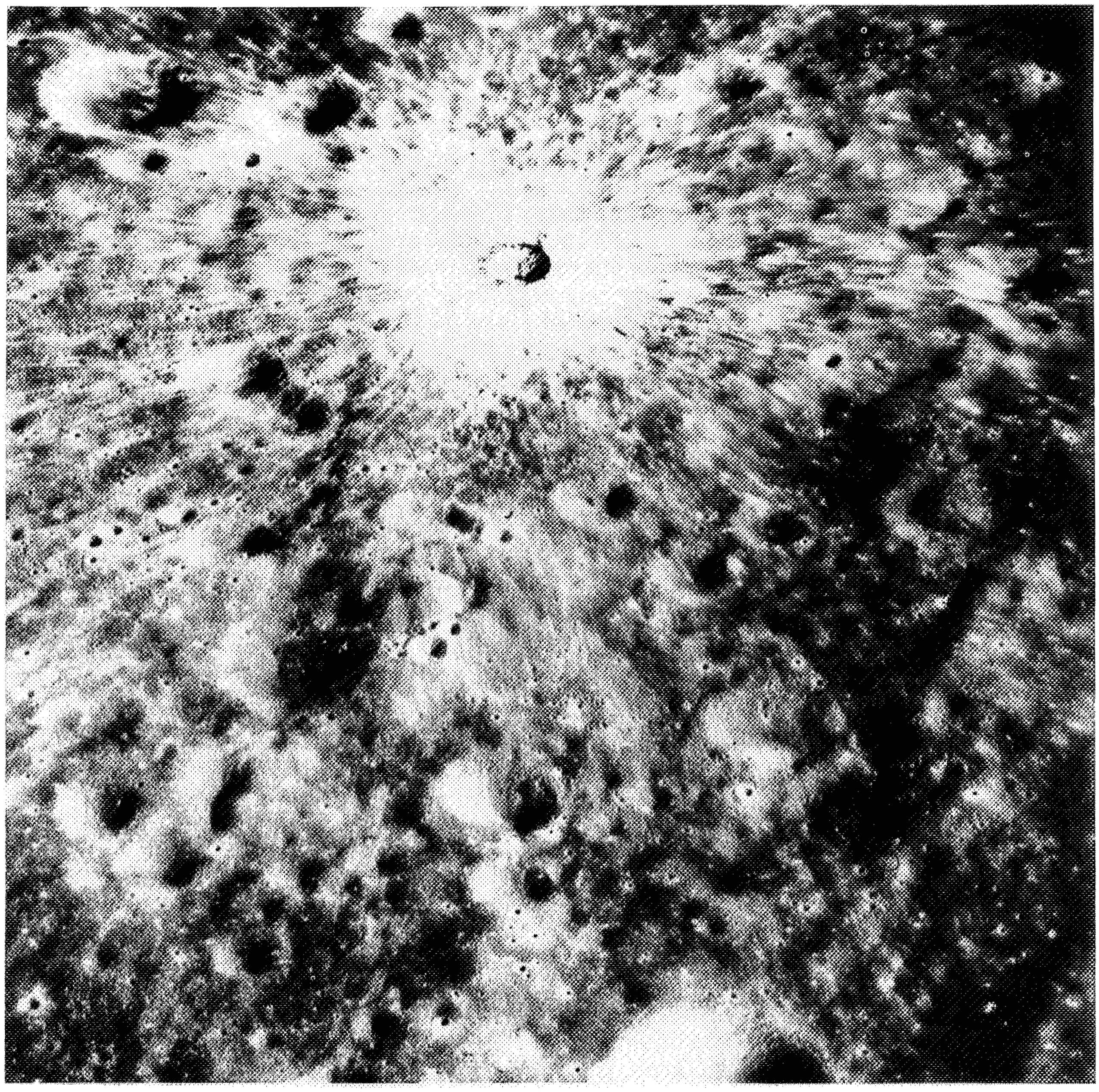

Figure 3-3a. Simple crater. Notice its bright ejecta deposit and rocky rim (AS 17-2301).

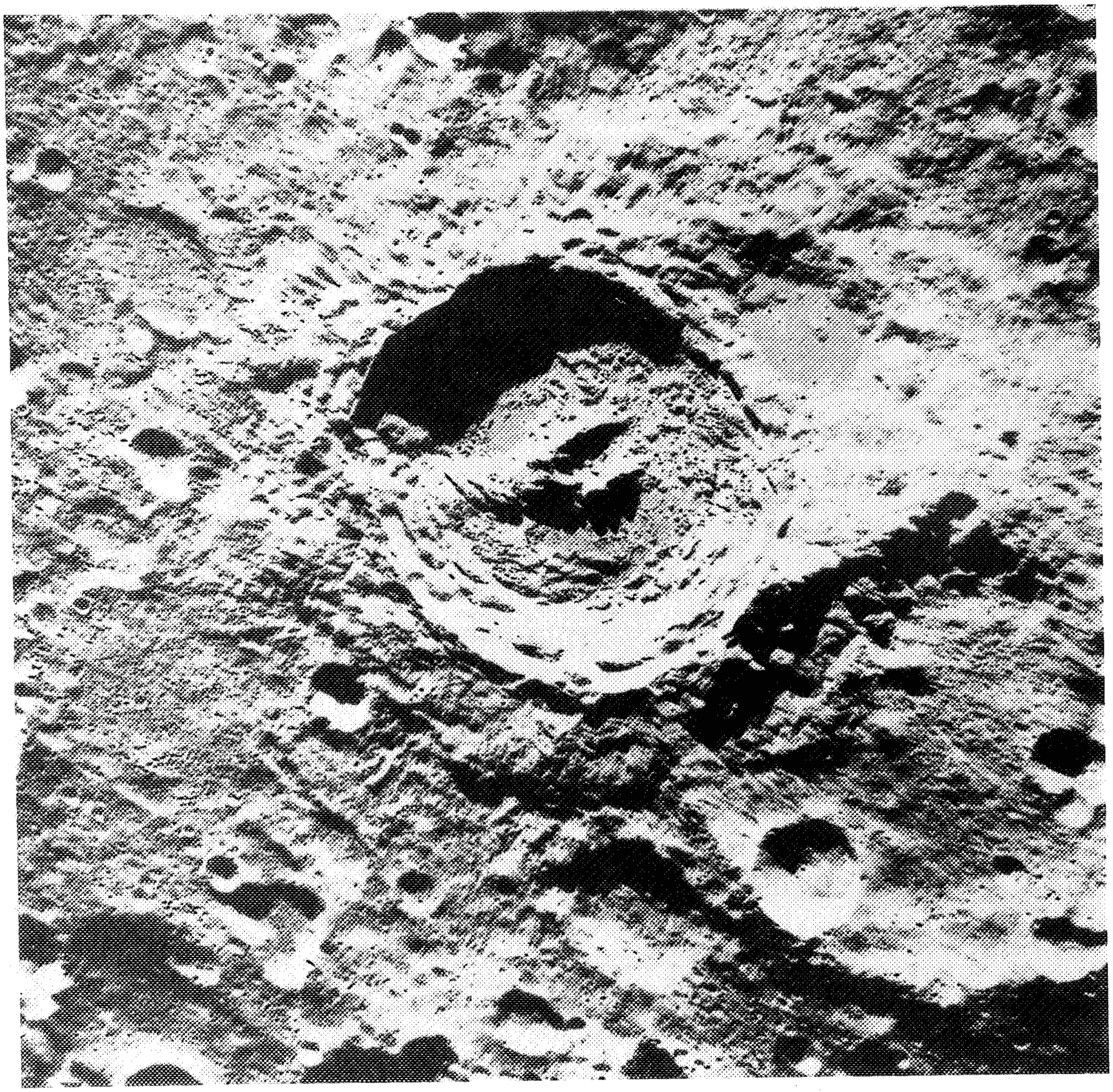

Figure 3-3b. Complex crater with terraced walls and central peak (AS 16-19580).

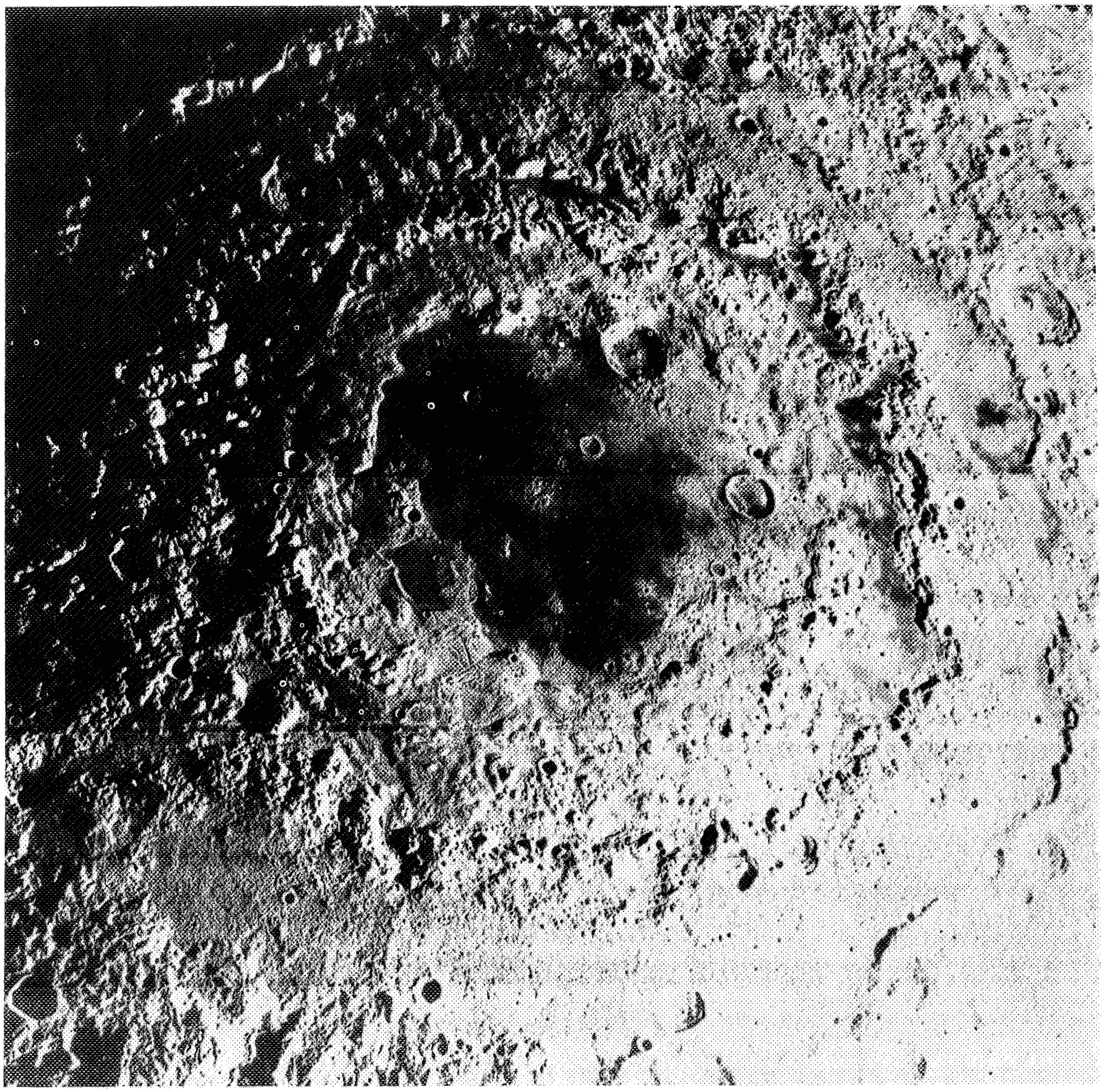

Figure 3-3c. Orientale basin, the youngest multi-ringed basin on the Moon. It is only partially filled by mare lavas (LO-IV-194M).

3.5.1.3 The Maria

The lunar maria are concentrated in topographic basins on the near side of the Moon. The average normal albedo of the maria is a rather low 7 percent. Some maria occur within large circular impact basins such as Crisium, Serenitatis, and Imbrium, whereas others, like Oceanus Procellarum, occupy irregular depressions. The lunar maria are vast plains composed of basaltic lava flows that were erupted after the highlands and the impact basins formed [3-41]. The basalt in the middle of the basins may be several kilometers thick but is still only a small part of the crust that is approximately 60-km thick.

Lunar basalts are chemically and mineralogically similar to their terrestrial counterparts (paragraph 3.5.4), differing only in their high abundance of Ca-plagioclase and titanium and the total absence of hydrous minerals. Experimental studies of lunar basalts demonstrate that they resulted from partial melting of rocks from 150- to 450-km deep within the lunar mantle [3-35]. These magmas rose through the fractured crust and were modified only slightly before they were extruded onto the surface.

Lunar lava appears to have flowed from a variety of vents and fissures, but there are no large composite cones and shield volcanoes like those on Earth and Mars. Small domes several kilometers across may have been the sources for some flows [3-42]. In addition voluminous flows issued from large, irregular depressions associated with meandering lava channels known as sinuous rilles [3-43,3-44]. Hadley Rille, visited during the Apollo 15 mission, a typical rille, is 135-km long and approximately 1-km wide. Many large lava flows have no apparent vents and may have issued from long fissures like the terrestrial ones that fed the Columbia Plateau basalts in Washington State [3-42].

Other features characteristic of the maria are narrow ridges, several kilometers wide, with sinuous outlines that extend discontinuously for great distances and, in some cases, transect highland surfaces as well [3-45] (Fig. 3-4). "Wrinkle" ridges, as they are sometimes called, are believed to be formed by compression as mare basins subsided, adjusting to the load of accumulating basaltic lavas. Others have suggested that the mare ridges reflect a change in the style of tectonic deformation as the Moon began to cool and contract after an early period of slight planetary expansion [3-46]. Linear rilles, narrow, fault-bounded valleys, criss-cross some of the maria as well. These rilles appear to be more than 3.5 billion years old and may be the result of local adjustments to the weight of lava or may have been due to slight planetary expansion in an initially warm Moon [3-47].

3.5.1.4 The Regolith

The surface of the Moon is strongly brecciated or fragmented. This mantle of weakly coherent debris, called the regolith, consists of shocked fragments of rocks, minerals, and glass spherules formed by meteorite impact. The thickness of the regolith is highly variable and depends on the age of the underlying bedrock and the location with respect to nearby craters and their ejecta blankets. In general, the maria are covered by 3 to 16 m of regolith, whereas the older highlands have developed a "soil" at least 10-m thick [3-48]. The thickness of the regolith at the Apollo 17 landing site (near a highlands-mare boundary) ranged from 6 to 37 m [3-35].

Figure 3-4. Wrinkle ridges and lunar rilles are prominent features in this photograph of the margin of Mare Serenitatis. The linear rilles are on an older surface that was partially buried before the ridges formed (AS-17-601).

3.5.2 Detailed Lunar Surface Mapping

For specific areas on the Moon, extremely detailed contour maps have been constructed using data obtained from panoramic camera stereophotography. An example is shown in Figure 3-5 [3-49]. Detailed maps may be obtained from the Defense Mapping Agency, Aerospace Center, St. Louis, Missouri [3-50].

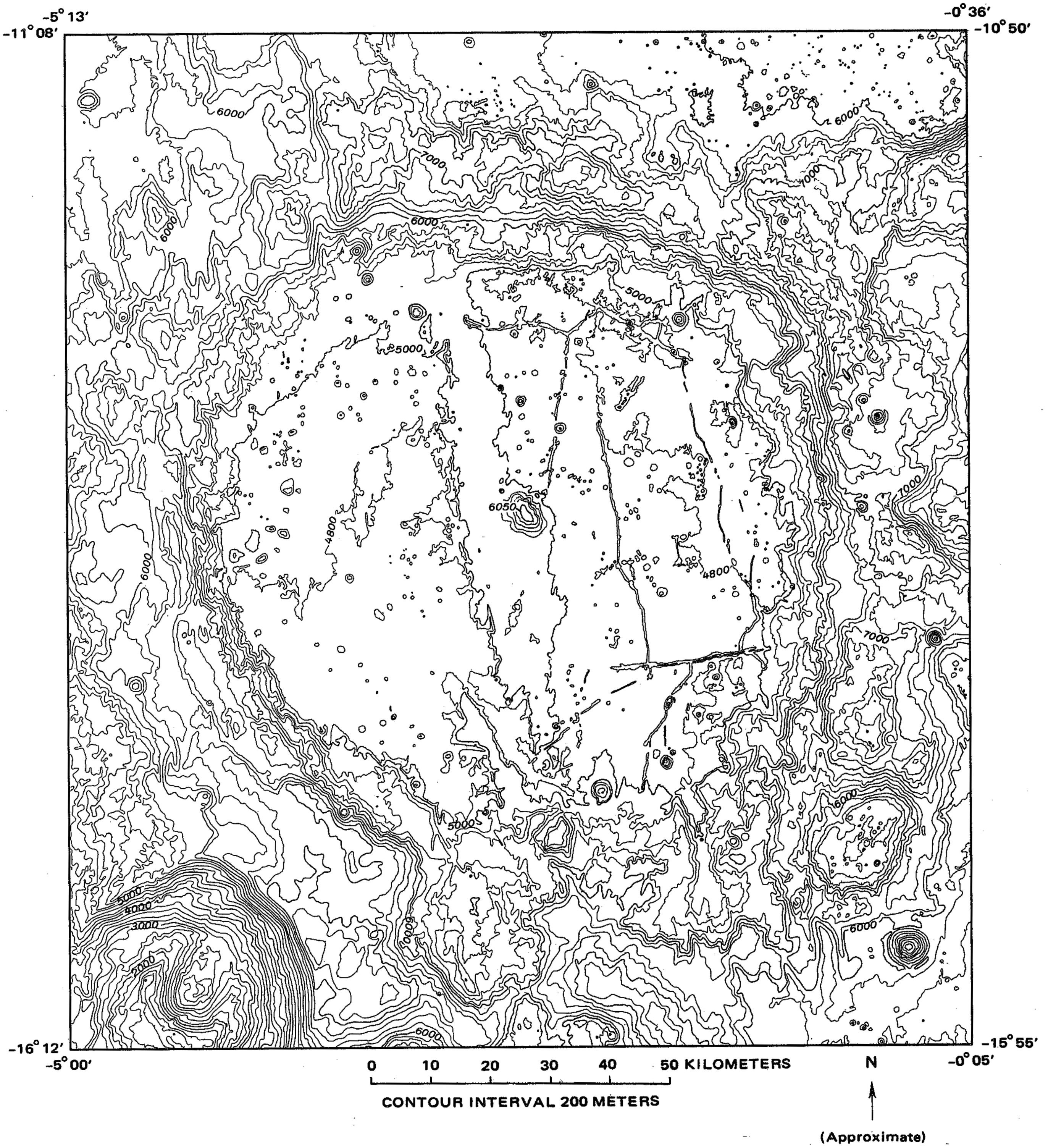

Figure 3-5. Contour map of Alphonsus compiled from oblique Apollo 16 mapping camera photographs [4-49].

3.5.3 Statistics of Lunar Surface Features

For the design of lunar roving vehicles, as well as estimates of ages of observed features and studies of morphological changes, it is important to have statistics of terrain features such as size distributions of craters and slope-probability distributions, which are given in the following paragraphs. For further details as might be needed for lunar trafficability studies consult References 3-51 through 3-53.

3.5.3.1 Crater Size Distribution

Lunar crater cumulative size distributions follow the equation $N = K\,D^{\alpha}$ reasonably well. The limiting steady-state distribution for lunar plains has $\alpha = -2$, while some actual distributions are better represented with $\alpha = -3$. Reference 3-52 gives the following expressions:

a) Rough mare:

$$N = 10^{-1}D^{-2} \quad (D < 100\ \text{m})$$

$$N = 10\ \ D^{-3} \quad (D > 100\ \text{m})$$

b) Smooth mare:

$$N = 10^{-1}D^{-2} \quad (D < 40\ \text{m})$$

$$N = 10^{0.602}D^{-3} \quad (100\ \text{m} > D > 40\ \text{m})$$

$$N = 10^{-2.038}D^{-1.68} \quad (200\ \text{m} > D > 100\ \text{m})$$

$$N = 10\ D^{-3} \quad (D > 200\ \text{m})$$

c) Some uplands:

$$N = 10^{-1}D^{-2} \quad (D < 1000\ \text{m})$$

$$N = 10^{2}\ D^{-3} \quad (D > 1000\ \text{m})$$

d) Slopes 17 degrees and larger:

N is negligible.

e) Heavily cratered surfaces:

$$N = 10^{-1}D^{-2} \quad (D < 10{,}000\ \text{m})$$

f) All craters on "steady state" surfaces (fresh, young, mature, and old craters):

$$N = 10^{-1}D^{-2}$$

g) All craters on "steady state" surfaces that are fresh:

$$N = 3.1 \times 10^{-3}D^{-2}$$

h) All craters on "steady state" surfaces that are fresh and young:

$$N = 2.5 \times 10^{-2} D^{-2}$$

i) All craters on "steady state" surfaces that are fresh, young, and mature:

$$N = 5 \times 10^{-2} D^{-2}$$

where: N is the cumulative frequency of craters/m^2

D is crater diameters in meters.

If the exponent $\alpha = -2$, then the area covered by craters with diameters between any two logarithmic intervals is the same. Thus, craters with diameters between 100 and 200 m would occupy the same total area as those between 10 and 20 m. Figure 3-6 shows recently compiled crater distribution data.

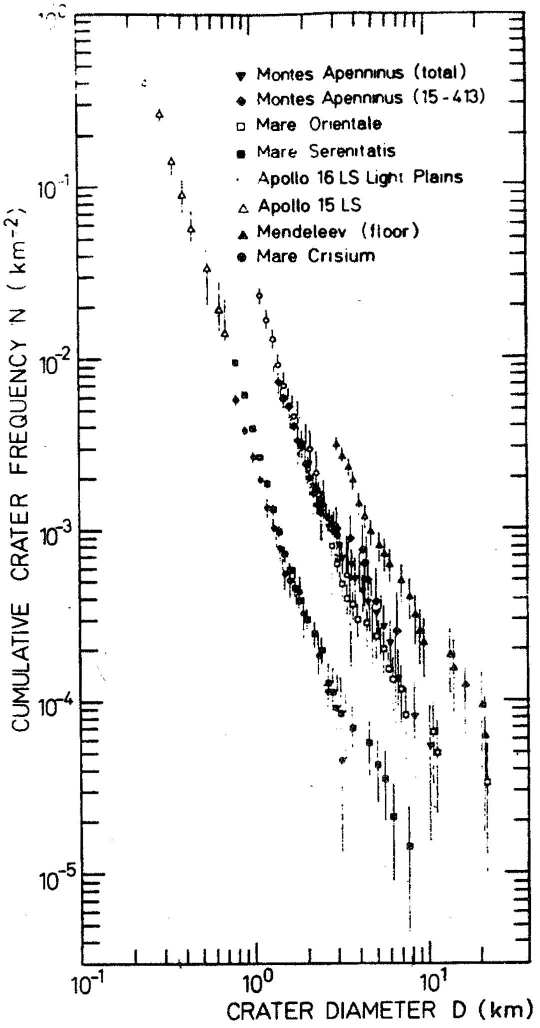

Figure 3-6. Absolute cumulative size-frequency distribution of crater populations [3-54].

3.5.3.2 Slope Distributions

Slope distributions have been derived from photogrammetric analysis [3-49] and from bistatic radar [3-55,3-56]. (In this context, "bistatic radar" refers to the technique of illuminating a spot on the lunar surface by a radar signal transmitted from an orbiter and receiving the scattered signal on the Earth.) The two techniques compare very well except where many slopes exceed 20 deg, a cutoff point for bistatic radar. The radar method appears to underestimate the roughness of upland terrain at small scale lengths.

Distributions generally are approximately semi-logarithmic (Figs. 3-7a and 3-7b) [3-49]. Cumulative slope probability distributions, if assumed to be Gaussian, show standard deviations that are typically:

For Maria	approximately 3.7 deg
For Highlands	4.5 to 6 deg and higher.

However, some actual distributions depart from the Gaussian form and show structures characterized as "complex" (bumps and wiggles) or "tailed" (more slopes at larger angles than a Gaussian) (Fig. 3-7c).

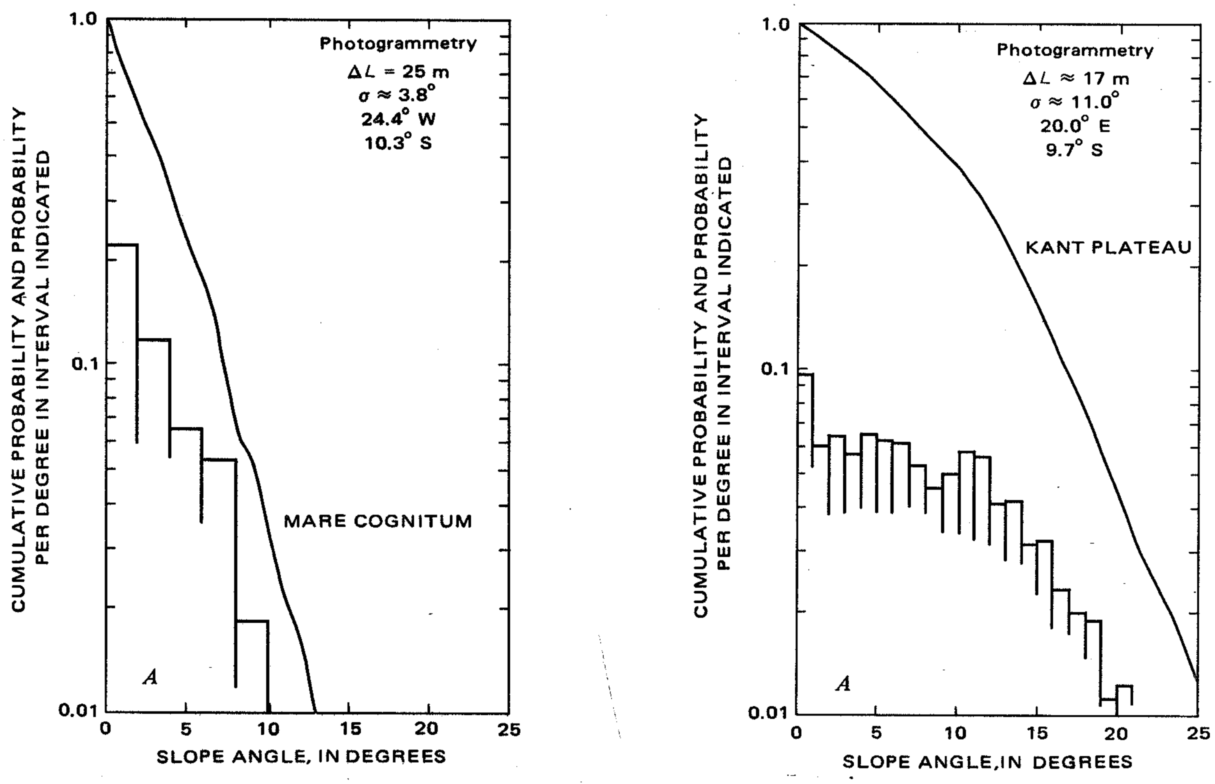

(a) Lunar cratered plains.

(b) Uplands.

Figure 3-7. Slope probability distributions by photogrammetry of selected lunar plains and upland regions [3-49].

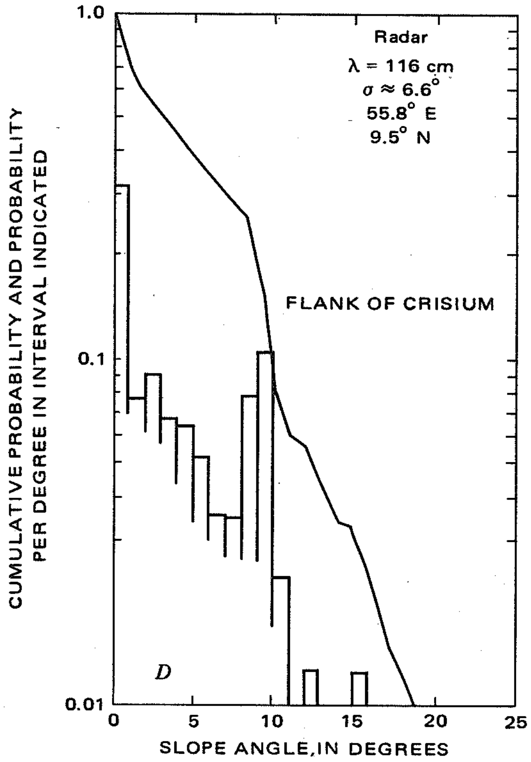

(c) Uplands-complex.

Figure 3-7. (Concluded)

3.5.3.3 Block Distributions

Block fields present obstacles to lunar roving vehicles. In an unpublished report, Moore [3-51] presents detailed counts; his data are summarized in Figures 3-8 and 3-9 [3-53].

3.5.3.4 Radar Studies

Radar signals transmitted from Earth have been used to probe the lunar surface. Tyler has suggested that the strength of the wavelength dependence in the reflected signal correlates with the size of craters near the upper limit of a steady state crater distribution on the maria and can therefore be used to determine not only surface roughness but also the age of the surface [3-57]. Review References 3-58 and 3-59.

3.5.4 Chemistry of Lunar Surface

Table 3-4 summarizes the major chemical elements found on the lunar surface.

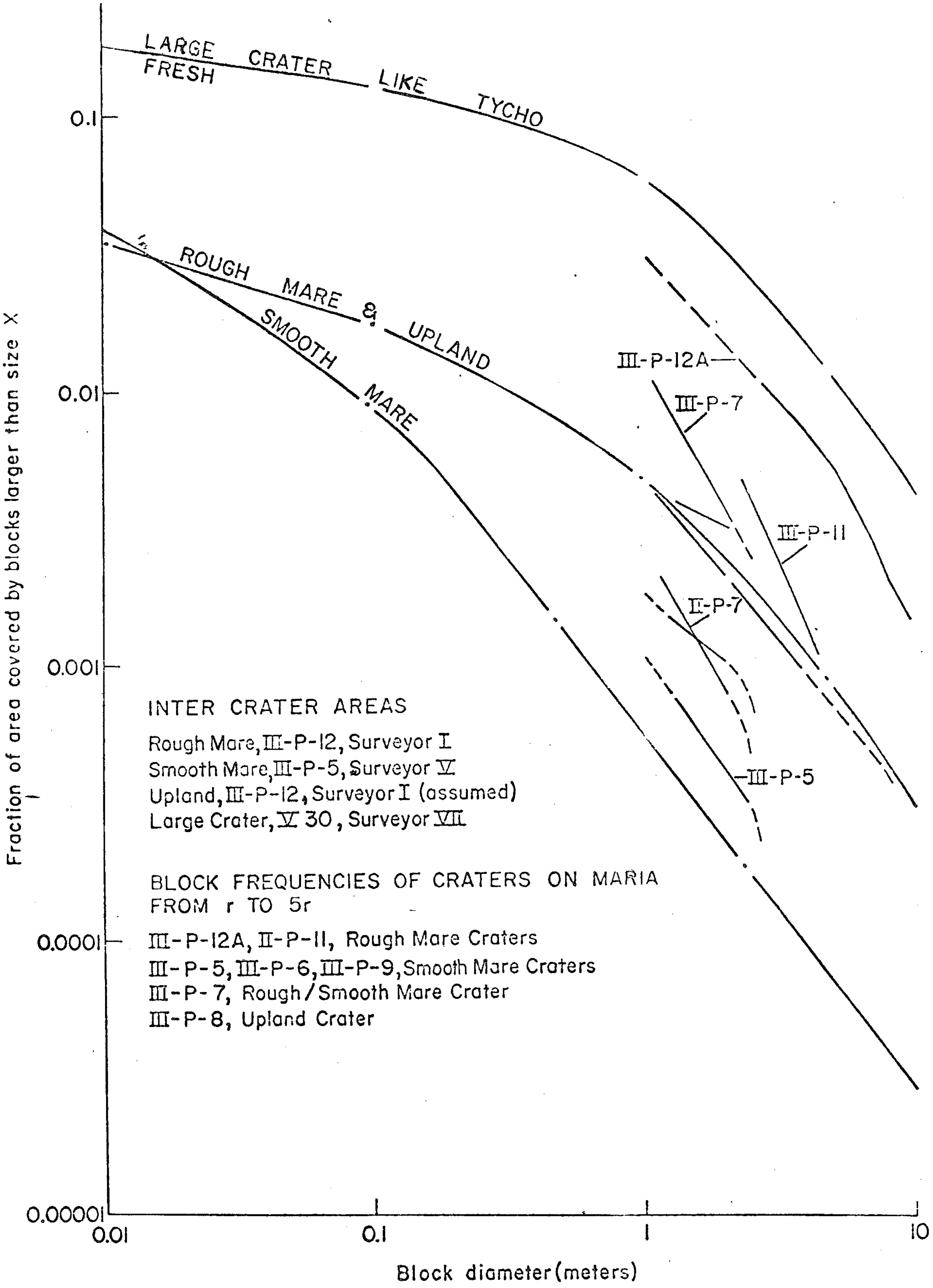

Figure 3-8. Block distributions - craters, intercrater areas, and smooth Maria [3-51].

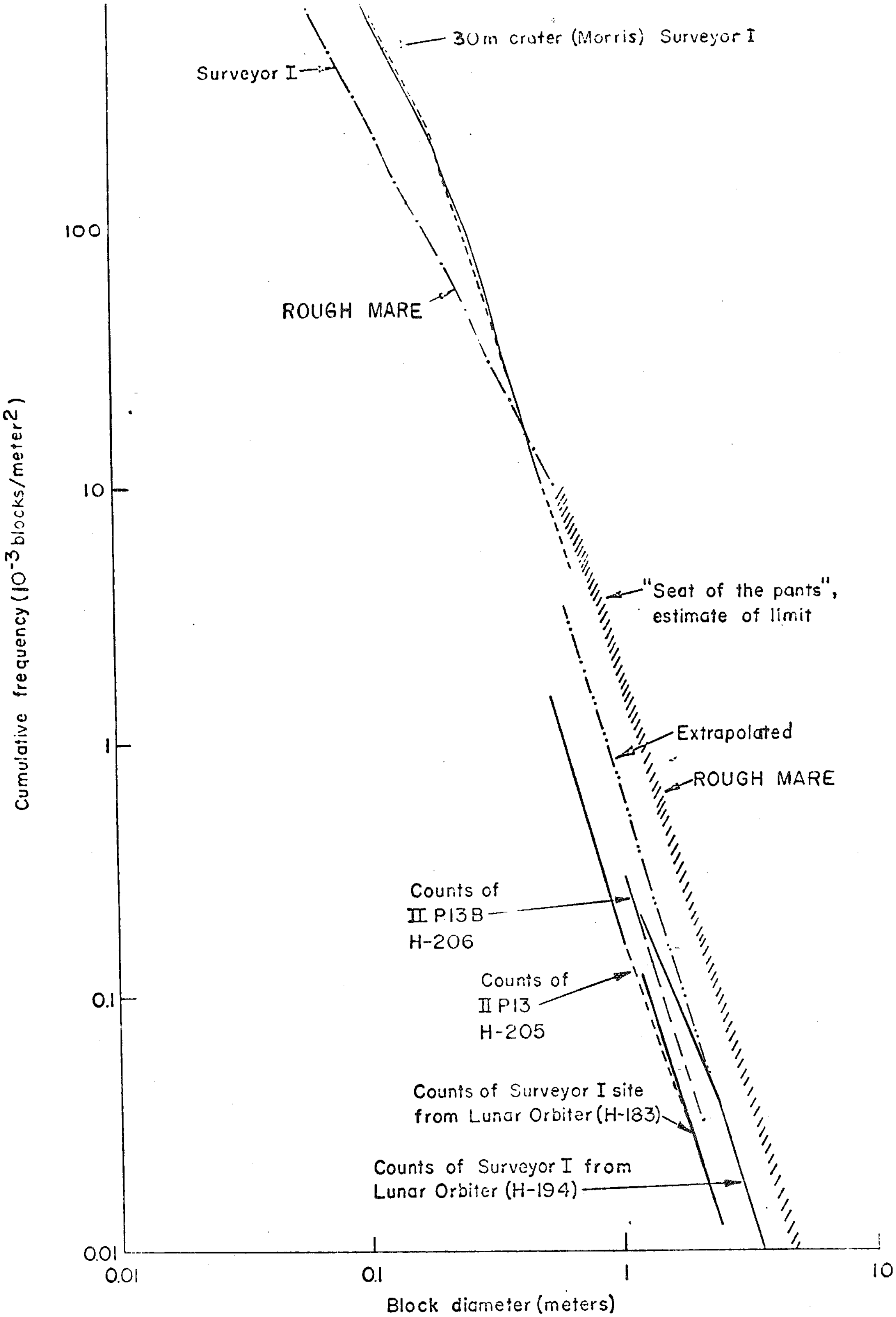

Figure 3-9. Block distributions - rough Maria [3-51].

TABLE 3-4. CHEMISTRY OF MAJOR LUNAR ROCK TYPES [3-4]

	Highland Rocks		Mare Basalts	
	Anorthositic Gabbro	Gabbroic Anorthosite	Olivine Basalt (A12)	Green Glass (A15)
SiO_2	44.5	44.5	45.0	45.6
TiO_2	0.39	0.35	2.90	0.29
Al_2O_3	26.0	31.0	8.59	7.64
FeO	5.77	3.46	21.0	19.7
MnO	--	--	0.28	0.21
MgO	8.05	3.38	11.6	16.6
CaO	14.9	17.3	9.42	8.72
Na_2O	0.25	0.12	0.23	0.12
K_2O	--	--	0.064	0.02
P_2O_5	--	--	0.07	--
Cr_2O_3	0.06	0.04	0.55	0.41
Total	99.9	100.2	99.77	99.4

The chemical composition of the regolith is dominated by the composition of the underlying bedrock, indicating that it is derived from local sources. Although components from more distant sources have also been identified, about half the regolith appears to come from within approximately 3 km of the point of collection [3-60]. There is no major transfer of material across the highland-mare boundaries, and vertical mixing is limited [3-61]. Although the upper 0.5 mm is estimated to have turned over around 100 times in 1 million years, there is only a 50-percent chance that material only 1-cm deep will have been disturbed. (For another estimate review Reference 3-62.)

Turkevich [3-63] summarizes the elemental composition of the lunar surface in Table 3-5.

3.5.5 Lunar Soil Particle Size Distribution

Grain size distributions in lunar soils are summarized in Figure 3-10 [3-64].

The lunar regolith generally consists of particles less than 1 mm in diameter, about the size of silt to fine sand, with a few scattered rocks. The size distribution of fine particles (<1 mm in diameter) is approximately log-normal, but a slight

TABLE 3-5. ELEMENTAL COMPOSITION OF LUNAR SURFACE

Element	Average Lunar Surface Percent of Atoms	Comments
O	61.0	
Na	0.4	
Mg	4.3	
Al	9.5	more Al in Terrae than in Maria
Si	16.3	
Ca + K	6.0	
Ti	0.3	very little Ti in Terrae
Fe	2.3	3 times as much Fe in Maria as in Terrae

bimodal tendency has been noted [3-65]. The bimodality may be due to the formation of glassy agglutinates (60 to 500 μm) and the accumulation of very fine ejecta (approximately 31 μm) from distant craters.

Lunar core samples show the regolith to consist of discrete layers deposited as ejecta blankets from small craters.

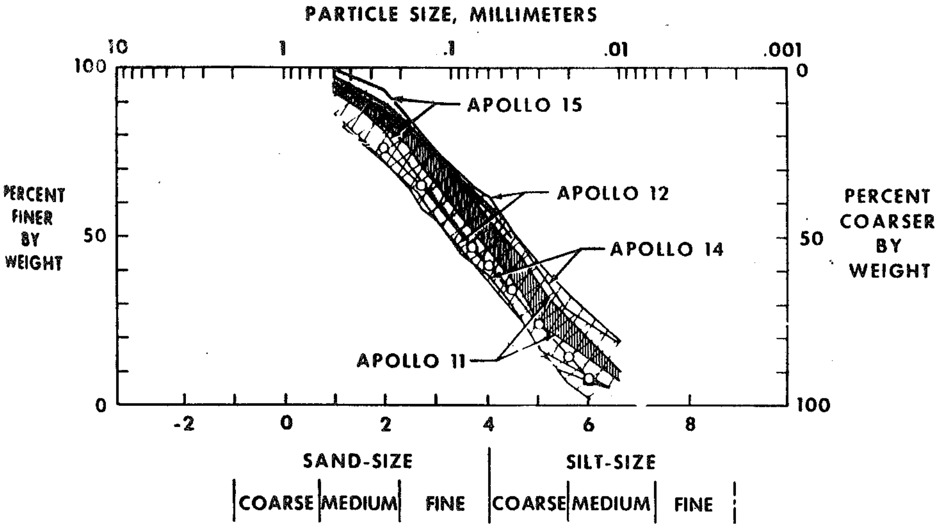

Figure 3-10. Submillimeter grain size distribution for Apollo 11, 12, 14, and 15 soil samples [3-64].

3.5.6 Mechanical Properties of Lunar Surface Material

The mechanical properties of lunar soils resemble those of terrestrial soils of comparable particle size, such as silty fine sand, even though composition may be dissimilar [3-66].

Table 3-6 lists some mechanical properties of lunar surface material.

TABLE 3-6. MECHANICAL PROPERTIES OF LUNAR SURFACE

Lunar Soil Parameter	Value	Reference or Comment
Density	near 1.0 g cm^{-3} 1.5 to 2.0	surface 10- to 20-cm depth [3-66]
Angle of internal friction	30 to 50 deg	higher for lower porosities [3-66]
Mean porosity	4.3 ± 2.8 percent	all Apollo sites for upper 15 cm [3-67]
Cohesion	0.03 to 0.3 N cm^{-2}	increase in cohesion for density increase from 0.99 to 1.87 g cm^{-3} [3-68]
Bearing strength	0.02 to 0.04 N cm^{-2} 30 to 100 N cm^{-2}	density: 1.15 g cm^{-3} density: 1.9 g cm^{-3} [3-69]

Most of these measurements, obtained by the Apollo science teams, were anticipated by the Surveyor missions [3-70].

3.5.7 Electrical Properties of Lunar Surface Material

Electrical properties of lunar rocks are generally similar to Earth minerals (although a recent laboratory study found anomalously high conductivities [3-71].

Data on dielectric constant and loss tangent for lunar soils and rocks are given in Figure 3-11 [3-72,3-73].

3.5.8 Optical Properties of the Lunar Surface

The normal albedo is 0.051 (Oceanus Procellarum) to 0.176 (floor of Aristarchus).

(Note: The Bond albedo, the ratio of the light reflected into all directions to the incident light, an important physical quantity, is difficult to measure. Usually, normal albedo, the ratio at zero phase angle of the brightness of an area to the brightness of a Lambert disk, is all that can be specified.)

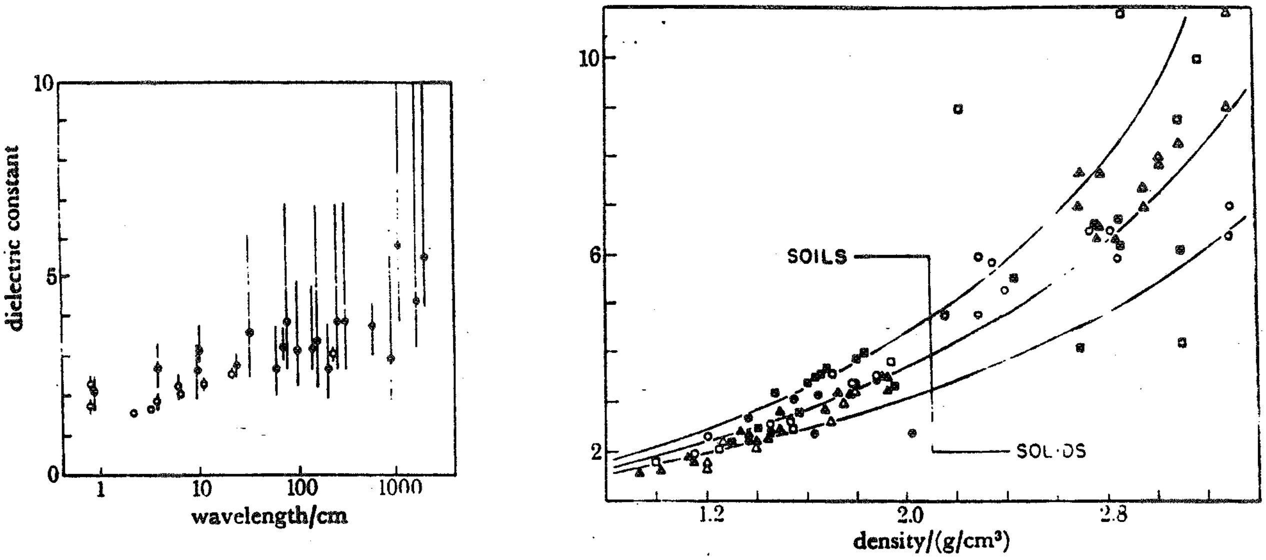

a. Dielectric constant as a function of wavelength.

b. Dielectric constant as a function of density.

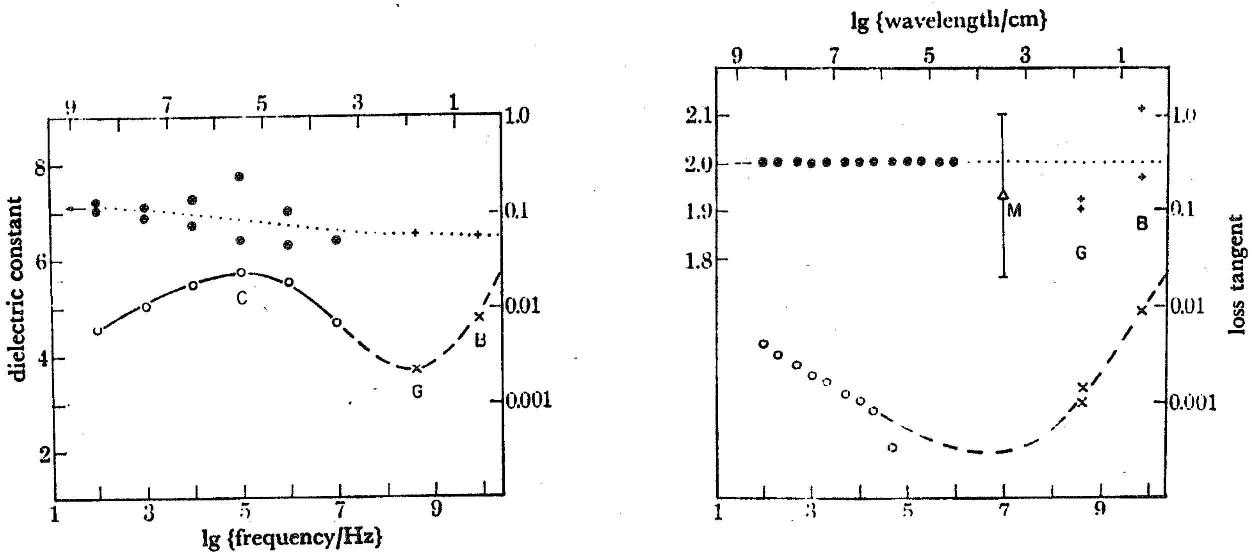

c. Dielectric constant (solid circles, +) and loss tangent (open circles, x) for rock sample.

d. Dielectric constant (solid circles, +) and loss tangent (open circles, x) for soil sample.

Figure 3-11. Dielectric constant and loss tangent for lunar materials.

Hapke [3-20] summarizes the optical properties of the lunar surface as follows:

a) Low albedo. The Moon reflects approximately 7 percent of incident light. The brightest areas exceed the darkest by 3.5:1.

b) Reddish color. The albedo increases monotonically with wavelength in the visible.

c) Full Moon. There is a strong peaking of brightness for every area at the time of a full Moon.

d) Low polarization. Near quadrature, polarization is approximately 8 percent. Maximum variation place to place is about 3.5:1.

e) The preceding "laws" apply for all known locations on the lunar surface.

(Reference 3-20 gives a detailed discussion of phase functions, polarization, and other optical properties.)

3.5.9 Temperatures of the Lunar Surface

Since there is no moderating atmosphere, surface temperatures are extreme. At the Apollo 17 site the temperature ranged from 384°K during the day to 102°K just before sunrise [3-21]. A detailed study of infrared radiation at 11 μm from the eclipsed lunar surface revealed over a thousand small anomalously warm regions [3-74]. There is an approximate anticorrelation between infrared eclipse temperature and albedo. Local high temperature anomalies have been interpreted as due to the presence of an excess of bare rocks on the surface [3-75].

Reference [3-53] quotes a thermal inertia $(k\rho c)^{-\frac{1}{2}}$ of approximately 800 near the lunar equator, with a range of possible values 25 to 1400 $\mathrm{cm^2 s^{\frac{1}{2}} K/cal}$.

3.6 ATMOSPHERE

There is no continuous "lower atmosphere;" the Moon only has an exosphere. The "upper atmosphere" of the Moon, which extends to the surface, is a nearly collisionless gas. There are no "aeolean" effects. Measurements of atmospheric density were performed by the Apollo science team and indicate that the surface level nighttime atmosphere contains approximately 2×10^5 molecules/cm^3 [3-22].

3.6.1 Composition

Table 3-7 summarizes the composition of the lunar atmosphere [3-76].

3.6.2 Sources of the Atmosphere

The sources of the lunar atmosphere include (1) diffusive and/or sputter release of implanted solar wind noble gases and possibly some molecular gases formed by reduction of lunar minerals by solar wind hydrogen; (2) radioactive decay of K,

TABLE 3-7. LUNAR ATMOSPHERE

Gas	Concentration (molecules/cm^3)	
	Day	Night
H_2	$<6 \times 10^3$	$<4 \times 10^4$
^4He	2×10^3	4×10^4
^{20}Ne	–	$<10^5$
^{36}Ar	–	$<3 \times 10^3$
^{40}Ar	–	4×10^4

U, and Th within the interior, producing ^{40}Ar, ^{222}Ra, and He; (3) meteorite and comet impact vaporization, providing water vapor and CO_2; (4) possibly some small contributions by degassing from impact events or gas venting; and (5) contamination by the spacecraft making the measurements [3-4]. To avoid contamination, mass spectrometer measurements were conducted at the Apollo 17 site at night when most gases would be condensed [3-22].

The lunar atmosphere loses helium at approximately the same rate as solar wind helium is intercepted [3-77]. Helium concentration goes through a maximum during the lunar night. Argon is adsorbed on soil grains at night, producing a nighttime minimum. Loss mechanisms include (1) thermal evaporation of gas molecules, (2) photo-ionization, and (3) gravitational (solar and terrestrial) perturbation of atoms in the atmosphere. The lunar atmosphere is in effect a reservoir providing temporary storage for free atoms that eventually escape into space. It also provides a channel for lateral transport of condensable gases to high-latitude cold traps where large deposits of water ice and other solidified compounds have probably accumulated over the past 2 billion years [3-78].

3.7 MAGNETOSPHERE

The Moon has no magnetosphere per se. The solar wind impinges on the lunar surface; there is no bow shock.

3.8 SPACE ENVIRONMENT

3.8.1 Radiant Energy Fluxes

The spectral distribution of sunlight is approximately blackbody at 5760°K. Energy flux at the Earth-Moon system is 1.97 cal/(cm^2min) or 1371 ± 5 W m^{-2}.

Other than direct sunlight, the most important source of radiant flux at the Moon is earth shine (sunlight reflected from the Earth) and thermal radiation from the Earth's surface and atmosphere. For a discussion, review Section 2.0 on the Earth's upper atmosphere.

3.8.2 Charged Particle Flux

The Moon does not have a magnetic field strong enough to prevent the direct impingement of ionized particles on its surface. There are three sources for the charged particles that have been detected at the surface of the Moon (1) the solar wind, (2) solar cosmic rays, and (3) high-energy galactic cosmic rays originating outside the solar system.

Table 3-8 summarizes the charged particle environment at the Moon's surface [3-4].

TABLE 3-8. CHARGED PARTICLE ENVIRONMENT AT LUNAR SURFACE

Source	MeV/nucleon	Proton Flux (Ncm^{-2} sec^{-1})	Penetration Depth (cm)
Solar wind	10^{-3}	10^{8}	10^{-6}
Solar cosmic rays	1 to 10^{2}	10^{2}	1 to 10^{-3}
Galactic cosmic rays	10^{2} to 10^{4}	1	1 to 10^{3}

3.8.2.1 Solar Wind Plasma

The solar wind plasma consists mostly of H and He nuclei and, as noted earlier, is the dominant source of the lunar atmosphere. Surface features exposed to the solar wind with a velocity of approximately 400 km/sec are gradually smoothed by a process known as sputtering. This process poses little hazard to equipment on the lunar surface, however, because the erosion lifetime of a rock with a diameter of only 10^{-6} m is estimated to be 10^{5} years [3-79].

3.8.2.2 Solar Cosmic Rays

Solar cosmic rays are ejected from the Sun during the violent explosions associated with solar flares. Long-period variations in solar cosmic rays correlate with the well-known 11-year cycle of sunspot activity. The nuclei of light atoms (H, He) are dominant, but heavier nuclei (Ca, Fe) also occur. Since there is no blanketing atmosphere, these high-energy particles reach the surface unhindered, penetrating typical lunar surface materials to a depth of 1 cm [3-4]. Studies of tracks (revealed by etching rock samples with acid) and the isotopic changes produced by this bombardment have been used to determine deposition and erosion rates on the lunar surface, as well as to determine the nature and extent of mixing within the regolith. Preserved in these lunar rocks is a record of the Sun's activity, and studies indicate that the solar cosmic ray flux has been fairly constant over the past 10 million years [3-80], although short cessations on the order of 50 years in length may have occurred [3-81].

3.8.2.3 Galactic Cosmic Rays

The most energetic charged particles reaching the Moon's surface come from outside the solar system in the form of galactic cosmic rays. Galactic cosmic ray particles (atomic nuclei) have lunar penetration depths that exceed 1 m, but the flux rate is substantially lower than for solar cosmic rays.

3.8.3 Meteoroids

The Moon is bombarded with meteoroids and micrometeoroids. With no protection from an atmosphere, impact velocities range from 2.4 to 72 km/sec, even for small objects [3-82]. Micrometeoroids compromise three classes (1) cometary debris, (2) interstellar grains, and (3) lunar ejecta.

3.8.3.1 Meteoroid Hazard

The hazard posed to astronauts on the surface by meteoroid bombardment is small [3-83]. The impact rate per cm^2 appears to be between 1.1 and 50 craters per million years for pits greater than 500 μm in diameter [3-84].

3.8.3.2 Flux of Larger Meteoroids

The direct measurement of the meteoroid flux has been accomplished for particles larger than about 100 g by using the lunar seismic network. Between 70 and 150 events were recorded each year until the experiment was discontinued. The present-day flux has been described by the equation:

$$\log N = -1.62 - 1.16 \log m$$

where N is the number of impacting bodies per km^2 per year with a mass greater than m [3-36]. The distribution appears to be the result of two populations of impacting bodies, one that varies little throughout the year and larger objects that intersect the Moon's orbit during April, May, and June, producing a higher than average flux. A correlation between known meteor showers and the flux rate has been proposed [3-85]. (For more details on meteoroids, review Section 2.6.)

3.8.3.3 Flux of Micrometeoroids

For micrometeoroid flux in space in the vicinity of the Moon, review Section 2.0 on the Earth's upper atmosphere. For the flux of particles ejected from micrometeoroid impacts on the lunar surface, review paragraph 4.1.3.4 of Reference 3-53.

3.9 SUPPLEMENTARY MATERIAL

3.9.1 Origin of the Moon

In the excitement of the early days of space exploration many scientists believed that the origin of the Moon would soon be understood. However, the lunar samples revealed that even the Moon, as small as it is, has experienced a complex history that reprocessed all of its original material, obscuring its primordial nature. A better understanding of the Moon's evolution after its origin about 4.6 billion years ago may come from additional studies of the data gathered by the Apollo and Luna missions, but it appears that further spacecraft landings, new missions such as lunar polar orbit, or new analysis techniques will be required.

Three theories concerning lunar origins are currently popular. The least exotic proposal suggests that the Moon and the Earth accreted from a nebula of gas and dust that surrounded the primordial Sun in much the same relative positions that they occupy today. Another theory postulates that the Moon formed in a different part of the solar nebula but was later captured by the Earth. The Moon may have survived intact or it may have fragmented and then reaccumulated in Earth orbit. A third hypothesis suggests the Moon separated from a partly differentiated Earth during a rapid rotational instability shortly after accretion [3-4,3-40,3-86].

3.9.2 Where Do We Go From Here?

As our nearest planetary neighbor, the Moon should continue to receive scientific attention in the coming decades. Possible future missions include a polar orbiter equipped with imaging and remote sensing devices to explore portions of the Moon not yet observed in detail. Unmanned sample return missions (such as those sponsored by the U.S.S.R.) could play an important role in future exploration, while avoiding the risk and expense of manned missions. Visionaries urge the eventual colonization of the Moon and have offered plans using its natural resources as partial justification for such ventures [3-87,3-88].

3.9.3 Chronology of Lunar Exploration

A complete chronology of lunar missions is found in Table 3-9.

TABLE 3-9. CHRONOLOGY OF LUNAR MISSIONS

Name	Country	Launch Date	Objective	Result
Pioneer 0	USA	August 17, 1958	Lunar orbit	Launch failure
Pioneer 1	USA	October 11, 1958	Lunar orbit	Launch failure
Pioneer 2	USA	November 8, 1958	Lunar orbit	Launch failure
Pioneer 3	USA	December 6, 1958	Lunar impact	Launch failure
Luna 1	USSR	January 2, 1959	Lunar impact	Missed Moon
Pioneer 4	USA	March 3, 1959	Lunar impact	Missed Moon
Lunar 12	USSR	September 12, 1959	Lunar impact	First lunar impact
Pioneer (P-1)	USA	September 24, 1959	Lunar orbit	Exploded on launching pad
Luna 3	USSR	October 4, 1959	Lunar flyby	First farside photography
Pioneer (P-3)	USA	November 26, 1959	Lunar orbit	Launch failure
Pioneer (P-30)	USA	September 25, 1960	Lunar orbit	Launch failure
Pioneer (P-31)	USA	December 15, 1960	Lunar orbit	Launch failure
Ranger 3	USA	January 26, 1962	Lunar impact	Missed Moon
Ranger 4	USA	April 23, 1962	Lunar impact	Spacecraft failure
Ranger 5	USA	October 18, 1962	Lunar impact	Missed Moon
U-8*	USSR	January 14, 1963	Lunar lander	Failed to leave Earth orbit
Luna 4	USSR	April 2, 1963	Lunar lander	Missed Moon
Ranger 6	USA	January 30, 1964	Lunar impact	Impact, but camera failed
Ranger 7	USA	July 28, 1964	Lunar impact	Success
Ranger 8	USA	February 17, 1965	Lunar impact	Success
Cosmos 60	USSR	March 12, 1965	Lunar landing	Failed to leave Earth orbit
Ranger 9	USA	March 21, 1965	Lunar impact	Success
Luna 5	USSR	May 9, 1965	Lunar landing	Crashed on Moon
Luna 9	USSR	January 31, 1966	Lunar landing	First soft landing
Cosmos III	USSR	March 1, 1966	Lunar orbit	Failed to leave Earth orbit

*Unannounced

TABLE 3-9. (Continued)

Name	Country	Launch Date	Objective	Result
Luna 10	USSR	March 31, 1966	Lunar orbit	First lunar orbiter
Surveyor 1	USA	May 30, 1966	Lunar landing	Success
Explorer 33	USA	July 1, 1966	Lunar orbit	Failed to achieve lunar orbit
Lunar Orbiter 1	USA	August 10, 1966	Lunar orbit	Success
Luna 11	USSR	August 24, 1966	Lunar orbit	Success; no imagery
Surveyor 2	USA	September 24, 1966	Lunar landing	Crashed on the Moon
Luna 12	USSR	October 22, 1966	Lunar orbit	Success
Lunar Orbiter 2	USA	November 6, 1966	Lunar orbit	Success
Luna 13	USSR	December 21, 1966	Lunar landing	Success
Lunar Orbiter 3	USA	February 4, 1967	Lunar orbit	Success
Surveyor 3	USA	April 17, 1967	Lunar landing	Success
Lunar Orbiter 4	USA	May 4, 1967	Lunar orbit	Success
Surveyor 4	USA	July 14, 1967	Lunar landing	Communications lost
Explorer 35	USA	July 19, 1967	Lunar orbit	Success
Lunar Orbiter 5	USA	August 2, 1967	Lunar orbit	Success
Surveyor 5	USA	September 8, 1967	Lunar landing	Success; soil analysis
Surveyor 6	USA	November 7, 1967	Lunar landing	Success; soil analysis
Surveyor 7	USA	January 7, 1968	Lunar landing	Success; soil analysis
Zond 4	USSR	March 2, 1968	Circumlunar	Engineering Test
Luna 14	USSR	April 7, 1968	Lunar orbit	Success
Zond 5	USSR	September 14, 1968	Circumlunar	Success; first recovery
Zond 6	USSR	November 10, 1968	Circumlunar	Success
Apollo 8	USA	December 21, 1968	Circumlunar	First manned lunar orbit
Apollo 10	USA	May 18, 1969	Circumlunar	Success; manned
Luna 15	USSR	July 13, 1969	Lunar landing	Crashed on Moon

TABLE 3-9. (Concluded)

Name	Country	Launch Date	Objective	Result
Apollo 11	USA	July 16, 1969	Lunar landing	First manned lunar landing
Zond 7	USSR	August 7, 1969	Circumlunar	Success
Cosmos 300	USSR	September 23, 1969	Lunar landing(?)	Failed to leave Earth orbit
Cosmos 305	USSR	October 22, 1969	Lunar landing(?)	Failed to leave Earth orbit
Apollo 12	USA	November 14, 1969	Lunar landing	Success; manned landing
Apollo 13	USA	April 11, 1970	Lunar landing	Landing cancelled en-route
Luna 16	USSR	September 22, 1970	Lunar landing	First unmanned sample return
Zond 8	USSR	October 20, 1970	Circumlunar	Success
Luna 17	USSR	November 10, 1970	Lunar landing	First "rover"
Apollo 14	USA	January 31, 1971	Lunar landing	Success; manned landing
Apollo 15	USA	July 26, 1971	Lunar landing	Success; manned landing
Luna 18	USSR	September 2, 1971	Lunar landing	Communications lost
Luna 19	USSR	September 28, 1971	Lunar orbit	Success
Luna 20	USSR	February 25, 1972	Lunar landing	Returned samples
Apollo 16	USA	April 16, 1972	Lunar landing	Success; manned landing
Apollo 17	USA	December 7, 1972	Lunar landing	Success; manned landing
Luna 21	USSR	January 8, 1973	Lunar landing	Success
Explorer 49	USA	June 10, 1973	Lunar orbit	Success
Luna 22	USSR	March 21, 1974	Lunar orbit	Success
Luna 23	USSR	October 28, 1974	Lunar landing	Crashed
Luna 24	USSR	August 1976	Sample return	Success

REFERENCES

3-1. Mutch, T. A.: Geology of the Moon: A Stratigraphic View. Princeton University Press, Princeton, New Jersey, 1972.

3-2. Kaula, W. M. and Harris, A. W.: Dynamically plausible hypotheses of lunar origin. Nature, vol. 245, 1973, pp. 367-369.

3-3. Wood, J. A.: Origin of the Earth's Moon. In J. A. Burns (ed.), Planetary Satellites, University of Arizona Press, Tucson, 1977, pp. 513-529.

3-4. Taylor, S. R.: Lunar Science: A Post-Apollo View. Pergamon, New York, 1975.

3-5. Guest, J. R. and Greeley, R.: Geology on the Moon. Wykeham Publications Ltd., London, 1977.

3-6. Kopal, Z.: An Introduction to the Study of the Moon. D. Reidel Publishing Co., Dordrecht-Holland, 1966.

3-7. Kopal, Z. (ed.): Physics and Astronomy of the Moon. Academic Press, New York, 1971.

3-8. Cole, G. H. A.: The Structure of the Planets. Wykeham Publishing Ltd., London, 1978.

3-9. Newburn, R.: Planetary Data. Proc. Lunar and Planetary Sci. Conf. 9th, (frontispiece), 1978.

3-10. American Ephemeris and Nautical Almanac. U. S. Naval Observatory, 1980.

3-11. Moutsoulas, M. D.: Libration of the Lunar Globe. In Physics and Astronomy of the Moon, Academic Press, New York, 1971, pp. 29-61.

3-12. Burns, J. A.: Orbital Evolution. In J. A. Burns (ed.), Planetary Satellites, University of Arizona Press, Tucson, 1977, pp. 113-156.

3-13. Goldreich, P.: History of the Lunar Orbit. Rev. Geophys., vol. 4, 1966, pp. 411-439.

3-14. Kaula, W. M. and Harris, A. W.: Dynamics of lunar origin and orbital evolution. Rev. Geophys. Space Phys., vol. 13, 1975, pp. 363-371.

3-15. Kaula, W. M., Schubert, G., Lingenfelter, R. E., Sjogren, W. L., and Wollenhaput, W. R.: Apollo laser altimetry and interference as to lunar structure. Proc. Lunar Sci. Conf. 5th, 1974, pp. 3049-3058.

3-16. Opik, E. J.: Comments on lunar origin. Irish Astonom. J., vol. 10, 1972, pp. 190-238.

3-17. Mulholland, J. D.: Scientific achievements from ten years of lunar laser ranging. Rev. Geophys. Space Phys., vol. 18, 1980, pp. 549-564.

3-18. Brown, E. W.: An Introductory Treatise on the Lunar Theory. Cambridge University Press, 1896. (Reprinted by Dover, New York.)

3-19. Deprit, A.: The motions of the Moon in Space. In Physics and Astronomy of the Moon, Academic Press, New York, 1971, pp. 1-21.

3-20. Hapke, B.: Optical properties of the lunar surface. In Physics and Astronomy of the Moon, Academic Press, New York, 1971, pp. 155-211.

3-21. Keihm, S. J. and Langseth, M. G.: Surface brightness temperatures at the Apollo 17 heat flow site: Thermal conductivity of the upper 15 cm of regolith. Proc. Lunar Sci. Conf. 4th, 1973, pp. 2503-2513.

2-22. Johnson, F. S., Carroll, J. M., and Evans, D. E.: Lunar atmospheric measurements. Proc. Lunar Sci. Conf. 3rd, 1972, pp. 2231-2242.

2-23. Toksoz, M. N. and Johnson, D. H.: The evolution of the Moon. ICARUS, vol. 21, 1974, pp. 369-414.

3-24. Liu, A. S. and Laing, P. A.: Lunar gravity field as determined by orbiters. Space Research XII, COSPAR, Akademie-Verlag, Berlin, 1972, pp. 163-177.

3-25. Muller, P. M. and Sjogren, W. L.: Mascons: lunar mass concentrations. Science, vol. 161, 1968, pp. 680-684.

3-26. Thurber, C. H. and Solomon, S. C.: An assessment of crustal thickness variations and the lunar near side: models uncertainties and implications for crustal differentiation. Proc. Lunar and Planetary Sci. Conf. 9th, 1978, vol. 3481-3497.

3-27. Bills, B. G. and Ferrari, A. J.: A lunar density model consistent with topographic, gravitational, librational, and seismic data. J. Geophys. Res., vol. 82, 1977, pp. 1306-1314.

3-28. Fuller, M., Meshkov, E., Cisowski, S. M., and Hale, C. J.: On the natural remanent magnetism of certain Mare basalts. Proc. Lunar and Planetary Sci. Conf. 10th, 1979, pp. 2211-2233.

3-29. Hood, L. L., Coleman, P. J., and Wilhelms, D. E.: Lunar nearside magnetic anomalies. Proc. Lunar and Planetary Sci. Conf. 10th, 1979, pp. 2235-2257.

3-30. Nagata, T., Fisher, R. M., Schwerer, F. C., Fuller, M. D., and Dunn, J. R.: Rock magnetism of Apollo 14 and 15 materials. Proc. Lunar Sci. Conf. 3rd, 1972, pp. 2423-2447.

3-31. Runcorn, S. K.: On the interpretation of lunar magnetism. Phys. of the Earth and Planetary Interiors, vol. 10, 1975, pp. 327-335.

3-32. Runcorn, S. K.: An iron core in the Moon generating an early magnetic field?" Proc. Lunar and Planetary Sci. Conf. 10th, 1979, pp. 2325-2333.

3-33. Srnka, L. J.: Spontaneous magnetic field generation in hypervelocity impacts. Proc. Lunar Sci. Conf. 8th, 1977, pp. 785-792.

3-34. Latham, G., Nakamura, Y., Lannlein, D., Dorman, J., and Duennebier, F.: Structure and state of the lunar interior based upon seismic data. Lunar Science V, 1974, p. 434.

3-35. Toksoz, M. N., Dainty, A. M., Solomon, S. C., and Anderson, R.: Velocity structure and evolution of the Moon. Proc. Lunar Sci. Conf. 4th, 1973, pp. 2529-2547.

3-36. Latham, G., Dorman, J., Duennebeir, F., Ewing, M., Lammlein, D., and Nakamura, Y.: Moonquakes, meteoroids, and the state of the lunar interior. Proc. Lunar Sci. Conf. 4th, 1973, pp. 2515-2527.

3-37. Head, J. W.: Some geologic observations concerning lunar geophysical models. NASA SP-370, pt. 1, 1976, pp. 407-416.

3-38. Simmons, G., Todd, T., and Wang, H.: The 25-km discontinuity: implications for lunar history. Science, vol. 182, 1973, pp. 158-161.

3-39. Minear, J. W. and Fletcher, C. R.: Crystallization of a lunar magma ocean. Proc. Lunar and Planetary Sci. Conf. 9th, 1978, pp. 263-283.

3-40. Wood, J A., Dickey, J. S., Marvin, U. B., and Powell, B. N.: Lunar anorthosites and a geophysical model of the Moon. Proc. of the Apollo 11 Lunar Science Conf., 1970, pp. 965-988.

3-41. Head, J. W.: Lunar volcanism in space and time. Rev. Geophys. Space Phys., vol. 14, 1976, pp. 265-300.

3-42. Greeley, R.: Modes of emplacement of basalt terrains and an analysis of Mare volcanism in the Orientale Basin. Proc. Lunar Sci. Conf. 7th, 1976, pp. 2747-2759.

3-43. Wilding-White, T. M.: Jane's Pocket Book of Space Exploration. Collier Books, New York, 1977.

3-44. Wilson, L. and Head, J. W.: The formation of eroded depressions around the sources of lunar sinuous rilles: theory. Lunar and Planetary Science XI, 1980, pp. 1260-1262.

3-45. Lucchitta, B. K.: Mare ridges and related highland scarps: results of vertical tectonism. Proc. Lunar Sci. Conf. 7th, 1976, pp. 2761-2782.

3-46. Solomon, S. C. and Head, J. W.: Vertical movement in Mare basins: relation to Mare emplacement, basin tectonics, and lunar thermal history. J. Geophys. Res., vol. 84, 1979, pp. 1667-1682.

3-47. Lucchitta, B. K. and Watkins, J. A.: Age of graben systems on the Moon. Proc. Lunar and Planetary Sci. Conf. 9th, 1978, pp. 3459-3472.

3-48. Quaide, W. L. and Oberbeck, V. R.: Thickness determinations of the lunar surface layer from lunar impace craters. J. Geophys. Res., vol. 73, 1968, pp. 5247-5270.

3-49. Wu. S. S. C. and Moore, H. J.: Experimental Photogrammetry of Lunar Images. U.S.G.S. Professional Paper 1046-D, U.S. Government Printing Office, Washington, D.C., 1980.

3-50. Kinsler, D. C.: User Guide to the 1: 250,000 Scale Lunar Maps. Lunar Science Institute, Houston, 1975.

3-51. Moore, H J.: Distribution of blocks on the lunar surface. In Lunar Terrain and Traverse Data for Lunar Roving Vehicle Design Study, unpublished report prepared by the U.S.G.S. for NASA, March 19, 1969.

3-52. Moore, H. J., Pike, R. J., and Ulrich, G. E.: Lunar Terrain and Traverse Data for Lunar Roving Vehicle Design Study. Unpublished report prepared by the U.S.G.S. for NASA, March 19, 1969.

3-53. NASA TM 78119, Space and Planetary Environment Criteria Guidelines for Use in Space Vehicle Development, 1977 Revision, 1977.

3-54. Neukum, G., Konig, B., and Arkani-Hamed, J.: Study of lunar impact crater size distributions. The Moon, vol. 12, 1975, pp. 201-229.

3-55. Moore, H. J.: Bistatic radar. In Lunar Remote Sensing and Measurements, U.S.G.S. Professional Paper 1046-B, U.S. Government Printing Office, Washington, D.C., 1980.

3-56. Tyler, G. L. and Howard, H. T.: Dual-frequency bistatic-radar investigations of the Moon with Apollos 14 and 15. J. Geophys. Res., vol. 78, 1973, pp. 4852-4874.

3-57. Tyler, G. L.: Comparison of quasi-specular radar scatter from the Moon with surface parameters obtained from images. ICARUS, vol. 37, 1979, pp. 29-45.

3-58. Moore, H. J. and Tyler, G. L.: Comparison between photogrammetric and bistatic-radar slope-frequency distributions. Apollo 17 Preliminary Science Report, NASA SP-330, 1973, pp. 33-17 to 33-26.

3-59. Moore, H. J. and Zisk, S. H.: Calibration of radar data from Apollo 17 and other mission results. Apollo 17 Preliminary Science Report, NASA SP-330, 1973, pp. 33-10 to 33-17.

3-60. Shoemaker, E. M., Hait, M. H., Swann, G. A., et al.: Origin of the lunar regolith at Tranquility Base. Proc. Apollo 11 Lunar Science Conference, 1971, pp. 2399-2412.

3-61. Gault, D. E., Horz, F., Brownlee, D. E., and Hartung, J. B.: Mixing of the lunar regolith. Proc. Lunar and Planetary Sci. Conf. 5th, 1974, pp. 2365-2386.

3-62. Morris, R. V.: In situ reworking (gardening) of the lunar surface: evidence from the Apollo cores. Proc. Lunar Sci. Conf. 9th, 1978, pp. 1801-1811.

3-63. Turkevich, A. L.: Average chemical composition of the lunar surface. The Moon, vol. 8, 1973, pp. 365-367.

3-64. Carrier, W. D.: Lunar soil grain size distribution. The Moon, vol. 6, 1973, pp. 250-263.

3-65. King, E. A.: The lunar regolith: physical characteristics and dynamics. Phil. Trans., Roy. Soc. London, Series A, 1977, pp. 273-278.

3-66. Mitchell, J. K., Houston, W. N., Scott, R. F., Costes, N., Carrier, W. D., and Bromwell, L. G.: Mechanical properties of lunar soil: density, porosity, cohesion, and angle of internal friction. Proc. Lunar Sci. Conf. 3rd, 1972, pp. 3235-3253.

3-67. Houston, W. M., Mitchell, J. K., and Carrier, W. P.: Lunar soil density and porosity. Proc. Lunar Sci. Conf. 4th, 1974, pp. 2361-2364.

3-68. Jaffe, L. D.: Shear strength of lunar soil from Oceanus Procellarum. The Moon, vol. 8, 1973, pp. 58-72.

3-69. Jaffe, L. D.: Bearing strength of lunar soil. The Moon, vol. 3, 1971, pp. 337-345.

3-70. NASA Special Publication 184: Surveyor – Program Results. 1969, p. 423.

3-71. Nagato, R., Rikitako, T., and Kono, M.: Electrical conductivity and the age of the Moon. Space Research XI, COSPAR, 1971, pp. 85-87.

3-72. Strangway, D. W. and Olhoeft, G. R.: Electrical properties of planetary surfaces. Phil. Trans., Roy. Soc. London, Series A, vol. 285, 1977, pp. 441-450.

3-73. Bussey, H. E.: Microwave dielectric measurements of lunar soil with a coaxial line resonator method. Proc. Lunar and Planetary Sci. Conf. 10th, 1979, pp. 2175-2182.

3-74. Shorthill, R. W.: Infrared atlas charts of the eclipsed Moon. The Moon, vol. 7, 1973, pp. 22-45.

3-75. Moore, H. J.: Infrared Eclipse Temperatures. In Lunar Remote Sensing and Measurements, U.S.G.S. Professional Paper 1046-B, U.S. Government Printing Office, Washington, D.C., 1980.

3-76. Hodges, R. R., Hoffman, J. H., and Johnson, F. S.: The lunar atmosphere. ICARUS, vol. 21, 1974, p. 415.

3-77. Hodges, R. R.: Gravitational and radiative effects on the escape of helium from the Moon. Proc. Lunar and Planetary Sci. Conf. 9th, 1978, pp. 1749-1764.

3-78. Arnold, J. R.: Ice on the Lunar Polar Regions. J. Geophys. Res., vol. 84, 1979, pp. 5659-5668.

3-79. McDonnell, J. A. M., Ashworth, D. G., Flavill, R. P., Carey, W. C., Bateman, D. C., and Jennison, R. C.: The characterization of lunar surface. Phil. Trans., Roy. Soc. London, Series A, vol. 285, 1978, pp. 303-308.

3-80. Kohl, C. P., Murrell, M. T., Russ, G. D., and Arnold, J. R.: Evidence for the constancy of the solar cosmic ray flux over the past ten million years: ^{53}Mn and ^{26}Al measurements. Proc. Lunar and Planetary Sci. Conf. 9th, 1978, pp. 2299-2310.

3-81. Eddy, J. A.: The Maunder Minimum. Science, vol. 192, 1976, pp. 1189-1201.

3-82. Berg, O. E., Richardson, F. F., and Burton, H.: Lunar ejecta and meteorites experiment. Apollo 17 Preliminary Science Report, NASA SP-330, 1973, pp. 16-1 to 16-9.

3-83. Berg, O. E. and Gerloff, U.: More than two years of micrometeorite data from Pioneer satellites. Space Research XI, COSPAR, Akadamie-Verlag, Berlin, 1971, pp. 225-235.

3-84. Horz, F., Morrison, D. A., Gault, D. E., et al.: The micrometeoroid complex and evolution of the lunar regolith. NASA SP-370, pt. 2, 1977, pp. 605-635.

3-85. Dorman, J., Evans, S., Nakamura, Y., and Latham, G.: On the time-varying properties of the lunar seismic meteoroid population. Proc. Lunar and Planetary Sci. Conf. 9th, 1978, pp. 3615-3626.

3-86. Ringwood, A. E.: Origin of the Earth and Moon. Springer-Verlag, New York, 1979.

3-87. Johnson, R. D. and Holbrow, C. (eds.): Space Settlements: a Design Study. NASA SP-413, 1977.

3-88. O'Neill, G. K.: The High Frontier: Human Colonies in Space. Bantam Books, New York, 1977.

SECTION 4. MERCURY

4.1 INTRODUCTION

Mercury, the innermost planet, orbits the Sun at 0.4 AU. In size it is between the Moon and Mars. The planet is difficult to observe telescopically from the Earth, since it is never more than 28 deg from the Sun. This means that observations must be made either at twilight or at dawn, and the observer must look close to the horizon through a thick layer of the Earth's atmosphere. Thirteen times a century Mercury transits across the solar disk. (The next two transits will be in November 1986 and November 1999.)

Astronomers in the past attempted to draw sketch maps of albedo features, but the first detailed observations came during the late 1960s when radar signals were scattered from the planet [4-1]. Analysis of the radar return signals revealed a rough surface and led to the first correct determination of the rotation rate. Then in 1974 and 1975 NASA's Mariner 10 Spacecraft provided the first close look during its triple flyby encounter with the planet. Mariner 10 followed a trajectory from the Earth that allowed it to skim past Mercury March 29, 1974, then loop around the Sun making another rendezvous the following September, repeating the process for the final encounter March 16, 1975. (In the literature the three Mariner 10 encounters are designated Mercury I, II, and III.) Pictures from Mariner 10 showed a surface closely resembling that of the Moon. No atmosphere was found other than a minute amount of helium and a trace of hydrogen. A surprise was the discovery of an intrinsic planetary magnetic field. Figure 4-1 illustrates the Mariner 10 closest approach points for the three encounters [4-2].

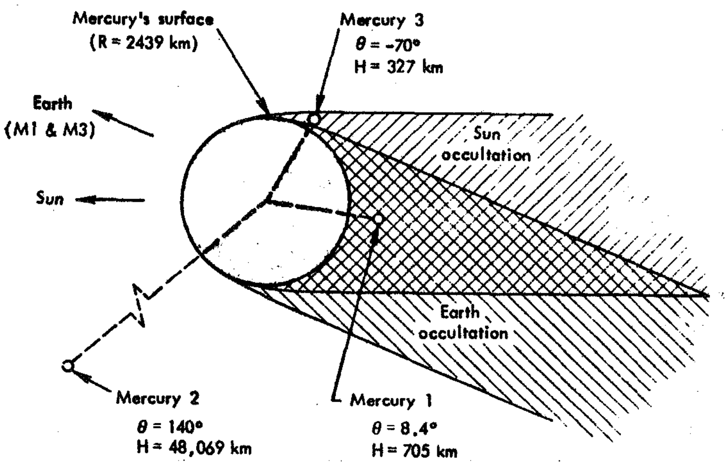

Figure 4-1. Mercury flyby points.

Because of its short orbital period, Mercury makes its closest approach to Earth (inferior conjunction) three times a year. The flexibility in trajectory and launch parameters allowed by the planet's orbit makes it an attractive planetary probe target in spite of communications problems posed by its small angular separation from the Sun, as viewed from the Earth and frequent solar occultations, as its orbit takes it behind the Sun. Important scientific questions abound that deal not only with the planet itself, but with the early history of the solar system, how the solar wind interacts with planetary magnetospheres, planetary magnetic dynamos, and many other matters of a fundamental nature.

4.2 DYNAMIC PROPERTIES

The dynamic properties of Mercury are given in Table 4-1.

TABLE 4-1. DYNAMIC PROPERTIES [4-3]

Parameter	Value	Comments
Semi-major axis	5.79×10^7 km	0.3871 AU
Perihelion distance	4.60×10^7 km	0.3075 AU
Aphelion distance	6.98×10^7 km	0.4667 AU
Eccentricity	0.20563	
Orbit inclination	7.004 deg	
Mean orbital velocity	47.87 km sec^{-1}	
Sidereal year	87.969 days	
Sidereal day	58.646 ± 0.0005 days	[4-4]
Synodic period	115.88 days	time between inferior conjunctions
Maximum angle from Earth-Sun line	28 deg	
Obliquity of rotation axis	within 1 deg of normal to orbit plane	[4-4]
Earth-Mercury distance		
Maximum	20.25×10^7 km	
Minimum	8.94×10^7 km	

4.2.1 Comments

Prior to ground-based radar observations made in the late 1960s, astronomers believed that Mercury always kept the same face toward the Sun. However, radar scattering data revealed that the planet turns on its axis with a period of 58.65 days. This measurement was refined by analysis of the Mariner 10 pictures, which also enabled the obliquity of the rotation axis to be determined. It was found to be within 1 deg of normal to the planet's orbit plane [4-4]. The rotational period is exactly two-thirds of the orbital period – at least within one part in 10^4. This relationship arises from a resonance which, in the case of Mercury, should be stable [4-5].

The eccentricity of Mercury's orbit (0.205) and the orbital inclination (7 deg) are both the largest for any planet except for Pluto. The peculiarity of the orbit has led to a number of analyses of its ultimate stability and to speculations about its origin [4-6]. Mercury's distance to the Sun varies between 46 and 70 million kilometers. If the planet had an atmosphere this would lead to very large seasonal changes caused by variation in solar radiation flux.

Precise observations over many decades have shown that the longitude of perihelion passage is precessing by about 45 sec of arc per century more than can be accounted for classically, taking into account the perturbing effects of all the other planets. This precession was predicted by Einstein's General Theory of Relativity and is an important piece of confirming evidence for that theory.

4.3 PHYSICAL DATA

4.3.1 Mass, Figure, and Other Physical Properties

Table 4-2 summarizes Mercury's physical data.

TABLE 4-2. PHYSICAL DATA [4-3]

Parameter	Value	Comments
Radius (mean equatorial)	2439 km	0.38 Earth
Mass	3.302×10^{23} kg	0.055 Earth
Mean Density	5.44 g cm^{-3}	Earth = 5.52 Mars = 3.98 Moon = 3.34
Gravity at surface	370 cm sec^{-2}	Earth = 980 Mars = 372 Moon - 162
Escape velocity	4.25 km sec^{-1}	Earth = 11.2
(Solar mass)/(Mass of planet)	6023700 ± 300	[4-7]
GM	22031.8 ± 1.0 km^3 sec^{-2}	[4-7]
J_2	$(8 \pm 6) \times 10^{-5}$	[4-7]
Magnetic dipole moment	5×10^{22} G cm^3	see text
Normal albedo	0.125	average over visible
Surface temperature extremes	-173°C to 427°C	
Surface atmospheric pressure	$<2 \times 10^{-10}$ mbar	[4-8]
Flux of Solar Radiation	14490 W m^{-2} (perihelion) 6290 W m^{-2} (aphelion)	

4.3.2 Comments

The large mean density of Mercury is striking considering the small size of the planet and the fact that it more closely resembles the Moon and other satellites than it does the other planets. The implication is that it possesses an anomalously large concentration of iron, very likely in the form of a differentiated core some 70 to 75 percent of the total radius. The composition of Mercury is a matter of great interest to planetologists because of what it may reveal about the origin and early history of the solar system. (It is interesting that the surface gravity of Mercury and Mars are nearly equal because of Mercury's larger density and smaller radius.)

4.3.3 Mapping

Antoniadi and other astronomers sketched maps of the light and dark areas on the planet's surface from visual observations.[1] Names suggested by Antoniadi have been retained by the International Astronomical Union (IAU) for albedo features [4-2]. The relationship between albedo variations and surface topography as shown by Mariner 10 pictures is different for Mercury than for the Moon, where dark areas correspond to the Maria. On Mercury no great albedo difference exists between cratered terrain and plains; regions of high albedo appear to correspond to ray systems.

Many of the large craters have been given names – usually famous authors, artists, and musicians (Fig. 4-2) [4-2].

The prime meridian is defined by the IAU dynamically as containing the subsolar point at the first perihelion passage of 1950 (J.D. 2433292.63). However, the Mariner 10 system, tied to the planet's surface, takes the 20 deg longitude line as passing through a small crater designated Hun Kal. Davies and Batson [4-9] discuss this and point out that at present there is a discrepancy of about 0.49 deg (20 km) between the two systems.

4.3.4 Gravity Field

The gravity field of Mercury was estimated by Esposito, Anderson, and Ng [4-7] from Doppler and round-trip time delay radio data during the first and third Mariner 10 encounters with the planet. The results are far inferior to what could be obtained from an orbiter, but an estimate of J_2 was obtained:

$$J_2 = (8 \pm 6) \times 10^{-5} .$$

Terms in the spherical harmonic expansion through C_{22}, S_{22} were carried in the analysis, but reliable estimates could not be obtained. They remark that taking a few point masses, rather than higher order terms, dramatically reduced the Doppler residuals, suggesting that Mercury may possess local gravity anomalies analogous to the lunar mascons. More detailed information about Mercury's gravitational field would be extremely useful in studies of the interior structure of the planet – for example, to decide whether or not it has a differentiated core, as other evidence strongly suggests.

---

[1] It should be noted, however, that the features sketched by early astronomers bear little relationship to the albedo features now known.

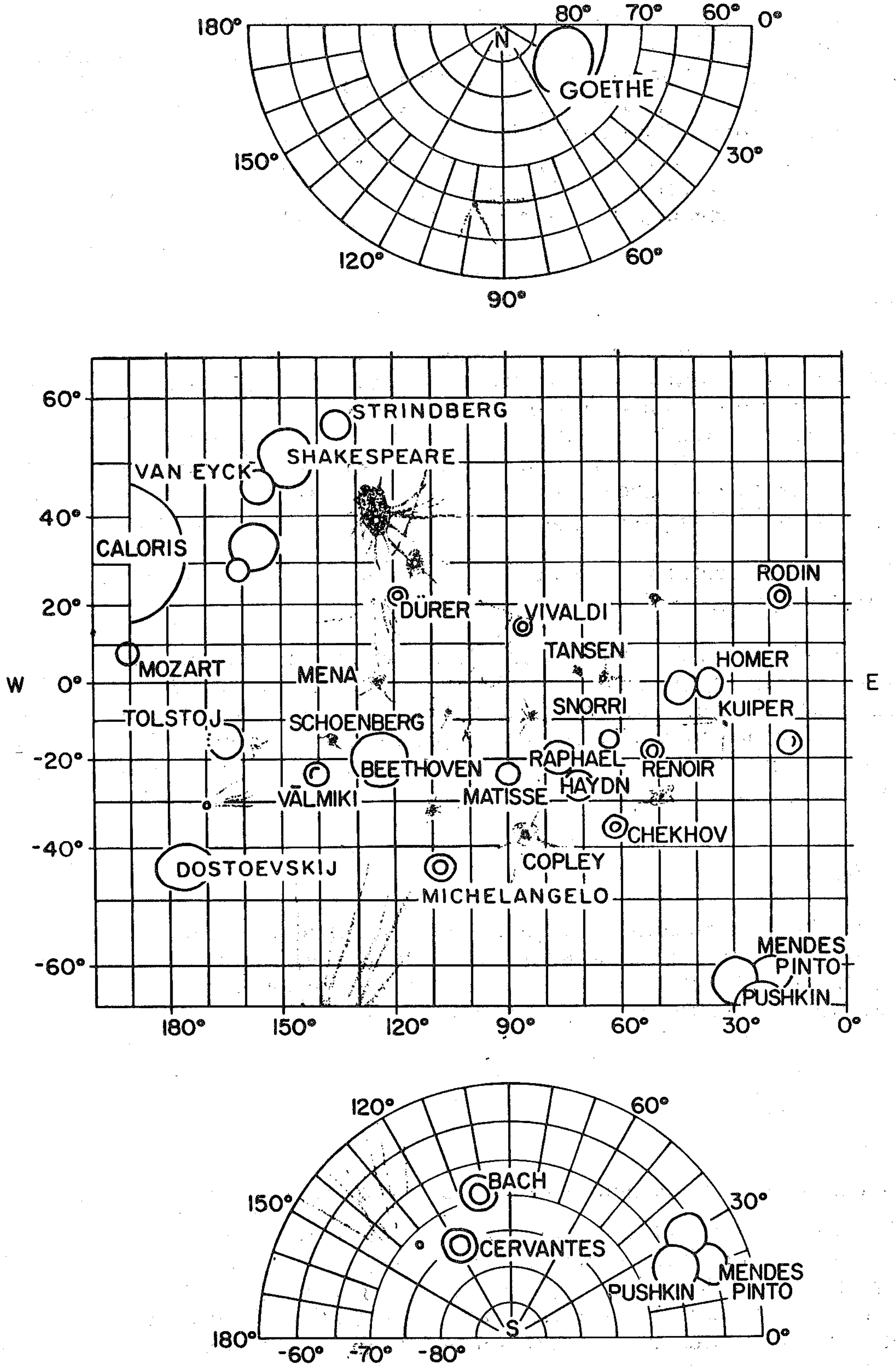

Figure 4-2. Basin and ray systems.

4.3.5 Magnetic Field

Mariner 10's discovery of a magnetic field intrinsic to the planet (that is, not induced by interaction with the solar wind) was unexpected [4-10]. The maximum field intensity measured (encounter Mercury III) was 400 gammas, a factor of 20 larger than the ambient solar field [4-11]. Estimates of the dipole intensity range from 2 to 6 × 10^{22} G cm^3 [4-12], depending upon assumptions regarding solar wind conditions at the time of the Mariner 10 encounters. Two mechanisms have been suggested (1) a planetary dynamo produced by the core, assuming that it is fluid [4-13] or (2) a frozen-in crustal field, the remnant of an early dynamo or external field [4-14].

Attempts have been made to calculate quadrupole and octupole components from the data, but this analysis is still controversial [4-12]. The derived dipole has a strength about 5 × 10^{22} G cm^3, inclined about 11 deg to the axis of rotation, with the same polarity as the Earth's field [4-3].

4.4 INTERIOR

4.4.1 Core

Mercury's high density (5.44 g cm^{-3}) is similar to the Earth (5.52) and Venus (5.25), but considerably higher than other comparable bodies in the solar system, the Moon (3.34) and Mars (3.98). The implication is that the planet must be largely metallic with up to 70 percent of its mass in an iron-nickel core with overlying silicate mantle and crust. If fully differentiated, the core is estimated to extend to about 75 percent of the planetary radius or 42 percent of its volume [4-3]. The last figure is huge compared to values for the Earth (16 percent), Venus (12 percent), and other planets. Mercury's intrinsic magnetic field may imply a differentiated metallic core [4-15]. Mercury's assumed core is larger than the total volume of the Moon.

4.4.2 Mantle and Crust

Overlying the core, Mercury has a silicate mantle. The surface appears to be covered by a fine-grained fragmental layer quite similar to the Moon's regolith.

4.5 SURFACE

The results of the Mariner 10 imaging experiments were reported by Murray and others [4-16] and the planetological and geological implications have been extensively reviewed [4-3,4-17]. Here we attempt only to indicate a few of the major current ideas regarding Mercury's surface.

4.5.1 The Mariner 10 Imaging Experiments

During its three encounters, Mariner 10 collected more than 2700 pictures ranging in resolution from 4 km down to a best resolution of 100 m – approximately the same as the best resolution of the lunar surface obtainable with terrestrial telescopes. In all, about 45 percent of Mercury's surface was observed. Stereoscopic coverage was obtained for parts of the southern hemisphere. (The high-solar elevation angles for some of the imagery make analysis and interpretation of topography and morphology difficult.)

NASA's Atlas of Mercury [4-2] gives pictorial coverage and discussion. Figure 4-3, adapted from Reference 4-18, compares coverage and ground resolution for Mercury from Mariner 10 with the Moon and Mars.

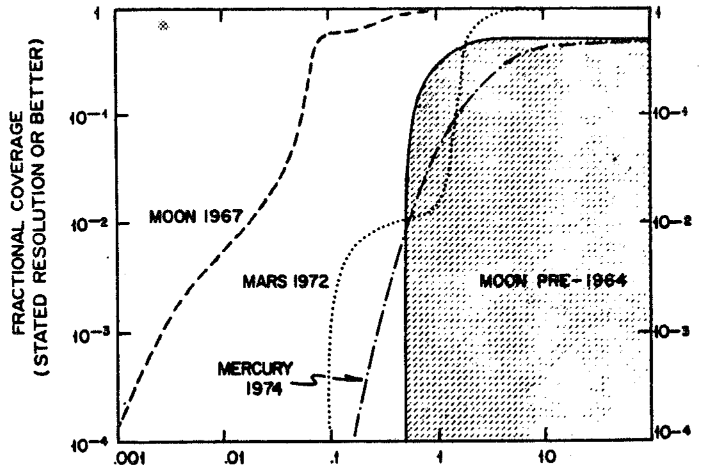

Figure 4-3. Ground resolution (km).

4.5.2 Surface Morphology

The appearance of Mercury is very similar to the Moon. Impact craters are numerous, with crater diameters covering a full spectrum from lunar-basin sizes like the Caloris Basin at 1300 km, down to the 100-m resolution limit of the imaging camera. There is no reason not to suspect a full range of small crater sizes as found on the Moon. The presence of a regolith (fine well-churned soil) shows that Mercury, like the Moon, has been bombarded by micrometeoroids throughout its history. In the absence of an atmosphere, micrometeoroids reach the surface, which they have gradually degraded and weathered. The degree of degradation covers a wide range and depends on the age of the crater and subsequent meteoric flux. But, in addition to weathered craters, many fresh sharp-rimmed craters are seen which still possess bright ray systems of ejecta, indicative of their relatively recent origin. A geologic map of Mercury was published by Trask and Guest [4-19].

Three main types of surface [4-17] are described in the following paragraphs.

4.5.2.1 Heavily Cratered Terrain

The heavily cratered terrain is made up of large craters (thirty to hundreds of kilometers in diameter) so closely packed together that they frequently overlap. Inside these craters are often found smooth plains that are only lightly cratered and, therefore, are considered to be younger than the intercrater plains surrounding the large craters. Heavily cratered terrain resembles the Lunar highlands.

4.5.2.2 Intercrater Plains

The intercrater plains surround and merge with the large craters of the heavily cratered terrain. These plains, which cover much of the planet, have rolling slopes and are densely covered with small craters (5 to 10 km) which frequently are elongated and occur in groups or chains and, therefore, are thought to be secondary in origin. The intercrater plains are generally thought to be among the oldest surface features on the planet since they apparently were formed at a period of high meteor flux. They do not appear to be derived from the ejecta of the major (basin-forming) meteor impacts, since Mercury, unlike the Moon, has relatively few large basins. They may have formed later from volcanic extrusions at a time between the formation of the heavily cratered terrain and the smooth plains. (It is, however, not known for certain that such a period of volcanic activity actually occurred.)

4.5.2.3 Smooth Plains

The smooth plains are relatively flat areas with little evidence of major cratering. They may, therefore, be among the youngest features on the planet's surface. They resemble the lunar Maria and have sinuous ridges similar to features seen both on the Moon and Mars. However, unlike the lunar Maria which contrasts distinctively with the highlands because of their lower albedo, the smooth plains are similar in brightness to both the heavily cratered terrain and the intercrater plains.

The smooth plains often exist within and about the Mercurian basins, such as Caloris and the various basins in the north polar region, and in the floors of other large craters. The smooth plain material is thought to be derived either from volcanic magma, impact ejecta, or from melt.

4.5.2.4 Other Surface Features: Chaotic Terrain and Lobate Scarps

At the antipodal point to the Caloris Basin, the largest impact structure seen on Mercury, is a particularly hummocky and disrupted region. Prominent hills and valleys are seen, with many broken crater rims. This region is generally interpreted as having been produced by seismic waves generated by the Caloris impact and focused at the antipodal region.

Widespread over Mercury's surface are series of lobate scarps thought to be thrust or high-angle reverse faults from a global crustal shortening. Their origin has been extensively discussed [4-20,4-21]. The accepted interpretation is that they are due to a combination of early tidal de-spinning of the planet and contraction associated with cooling of the planet's large core and thin mantle. (The thermal history of Mercury has been investigated by Toksoz, Hsui, and Johnston [4-22].)

4.5.2.5 Other Comments on Surface Characteristics [4-3]

a) The intercrater plains are the predominant surface feature, covering much of the planet so far surveyed.

b) Albedos of the younger plains and the older features are not greatly different. Only a slight correlation with surface morphology has been established.

c) The Mercurian craters do not expel ejecta blankets or secondary missiles to as great distances as on the Moon, since the surface gravity is stronger.

d) The widespread distribution of scarps seen on Mercury are not observed on the Moon.

4.5.2.6 Surface Feature Statistics

Strom [4-3] notes that the crater diameter/density distribution of craters in the Mercurean highlands is very similar to the distribution in the lunar highlands and the heavily cratered regions of Mars. For planning purposes, therefore, it would be reasonable to adopt for Mercury the statistical distributions for craters and blocks that have been proposed for the Moon for regions that appear similar.

One difference is that ejecta from Mercurean craters cover a smaller area than those from lunar craters, due to the larger gravity [4-23]. Similarly, for Mercury the areal density of secondary craters peaks closer to the primary crater than is the case for the Moon.

4.5.2.7 Volcanism

There is no present day volcanic activity. The absence of volatiles in the atmosphere can be cited, along with the lack of pictorial evidence from Mariner 10. Certain surface features have been interpreted as implying volcanism in the past [4-24], although the issue is still considered open [4-25].

4.5.2.8 Surface Chemistry

There is very little information available on the chemistry of Mercury's surface. McCord and Clark [4-26] detected the Fe^{++} ion from ground-based observations at 0.89 microns. (This is an example of the continuing importance of telescopic observations of the planet.) Although the surface appears similar to the Moon, color differences suggest differences in Fe and Ti abundances [4-27]. Requirements of vapor-phase deposition from micrometeoroid impacts sets the FeO content of the surface layer between 3 and 6 percent. The absence of argon in the atmosphere could be interpreted as indicating a deficiency of potassium in surface materials, since ^{40}Ar results from the radioactive decay of ^{40}K. Such a deficiency was predicted, but it is premature to set a definite limit [4-8].

4.5.2.9 Optical Properties

The optical properties of Mercury are given in Table 4-3.

Bright craters and their ray systems are bluer than their surroundings by about 12 percent.

Mercury spectral reflectance increases linearly from 330 to 1060 nm. (terrestrial observations); the reflectance spectra for Mercury closely resemble those for mature lunar soils [4-28].

TABLE 4-3. ALBEDO

Region	Typical Albedo at 486 nm [4-27]
Bright craters	0.35
Smooth plains	0.12
Intercrater plains	0.14
Hummocky plains	0.13
Bright rays	0.22
Flat bottom craters	0.15
Secondary crater fields	0.13
Normal albedo	0.125 [4-3]

The bolometric emissivity for the planet, assumed to be independent of wavelength and directionality, was reported by Hansen [4-29] to be 0.82 ± 0.06. (This determination was based on an ingenious application of ground-based observations.)

4.5.2.10 Thermal Properties: Temperatures

At the equator near local midnight, a minimum temperature of 100°K was measured by the Mariner 10 infrared radiometer. At the subsolar point near perihelion the temperature reaches about 700°K, in excess of the melting point of lead. Because of the peculiar rotational and orbital relations, together with the large orbital eccentricity, mid-day lasts significantly longer at 0 to 180 deg longitudes, than at the 90 and 270 deg longitudes. Hence, at low latitudes, mean temperature and temperature extremes vary with longitude. The surface temperature at the poles remains well below 0°C [4-30]. A typical thermal inertia, $(k\rho c)^{-\frac{1}{2}}$, was found to be

$$600 \text{ cm}^2 \text{ s}^{\frac{1}{2}} \text{ K/cal}$$

from the cooling curve. Areas were found where this parameter is as much as twice the quoted value. Strom [4-3] interprets these findings as consistent with a layer of insulating silicate dust similar to the lunar regolith, with large-scale regions that are more compacted, or where rock outcrops or boulders are not blanketed by dust. The thermal surface properties closely resemble those of the Moon suggesting similar soil properties [4-31].

4.6 ATMOSPHERE

Prior to Mariner 10, although ground-based observations had failed to detect an atmosphere for Mercury, a surface pressure of as much as 0.1 mbar could not be ruled out. The pressure is now known to be at least nine orders of magnitude less than that. Mariner 10 carried two spectrometric instruments, one for remote atmospheric sensing of radiation below 95 nm during solar eclipse by the planet and the other for observation of emissions at discrete locations in the spectrum [4-32]. The result was that He and H, and probably O, were detected. For other gases that were not detected, upper limits were estimated. Even at the surface gas molecules very rarely collide, so the Mercurean "atmosphere" is really an exosphere. It is not possible or useful to compute model atmospheres for the planet.

4.6.1 Pressure

The total pressure at the surface was determined to be less than 2×10^{-10} mbar.

4.6.2 Composition

Only helium and hydrogen (and O with less certainty) were detected directly. No volatiles were detected, nor was argon, a popular candidate because of its generation by radioactive decay of ^{40}K. (Review the discussion in Reference 4-8.) Upper limits were estimated for Ne, Ar, Xe, H_2, C, CO_2, and H_2O. Possible constituents and partial pressures at the subsolar point [4-33] are given in Table 4-4.

TABLE 4-4. ATMOSPHERIC PARAMETERS

Possible Constituent	Subsolar Point Density (atoms/cm^3)	Partial Pressure (mbar)
He	4500	5×10^{-13}
H	8 (thermal component) 82 (non-thermal component)	
Ne		$< 1.2 \times 10^{-10}$
Ar		$< 6.9 \times 10^{-11}$
O		$< 5.6 \times 10^{-13}$
C		$< 1.5 \times 10^{-14}$

No measurable absorption was obtained in the 30 to 95 nm wavelength region for sunlight when Mariner 10 passed into the umbra of the planet. Most gases have large absorption cross-sections in this region and, thus, limits can be placed on the densities of many gases of interest near the surface. He, Ar, O, CO_2, H_2O, O_2, N_2, and H_2 densities at 8-km altitude are all set at less than 2 to 4×10^{-7} molecules/cm^3 [4-33].

4.6.3 Origin

Helium atoms escape thermally from the planet and must, therefore, be made up either by accretion from the solar wind or through radioactive decay of uranium and thorium in the crust.

Hydrogen may be supplied from outgassing of the crust in the form of water vapor or hydrocarbons, or from the solar wind. A likely mechanism is photodissociation of H_2O (concentration below the detectability threshold). The source of the assumed H_2O vapor could be outgassing, interaction of solar wind protons with the soil, or meteoroid flux [4-8].

4.7 IONOSPHERE

No ionosphere was detected by Mariner 10 radio occultation experiments [4-34]. Upper limits:

4000 electrons/cm^3 nightside

1500 electrons/cm^3 dayside.

(The difference is due to h-f signal fluctuations probably not planet-related.)

4.8 MAGNETOSPHERE

Experiments aboard Mariner 10 showed the existence of a planetary magnetic field; a permanent magnetic dipole about 0.06 percent of the terrestrial strength [4-13]. Though weak, this field is sufficient to give rise to a magnetosphere. The plasma science experiment, along with the magnetometer, identified a magnetopause, magnetosheath, and bow-shock associated with the magnetosphere (Fig. 4-4 [4-3]). The presence of a magnetotail is generally accepted, although Mariner 10's trajectory did not allow it to collect data in this region. Time-dependent processes similar to the magnetospheric substorms on Earth may have been observed [4-35].

The magnetosphere of Mercury is relatively much smaller than Earth's and only extends to about 1.5 planetary radii whereas the terrestrial magnetosphere extends to over 10 Earth radii. Moreover, the size and shape of the magnetosphere were found to vary markedly with the flux of incident solar wind. The magnetosphere may even be compressed to the surface at the planet at times [4-12]. The weakness of the magnetosphere and the ease with which it distorts rule out trapped particle regions such as Earth's Van Allen Belts.

4.9 SPACE IN THE VICINITY OF MERCURY – FIELDS AND FLUXES

A. Solar radiative flux

Mean solar flux at 0.38 AU: 9260. W m^{-2}.

NOTE: Except in the visible, solar fluxes are highly variable [4-36,4-37].

B. Solar magnetic field

Twenty to sixty gammas at Mercury orbit during Mariner 10 encounters [4-12].

C. Solar wind (typical values)

velocity	550 km/sec	
density	14 particles cm^{-3}	(Mercury I [4-12])

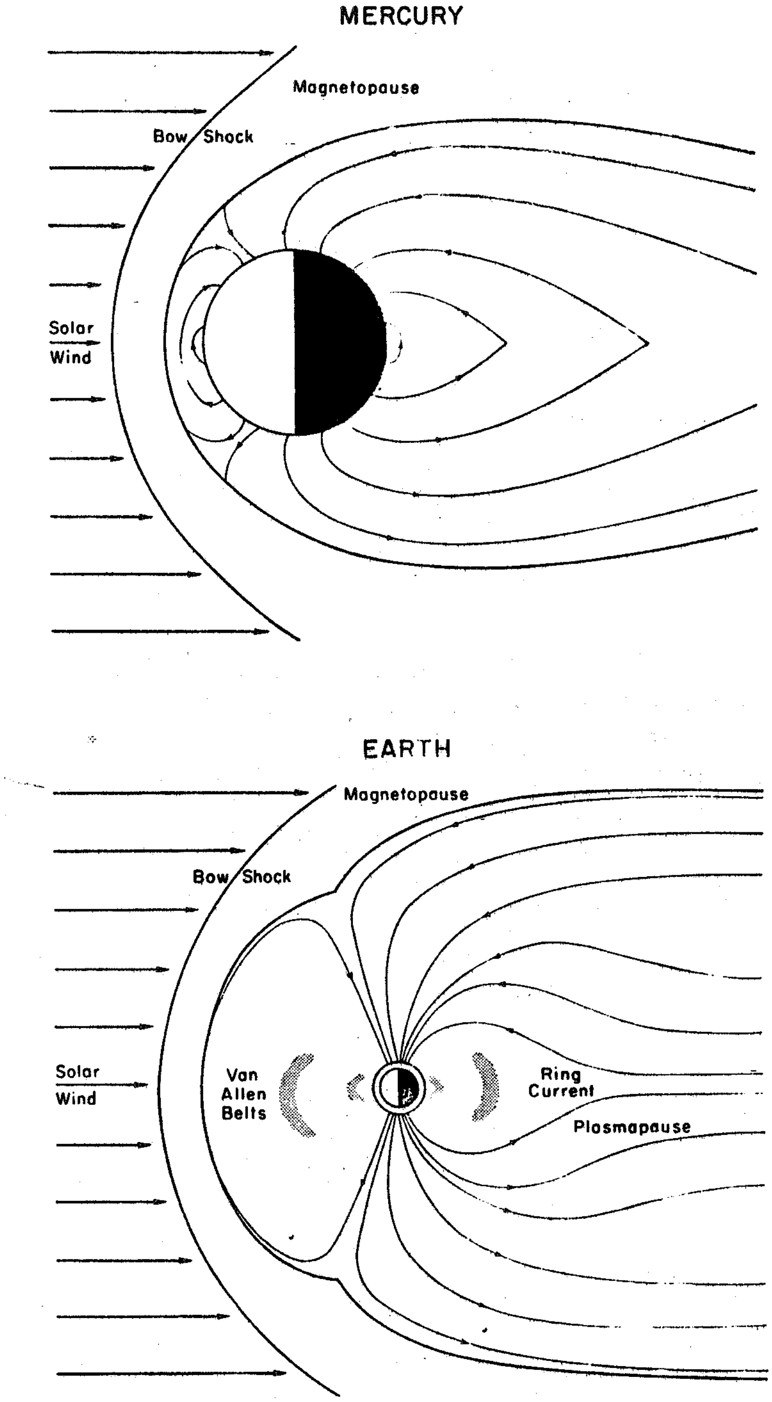

Figure 4-4. Comparison of the magnetic fields of Mercury and Earth [4-3].

REFERENCES

4-1. Goldstein, R. M.: Radar Observations of Mercury. Astron. J., vol. 76, 1971, pp. 1152-1154.

4-2. Davies, M. E., Dwornik, S. E., Gault, D. E., and Strom, R. G.: Atlas of Mercury. NASA SP-423, 1978.

4-3. Strom, R. G.: Mercury: A Post-Mariner 10 Assessment. Space Sci. Rev., vol. 24, 1979, pp. 3-79.

4-4. Klaasen, K. P.: Mercury's Rotation Axis and Period. ICARUS, vol. 28, 1976, pp. 469-478.

4-5. Goldreich, P. and Peak, S. L.: The Dynamics of Planetary Rotations. Ann. Rev. Astron. Astrophys., vol. 6, 1968, pp. 287-320.

4-6. Van Flandern, T. C. and Harrington, R. S.: A Dynamical Investigation of the Conjecture That Mercury is an Escaped Satellite of Venus. ICARUS, vol. 28, 1976, pp. 435-440.

4-7. Esposito, P. B., Anderson, J. D., and Ng, A. T. Y.: Experimental Determination of Mercury's Mass and Oblateness. COSPAR Space Res., vol. 17, 1977, pp. 638-644.

4-8. Kumar, S.: Mercury's Atmosphere: A Perspective After Mariner 10. ICARUS, vol. 28, 1976, pp. 579-591.

4-9. Davies, M. E. and Batson, R. M.: Surface Coordinates and Cartography of Mercury. J. Geophys. Res., vol. 80, 1975, pp. 2417-2430.

4-10. Herbert, F., Wiskerchen, M., Sonett, C. P., and Chao, J. K.: Solar Wind Induction in Mercury: Constraints on the Formation of a Magnetosphere. ICARUS, vol. 28, 1976, pp. 489-500.

4-11. Ness, N. F., Behannon, K. W., Lepping, R. P., and Whang, Y. C.: Observations of Mercury's Magnetic Field. ICARUS vol. 28, 1976, pp. 479-488.

4-12. Russell, C. T.: Planetary Magnetism. Rev. Geophys. and Space Phys., vol. 18, 1980, pp. 77-106.

4-13. Gubbins, D.: Speculations on the Origin of the Magnetic Field of Mercury. ICARUS, vol. 30, 1977, pp. 186-191.

4-14. Stephenson, A.: Crustal Remnance and the Magnetic Moment of Mercury. Earth Planet. Sci. Lett., vol. 28, 1976, pp. 454-458.

4-15. Solomon, S. C.: Some Aspects of Core Formation in Mercury. ICARUS, vol. 28, 1976, pp. 509-521.

4-16. Murray, B. C., Belton, M. J. S., et al.: Mercury's Surface: Preliminary Description and Interpretation from Mariner 10 Pictures. Science, vol. 185, 1974, pp. 168-179.

4-17. Gault, D. E., Burns, T A., Cassen, P., and Strom, R. G.: Mercury. Ann. Rev. Astron. Astrophys., vol. 15, 1977, pp. 97-126.

4-18. Murray, B. C.: The Mariner 10 Pictures of Mercury: An Overview. J. Geophys. Res., vol. 80, 1975, pp. 2342-2356.

4-19. Trask, N. J., and Guest, J. E.: Preliminary Geologic Terrain Map of Mercury. J. Geophys. Res., vol. 80, 1975, pp. 2461-2477.

4-20. Melosh, H. J. and Dzurin, D.: Mercurian Global Tectonics: A Consequence of Tidal Despinning? ICARUS, vol. 35, 1978, pp. 227-236.

4-21. Peckmann, J. B. and Melosh, H. J.: Global Fracture Patterns of a Despun Planet: Application to Mercury. ICARUS, vol. 38, 1979, pp. 243-250.

4-22. Toksoz, M. N., Hsui, A. T., and Johnston, D. H.: Thermal Evolutions of the Terrestrial Planets. The Moon and the Planets, vol. 18, 1978, pp. 281-320.

4-23. Gault, D. C., Guest, J. E., et al.: Some Comparisons of Impact Craters on Mercury and the Moon. J. Geophys. Res., vol. 80, 1975, pp. 2446-2460.

4-24. Trask, N. J. and Strom, R. G.: Additional Evidence of Mercurian Volcanism. ICARUS, vol. 28, 1976, pp. 559-563.

4-25. Wilhelms, D. E.: Mercurian Volcanism Questioned. ICARUS, vol. 28, 1976, pp. 551-558.

4-26. McCord, T. B. and Clark, R. N., Jr.: The Mercury Soil: Presence of Fe^{++}. J. Geophys. Res., vol. 84, 1979, pp. 7664-7668.

4-27. Hapke, B., Danielson, G. E., Jr., Klaasen, K., and Wilson, L.: Photometric Observations of Mercury from Mariner 10. J. Geophys. Res., vol. 80, 1975, pp. 2431-2443.

4-28. Vilas, F., and McCord, T. B.: Mercury: Spectral Reflectance Measurements (0.33-1.06 microns) (1974/75). ICARUS, vol. 28, 1976, pp. 593-599.

4-29. Hansen, O. L.: Surface Temperature and Emissivity of Mercury. Astrophys. J., vol. 190, 1974, pp. 715-717.

4-30. Guest, J. E. and O'Donnell, W. P.: Surface History of Mercury: A Review. Vistas in Astronomy, vol. 20, 1977, pp. 273-300.

4-31. Chase, S. C., Jr., Miner, E. D., Morrison, D., Münch, G., and Neugebauer, G.: Mariner 10 Infrared Radiometer Results: Temperatures and Thermal Properties of the Surface of Mercury. ICARUS, vol. 28, 1976, pp. 565-578.

4-32. Broadfoot, A. L., Shemansky, D. E., and Kumar, S.: Mariner 10: Mercury Atmosphere. Geophys. Res. Lett., vol. 3, 1976, pp. 577-580.

4-33. Broadfoot, A. L.: Ultraviolet Spectrometry of the Inner Solar System from Mariner 10. Rev. Geophys. and Space Phys., vol. 14, 1976, pp. 625-627.

4-34. Howard, H. T., Tyler, G. L., et al.: Mercury: Results on Mass, Radius, Ionosphere and Atmosphere from Mariner 10 Dual-Frequency Radio Signals. Science, vol. 185, 1974, pp. 179-180.

4-35. Siscoe, G. L , Ness, N. F., and Yeates, C. M.: Substorms on Mercury? J. Geophys. Res., vol. 80, 1975, pp. 4359-4363.

4-36. Burlega, L. F.: Magnetic Fields, Plasmas and Coronal Holes: The Inner Solar System. Space Sci. Rev., vol. 23, 1979, pp. 201-216.

4-37. White, O. R. (ed.): The Solar Output and Its Variation. Colorado Assoc. Univ. Press, Boulder, CO, 1977.

SECTION 5. VENUS

5.1 INTRODUCTION

The second planet out from the Sun is Venus, named after the Roman goddess of love and beauty. Venus is similar to the Earth in size and density, but there the similarity stops. It rotates extremely slowly in the retrograde direction, one revolution in 243 days. A thick atmosphere, largely carbon dioxide, blankets the planet. The surface atmospheric pressure is 90 times that of the Earth and the temperature exceeds 700°K. Because of uninterrupted cloud cover the surface can only be "seen" by using radio wavelengths in which the clouds are not opaque.

From the Earth, Venus appears through a telescope to be a bright object, essentially featureless in visible light, with a slightly yellowish color. Infrared observations also fail to reveal features, but in the ultraviolet, dark markings, often of a characteristic horizontal Y shape, appear in the clouds that enshroud the planet (Fig. 5-12).

Venus is often called the morning or evening star, since when it is prominent in the sky it is always seen near the rising or setting Sun. It is the third brightest object in the sky, behind the Sun and the Moon, attaining a visible magnitude of -4.3. Observed from the Earth, Venus occasionally transits across the face of the Sun, though less frequently than Mercury. The last transits were in 1874 and 1882, and the next will be June 7, 2004, and June 5, 2012.

Venus has recently been the destination of a number of planetary probes. The U.S.S.R. has concentrated its planetary program on Venus; between 1965 and 1979 12 Venera spacecraft impacted, soft-landed, or flew by the planet. The U.S. program has included flybys in 1962 by Mariner 2, in 1967 by Mariner 5, in 1974 by Mariner 10 and, most recently, the extremely successful Pioneer Venus Project.

Pioneer Venus consisted of two spacecraft, the Orbiter and the Multiprobe. Both were launched in the summer of 1978 and reached the planet in December, 1978. The Orbiter was placed in a highly eccentric orbit about the planet. Perigee altitude was initially controlled to stay within the upper atmosphere, at 160 km, with apoapsis 66,900 km, period 24.03 hr. Perigee control was halted during the summer of 1980, retaining sufficient propellant to allow attitude control for many more years. (Data continues to be received from the Orbiter.) Solar perturbations will eventually cause perigee to increase to a maximum of about 2200 km in 1986, with corresponding decrease in apogee. Then the perigee will begin to decrease and, eventually, in 1992, the Orbiter will burn up in the venusian atmosphere [5-1].

The Multiprobe consisted of a main bus similar to the Orbiter, together with four separate entry probes: the large Sounder Probe and three other identical small probes (North Probe, Day Probe, and Night Probe). All of these vehicles entered the atmosphere of Venus on December 9, 1978. The four probes entered first, staggered over a 10-min interval; followed by the bus entry 90 min later. The small probes, falling freely, reached the surface at different locations; the bus burnt up at about 110 km. The probes transmitted information for about 55 min until impact, except for blackouts lasting about 1 min. The Day Probe survived for 67 min after impact. Figure 5-1 shows the locations of the probe landing points in the IAU coordinate system [5-1]. The landing points for various Venera missions are also shown, along with tics at the top that indicate the longitudes of the subsolar points at the

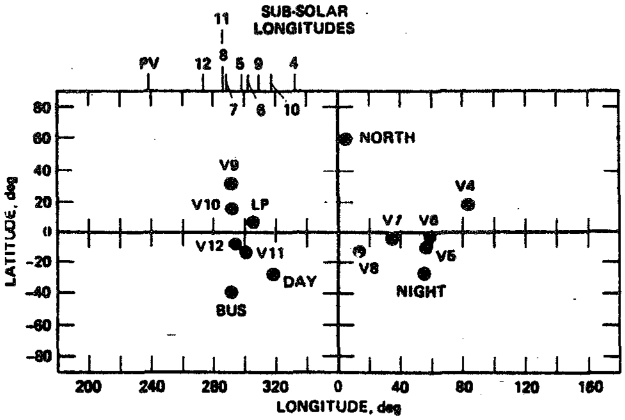

Figure 5-1. Venus landing coordinates, IAU.

time of landings. The U.S.S.R. also took advantage of the 1978 launch opportunity, and the Venera 11 and 12 probes softlanded on Venus on December 25 and December 21, 1978.

5.1.1 General References

A. May and June, 1977, issues of Space Science Reviews [5-2,5-3] gave planning data for Pioneer Venus a year before launch.

B. Special issues of Science, February and July, 1979, gave preliminary results from Pioneer Venus [5-4,5-5].

C. The most comprehensive collection of papers on Pioneer Venus experimental results and their implications is in the special edition of the Journal of Geophysical Research [5-6]. This section draws heavily on this source.

D. U.S.S.R. Venera results are summarized by Marov [5-7]. Preliminary results for Venera 11 and 12 are given in COSPAR 1980 [5-8]. A comprehensive account of Russian and U.S. results through 1979 and most of 1980 appears in the review by Moroz [5-9].

E. The recent Scientific American article "The Atmosphere of Venus" [5-10].

F. Venus, eds. D. M. Hunten, L. Colin, T. M. Donahue, and V. I. Moroz, University of Arizona Press, Tucson (expected publication date: late 1982).

Other than for historical interest, much pre-Pioneer Venus information about Venus must be considered obsolete. Exceptions are orbital data, Earth-based radar imaging, and some photometric and spectroscopic measurements.

5.2 DYNAMIC PROPERTIES

The dynamic properties of Venus are given in Table 5-1.

TABLE 5-1. DYNAMIC PROPERTIES [5-1,5-11,5-12,5-13,5-14]

Semi-major axis	1.082×10^8 km (0.7233AU)
Perihelion Distance	1.075×10^8 km (0.71844AU)
Aphelion Distance	1.089×10^8 km (0.72824AU)
Eccentricity	0.0068
Inclination of orbit	3.393 deg
Mean Orbital Velocity:	
Linear	35.01 km $\sec^{-1}$
Angular	1.602 deg day^{-1}
Sidereal Year	224.701 day
Sidereal Day	243.0 ± 0.1 day (retrograde)
Local (Solar) Day	116.75 days
Inclination of equator to the orbit	2.2 deg (cf. Earth 23.5 deg)
Synodic Year	583.92 days (time between inferior conjunctions)
Earth-Planet Distance:	
Maximum	2.5861×10^8 km (1.7292AU)
Minimum	0.4327×10^8 km (0.2893AU)

5.2.1 Comments

At closest approach, just over 43 million kilometers, Venus is our nearest planetary neighbor. Mars never comes closer then 56 million kilometers.

The spin-axis of the planet is very near perpendicular to its orbit plane, unlike the Earth. The spin-period, besides being very long, is retrograde (clockwise, looking down on the Solar System – in the opposite sense from the orbital motion). Venus' rotation is almost (but not quite) in resonance with the orbit of the Earth, so that nearly the same face is presented at each inferior conjunction.

Of the planets, Venus and Neptune have the most nearly circular orbits, with orbital eccentricies less than 0.01.

5.3 PHYSICAL DATA

Table 5-2 summarizes the physical data of Venus.

TABLE 5-2. PHYSICAL DATA [5-9,5-12,5-14,5-15]

Radius, equatorial	6051.3	(≅0.95 Earth)
Mass	4.870×10^{24} kg	(≅0.8150 Earth)
Mean Density	5.24 g cm^{-3}	(Earth ≅ 5.41)
Surface Gravity	887 cm sec^{-2}	(Earth = 980)
Escape Velocity at the Surface	10.4 km sec^{-1}	(Earth = 11.2)
Magnetic Dipole Moment	Probably zero	Paragraph 5.3.3
Albedo, Average Over the Visible Spectrum	0.80 ± 0.02	
Surface Atmospheric Pressure	93 ± 1.5 bar	(∿95 × Earth)
Surface Temperature	≅740°K	
Oblateness (J_2)	6×10^{-6}	(Earth = 1083×10^{-6})
Solar Flux	2620 ± 35 W m^{-2}	Range in orbit
Bond Albedo	0.75 ± 0.03	

5.3.1 Comments

The atmosphere of Venus is quite unlike the Earth's atmosphere. Its unusual properties are discussed at length in paragraph 5.6.

The limit quoted for Venus' magnetic dipole is a limit only and not to be construed to imply that Venus has any intrinsic magnetic moment [5-16].

A striking feature of the planet is its extreme sphericity.

An albedo of 0.75 is required for balance between absorbed and emitted energy and is thought to be acceptable within realistic error bounds.

5.3.2 Gravity Field

The global gravity field was estimated from long-term orbital perturbations of the Pioneer Venus Orbiter [5-17]. The oblateness ($J_2 = -C_{20}$) is estimated to be about 6×10^{-6}. Estimates of unnormalized coefficients to order and degree 6 are given in Table 5-3.

For any practical orbital calculations, only J_2 ($= -C_{20}$) and C_{22} would be used (paragraph 3.3.2).

TABLE 5-3. SIXTH-DEGREE AND SIXTH-ORDER UNNORMALIZED COEFFICIENT ESTIMATES AND THEIR UNCERTAINTIES [5-17]

l	m	C_{lm}	$\sigma_{C_{lm}}$	S_{lm}	$\sigma_{S_{lm}}$
2	0	−0.597*E*−5*	0.32*E*−5		
2	1	0.640*E*−8	0.11*E*−5	−0.299*E*−6	0.13*E*−5
2	2	−0.332*E*−6	0.81*E*−6	−0.174*E*−5	0.74*E*−6
3	0	0.779*E*−5	0.73*E*−5		
3	1	0.191*E*−5	0.26*E*−5	0.985*E*−6	0.24*E*−5
3	2	−0.175*E*−6	0.51*E*−6	0.438*E*−6	0.56*E*−6
3	3	−0.150*E*−7	0.15*E*−6	0.413*E*−7	0.13*E*−6
4	0	−0.165*E*−5	0.42*E*−5		
4	1	−0.198*E*−6	0.14*E*−5	0.127*E*−6	0.14*E*−5
4	2	0.421*E*−6	0.33*E*−6	0.220*E*−6	0.33*E*−6
4	3	−0.560*E*−7	0.54*E*−7	−0.234*E*−7	0.56*E*−7
4	4	−0.179*E*−7	0.15*E*−7	0.173*E*−8	0.14*E*−7
5	0	−0.691*E*−6	0.32*E*−5		
5	1	−0.379*E*−7	0.84*E*−6	0.404*E*−8	0.84*E*−6
5	2	0.156*E*−7	0.16*E*−6	0.925*E*−7	0.16*E*−6
5	3	0.115*E*−7	0.30*E*−7	−0.541*E*−8	0.29*E*−7
5	4	0.743*E*−8	0.52*E*−8	0.296*E*−8	0.54*E*−8
5	5	0.102*E*−8	0.13*E*−8	−0.163*E*−8	0.14*E*−8
6	0	−0.424*E*−6	0.24*E*−5		
6	1	−0.180*E*−7	0.54*E*−6	0.546*E*−8	0.54*E*−6
6	2	0.711*E*−8	0.85*E*−7	0.159*E*−7	0.85*E*−7
6	3	0.152*E*−9	0.14*E*−7	0.225*E*−8	0.14*E*−7
6	4	0.404*E*−11	0.33*E*−8	0.179*E*−8	0.23*E*−8
6	5	0.305*E*−10	0.41*E*−9	−0.138*E*−9	0.38*E*−9
6	6	−0.120*E*−9	0.91*E*−10	−0.109*E*−9	0.89*E*−10

* Read −0.597*E*−5 as -0.597×10^{-5}

5.3.3 Magnetic Field [5-16]

Venus lacks a dipole magnetic field that might be associated with a planetary dynamo. Reference 16 reports an upper limit for an intrinsic planetary dipole of 4.3×10^{16} G m^3, based on measurements made by the Pioneer Venus orbiter. The observations are consistent with zero intrinsic planetary moment.

5.3.4 Mapping of the Planet

The IAU has established a coordinate grid for Venus. By agreement, the IAU approve all feature names. The prime meridian is placed at the point that faces the Earth at inferior conjunction; the bright feature, the summit of Maxwell Montes, is at longitude 2.2 deg. Figure 5-2 shows a contour map of Venus with identification of the major named features [5-18].

5.4 INTERIOR

5.4.1 Core

Venus has a mean density similar to the Earth and Mercury. Its relatively high value leads to the expectation of a compacted core.

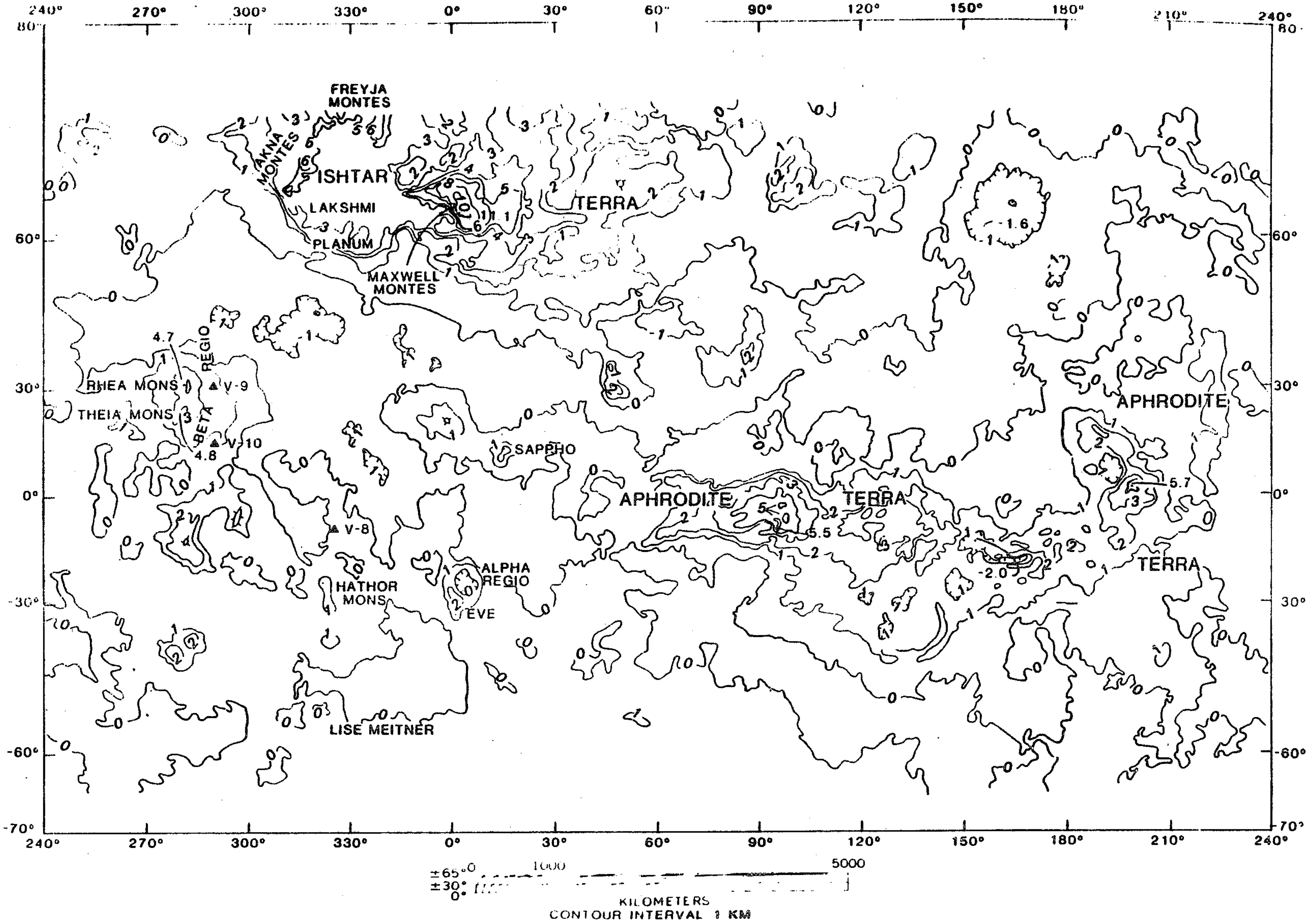

Figure 5-2. Contour map of Venus.

Generalized topographic map of Venus showing elevations of surface features. Contour interval is 1.0 km. The highest point is the summit of Maxwell Montes (11.1 km) [5-18].

Although the absence of a planetary magnetic field of interior origin counts against a liquid core, the near resonance between the spin and orbit of Venus and the Earth's orbit suggests that the frictional damping of a liquid core existed at some stage in the planet's history. Further evidence is the existence of basaltic rocks at the landing sites of some of the later Venera landers [5-7].

5.4.2 Crust and Mantle

The presence of basaltic rocks at some surface locations indicates that the outer layers of Venus at some time in the past underwent volcanic episodes.

Data from ground-based radar observations suggested an offset of the center-of-mass of Venus of as much as 1.5 km toward the Earth at inferior conjunction. However, analysis of Pioneer Venus data indicates less than a 0.5-km offset [5-15].

Many gravity anomalies have been noted although they are not nearly as large as those for the Moon or Mars. They correlate with topography [5-19] with important exceptions. The most prominent highland area, Ishtar Terra, does not show a corresponding gravity anomaly. Aphrodite Terra and Beta Regio, other highland regions, however, do correspond to gravity anomalies, suggesting basic differences between their geology and Ishtar's [5-18].

Some linear features have been interpreted as due to local or regional tectonic activity [5-15].

5.5 SURFACE PROPERTIES

Although the surface of Venus is obscured in visible, ultraviolet, and infrared wavelengths, the cloud layers are transparent at radio wavelengths and since 1961 many radar studies have been made [5-20]. The first spacecraft close-up radar observations were made by Venera 9 and 10 in 1975 [5-7], using a bistatic system. Since 1978 the Pioneer Venus Orbiter's monostatic radar imaging system has been in operation, returning altimetry and imaging data to the Earth [5-21]. Global topography of Venus has become available from PV Orbiter imaging data. The Goldstone terrestrial radar provides better imaging resolution (several tens of km), though limited coverage [18].

In situ measurements of venusian surface characteristics were made by Venera soft-landers. Venera 9 and 10 each sent back one TV picture (Fig. 5-5).

5.5.1 Surface Morphology

Venus has a flat surface compared to the Earth, the Moon, or Mars. Ninety percent of the surface lies within a height interval of 3 km. Extremes: the highest point, Maxwell Montes, is 11.1 km above the planetary datum; the lowest, a trench named Diana Chasma, is 2.0 km below datum. Total relief, 13 km, is two-thirds that on Earth (20 km). Venusian highlands are relatively small in area and low in elevation. The two major highland regions, Ishtar and Aphrodite Terrae, resemble continents on the Earth in area.

Analysis of the Pioneer Venus Orbiter radar data (wavelength: 17 cm) shows that the largest percentage of Venus' surface has meter-scale rms slopes in the range of 1 to 3 deg, much smoother than the Moon or Mars.

5.5.1.1 Rolling Plains Province

The rolling plains, the white areas in Figure 5-3, make up about 65 percent of the surface. They are at elevation 0 to 2 km above datum, with low slopes (1.5 to 3 deg), and a number of craters. Volcanic features appear to be present. The rolling plains may be an ancient surface that represents the original venusian crustal differentiate. Venera 8 obtained a "granitic" composition from gamma ray spectrometry data [5-7].

5.5.1.2 Highlands

The highlands make up less than 8 percent of the imaged surface of Venus, but their radar brightness and elevation are striking. They occur in three areas (1) Ishtar Terra, centered at latitude 65 deg N, longitude 350 deg; (2) Aphrodite Terra, on and south of the equator between longitude 60 and 205 deg; and (3) Beta Regio, between latitude 15 and 40 deg N and longitude 275 and 296 deg. Aphrodite is roughly the size of Africa; Ishtar the size of Australia. Ishtar contains the central mountainous area of Maxwell Montes.

Maxwell Montes is a very bright radar feature, implying very steep debris-laden slopes. There is no corresponding gravity anomaly, a condition that implies isostatic compensation. Maxwell may be more silicic than Beta, which is probably basaltic.

Complex terrain is found in the Eastern Ishtar Terra region, with ridges, troughs, and relatively less boulders and other debris than on Maxwell's slopes. Aphrodite Terra also shows complex topography and a bright radar return, though somewhat less pronounced than Maxwell.

Beta Regio is dominated by the irregular shield-shaped features Theia Mons and Rhea Mons, near which Venera 9 and 10 landed. These features are thought to be volcanic, and Beta may be one of the youngest volcanic regions on the planet.

5.5.1.3 Lowlands

The most extensive lowland basin on the planet is Atalanta Planitia, centered at latitude 65 deg N, longitude 165 deg. It is about the size of the Gulf of Mexico and is about 1.5 km below datum. It appears very smooth, like the lunar maria, and shows no apparent cratering. Thus, it may represent a basaltic lava flow. (Venera landers derived a basaltic composition for volcanic rocks near Beta, which lends credance to this hypothesis [5-7]).

5.5.1.4 Tectonic Features

A number of linear features have been observed, associated with Alpha Regio, Maxwell Montes, Beta Regio, and regions east of Ishtar and Aphrodite Terrae. Classed as ridge-and-trough systems, lineaments and scarps, it is possible to interpret them as tectonic faults. (The suggested tectonic activity is local or regional, not global.)

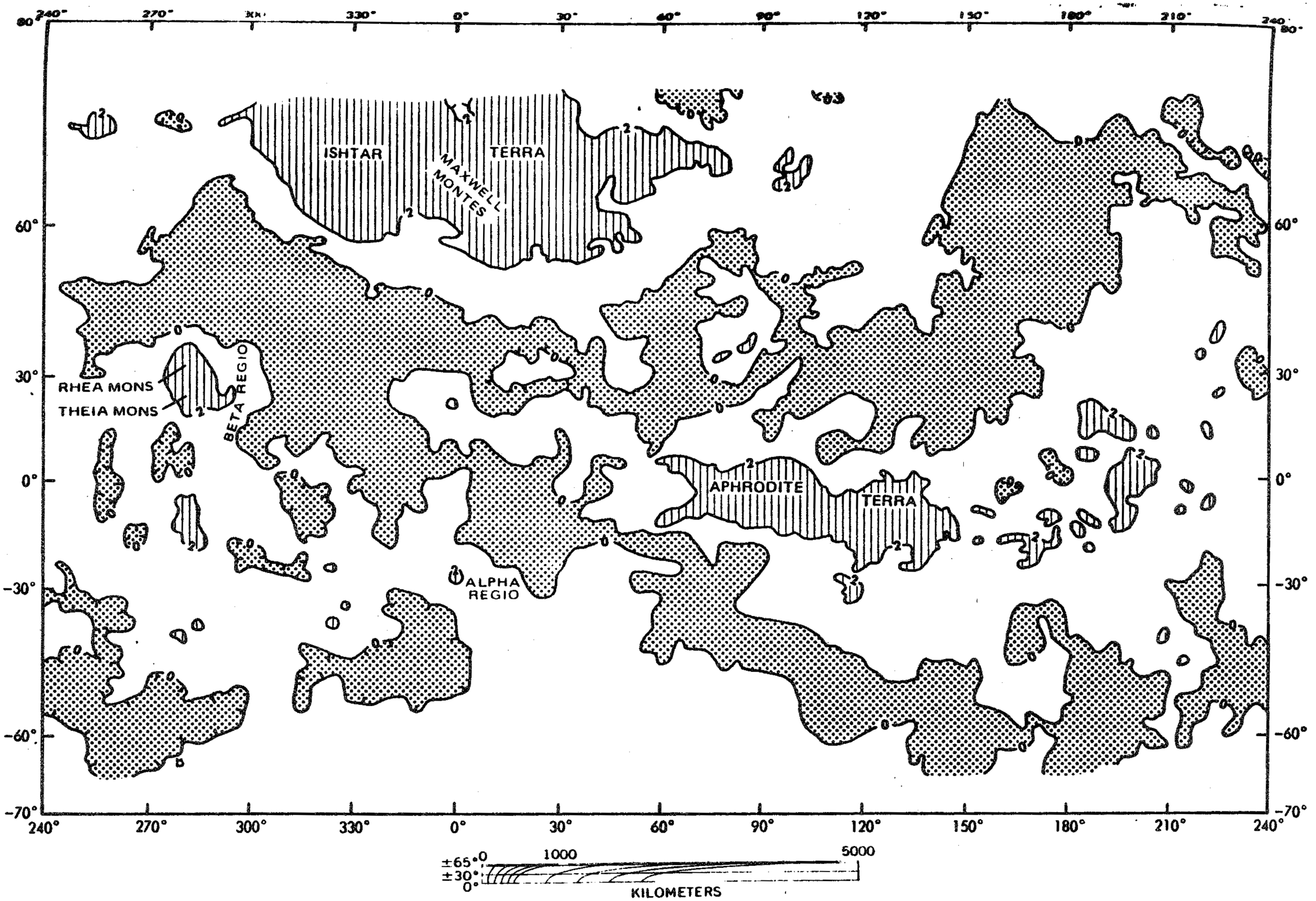

Figure 5-3. Venus topographic provinces.

Map showing distribution of topographic provinces on Venus: rolling plains (no pattern), 0(6051.0) to 2 km (6053.0); highlands (hatching), higher than 2 km (6053.0-6062.1); and lowlands (dotted pattern), lower than 0 km (6049.0-6051.0). The numbers in parentheses are planetary radii in kilometers [5-18].

5.5.1.5 Volcanic Features

The resolution available so far does not allow for positive distinction between volcanic and impact features. However, the morphology of regions such as Beta Regio and differences between crater densities and preservation in different regions indicates volcanic activity and, presumably, associated tectonic activity.

5.5.1.6 Craters

The smallest detectable crater is about 20 km in diameter. Crater statistics are given in Figure 5-4 [5-18].

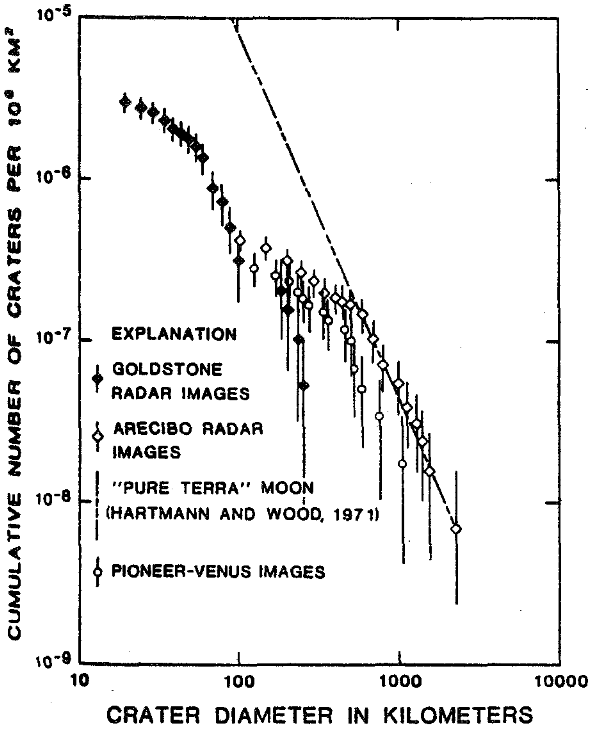

Figure 5-4. Venusian crater densities.

A tentative conclusion from the crater statistics is that the venusian surface is relatively young. However, better data await improved surface imaging resolution, either from a planetary orbiter or by using synthetic aperture radar from the Earth [5-15].

5.5.2 Surface Characteristics

In situ observations have only been made by the Venera soft-landers. The Venera TV pictures (Fig. 5-5) show a rocky desert-like terrain. Weathering appears to be extreme, presumably due to high-temperature sintering, corrosion, and aeolian processes. Wind velocities of up to several meters per second are plenty high enough to move surface material [5-22].

Figure 5-5. Phototelepanoramas of the Venus surface from Venera 9 (top) and Venera 10 (bottom) [5-7].

The Pioneer Venus Day Probe raised a dust cloud upon impact – it appeared to be composed of particles in the 10- to 100-micron diameter size range [5-23].

5.5.3 Chemical Composition – Mineralogy

Gamma-ray spectrometers on Venera 8, 9, and 10 landers measured the surface abundances of Uranium, Thorium, and Potassium (Table 5-4). The inference is that rocks at the Venera 8 landing site resemble terrestrial granites, while at Venera 9 and 10 sites basalts predominate.

TABLE 5-4. SURFACE ABUNDANCES OF U, Th, AND K [5-7]

	Uranium	Thorium	Potassium
Venera 8	2.2 ± 0.7 ppm	6.5 ± 2.0 ppm	4.9 ± 1.3 percent
Venera 9	0.5 ± 0.2 ppm	4.0 ± 0.25 ppm	0.9 ± 0.2 percent
Venera 10	0.7 ± 0.2 ppm	1.1 ± 0.2 ppm	0.3 ± 0.1 percent
Typical Terrestrial Rocks:			
Granite	9.04	21.9	3.24
Basalt	0.86	2.1	0.76

5.5.4 Physical Properties

The density of material at the Venera 10 site was determined to be about 2.7 g cm^{-3} for the top few decimeters. This value is about what would be expected for basaltic rocks and is not in conflict with estimates previously made from radar reflectivities [5-7].

5.6 ATMOSPHERE

Observations of Venus from the Earth show only the top of a thick cloud layer, whose nature was one of the key scientific questions leading to exploration of the planet. The extremely high-atmospheric temperature and pressure at the surface (740°K, 92 atm) and the fact that CO_2 is the major constituent, were known prior to Pioneer Venus. Terrestrial observations had led to the identification of cloud particles as micron-sized sulfuric acid droplets [5-24]. However, the Pioneer Venus mission produced many surprises. One was the discovery of solid crystals in the clouds in addition to sulfuric acid droplets. The structure of the lower atmosphere was studied by instruments carried on the probes, as well as indirectly from the Orbiter. The structure of the upper atmosphere was derived from the atmospheric drag on the Orbiter. This led to one of the most important and perplexing results to come out of the Pioneer Venus mission: the very low temperature, near 100°K, determined for the upper atmosphere on the nightside (Contrast the nightside exospheric temperature on the Earth of greater than 800°K.)

The three major altitude regions of the atmosphere of Venus will be discussed separately below. They are (1) the Lower Atmosphere, below 65 km, which includes the cloud layer from 25 to 65 km; (2) the Middle Atmosphere from 65 to 120 km; and (3) the Upper Atmosphere, above 120 km. The information reported was derived almost entirely from the Pioneer Venus mission. A recent general review can be found in Reference 10.

5.6.1 Lower Atmosphere

State properties of the Lower Atmosphere were measured by instruments carried on the four Probes and by Venera probes and landers. The information obtained is given in the following paragraphs.

Temperature and pressure data from the four probes were quite similar. Figure 5-6 [5-25] shows contrast between the probes (as compared to data from the Sounder Probe).

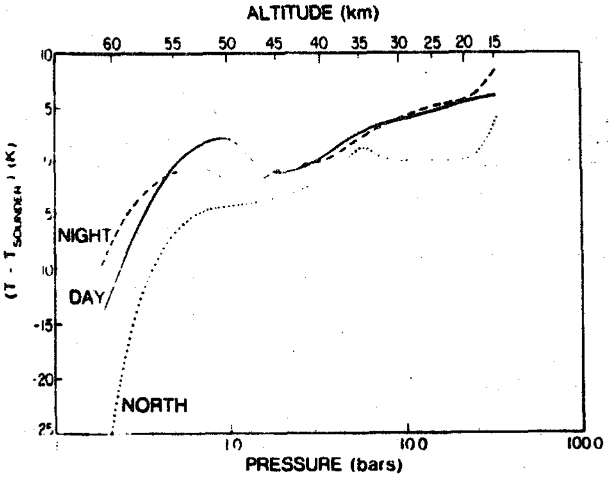

Figure 5-6. Temperature soundings of the Venus atmosphere. The altitude scale is for the Sounder Probe.

5.6.1.1 Models of the Lower Atmosphere

Table 5-5 contains thermodynamic properties of the lower atmosphere of Venus for latitudes <45 deg.

TABLE 5-5. THERMODYNAMIC PROPERTIES OF THE LOWER ATMOSPHERE (<45 deg) [5-9]

Altitude (km)[a]	Average model			Maximal model			Minimal model		
	T (K)	P (atm)	ρ (kg m^{-3})	T (K)	P (atm)	ρ (kg m^{-3})	T (K)	P (atm)	ρ (kg m^{-3})
−6	780			783			777		
−4	765	115.3	79.9	768	117.3	81.3	762	112.9	78.5
−2	750	102.0	72.1	753	104.2	73.4	747	99.8	70.8
0	735	90.0	64.8	738	92.0	66.1	732	89.0	63.7
2	720	79.2	58.3	723	81.0	59.4	717	77.4	57.3
4	705	69.6	52.3	708	71.2	53.3	702	67.9	51.3
6	689	60.9	46.8	692	62.3	47.7	686	59.4	45.6
8	674	53.2	41.8	678	54.4	42.6	670	51.8	41.0
10	658	46.2	37.3	661	47.4	38.0	655	45.1	36.5
12	642	40.1	33.1	645	41.1	33.8	639	39.1	32.4
14	626	34.7	29.4	629	35.6	30.0	623	33.7	28.8
16	609	29.9	26.0	612	30.6	26.5	606	29.0	25.4
18	593	25.6	22.9	596	26.3	23.4	590	24.9	22.4
20	576	21.9	20.1	579	22.5	20.6	573	21.1	19.6
22	560	18.6	17.6	563	19.1	18.0	557	18.0	17.2
24	543	15.7	15.4	546	16.2	15.7	540	15.2	15.0
26	526	13.3	13.4	529	13.6	13.7	523	12.3	13.0
28	509	11.1	11.6	512	11.4	11.8	506	10.7	11.2
30	492	9.23	9.95	495	9.54	10.2	489	8.92	9.67
32	476	7.63	8.51	479	7.90	8.73	473	7.36	8.24
34	460	6.27	7.23	463	6.49	7.44	457	6.04	7.01
36	444	5.12	6.11	447	5.31	6.29	441	4.92	5.92
38	428	4.15	5.13	431	4.31	5.29	425	3.99	4.96
40	413	3.34	4.28	416	3.47	4.42	410	3.20	4.14
42	400	2.67	3.53	403	2.78	3.65	397	2.55	3.40
44	387	2.11	2.89	390	2.21	2.99	[illegible]	2.02	2.79
46	374	1.66	2.36	378	1.74	2.43	370	1.59	2.27
48	361	1.30	1.91	368	1.36	1.96	355	1.23	1.84
50	347	1.00	1.53	357	1.06	1.57	340	9.45E-1	1.46
52	328	7.64E-1	1.24	338	8.11E-1	1.28	319	7.15E-1	1.19
54	308	5.73E-1	9.87E-1	319	6.14E-1	1.03	300	5.23E-1	9.43E-1
56	289	4.22E-1	7.75E-1	300	4.58E-1	8.11E-1	280	3.90E-1	7.36E-1
58	274	3.05E-1	5.91E-1	285	3.36E-1	6.23E-1	265	2.79E-1	5.58E-1
60	261	2.17E-1	4.41E-1	272	2.42E-1	4.70E-1	252	1.96E-1	4.12E-1
62	250	1.52E-1	3.23E-1	262	1.72E-1	3.50E-1	240	1.35E-1	2.98E-1
64	245	1.05E-1	2.29E-1	257	1.21E-1	2.50E-1	236	9.21E-2	2.08E-1
66	241	7.24E-2	1.58E-1	252	8.49E-2	1.79E-1	232	6.24E-2	1.43E-1
68	236	4.95E-2	1.11E-1	248	5.90E-2	1.25E-1	227	4.20E-2	9.79E-2
70	232	3.36E-2	7.68E-2	243	4.08E-2	8.91E-2	222	2.80E-2	6.69E-2
75	220	1.20E-2	2.90E-2	230	1.59E-2	3.52E-2	210	9.95E-3	2.41E-2
80	208	4.07E-3	1.03E-2	218	5.44E-3	1.32E-2	200	3.09E-3	8.19E-3
85	192	1.27E-3	3.50E-3	202	1.80E-3	4.71E-2	187	9.29E-4	2.63E-3
90	182	3.69E-4	1.07E-3	192	5.55E-4	1.53E-3	175	2.58E-4	7.84E-4
95	187	1.02E-4	3.03E-4	190	2.01E-4	4.53E-4	165	6.61E-5	2.11E-4
100	175	2.72E-5	8.25E-5	190	4.87E-4	1.35E-4	160	1.58E-5	5.26E-5

[a] Above reference level $R = 6052$ km.

5.6.1.2 Vertical Stability

Estimates of atmospheric vertical stability are difficult since they depend upon the z-derivative of the temperature. The atmosphere was found to be stably stratified for all altitudes down to about 28 km, except for a nearly adiabatic region in the clouds at 50 to 55 km. The lapse rate is nearly adiabatic again from 20 to 28 km, and the Pioneer Venus probes measured stable stratification again from 20 km down to 10 km. Their estimates do not extend below this level [5-25]. Venera 10 data confirm these findings and extend stability estimates down to the surface, showing a neutral stability layer below 5 km. Detailed information is given in Reference 5-25.

5.6.1.3 Chemical Composition

The mean molecular weight for all altitudes below 80 km is about 43.44 [5-26].

Gas chromatographic data on atmospheric composition were obtained at 51.6, 41.7, and 21.6 km altitudes. The data for 21.6 km are given in Table 5-6 [5-27].

TABLE 5-6. COMPOSITION OF ATMOSPHERE AT 21.6 km [5-27]

Gas	Volume Mixing Ratio (Percent)	Comments
CO_2	96.4 ± 1.0	
N_2	3.41 ± 0.01	
H_2O	0.135	Upper limit; the value is uncertain. H_2SO_4 in the clouds is a sink for H_2O [5-27].
O_2	$16.0 \pm 7.4 \times 10^{-4}$	This is the 41-km value (upper limit) [5-9].
Ar	$67.2 \pm 2.3 \times 10^{-4}$	Note isotope ratio in following table.
CO	$19.9 \pm 3.12 \times 10^{-4}$	Mixing ratio falls off rapidly with altitude.
Ne	$4.31 \pm 4 \times 10^{-4}$	
SO_2	$185\ (+350 - 155) \times 10^{-4}$	Only sulfur compound actually detected.

Using the mixing ratios measured directly, together with the assumption of equilibrium conditions, model curves were calculated for two values of water vapor as shown in Figure 5-7 [5-27].

Table 5-7 gives values for atmospheric constituents based on Venera and earlier spectroscopic data [5-28,5-29].

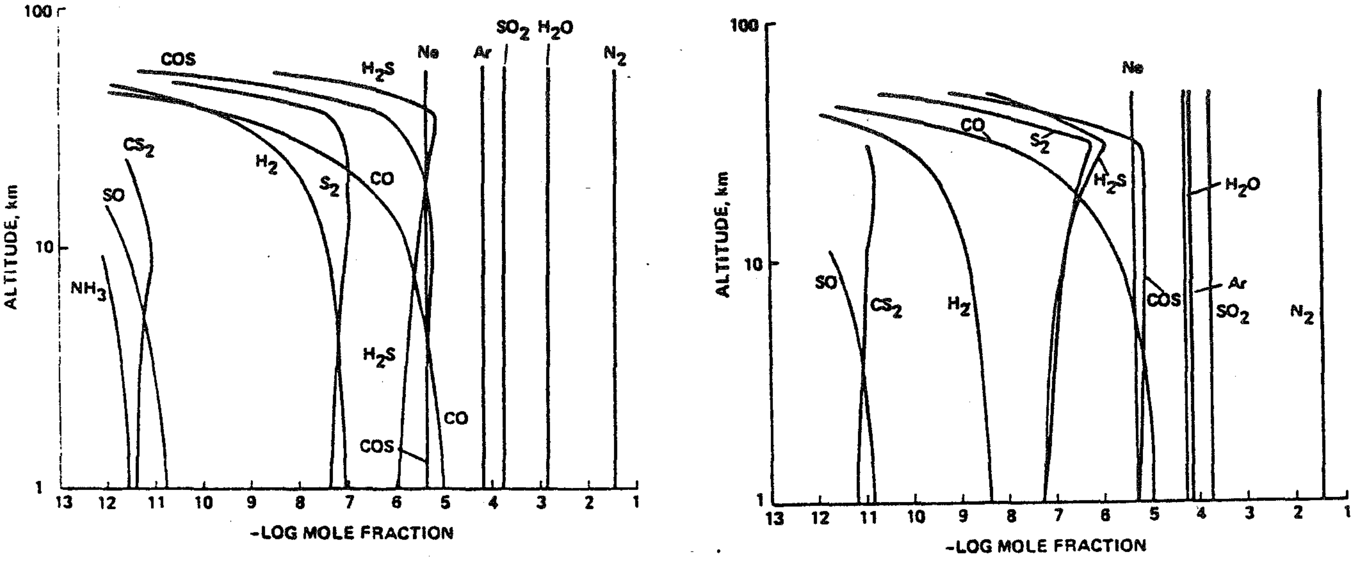

(a)

(b)

Figure 5-7. Models of the composition of the Venus atmosphere as a function of altitude. (a) Water = 0.135 percent (one observation by Pioneer Venus) and (b) water = 50 ppm (reported Venera value).

TABLE 5-7. ATMOSPHERIC COMPOSITION BASED ON VENERA AND EARLIER DATA [5-28]

Gas	CO_2	N_2	SO_2	H_2O	S_2	HCl	HF	CO	COS	H_2S	H_2
Mixing Ratio	0.96	$3.4 \cdot 10^{-2}$	$1.3 \cdot 10^{-4}$	$2 \cdot 10^{-4}$	$1 \cdot 10^{-7}$	$1 \cdot 10^{-6}$	$1 \cdot 10^{-8}$	$1.5 \cdot 10^{-5}$	$2 \cdot 10^{-5}$	$3 \cdot 10^{-7}$	$2 \cdot 10^{-8}$

The Neutral Mass Spectrometer on the Pioneer Venus Sounder Probe provided independent data on mixing ratios for minor constituents. Agreement was found with the Gas Chromatograph data except for possible discrepancies for water vapor. Upper limits were put on the carbonyl sulfide (COS) and sulfur dioxide (SO_2) mixing ratios, data of importance in atmospheric chemistry [5-30].

		Mixing Ratio, ppm
SO_2	55 km	< 10
	below 24 km	<300
COS	above 24 km	< 3
	below 24 km	<500

5.6.1.4 Isotopic Composition [5-30]

A comparison of the isotopic ratios of some gases in the Venus atmosphere to the Earth's atmosphere is presented in Table 5-8.

TABLE 5-8. ISOTOPIC RATIOS OF SOME SUBSTANCES FOUND IN THE VENUS ATMOSPHERE

Gas	Venus Atmosphere Isotopic Ratio	Earth Atmosphere Isotopic Ratio
$^{3}He/^{4}He$	$<3 \times 10^{-4}$	1.4×10^{-6}
$^{22}Ne/^{20}Ne$	0.07 ± 0.02	0.097
$^{20}Ne/^{36}Ar$	0.3 ± 0.2	0.58
$^{38}Ar/^{36}Ar$	0.18 ± 0.02	0.187
$^{40}Ar/^{36}Ar$	1.03 ± 0.04	296
$^{13}C/^{12}C$	$\leq 1.19 \times 10^{-2}$	1.11×10^{-2}
$^{18}O/^{16}O$	$2.0 \pm 0.1 \times 10^{-3}$	2.04×10^{-3}

The neon isotopic ratio, $^{22}Ne/^{20}Ne$, is about 25 percent lower than the value for the Earth, but is close to that of the solar wind.

The major Venus-Earth difference is for the argon isotopes, ^{40}Ar, which is radiogenic (from ^{40}K decay), and ^{36}Ar, which is non-radiogenic. Allowing for the differences in total atmospheric mass, the quantity of radiogenic argon in the Venus atmosphere is about one-third that of the Earth, while the Venus atmosphere contains about twice as much non-radiogenic argon as the Earth.

5.6.1.5 Winds in the Lower Atmosphere

The zonal winds in the lower atmosphere blow from east toward the west in all locations, that is, in the direction the planet rotates. Typical wind speeds are listed in Table 5-9 [5-25].

TABLE 5-9. TYPICAL WIND SPEED PROFILE

Altitude	Wind Speed
Surface	0.3 to 1.0 m sec^{-1}
7 km	1 m sec^{-1}
28 km	30 m sec^{-1}
65 km	100 m sec^{-1}

In the altitude range 28 to 65 km, zonal winds increase from the surface to 100 m sec^{-1} near cloud top, which is the 4-to-5 day "superrotation" observed from the Earth. The mechanism responsible for driving the zonal circulation is not yet well understood [5-1]. Figures 5-8 through 5-10 show the zonal winds: speed, mass-flow, and energy density from probe data [5-25]. Figure 5-11 shows sketches of possible meridional flows and eddies. In addition to zonal flow, Venus has meridional winds whose speed is an order of magnitude less. At cloud top, the meridional wind speeds are from a few to 10 m sec^{-1} in the poleward direction. This corresponds to the top of a Hadley cell circulation system, with equatorward flow at about 50- to 55-km altitude [5-25].

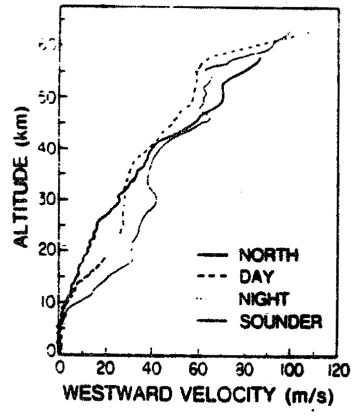

Figure 5-8. Zonal winds.

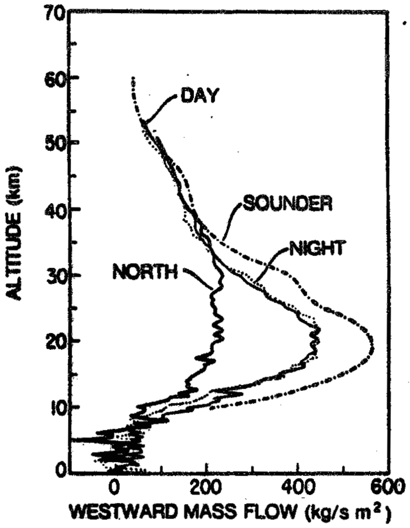

Figure 5-9. Zonal mass flow.

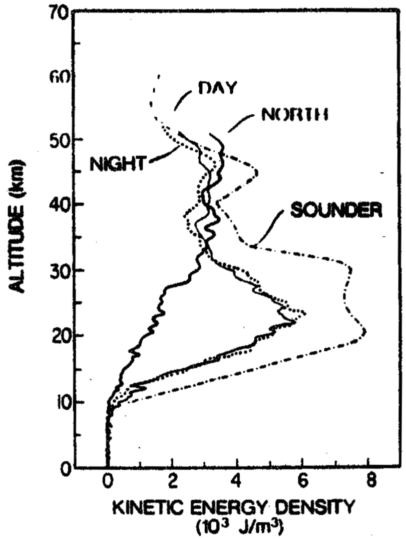

Figure 5-10. Zonal kinetic energy density.

5.6.1.6 Clouds

The cloud layer on Venus continuously obscures the surface. It is featureless except in the ultraviolet region of the spectrum, where low-contrast dark markings, often with a characteristic horizontal-Y shape, frequently appear and persist for hours or days. (Review paragraph 5.6.2.2 for a discussion of UV absorbers.). These recurrent features are shown diagrammatically in Figure 5-12, along with the descriptive names associated with their structure in the literature [5-31].

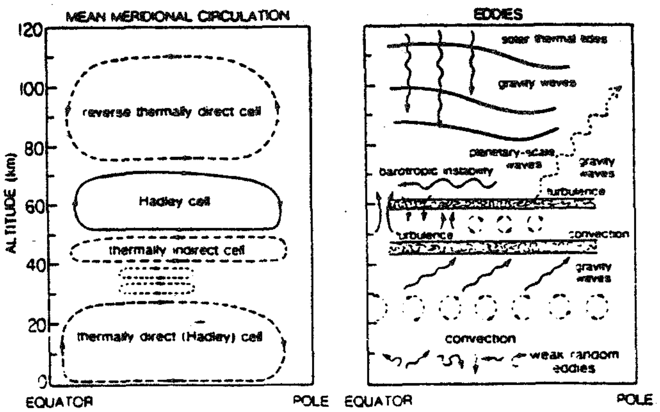

Figure 5-11. Meridional flows and eddies [5-25].

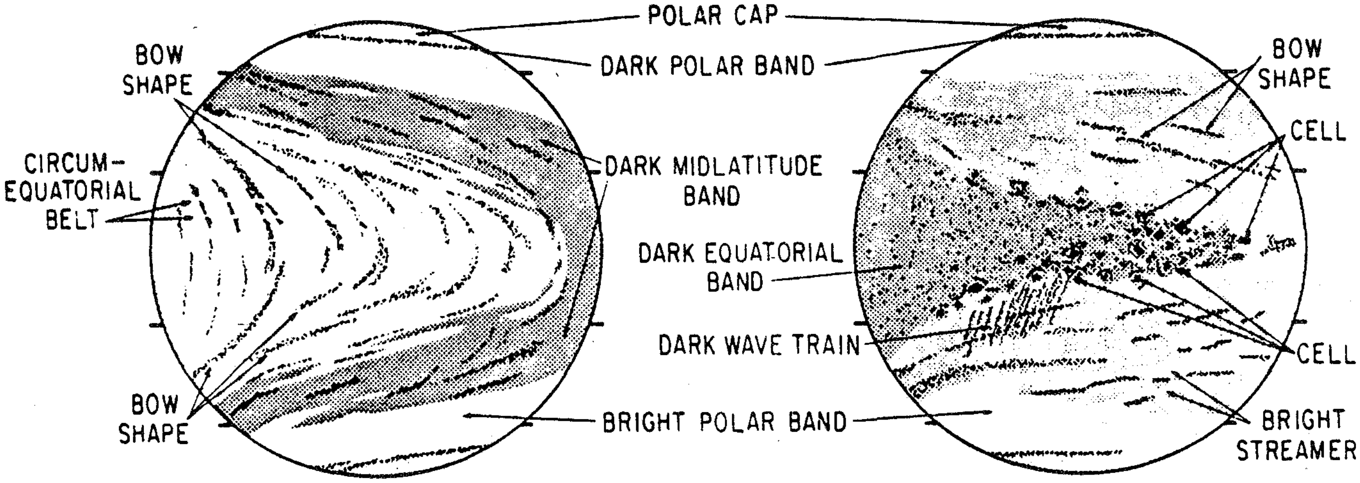

Figure 5-12. Schematic diagram defining the basic types of cloud features observed in Venus ultraviolet images. The two views depicted here typically occur 2 days apart and represent the maximum and minimum tilt configurations, respectively. Tick marks on each circle indicate 20 and 50 deg of latitude in each hemisphere.

The clouds play an important role in the radiation budget of the planet (paragraph 5.6.4). Prior to the Pioneer Venus mission, careful analysis of ground-based observations led to the remarkable conclusion that the clouds are made up of single-mode droplets of sulfuric acid with radius 1.05 microns [5-24]. The Sounder Probe instruments confirmed the presence of such droplets, but also found populations of smaller and larger particles. Data was collected both from the Orbiter and by direct measurements by the particle size spectrometer on the Sounder Probe during entry.

The great opacity of the cloud deck, which has an optical depth in excess of 30, results mainly from its very great thickness. Visibility within the clouds is nowhere less than several kilometers [5-32].

Haze exists throughout the atmosphere except in the lowest 25 km, which is remarkably clear. Haze extends upwards to altitudes of at least 90 km [5-32].

The particles that form the clouds may be divided into three clases: Mode 1, submicron aerosol "haze" particles; Mode 2, micron-sized H_2SO_4 droplets; and Mode 3, larger crystals. The Mode 3 crystals are known to be larger solid particles. Their form and composition is uncertain, though the current best guess is that they are a chloride [5-28,5-33] and are plate-like in crystalline form. They may account for the major fraction of the total columnar mass loading of cloud particles (approximately 1.8×10^{-2} g cm^{-2}).

Earth and Venus cloud system properties are compared in Table 5-10.

TABLE 5-10. COMPARATIVE VENUS AND EARTH CLOUD SYSTEM PROPERTIES [5-33]

Property	Earth	Venus
Percent coverage	40	100
Average optical depth	5–7	25–40
Maximum optical depth	300–400	40
Composition	solid and liquid H_2O	H_2SO_4 droplets, crystals, plus contaminants
Number density	100–1000 cm^{-3} (liquid) 0.1–50 cm^{-3} (ice)	50–300 cm^{-3} (liquid) 10–50 cm^{-3} (crystals)
Average mass loading (Mass Density)	0.3–0.5 g m^{-3}	0.01–0.02 g m^{-3}
Maximum mass loading (Mass Density)	10–20 g m^{-3}	0.1–0.2 g m^{-3}
Distribution function	normal-log normal bimodal (ice)	Multimodal
Typical background aerosol at cloud base 0.5 microns	1 cm^{-3}	100–200 cm^{-3}
Condensation process	homomolecular	heteromolecular
Average precipitable mass	0.03–0.05 mm	0.1–0.2 mm
Mean scattering size (diameter) (In the visible)	10 μm	2–4 μm
Mean mass size (diameter)	30 μm	10 μm
Dominant optical cloud form	stratiform	stratiform
Dominant mass cloud form	cumulus	stratiform
Potential latent instability	high	low
Temporal variability	high	slight
Dominant cloud atmosphere heat exchange process	latent heat	radiation

Table 5-11 summarizes the properties of the various regions [5-33]. For radiative properties review paragraph 5.6.4. Over the poles the cloud tops are 6 to 9 km lower [5-34].

5.6.1.7 Lightning

Whistler mode electromagnetic noise bursts were detected by the plasma wave instrument aboard the Pioneer Venus Orbiter [5-35]. Presumably these were produced by lightning discharges in the lower atmosphere, though no direct confirmation has been made. Several of the Venera spacecraft also detected electromagnetic noise signals that could be attributed to lightning [5-36]. An optical search for lightning

TABLE 5-11. SUMMARY OF VENUS CLOUD PROPERTIES

Region	Altitude, km	Temperature, °K	Optical Depth τ	Average Number Density N, cm^{-3*}	Mean Diameter, μm	Composition†
Upper haze‡	70–90	225°–190°	0.2–1.0	500	0.4	H_2SO_4 + contaminants
Upper cloud	56.5–70	286°–225°	6.0–8.0	(1) 1500 (2) 50	Bimodal 0.4 and 2.0	H_2SO_4 + contaminants
Middle cloud	50.5–56.5	345°–286°	8–10	(1) 300 (2) 50 (3) 10	Trimodal 0.3, 2.5, 7.0	H_2SO_4 + crystals
Lower cloud	47.5–50.5	367°–345°	6–12	(1) 1200 (2) 50 (3) 50	Trimodal 0.4, 2.0, 8.0	H_2SO_4 + crystals
Lower haze	31–47.5	482°–367°	0.1–0.2	(2) 20	0.2	H_2SO_4 + contaminants
Precloud layers	46 and 47.5	378° and 367°	0.05 and 0.1	50 and 150	Bimodal 0.3 and 2.0	H_2SO_4 + contaminants

flashes showed only that lightning activity on Venus is not greater than on the Earth. An upper limit was set of about 30 flashes per km^2 per year [5-37]. This does not appear to be enough activity to make lightning an important factor in the production of trace constituents in the atmosphere.

The origin of lightning in the Venus lower atmosphere poses an interesting problem. Even though the mechanisms responsible for production of lightning in Earth clouds are not completely understood, it is certain that microphysical processes involving water-ice play the key role. (The only important exception is for lightning associated with volcanic activity.) On Venus, the Mode 3 particles, since they are crystalline, may be responsible for charge separation [5-32].

5.6.2 The Middle Atmosphere

Above the cloud top level at 65 km to the homopause at approximately 130 km is the Middle Atmosphere. Temperature decreases to about 170°K between 90- and 100-km altitude, then increases again to around 190°K at 110 km (0.002 mb). The altitude variation of temperature with altitude (pressure) is strikingly different from the Earth as measured by infrared remote sensing from the Orbiter [5-38]. Thermodynamic properties of the middle atmosphere are listed in Table 5-12.

Tentative chemical composition results are available from a recent Soviet model calculation (Fig. 5-14) [5-28].

5.6.2.1 Winds in the Middle Atmosphere

No direct measurements of wind speeds were made above 60 km (cloud tops), but strong zonal wind flows are expected. Models predict a maximum zonal wind speed of about 150 m sec^{-1} at 70 km, decreasing to about 133 m sec^{-1} at 95 km, and increasing again to superrotation speeds at 150 km [5-25].

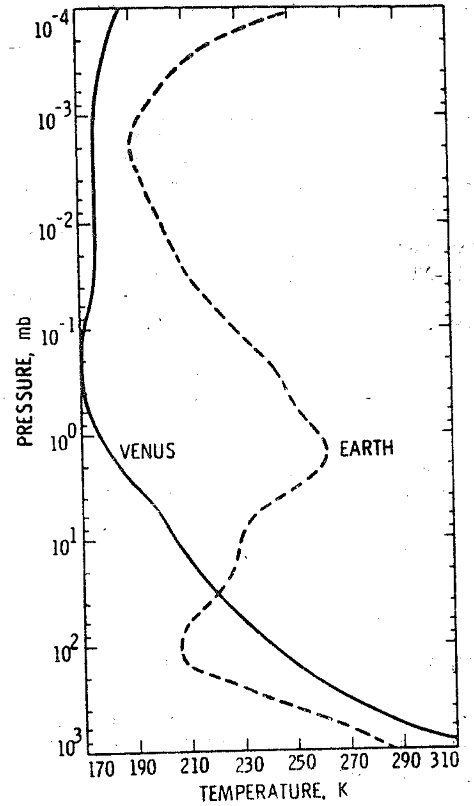

Figure 5-13. Profiles of temperature versus pressure at 30 deg N latitude [5-25,5-39].

TABLE 5-12. THERMODYNAMIC PROPERTIES OF THE VENUS MIDDLE ATMOSPHERE (SOUNDER PROBE)

Altitude, km	p, bars	T, K	ρ, kg/m^3
116	0.5199E − 06	190.2	0.1405E − 05
114	0.8255E − 06	190.2	0.2236E − 05
112	0.1318E − 05	190.2	0.3577E − 05
110	0.2075E − 05	194.4	0.5520E − 05
108	0.3273E − 05	196.3	0.8630E − 05
106	0.5171E − 05	190.1	0.1409E − 04
104	0.8338E − 05	183.0	0.2363E − 04
102	0.1362E − 04	180.7	0.3911E − 04
100	0.2252E − 04	174.1	0.6718E − 04
98	0.3773E − 04	173.3	0.1132E − 03
96	0.6350E − 04	168.9	0.1957E − 03
94	0.1078E − 03	168.9	0.3326E − 03
92	0.1848E − 03	167.1	0.5768E − 03
90	0.3168E − 03	165.4	0.9999E − 03
88	0.5469E − 03	165.2	0.1728E − 02
86	0.9402E − 03	163.8	0.2997E − 02
84	0.1634E − 02	164.7	0.5184E − 02
82	0.2757E − 02	181.1	0.7951E − 02
80	0.4449E − 02	195.8	0.1188E − 01
79	0.5577E − 02	204.1	0.1428E − 01
78	0.6926E − 02	212.4	0.1704E − 01
77	0.8553E − 02	215.1	0.2077E − 01
76	0.1054E − 01	216.9	0.2540E − 01
75	0.1296E − 01	221.1	0.3064E − 01
74	0.1587E − 01	227.3	0.3647E − 01
73	0.1934E − 01	227.8	0.4435E − 01
72	0.2349E − 01	233.5	0.5256E − 01
71	0.2850E − 01	234.9	0.6339E − 01
70	0.3440E − 01	243.5	0.7381E − 01
69	0.4166E − 01	230.5	0.9444E − 01

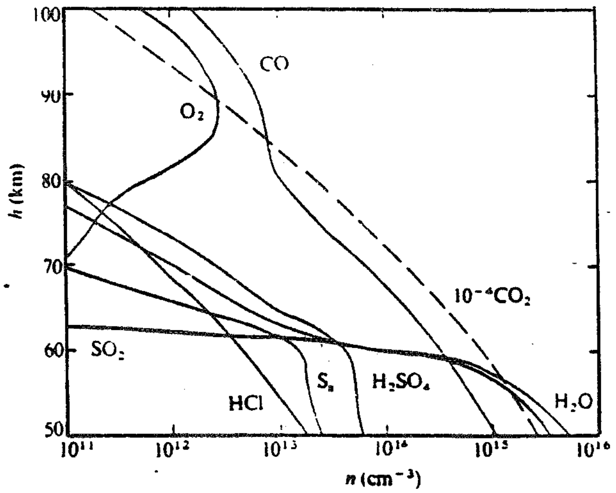

Figure 5-14. Composition of Venus atmosphere between 50 and 100 km (tentative).

5.6.2.2 Ultraviolet Absorbers

The dark patterns observed at ultraviolet wavelengths in the cloud tops have been shown by careful analysis to require the presence of at least two different UV absorbers in the middle atmosphere. The absorption from 2000 to 3200 Å can be accounted for by sulfur dioxide at around 75 km within the haze layer above the main cloud deck. At longer wavelengths the observed dark patterns cannot be explained by SO_2, since its absorption drops to too low a value. Therefore, a second broadband absorber is required in the first few optical depths of the upper cloud level [5-27]. Elemental sulfur was once suggested, but it has since been shown to be insufficient [5-40]. Chlorine gas or chlorine compounds are candidates, possibly $FeCl_3$ dissolved in the concentrated H_2SO_4 [5-28]. Interest in UV absorbers is spurred by recognition that they play an important role in the variation in local energy deposition in the atmosphere.

5.6.3 The Upper Atmosphere

The temperature of the dayside Upper Atmosphere had been well established by remote sensing prior to the Pioneer Venus mission [5-12]. The day-night temperature structure is compared to the Earth in Figure 5-15. Venus' dayside Upper Atmosphere is not unlike the Earth's thermosphere, although temperatures are considerably lower. However, the nightside upper atmosphere temperature structure is totally unfamiliar and has not yet been explained. (It has been termed a "cryosphere" [5-25].)

5.6.3.1 Upper Atmosphere Temperature

Asymptotic temperatures for great altitudes become:

Dayside: T ∿ 285°K

Nightside: T ∿ 110°K

Global Average: ∿ 199°K

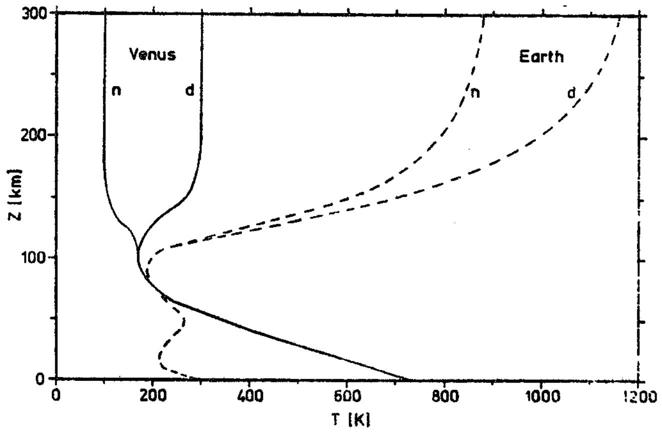

Figure 5-15. Comparison of the vertical thermal structures of the atmospheres of Venus and the Earth [5-25,5-39].

5.6.3.2 Upper Atmosphere Density and Composition

Representative densities for the dayside and nightside are [5-41]:

	Dayside g cm^{-3}	Nightside g cm^{-3}
150 km	about 8×10^{-13}	24 × less
170 km	about 7×10^{-14}	82 × less

The variation contrasts with a diurnal variation of only 1 percent on the Earth.

Figure 5-16 shows the diurnal variation in atmospheric density at 160-km altitude as derived from Orbiter drag data [5-41]. The temperature drops by 150°K going across the terminators within only 30 deg of longitude.

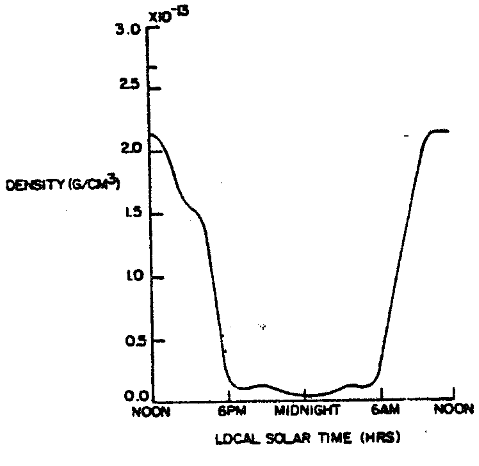

Figure 5-16. Diurnal variation of upper atmospheric density.

The temperatures shown in Figure 5-17 are also for 160 km, derived from Orbiter drag data. The curve labeled T_{115} represents the assumed daily variation of temperatures at the 115-km level [5-41].

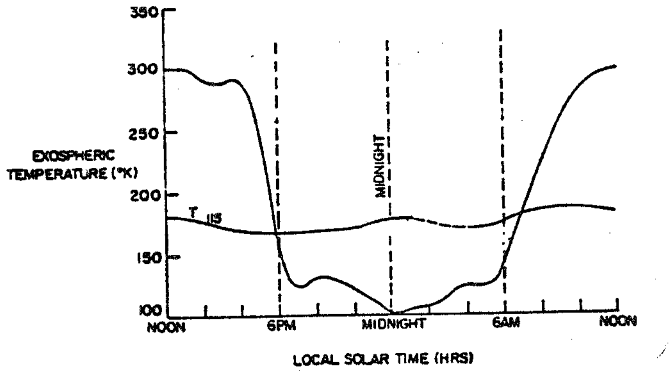

Figure 5-17. Diurnal variation of upper atmospheric temperature.

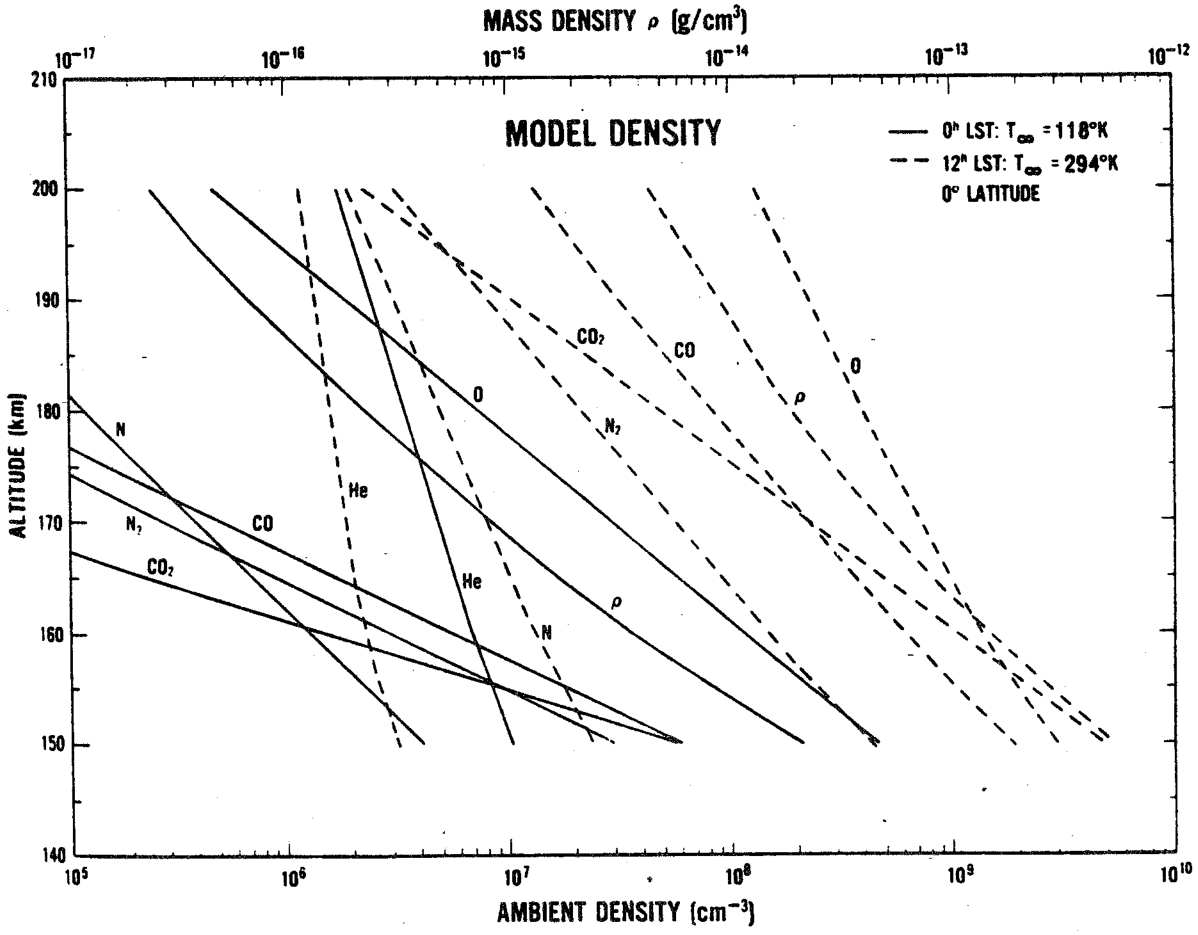

Figure 5-18. Tentative model number and total mass densities versus altitude [5-42].

According to the model results, oxygen atoms take over from CO_2 as the dominant constituent for all altitudes above 155 km on the dayside and at a somewhat lower altitude on the nightside. For all constituents except helium and hydrogen, dayside density exceeds nightside.

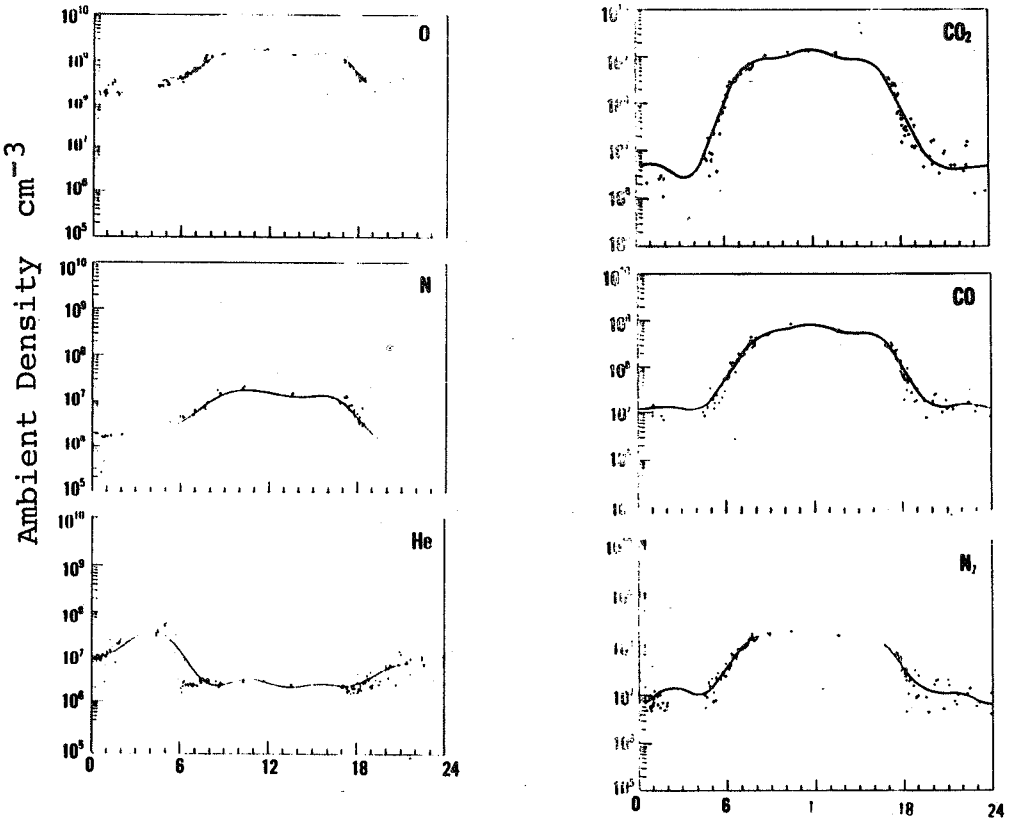

Figure 5-19. Diurnal variaton of He, N, O, N_2, CO, and CO_2 at 157-km altitude [5-42].

5.6.3.3 Winds in the Upper Atmosphere

Model calculations suggest wind speeds increasing from 100 m sec^{-1} at 125 km to 200 m sec^{-1} above 150 km [5-43]. Superrotation above 150 km is superposed on a general subsolar to antisolar flow and may only occur at low altitudes [5-25].

5.6.4 Radiative Properties of the Venus Atmosphere

Effective radiating temperature of the planet:	231 ± 7°K
Bolometric Bond Albedo:	0.75 ± 0.02

- conformed to flux (in or out) of 162 W m^{-2} [5-9].

5.6.4.1 The "Greenhouse"

A research problem of fundamental importance is to understand how the surface of the planet is maintained at a temperature near 740°K. The only viable explanation appears to be that the atmosphere as a whole acts as a "greenhouse" to trap infrared radiation from the surface, while admitting enough solar radiation to act as the primary heating source. Pioneer Venus data may not be fully consistent with the greenhouse hypothesis [5-44], but one-dimensional models have been fairly successful. The role of various absorbers in contributing to a recent greenhouse model is illustrated in Table 5-13 [5-45]. An interesting point is that in this model the clouds are not the major factor — they take third place behind CO_2 and water vapor. Any one-dimensional model must be incomplete, however, since horizontal motions must play the role of redistributing the nonuniform heating into the observed uniform temperature.

TABLE 5-13. DECREASE IN SURFACE TEMPERATURE ACCOMPANYING THE REMOVAL OF VARIOUS SOURCES OF INFRARED OPACITY [5-45]

Source Deleted	Change in Surface Temperature, K
HCl	0.1
CO	13
SO_2	52
Clouds	113
H_2O	218
CO_2	463

It is important to note that the exact role of water vapor in the infrared opacity will remain uncertain until discrepancies in the measurements of its concentration in the atmosphere are resolved. Another factor that undoubtedly contributes to the heat balance in the atmosphere is atmospheric circulation, but its exact role is uncertain at present. Reference 5-25 discusses questions of heat transport by meridional flow and eddy diffusion.

5.6.4.2 Optical Properties of the Venus Cloud System

The cloud layer has a profound influence on the penetration of solar energy and therefore on the input side of the radiative balance of the atmosphere. Figure 5-20 [5-32] shows the results of measurements made on the Sounder Probe.

5.7 IONOSPHERE

Extensive ionospheric data were obtained during the Pioneer Venus mission. The interactions between the ionosphere and the solar wind are complex and difficult to summarize. For details, review published accounts such as References 5-46 through 5-49.

5.7.1 Ionsopheric Ions - Temperature and Total Densities

Ion densities except for H^+ decrease by over an order of magnitude from the dayside to the nightside, while ion temperature, constant over the entire dayside, increases to peak at the antisolar point. Figures 5-21 and 5-22 summarize data on ion densities [5-48].

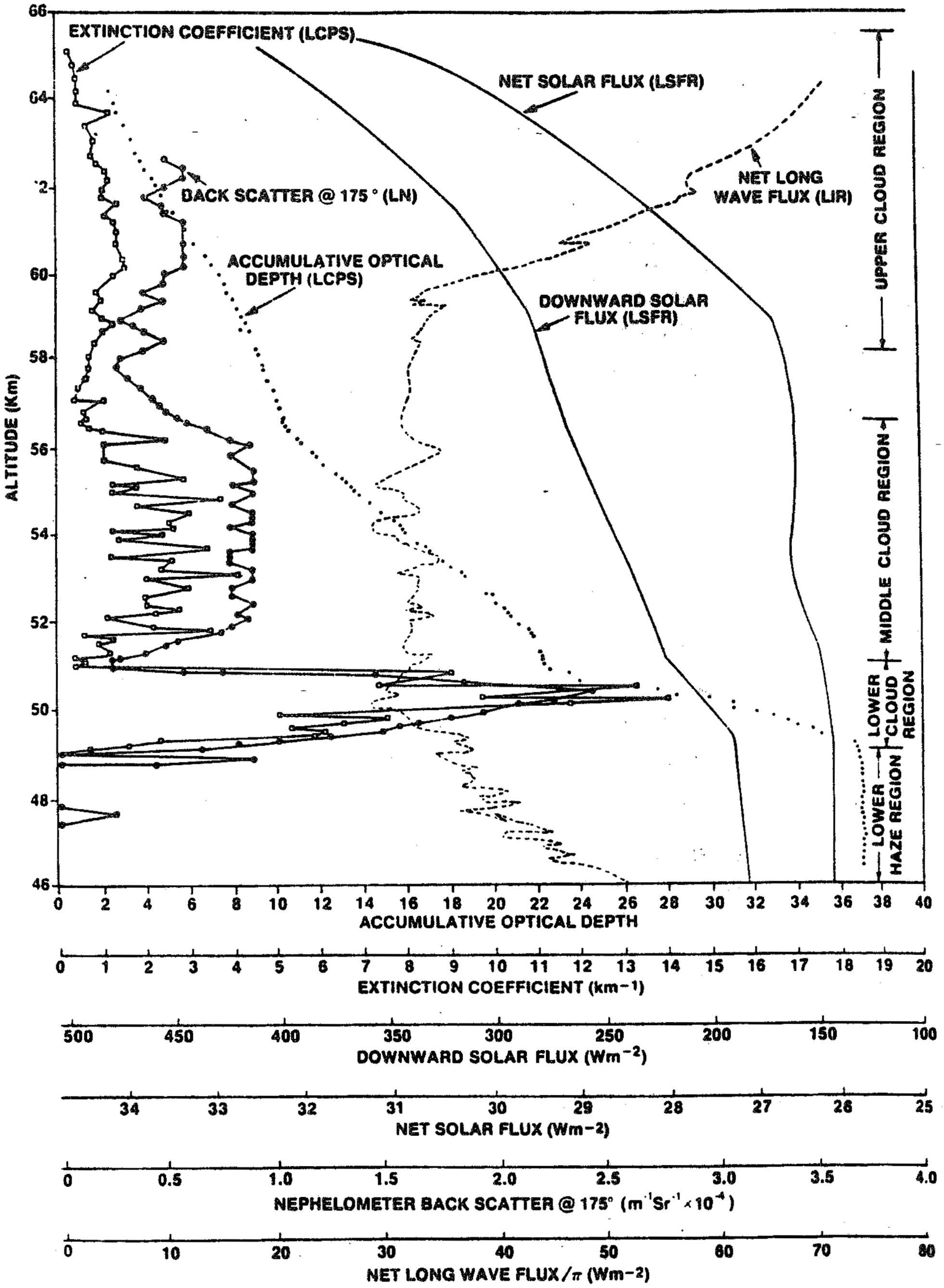

Figure 5-20. Venusian cloud system optical properties [5-32].

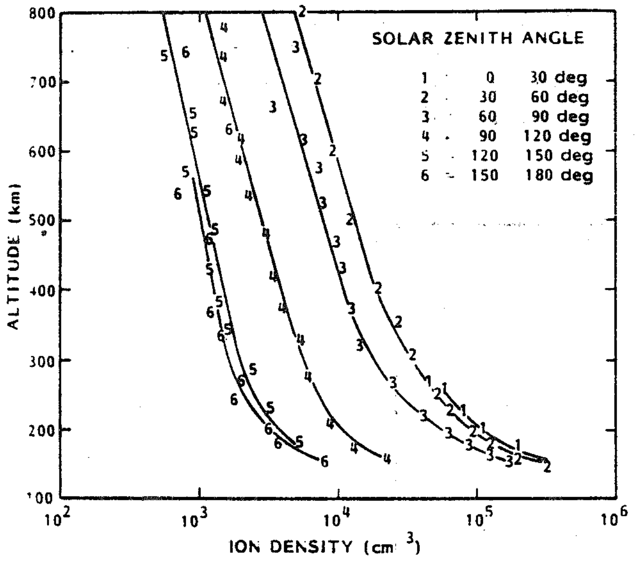

Figure 5-21. Ion density profiles.

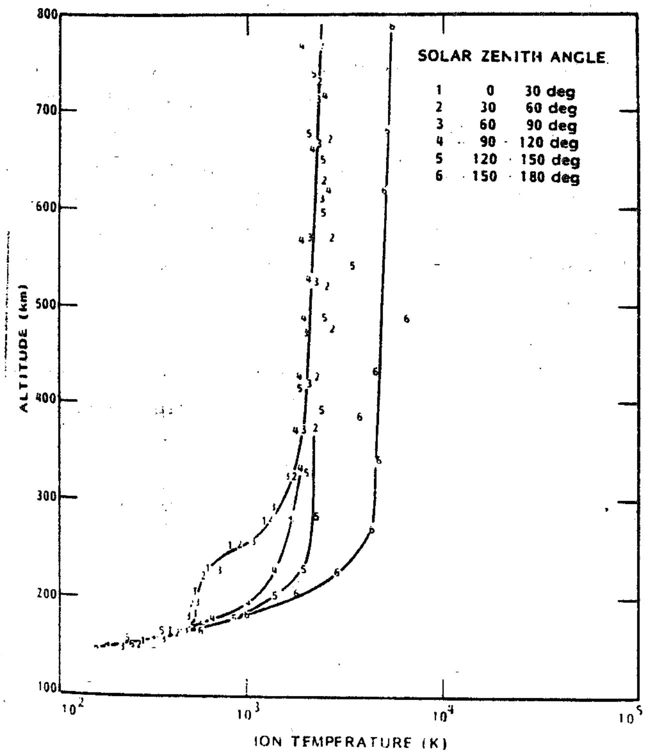

Figure 5-22. Ion temperature profiles.

5.7.2 Ions — Composition

The Venus ionosphere is mostly O^+ above 200 km and mostly O_2^+ below this, down to 160 km. All ions other than H^+ and He^+ are more abundant on the dayside, while the two lightest ions show asymmetric nightside bulges. Typical ion concentrations at 200 km at the Venus ionosphere are shown in Table 5-14.

TABLE 5-14. TYPICAL IONSOPHERIC ION DENSITIES AT 200 km (SUBSOLAR) [5-49]

Ion	Density Number cm^{-3}
O^+	10^5
O_2^+	6×10^4
H^+	20
NO^+	10^4
CO_2^+	2×10^3
He^+	100
CO^+ plus N_2^+	10^4
C^+	8×10^3
N^+	10^3

5.7.3 Ionospheric Electrons

Electron temperatures vary by less than a factor of two from subsolar point to antisolar point (Fig. 5-23). Below 180 km the electron temperature rises from dayside to nightside, while above this level the converse is true. Electron densities drop by two orders of magnitude from subsolar to antisolar point. Table 5-15 [5-48] summarizes the results of model calculations based upon Pioneer Venus data. The cut-off altitude in the table was taken as a representative ionopause location, though the actual ionopause was found to be extremely variable (paragraph 5.7.4).

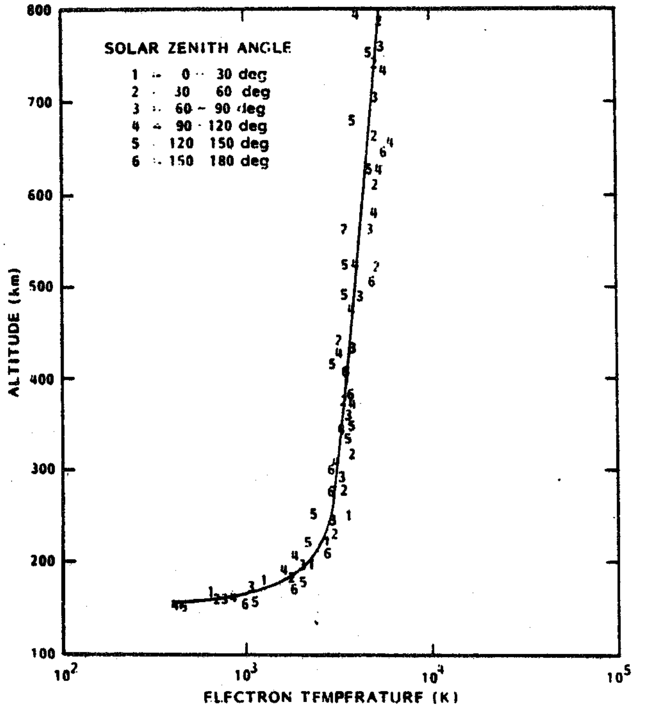

Figure 5-23. Median electron temperatures from 30 deg intervals in SZA showing the similarity of median electron temperature profiles at different solar zenith angles.

5.7.4 Ionospheric Variability

The extent of the ionosphere is highly dependent upon the pressure exerted by the solar wind. On the dayside the height of the ionopause may vary between 290 km at high solar wind pressure (above 4×10^{-8} dyn cm^{-2}) up to 100 km or more for low pressures (below 5×10^{-9} dyn cm^{-2}) [5-46]. The nightside ionopause height is even more variable, with low values below 200 km and high values in excess of 3500 km. On the nightside there is evidence of extreme spatial variation in plasma density and temperature. Mean ionopause heights are:

TABLE 5-15. COMPUTED MODEL VALUES FOR ELECTRON TEMPERATURE AND ELECTRON NUMBER DENSITY (T_e AND $\log_{10}(N_e)$) [5-48]

	Solar Zenith Angle, deg												
h, km	0	15	30	45	60	75	90	105	120	135	150	165	180
160	1136 5.50	1157 5.48	1210 5.46	1262 5.42	1279 5.40	1249 5.22	1197 4.88	1163 4.49	1180 4.15	1259 3.92	1383 3.81	1502 3.78	1552 3.78
170	1514 5.30	1530 5.30	1567 5.29	1598 5.28	1598 5.25	1560 5.07	1505 4.73	1467 4.35	1472 4.01	1528 3.78	1618 3.67	1703 3.63	1739 3.62
180	1893 5.18	1900 5.18	1915 5.17	1921 5.16	1902 5.13	1856 4.94	1801 4.61	1760 4.24	1753 3.91	1783 3.68	1838 3.56	1890 3.51	1912 3.50
190	2255 5.10	2253 5.10	2243 5.09	2221 5.06	2181 5.01	2129 4.84	2076 4.51	2034 4.14	2015 3.82	2020 3.59	2041 3.47	2062 3.42	2071 3.41
200	2589 5.05	2577 5.04	2542 5.02	2491 4.98	2433 4.91	2375 4.75	2324 4.43	2283 4.07	2254 3.75	2235 3.52	2225 3.40	2220 3.35	2218 3.34
225	3275 4.96	3240 4.94	3150 4.89	3040 4.81	2941 4.71	2871 4.57	2827 4.26	2790 3.92	2743 3.62	2679 3.40	2609 3.28	2555 3.23	2534 3.22
250	3757 4.88	3708 4.85	3581 4.78	3431 4.68	3305 4.56	3226 4.44	3184 4.15	3149 3.82	3092 3.53	3004 3.33	2902 3.21	2820 3.17	2789 3.16
275	4083 4.78	4027 4.75	3883 4.68	3712 4.57	3570 4.45	3482 4.35	3436 4.06	3400 3.74	3337 3.47	3239 3.28	3124 3.17	3032 3.14	2997 3.13
300	4304 4.67	4246 4.64	4099 4.58	3923 4.48	3773 4.36	3675 4.27	3621 3.99	3576 3.69	3509 3.43	3409 3.24	3295 3.15	3204 3.12	3169 3.11
350		4516 4.44	4391 4.40	4232 4.33	4083 4.23	3967 4.15	3881 3.89	3808 3.61	3726 3.37	3631 3.20	3535 3.12	3463 3.10	3436 3.10
400				4479 4.23	4346 4.14	4211 4.06	4085 3.82	3969 3.55	3864 3.32	3771 3.17	3697 3.11	3648 3.09	3631 3.10
450					4598 4.05	4450 3.99	4281 3.77	4115 3.51	3976 3.29	3876 3.15	3817 3.09	3788 3.09	3779 3.09
500					4846 3.96	4695 3.94	4484 3.72	4264 3.47	4084 3.26	3968 3.13	3913 3.08	3896 3.08	3894 3.08
600						5190 3.87	4920 3.64	4598 3.40	4323 3.20	4146 3.08	4066 3.04		
700						5634 3.85	5368 3.58	4972 3.33	4597 3.14	4332 3.03			
800							5775 3.53	5361 3.26	4897 3.09	4524 2.98			
900								5730 3.19	5207 3.03				
1000								6048 3.12					

	Approximate Mean and Variability
Subsolar Point	330 km ± 60 km
Solar Zenith Angle 90 deg (AM Terminator)	850 km ± 300 km
Solar Zenith Angle 120 deg	1200 km ± 550 km

At the ionopause the electron density drops abruptly, from the ionospheric value near 10^4 to less than 100 per cm^3. The electron temperature, however, remains unchanged across the ionopause (Fig. 5-23).

5.8 MAGNETOSPHERE

Venus lacks a planetary dipole field, and so lacks a magnetosphere of the sort possessed by the Earth. However, the interaction between the solar wind and the Venus ionosphere produces magnetic effects. Figure 5-24 shows the average magnetic field from this cause as a function of radial distance from the planet center [5-50]. The maximum field is only a few tens of gammas, but the resulting magnetohydrodynamic plasma effects are very complex [5-46 through 5-49].

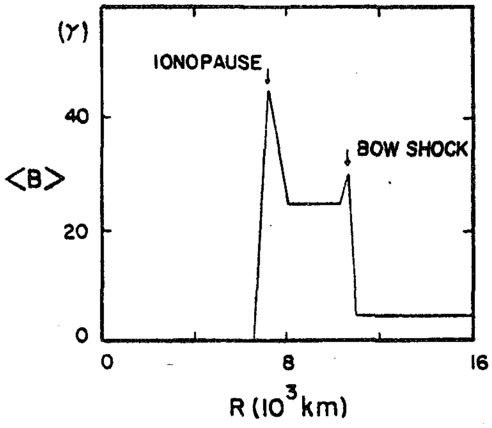

Figure 5-24. The average magnetic field strength for a field line intersecting the terminator at a radial distance r.

Figure 5-25 shows schematically the form of the interaction of Venus and the solar wind. The "mantle" is the transition region between the ionosheath and the ionosphere.

5.9 PROSPECTS FOR THE FUTURE

Venus presents a rich world for investigation; Pioneer Venus results have just begun to open the planet for exploration. Future exploration by orbiters and soft-landers will provide much interesting and valuable information about our strange sister planet and, by analogy and contrast, will enhance our understanding of the Earth.

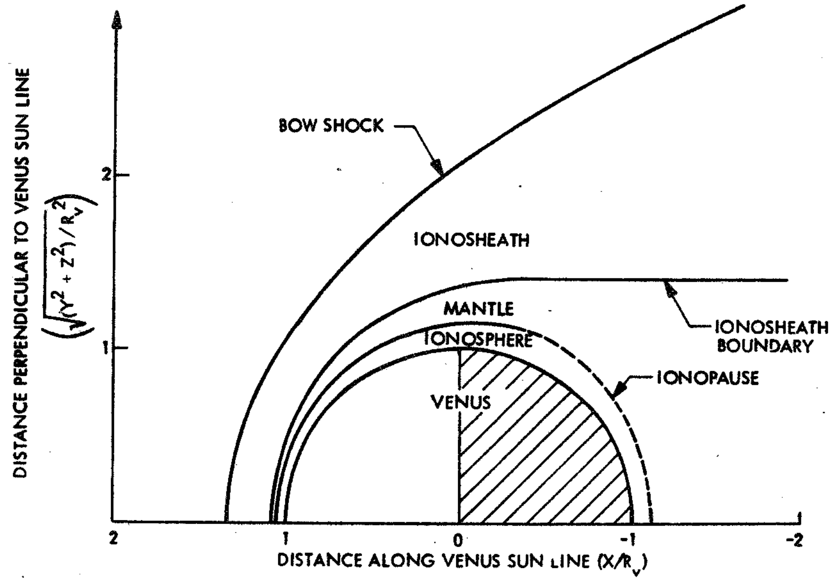

Figure 5-25. Schematic diagram of the interaction between the Venus ionosphere and the solar wind [5-51].

Previous probes to the plant Venus which provided the majority of the data in this section are listed in Table 5-16.

TABLE 5-16. SPACE PROBES TO VENUS [5-9]

Name of Mission	Type of Mission	Launch	Arrival	What was Measured
Mariner-2	fly-by[a] (35,000 km)	26.8.62	14.12.62	Infrared and radio brightness temperature, magnetic field.
Venera-4	descent probe	12.6.67	18.10.67	T, P, p (on altitudes 55-25 km), abundance of CO_2, N_2, O_2, H_2O, wind.
	+ fly-by			Lα and 01 1300 Å (resonance emissions).
Mariner-5	fly-by (4000 km)	14.6.67	19.10.67	Radio occultation, Lα.
Venera-5	descent probe	5.1.69	16.5.69	T, P (on altitudes 55-20 km), abundances of CO_2, N_2, O_2, H_2O, wind.
Venera-6	descent probe	10.1.69	17.5.69	The same.
Venera-7	lander	17.8.70	15.12.70	T (between 55 km and surface).
Venera-8	lander	26.1.72	22.7.72	T, P, abundance NH_3, flux of solar scattered radiation (between 55 km and surface), wind, K, U, Th abundance in the ground.
Mariner-10	fly-by (5800 km)	8.11.73	5.2.74	UV-imaging of the clouds, IR T_B, UV-spectrum, radio occultation.
Venera-9	lander	8.6.75	22.10.75	In the atmosphere T, P, chemical composition (mass-spectrometer and narrow-band photometer), solar flux, clouds (nephelometer and photometers), wind. On the ground: imaging of the surface, density of ground; K, U, Th.
	+ orbiter (1545 km)			Imaging of the clouds. IR T_B narrow-band photometry between 0.4 and 2.5 μm, polarimetry, spectrum of night-flow, Lα, radio occultation, solar wind, interaction, magnetic field.
Venera-10	lander + orbiter (1665 km)	14.6.75	25.10.75	The same as Venera-9.
Pioneer-Venus	Orbiter (150 km)	20.5.78	4.12.78	Imaging of clouds, IR thermal sounding, UV-spectrum, polarimetry, radio occultation, upper atmosphere's in situ measurements drag, neutral and ionic composition, T_B, n_e).
Pioneer-Venus	Multiprobe (large probe + 3 small probes + bus)	8.8.78	9.12.78	T, P, p, solar and planetary fluxes, chemical composition (mass-spectrometer and gas chromatograph), clouds particle size spectrometer and nephelometer.
Venera-11	lander	9.9.78	25.12.78	T, P, p, chemical composition (mass-spectrometer) spectrum of scattered solar radiation, thunderstorms, clouds (nephelometer).
	+ fly-by (40,000 km)			UV-spectrum.
Venera-12	lander	12.9.78	21.12.78	T, P, p chemical composition (mass-spectrometer and gas-chromatograph), spectrum of scattering solar radiation, clouds (composition).
	+ fly-by (40,000 km)			UV-spectrum.

a. For fly-by probes and orbiters the minimal distance to the surface is given.

REFERENCES

5-1. Colin, L.: The Pioneer Venus Program. J. Geophys. Res., vol. 85, 1980, pp. 7575-7598.

5-2. Space Science Reviews, vol. 20, No. 3, 1977 (entire issue).

5-3. Space Science Reviews, vol. 20, No. 4, 1977 (entire issue).

5-4. Science, vol. 203, No. 4382, 1979 (entire issue).

5-5. Science, vol. 205, No. 4401, 1979 (entire issue).

5-6. Journal of Geophysical Research, vol. 85, Pioneer Venus Special Issue, 1980, pp. 7575-8337.

5-7. Marov, M. Ya.: Results of Venus Missions. Ann. Rev. Astron. Astrophys., vol. 16, 1979, pp. 141-169.

5-8. COSPAR – Committee on Space Research: Proceedings, 23rd Plenary Meeting, Budapest, Hungary, 1980.

5-9. Moroz, V. I.: The Atmosphere of Venus. Space Sci. Rev., vol. 29, 1981, pp. 3-127.

5-10. Schubert, G., and Covey, C.: The Atmosphere of Venus. Sci. Am., vol. 245, July 1981, pp. 66-74.

5-11. The American Ephemeris and Nautical Almanac, U.S. Government Printing Office, Washington, D.C., 1980.

5-12. Hunten, D. M., McGill, G. E., and Nagy, A. F.: Current Knowledge of Venus. Space Sci. Rev., vol. 20, 1977, pp. 265-282.

5-13. Kopal, Z.: Planetary exploration by spacecraft. Contemp. Phys., vol. 21, 1980, pp. 359-380.

5-14. Royal Astronomical Society of Canada, Observer's Handbook, ed. J. R. Percy, 1980.

5-15. Pettengill, G. H., Eliason, E., Ford, P. G., Loriot, G. B., Masursky, H., and McGill, G. E.: Pioneer Venus Radar Results: Altimetry and Surface Properties. J. Geophys. Res., vol. 85, 1980, pp. 8261-8270.

5-16. Russell, C. T., Elphic, R. C., and Slavin, J. A.: Limits on the Possible Intrinsic Magnetic Field of Venus. J. Geophys. Res., vol. 85, 1980, pp. 8319-8332.

5-17. Ananda, M. P., Sjogren, W. L., Phillips, R. J., Wimberly, R. N., and Bills, B. G.: A low-order global gravity field of Venus and dynamical implications. J. Geophys. Res., vol. 85, 1980, pp. 8303-8318.

5-18. Masursky, H., Eliason, E., Ford, P. G., McGill, G. E., Pettengill, G. H., Schaber, G. C., and Schubert, G.: Pioneer Venus radar results: Geology from images and altimetry. J. Geophys. Res., vol. 85, 1980, pp. 8232-8260.

5-19. Sjogren, W. L., Phillips, R. J., Birkeland, P. W., and Wimberly, R. N.: Gravity Anomalies on Venus. J. Geophys. Res., vol. 85, 1980, pp. 8295-8302.

5-20. Goldstein, R. M., Green, R. R., and Rumsey, H. C.: Venus radar images. J. Geophys. Res., vol. 81, 1976, pp. 4807-4817.

5-21. Campbell, D. B., Dyce, R. B., Ingalls, R. P., Pettengill, G. H., and Shapiro, I. T.: Venus: Topography revealed by radar data. Science, vol. 175, 1972, pp. 514-516.

5-22. Masursky, H., Kaula, W. M., McGill, G. E., Pettengill, G. H., Phillips, R. J., Russell, C. T., Schubert, G., and Shapiro, I. I.: The surface and interior of Venus. Space Sci. Rev., vol. 20, 1977, pp. 431-449.

5-23. Ragent, B. and Blamont, J.: The Structure of the Clouds of Venus: Results of the Pioneer Nephelometer Experiment. J. Geophys. Res., vol. 85, 1980, pp. 8089-8106.

5-24. Hansen, J. E. and Hovenier, J. W.: Interpretation of the polarization of Venus. J. Atmos. Sci., vol. 31, 1974, p. 1137.

5-25. Schubert, G., Covey, C., Del Genio, A., Elson, L. S., Keating, G., Seiff, A., Young, R. E., Apt, J., Counselman, C. C. III, Kliore, A. J., Limaye, S. S., Revercomb, H. E., Sromovsky, L. A., Suomi, V. E., Taylor, F., Woo, R., and von Zahn, U.: Structure and Circulation of the Venus Atmosphere. J. Geophys. Res., vol. 85, 1980, pp. 8007-8025.

5-26. Seiff, A., Kirk, D. B., Young, R. E., Blanchard, R. C., Findlay, J. T., Kelly, G. M., and Sommer, S. C.: Measurements of Thermal Structure and Thermal Contrasts in the Atmosphere of Venus and Related Dynamical Observations: Results from the Four Pioneer Venus Probes. J. Geophys. Res., vol. 85, 1980, pp. 7903-7933.

5-27. Oyama, V. I., Carle, G. C., Woeller, F., Pollack, J. B., Reynolds, R. T., and Craig, R. A.: Pioneer Venus Chromatography of the Lower Atmosphere of Venus. J. Geophys. Res., vol. 85, 1980, pp. 7891-7902.

5-28. Krasnopolsky, V. A. and Parshev, V. A.: Chemical composition of the atmosphere of Venus. Nature, vol. 292, 1981, pp. 610-613.

5-29. Kucheryavenkov, A. I., Yakovlev, O. I., Pavelyev, A. G., Azarh, S. L., Matuygov, S. S., Kaevitser, V. I., Rogalsky, V. I., Polyakov, V. S., and Kalashnikov, I. E.: Soviet Space Res., vol. 14, 1976, pp. 693-696.

5-30. Hoffman, J. H., Hodges, R. R., Donahue, T. M., and McElroy, M. B.: Composition of the Venus lower atmosphere from the Pioneer Venus mass spectrometer. J. Geophys. Res., vol. 85, 1980, pp. 7882-7890.

5-31. Rossow, W. B., Del Genio, A. D., Limaye, S. S., Travis, L. D., Stone, P. H.: Cloud Morphology and Motions from Pioneer Venus Images. J. Geophys. Res., vol. 85, 1980, pp. 8107-8128.

5-32. Knollenberg, R., Travis, L., Tomasko, M., Smith, P., Ragent, B., Esposito, L., McCleese, D., Martonchik, J., and Beer, R.: The clouds of Venus: A synthesis report. J. Geophys. Res., vol. 85, 1980, pp. 8059-8081.

5-33. Knollenberg, R. and Hunten, D. M.: The microphysics of the clouds of Venus: Results of the Pioneer Venus particle size spectrometer experiment. J. Geophys. Res., vol. 85, 1980, pp. 8082-8088.

5-34. Cimino, J. B., Elachi, C., Kliore, A. J., McCleese, D. J., and Patel, I. R.: Polar cloud structure as derived from the Pioneer Venus Orbiter. J. Geophys. Rea., vol. 85, 1980, pp. 8082-8088.

5-35. Scarf, F. L., Taylor, W. W. L., Russell, C. T., and Brace, L. H.: Lightning on Venus: Orbiter Detection of Whistler Signals. J. Geophys. Res., vol. 85, 1980, pp. 8158-8166.

5-36. Ksanfomaliti, L. V.: Discovery of frequent lightning discharges in clouds on Venus. Nature, vol. 284, 1980, pp. 244-246.

5-37. Borucki, W. J., Dyer, J. W., Thomas, G. Z., Jordan, J. C., and Comstock, D. A.: Optical search for lightning on Venus. Geophys. Res. Lett., vol. 8, 1981, pp. 233-236.

5-38. Taylor, F. W., Beer, R., Chahine, M. T., Diner, D. J., Elson, L. S., Haskins, R. D., McCleese, D. J., Martonchik, J. V., Reichley, P. E., Bradley, S. P., Delderfield, J., Schofield, J. T., Farmer, C. B., Froidevaux, L., Leung, J., Coffey, M. T., and Gille, J. C.: Structure and Meteorology of the Middle Atmosphere of Venus: Infrared Remote Sensing from the Pioneer Orbiter. J. Geophys. Res., vol. 85, 1980, pp. 7963-8006.

5-39. Dickinson, R. E. and Redley, E. C.: Venus mesosphere and thermosphere structure, II, Day-night variations. Icarus, vol. 30, 1977, pp. 163-178.

5-40. Pollack, J. B., Toon, O. B., Whitten, R. C., Boese, R., Ragent, B., Tomasko, M., Esposito, L., Travis, L., and Wiedman, D.: Distribution and Source of the UV Absorption in Venus' Atmosphere. J. Geophys. Res., vol. 85, 1980, pp. 8141-8150.

5-41. Keating, G. M., Nicholson, J. Y. III, and Lake, L. R.: Venus upper atmospheric structure. J. Geophys. Res., vol. 85, 1980, pp. 7941-7956.

5-42. Niemann, H. B., Kasprzak, W. T., Hedin, A. E., Hunten, D. M., and Spencer, N. W.: Mass Spectrometric Measurements of the Neutral Gas Composition of the Thermosphere and Exosphere of Venus. J. Geophys. Res., vol. 85, 1980, pp. 7817-7827.

5-43. Mayer, H. G., Harris, I., Neimann, H. B., Brinton, H. C., Spencer, N. W., Taylor, H. A. Jr., Hartle, R E., Hoegy, W. R., and Hunten, D. M.: Dynamic properties of the thermosphere inferred from Pioneer Venus mass spectrometer measurements. J. Geophys. Res., vol. 85, 1980, pp. 7841-7848.

5-44. Ingersoll, A. P. and Pechman, J. B.: Venus lower atmosphere heat balance. J. Geophys. Res., vol. 85, 1980, pp. 8219-8222.

5-45. Pollack, J. B., Toon, O. B., and Boese, R.: Greenhouse Models of Venus' High Surface Temperature, as Constrained by Pioneer Venus Measurements. J. Geophys. Res., vol. 85, 1980, pp. 8223-8231.

5-46. Brace, L. H., Theis, R. F., Hoegy, W. R., Wolfe, J. H., Mihalov, J. D., Russell, C. T., and Nagy, A. F.: The dynamic behavior of the Venus ionosphere in response to solar wind interations. J. Geophys. Res., vol. 85, 1980, pp. 7663-7678.

5-47. Elphic, R. C., Russell, C T., Slavin, J. A., and Brace, L. H.: Observations of the dayside ionopause and ionosphere of Venus. J. Geophys. Res., vol. 85, 1980, pp. 7679-7696.

5-48. Miller, K. L., Knudsen, W. C., Spenner, K., Whitten, R. C., and Novak, V.: Solar Zenith Angle Dependence of Ionospheric Ion and Electron Temperatures and Density on Venus. J. Geophys. Res., vol. 85, 1980, pp. 7759-7764.

5-49. Taylor, H. A., Brinton, H. C., Bauer, S. J., Hartle, R. E., Cloutier, P. A., and Daniell, R. E. Jr.: Global Observations of the Composition and Dynamics of the Ionosphere of Venus: Implications for the Solar Wind Interaction. J. Geophys. Res., vol. 85, 1980, pp. 7765-7777.

5-50. Gombosi, T. I., Cravens, T. E., Nagy, A. F., Elphic, R. C., and Russell, C. T.: Solar wind absorption by Venus. J. Geophys. Res., vol. 85, 1980, pp. 7747-7753.

5-51. Spenner, K., Knudsen, W. C., Miller, K. L., Novak, V., Russell, C. T., and Elphic, R. C.: Observation of the Venus Mantle, the Boundary Region between Solar Wind and Ionosphere. J. Geophys. Res., vol. 85, 1980, pp. 7655-7662.

SECTION 6. MARS

6.1 INTRODUCTION

Mars, the fourth planet from the Sun, was once considered to be a likely candidate for extra-terrestrial life, but its atmosphere turns out to be thin and oxygen deficient; its surface is cold, dry, and apparently lifeless. Until the Mariner 4 flyby mission in 1965, ground-based observations provided the only information about the planet. NASA Special Publication 179, The Book of Mars [6-1], is a comprehensive guide to the early observations.

Mariner 4, followed by Mariners 6 and 7 flybys in 1969, yielded only brief looks at the planetary surface. Then, taking advantage of the favorable 1971 launch window Mariner 9 was successfully put into an orbit around the planet. At the time the spacecraft arrived at the planet, its surface was totally obscured by a dust storm. The storm subsided and by the end of the mission, over 7000 pictures had been returned electronically to Earth. The Geology of Mars [6-2] reviews the results of these missions and early Soviet missions.

Two Viking spacecraft, each consisting of an orbiter and a lander, reached Mars in 1976. A detailed account and analysis of the Viking missions is provided in References 6-3 and 6-4.

Knowledge of Mars has increased enormously with planetary landers. Much more could be learned from samples returned from the planet; undoubtedly, manned expeditions will eventually be sent to explore the planet and carry out observations on the surface and within the atmosphere. If the time ever comes when humans colonize the planets, Mars remains the most likely candidate.

6.2 DYNAMIC PROPERTIES

The dynamical properties of Mars are given in Table 6-1.

6.2.1 Comments

These data were adapted from The American Ephemeris and Nautical Almanac [6-6]. The orbit eccentricity is comparatively large, which means that there is a significant difference between perihelion and aphelion distances. The Earth-to-Mars configuration varies considerably from one opposition to another, affecting opportunities for spacecraft exploration.

The obliquity of the axis of rotation and the eccentricity of the Mars orbit are believed to have varied widely over geologic time. The obliquity has ranged from 10.8 to 38 deg, with oscillatory periods as rapid as 10^5 years. The orbital eccentricity has varied between 0.004 (circular) and 0.141 [6-7].

TABLE 6-1. DYNAMICAL PROPERTIES

Parameter	Value	Comments
Semi-major axis	22.794×10^7 km	1.523691 AU
Perihelion distance	20.665×10^7 km	1.381398 AU
Aphelion distance	24.918×10^7 km	1.666984 AU
Eccentricity	0.093387	Earth: 0.017
Orbit inclination	$1^{\circ}50'59.28''$	
Mean Orbital Velocity	24.129 km sec-1	
Sidereal year	686.97964 days	
Sidereal day	$24^{h}37^{m}22.663 \pm 0.002^{s}$	[6-5]
Solar day (1 "sol")	$24^{h}39^{m}35.238^{s}$	noon to noon
Synodic period	779.94657 days	time between Earth-Mars oppositions
Obliquity of rotation axis	25 deg	Earth: 23.5 deg
Longitude of perihelion from vernal equinox	253 deg	Epoch 1980
Earth-Mars opposition distance: max min	10.1×10^7 km 5.6×10^7 km	

6.3 PHYSICAL DATA

6.3.1 Mass, Figure, and Other Physical Properties

Table 6-2 summarizes the physical data of Mars.

6.3.2 Earth-Mars Configurations

Table 6-3 lists the Mars opposition distances through 1990 while Figure 6-1 shows some of the orbit transfer velocity data.

6.3.3 Mapping

The prime meridian for Mars passes through the small crater "Airy-O" within the large crater Airy at 5.19 deg S [6-10]. A very precise determination was made of the angle between Airy-O and the vernal equinox, allowing the longitudes of the Viking Landers to be determined accurately.

TABLE 6-2. PHYSICAL DATA

Parameter	Value	Comments
Radius		
Equatorial	3397.2 km	
Polar	3375.5 km	
Mass	6.418×10^{23} kg	0.1074 Earth
Mass Ratio: Sun/Mars	3098700.	
Mean density	3.933 g cm^{-3}	Earth: 5.41
Gravity at surface	372.52 cm sec^{-2}	Earth: 980.
Escape velocity	5.024 km sec^{-1}	Earth: 11.2
Flattening		
Dynamic	0.00522	Earth: 0.00335
Optical	0.00612	
GM	42828.32 km^3 sec^{-2}	
J_2	0.00196	Earth: 0.001083
Moment of inertia parameter (I/MR^2)	0.365	[6-8]
Magnetic dipole moment	less than 10^{22}G cm^3	see text
Direction of rotation axis (1976 epoch)	RA 317.340±0.003 deg Dec 57.710±0.002 deg	[6-5]
Normal albedo	0.1 to 0.4	
Surface temperature extremes	130 to 300°K	
Surface atmospheric pressure	5.9 to 15.0 mb	varies seasonally

TABLE 6-3. MARS OPPOSITION DISTANCES THROUGH 1990

Date	Distance (10^6 km)	Mars Season	Aerocentric Solar Longitude North
January 22, 1978	98	Spring	30
February 25, 1980	101	Spring	80
April 2, 1982	94	Summer	130
May 11, 1984	80	Summer	175
July 10, 1986	65	Fall	225
September 30, 1988	59	Fall	270
November 28, 1990	82	Winter	320

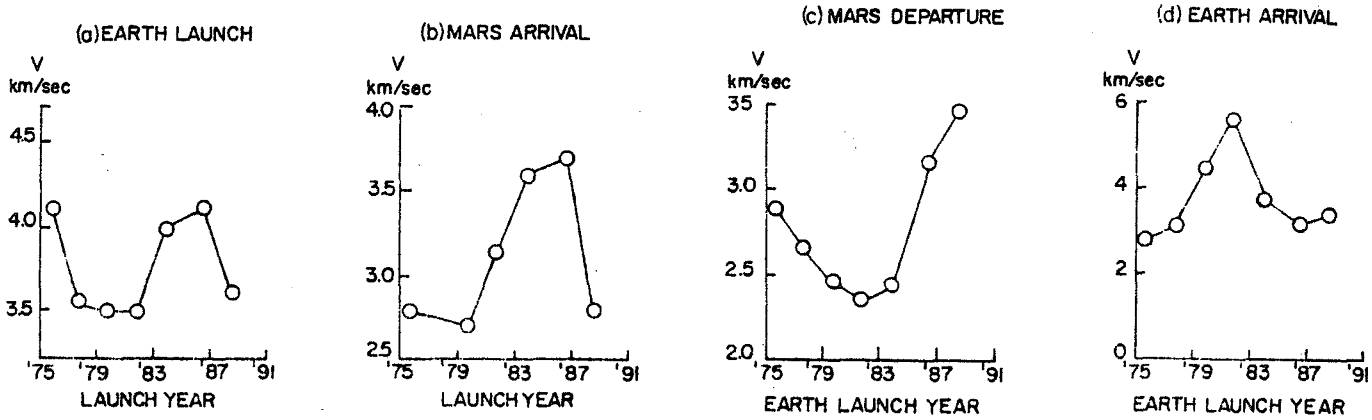

Figure 6-1. Earth-to-Mars transfer orbit velocity increments [6-9].

Topographic charts of Mars are available from the U.S. Geological Survey, as are detailed charts of Viking lander areas [6-11].

Figures 6-2a and 6-2b are global maps of Mars showing the major surface features and landforms [6-12].

6.3.4 Gravity Field

Spherical harmonic coefficients for the martian gravity field have been derived to degree and order six and twelve [6-13,6-14]. Table 6-4 gives the coefficients for normalized spherical harmonics. (To convert to unnormalized format review paragraph 2.7.1.)

Except for very specialized purposes, only C_{20} and C_{22} would be necessary to use (paragraphs 2.3.2 and 3.3.2).

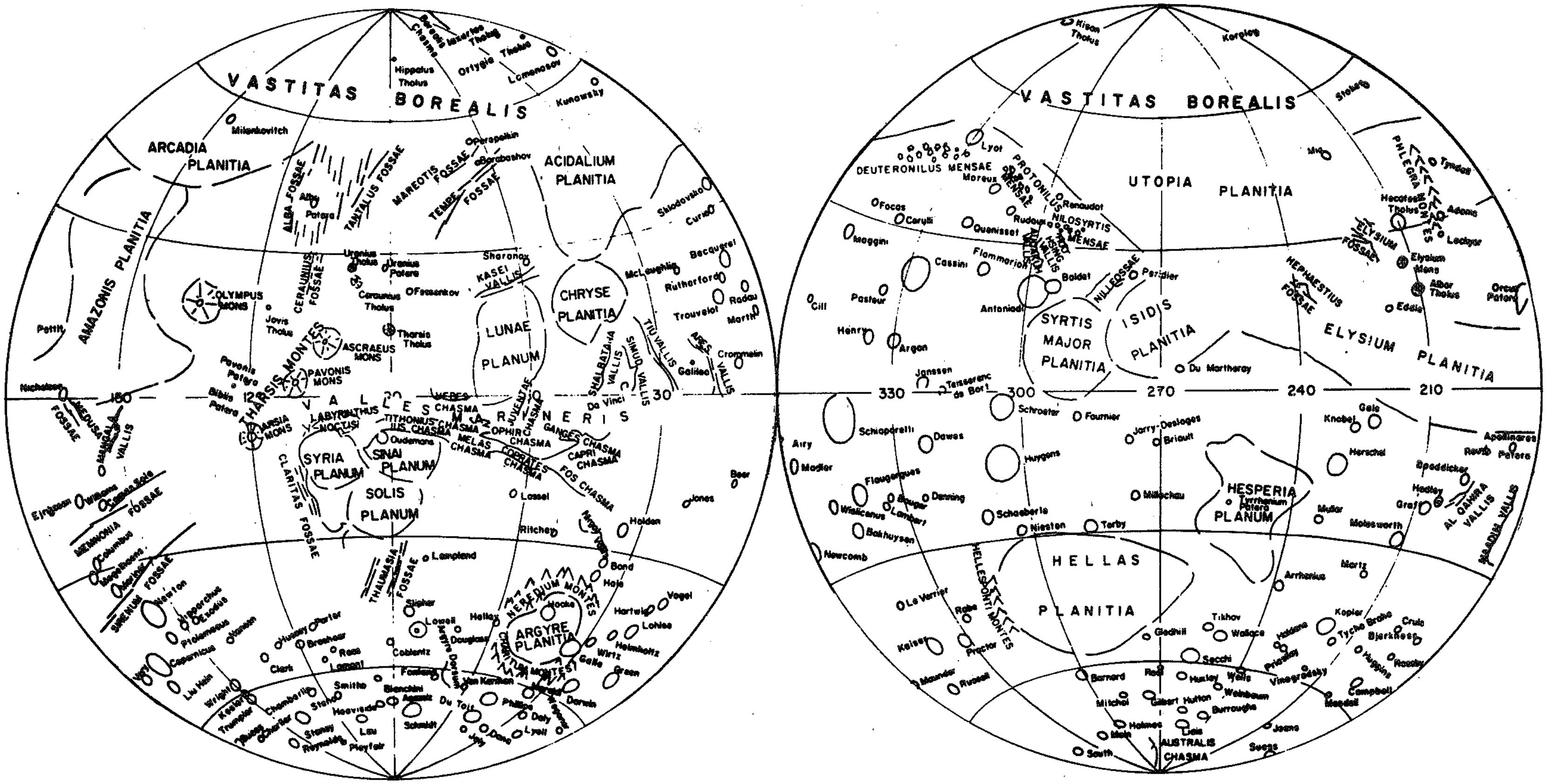

Figure 6-2a. Major landforms on Mars [6-12]. Modern nomenclature as established by the IAU.

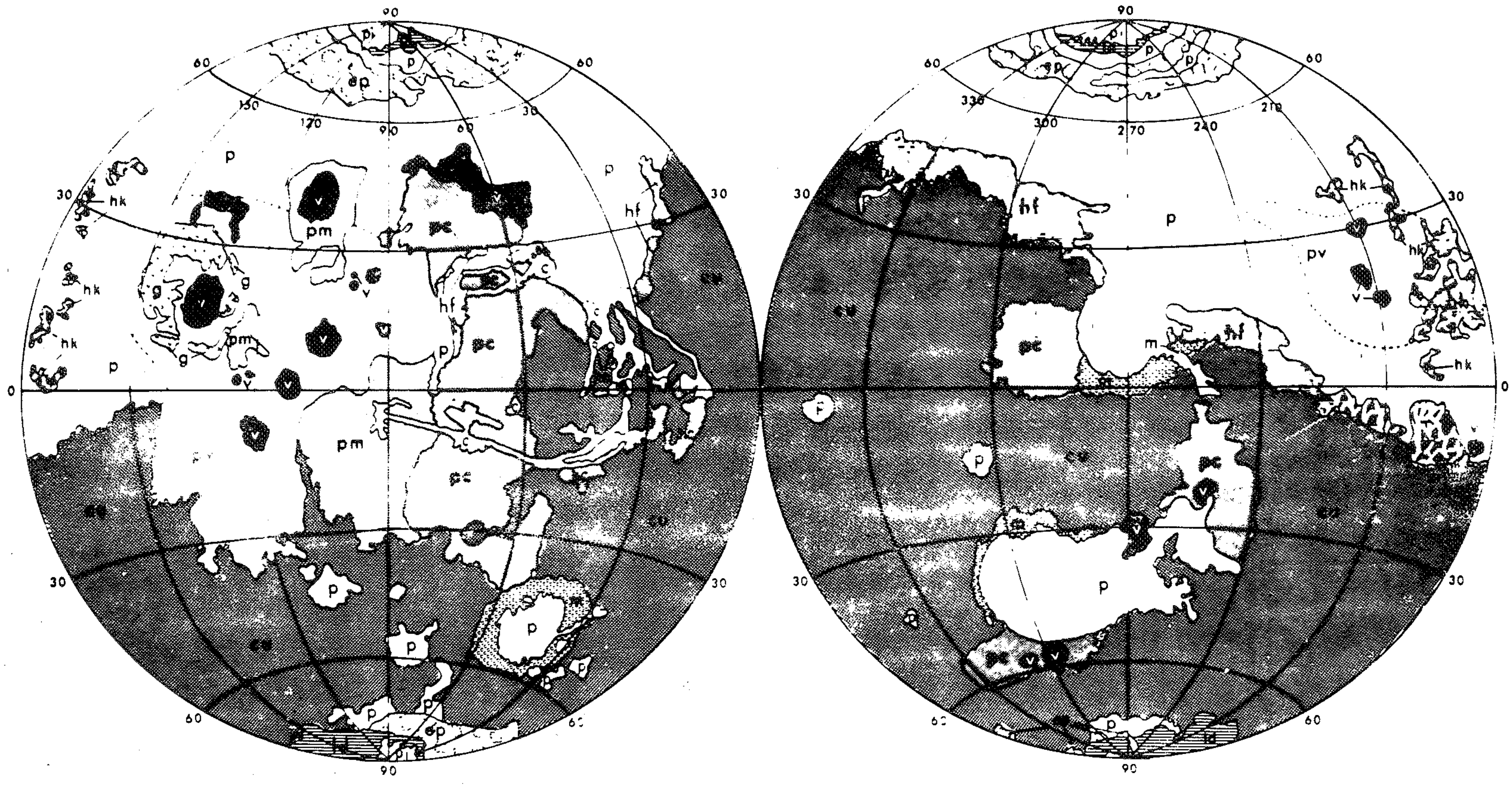

Legend:
pi (permanent ice)
ep (etched plains)
pc (cratered plains)
hk (hummocky-knobby)
p (plains, undivided)
cu (cratered terrain)
ld (layered deposits)
v (volcanic deposits)
hc (hummocky terrain, chaotic)
c (channel deposits)
g (grooved terrain)
m (mountainous terrain)

Figure 6-2b. Physiographic provinces of Mars [6-12].
(Based on Mariner 9 data.)

TABLE 6-4. NORMALIZED SPHERICAL HARMONIC COEFFICIENTS

n	m	$C_{nm} \times 10^7$	$S_{nm} \times 10^7$
2	0	−8746 ± 2*	. . .
2	2	−850 ± 3	497 ± 2
3	0	−126 ± 9	. . .
3	1	34 ± 3	243 ± 6
3	2	−157 ± 3	80 ± 3
3	3	352 ± 4	250 ± 4
4	0	61 ± 3	. . .
4	1	44 ± 3	−33 ± 4
4	2	−9 ± 2	−88 ± 3
4	3	68 ± 2	−1 ± 3
4	4	−2 ± 4	−121 ± 5
5	0	−23 ± 4	. . .
5	1	−2 ± 4	25 ± 3
5	2	−44 ± 3	−7 ± 4
5	3	30 ± 3	0 ± 3
5	4	−48 ± 6	−36 ± 4
5	5	−50 ± 6	31 ± 5
6	0	20 ± 6	. . .
6	1	24 ± 4	−1 ± 4
6	2	14 ± 5	20 ± 3
6	3	9 ± 4	−7 ± 4
6	4	23 ± 4	31 ± 5
6	5	21 ± 5	2 ± 6
6	6	28 ± 5	2 ± 5

*C_{20} = (−1.9557 ± 0.0004) × 10^{-3} unnormalized.

6.3.5 Magnetic Field

The magnetic field of Mars has not been adequately investigated. Interaction of the planet with the solar wind may imply the existence of an intrinsic dipole of the order 10^{23} G cm^3, (or 10^{-4} the terrestrial value) but this is at the present limit of detectability [6-15]. Such a small value is surprising, if Mars is assumed to have a core about the size of Mercury's (as some believe) since its rotation rate is close to Earth's. If there were an interior dynamo, it should produce a planetary magnetic moment about 1000 times greater than the limit placed by the experimental data [6-16]. It may be that Mars has some residual surface magnetism and lacks an operating dynamo, like the Earth's Moon.

Questions about Mars' magnetic field will only be resolved by placing magnetometers on the planet or in low orbit, or by return of rock specimens.

6.4 INTERIOR

6.4.1 Core

The average density of Mars (3.9 g cm^{-3}) is considerably less than Earth's, suggesting less pronounced core differentiation. Past volcanism requires a molten interior, at least at one time. Estimates of core size and composition limits are given in Reference 6-17: pure Fe: radius 0.4 R_m, pure FeS: radius 0.6 R_m. The center of figure for Mars is displaced from the center of mass by 2.5 km toward 62 deg S, 272 deg W. The geometric flattening (0.00612) is too large and the dynamic flattening (0.00522) is too small for Mars to be homogeneous and in hydrostatic equilibrium.

6.4.2 Crust

Assuming zero crustal thickness at Hellas, minimum crustal thickness is estimated to be 28 ± 4 km [6-18].

6.5 SURFACE

The global topographic contour and albedo (Fig. 6-3) map of Mars shows several large scale features: the Tharsis Bulge centered at 101 deg W, 14 deg S; the large southern basins of Hellas and Argyre at 290 deg W, 50 deg S, and 40 deg W; and the huge equatorial canyons comprising Valles Marineris just east of the Tharsis summit.

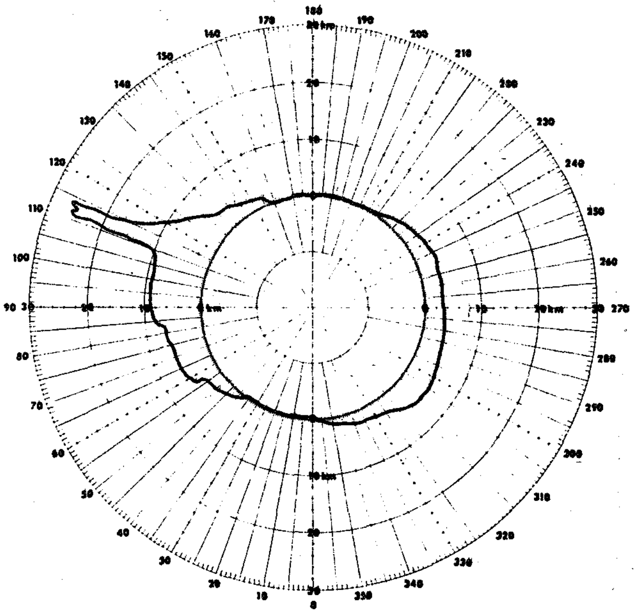

Figure 6-3. Topographic profile along martian equator. Zero circle represents topographic datum, and other radians represent elevation [6-19]. (Radial scale is greatly exaggerated.)

The distribution of craters is asymmetrical over the planet. The northern third is relatively lightly cratered; the southern two-thirds is heavily cratered. Light cratering of the north implies it is a younger region with a different crustal type or thickness [6-20].

The mean altitude above datum for the two hemispheres also is very different as clearly shown in Figure 6-4. Note the topographic lows surrounding the polar regions (Fig. 6-2b).

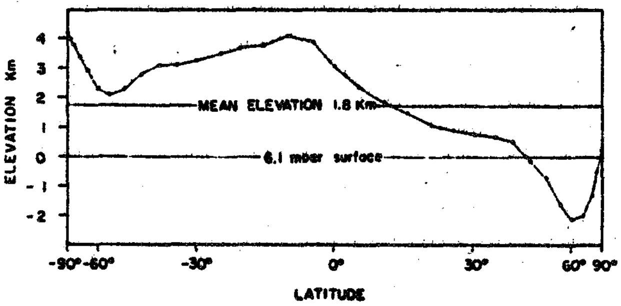

Figure 6-4. Average elevation of Mars latitude belts [6-2].

6.5.1 Surface Morphology

Mars exhibits a great variety of surface features: craters and cratered terrain, channels and fluvial features, tectonic features, volcanic features, aeolian features, and the polar regions. In this discussion, special attention is given to the Viking Lander sites, since detailed photographic information is available for them.

6.5.2 Cratered Terrain and Craters

Mars can be transected by a plane inclined approximately 40 deg to the equator such that over 90 percent of the densely cratered terrain lies on the southerly hemisphere so defined [6-21].

The sparsely cratered plains, common in northern latitude regions, appear to antedate the events which bombarded the ancient densely cratered terrain. They are, nonetheless, fairly old (3 to 4 billion years). On the sparsely cratered plains are a complex variety of features that have been attributed to the interplay of impact, volcanic, aeolian, and ice-related processes.

The largest impact crater on Mars is Hellas Planitia, centered at 40 deg S and 290 deg W. The basin is 1600 km in diameter and 6-km deep, more than 4 km below the datum at its lowest point. Roughly circular in outline, Hellas Planitia is undoubtedly an original impact structure, but it has been highly degraded. Argyre Planitia is a similar, although smaller, impact crater [6-2].

The majority of moderately sized craters (< 100 km) have ejecta blankets distinctively different from those on the Moon or Mercury. They show one or more layers of ejecta, each with a distinct outer ridge or rampart, and were given the name "rampart craters." Their characteristic ejecta configuration appears to be due to a radial outward flow of ground-hugging debris after crater formation, perhaps from melting ground ice or permafrost [6-21].

Pedestal craters, another feature peculiar to Mars, are found primarily in the northern hemisphere between 30 and 70 deg N. Typically, the crater is surrounded by a low, nearly circular platform or pedestal. Pedestal craters are believed to be the result of repeated deposition and erosion of extensive debris layers by wind. Such events appear to have occurred widely in this region of the northern hemisphere. The ejecta blanket is believed to have protected the underlying layers from removal, resulting in the pedestals [6-21].

The densely cratered hemisphere has been heavily modified into regions of chaotic, fretted, and knobby terrain.

Chaotic terrain refers to areas that have apparently sunk below the surrounding terrain to form irregularly shaped, jostled blocks. Large channels, often characteristic of fluvial flow, originate at many of the chaos areas. According to current theory, chaotic terrain was created when the ground collapsed after melting of subsurface ice.

Fretted terrain is characteristic of the boundary between the densely cratered highlands and the sparsely cratered lowlands. Typically, this terrain is a complex interfingering of high standing remnants of the densely cratered terrain and intercrater plains and, at a low elevation (usually 1 to 2 km), the more sparsely cratered plains. Throughout the fretted terrain, debris flow occurs at the boundary between the cratered plateaus and the lower plains. The mechanisms of debris flow may be linked to the melting of ground ice.

Knobby terrain represents the transition regions between the fretted terrain and the sparsely cratered plains to the north. Mechanisms responsible for the erosion and/or reformation of the northern plains seem to have reshaped the cratered plateaus of the fretted terrain into smaller, and form-rounded, equidimensional hills characteristic of the knobby terrain.

6.5.2.1 Crater Statistics

The observed distribution of craters is bimodal (Fig. 6-5), with two main types: larger craters (diameter > 5 km) which tend to be shallow with relatively low rims; and smaller craters that are generally bowl-shaped. Crater distribution varies with size. For very large craters (>64 km) the distribution is nearly saturated (like the lunar highlands).

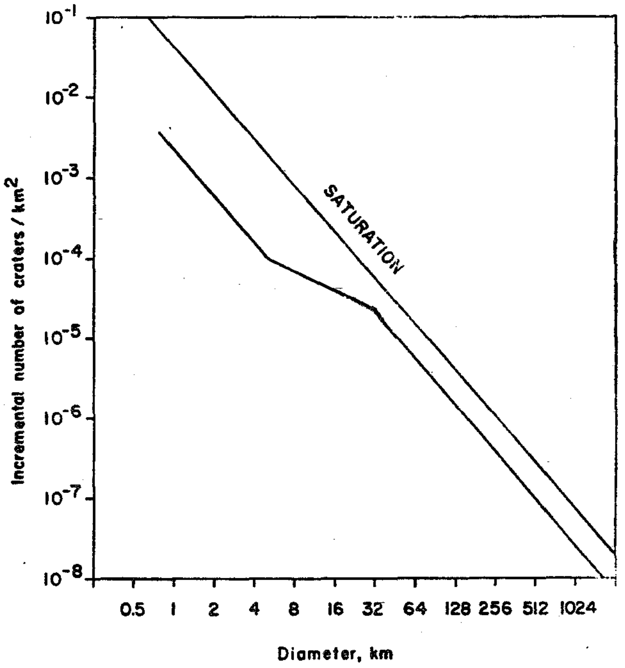

Figure 6-5. Crater distributions on Mars [6-2].

6.5.2.2 Block Distributions

Block distribution data have been derived for the Viking 1 and 2 landing sites from the detailed pictures sent back. Figure 6-6 shows rocks in the neighborhood of Viking Lander 2. Figure 6-7 shows derived size distributions. The similarity of the two sites, which differ geologically, lends some measure of confidence to regional extrapolations [6-22].

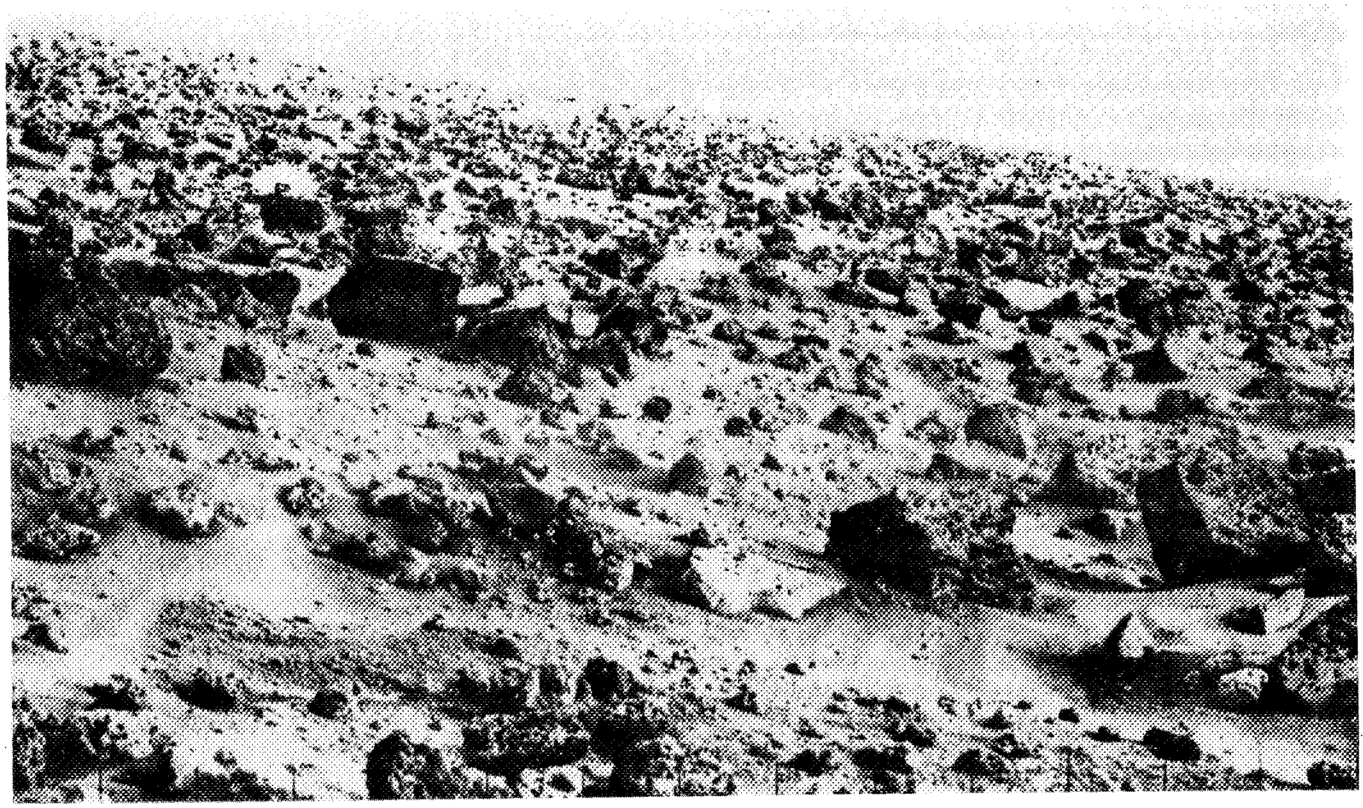

Figure 6-6. Viking Lander 2 site [6-12].

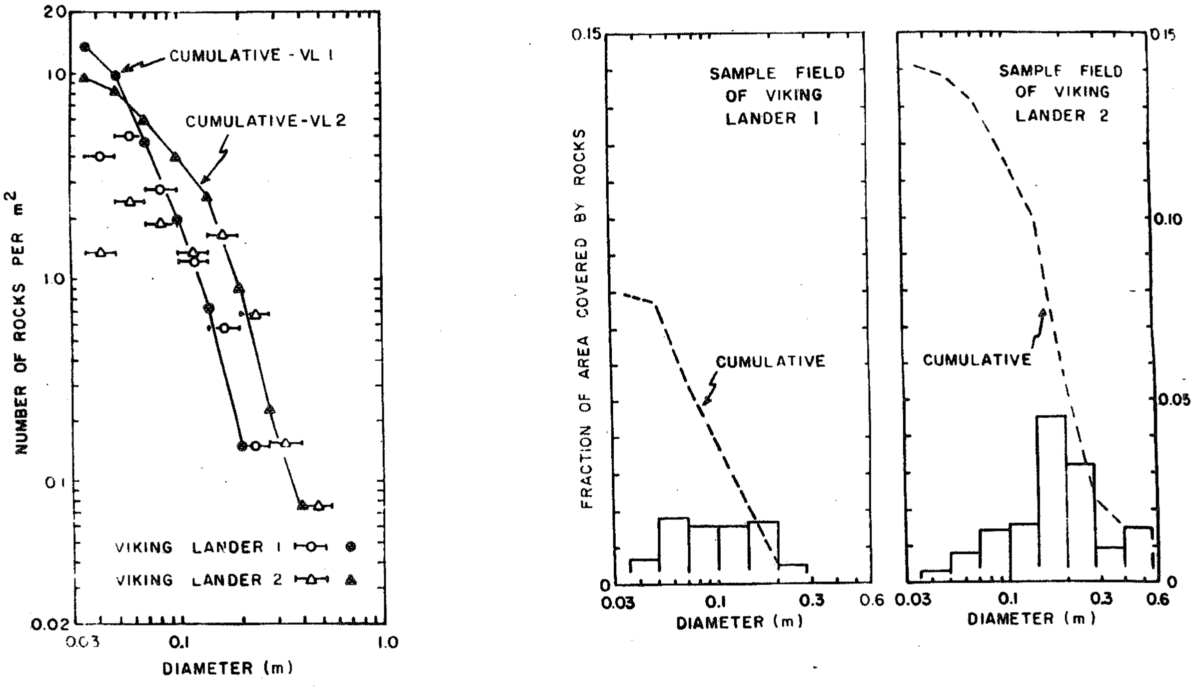

(a) Size frequency distributions.

(b) Fraction of area covered by rocks.

Figure 6-7. Size distributions in sample fields of Viking 1 and 2 landing sites [6-23].

6.5.3 Channels and Fluvial Features [6-21]

The observed channels suggest formation by running water. (There is no connection between these features and the famous "canals," which proved to be an optical illusion.) Liquid water cannot exist on Mars at present since the atmospheric pressure is below the triple-point; therefore, either the channels were formed by other processes, such as faulting, lava flows, or wind action, or atmospheric conditions were very different sometime in the past. There are three main types: fretted channels, runoff channels, and outflow channels.

Fretted channels are flat-floored sinuous valleys. They are mostly in fretted terrain which occurs in two latitudinal bands, 25 deg wide, centered on 40 deg N and 45 deg S.

Runoff channels typically start small and increase in size and depth downstream and have a characteristic V-shaped cross section. They almost exclusively occur in densely cratered terrain. The extensive, well-integrated tributary networks associated with these channels are strong evidence for water erosion in some past epoch.

The outflow channels appear to be the result of catastrophic flooding and most originate in chaotic terrain. They are deepest close to their sources and extend for hundreds of kilometers with widths typically tens of kilometers.

6.5.3.1 Tectonic Features: Tharsis and Valles Marineris

Compared to Earth, Mars is seismically inactive at present, though there is ample evidence for tectonic activity in the past. Most notable is the Tharsis Bulge, a roughly circular feature covering nearly a quarter of the planet's surface, with a summit at an elevation over 11 km above the datum. Most of the large shield volcanoes are found atop Tharsis. Surrounding Tharsis is a radial pattern of faults. As only the oldest surfaces retain the fault pattern, Tharsis is believed to have been formed early in the planet's history.

Valles Marineris is a collection of steep walled canyons extending east from the base of Tharsis for about 4500 km just south of the equator. Different canyon systems merge and in places reach depths of over 7 km and widths of 600 km [6-21]. The general alignment of Valles Marineris, the presence of fault scarps, and the absence of erosion deposits strongly suggest the canyons were produced by faulting, probably related to the formation of the Tharsis Bulge [6-24].

6.5.4 Volcanic Features

Mars has many volcanic features. Large shield volcanoes, roughly circular mountains with central caldera and gently sloping (<6 deg) flanks, are primarily clustered in regions of Tharsis and Elysium. The largest, Olympus Mons, is centered at 18 deg N, 133 deg W, with summit 22 km above the surrounding plains, 27 km above the datum.

At the base of the central edifice is an outward facing escarpment, 550 km in diameter and in places up to 6-km high. In many places lava flows drape over the escarpment and extend far beyond it, so the mean diameter of the shield is approximately 700 km. On the Tharsis Bulge are three other large shield volcanoes, Arisia Mons, Pavonis Mons, and Ascraeus Mons which resemble Olympus Mons, as well as terrestrial volcanic shields such as Mauna Loa.

On the Elysium Bulge are three volcanoes, Elysium Mons, Hecates Thalus, and Albor Thalus. The largest, Elysium Mons, is a shield volcano, 14-km high, 170-km wide, comparable to the Tharsis shields, though with significantly steeper flanks (10 to 12 deg).

Numerous volcanic features, which range in size down to the limit of resolution of the available photography, have been identified outside the two main provinces of Tharsis and Elysium.

6.5.5 Aeolian Features

Mars wind action is well known from the vast annual dust storms. Yet their erosional effect appears to be small; they mostly recirculate already eroded debris [6-21].

Extensive dune fields exist on Mars. Around the north pole is a nearly continuous belt of dunes which includes both transverse and barchanoid types [6-12]. The same pattern persists over large areas, suggesting a constant direction and strength for the wind that formed them. In a few areas several wind systems are implied. Dune fields are also common around the south pole, but are mostly restricted to the interiors of large craters. The mechanisms for forming sand-size particles are still unknown. The windblown dust particles deposited at the Viking Lander sites would not form dunes. It is not known whether dune forming processes are still active.

Dust storms primarily redistribute fine debris. This redistribution seems to explain the seasonal color changes that were once thought to be evidence of vegetation. (The bright regions are attributed to accumulations of a thin layer of fine debris, while the dark regions are the underlying solid surface.) The wind-driven debris deposits are thin, only centimeters or even millimeters thick.

A peculiar aeolian feature is the polar laminated terrain discussed in the following paragraph.

6.5.6 Polar Regions

The distinctive polar caps of Mars are easily visible from the Earth, and their seasonal advance and retreat have been observed for more than two centuries. The two caps are not symmetrical, they differ in maximum and minimum size, as well as in composition. The northern cap extends down to between 50 and 64 deg N at maximum and retreats to 87 deg N at minimum. The south polar cap extends down to 40 deg S at maximum, retreats more rapidly in the spring, and nearly disappears in summer. Both seasonal caps are CO_2 ice; the northern residual cap is H_2O ice, the residual south polar cap may be mostly CO_2 [6-25]. Their differences have been attributed to a number of factors: the planet's eccentric orbit and near coincidence of southern summer solstice and perihelion; high global dust-storm activity during southern summer, resulting in cooler surface temperatures and more isothermal atmospheric temperature profiles; and the different elevation and surrounding topography of the two polar regions.

Sequences of layered deposits form the unique laminated terrain of the martian polar regions. They apparently are thick accumulations of volatiles (most likely water-ice [6-21,6-26] and airborne dust [6-27 through 6-29]. The layered structure is believed to be due to climatic changes that have resulted either from orbit variations [6-7] or from variations in solar luminosity [6-29]. If the layered structure has, indeed, arisen from solar variations, its study could lead to better understanding of long-term climatic changes on the Earth.

The polar laminated terrain has been sculptured into a series of stair-like incised valleys and gently sloping escarpments, 100- to 1000-m high, 3- to 10-km wide, and hundreds of kilometers long [6-21,6-30]. The origin of these valleys and escarpments remains controversial [6-27,6-31,6-32,6-33,6-34].

6.5.7 Permafrost

There is evidence that a thick permafrost (mean annual temperature less than 273°K) covers the entire planet and extends to a depth of about 1 km at the equator and several kilometers at the pole. Within 40 deg of the equator, however, the ground is permanently dehydrated to depths of at least 1 m. Existence of water-ice below these depths depends on the permeability of the soil [6-12,6-35].

6.5.8 The Viking Lander Sites

Both Viking Lander sites are in the sparsely cratered northern lowlands. Viking 1 landed on Chryse Planitia, 47.97 deg W, 22.27 deg N, at about 16:00 local time. Viking 2 landed on Utopia Planitia, 225.75 deg W, 47.67 deg N, at about 10:00 local time. Both landed during local summer. The Viking 1 and Viking 2 sites are 1.5 km and 2.5 km below the mean pressure level of the planet, respectively [6-36].

The choice of lander sites was based upon a requirement for smooth terrain. The two sites are topographically similar: low rolling hills, mostly covered by fine-grain debris, and only 8 percent of each area contained rocks 3.5 cm or larger (Fig. 6-7).

The surface samples analyzed from both sites are similar and probably representative of fine debris everywhere on the planet. The atmospheric and meteorological observations from the two sites are also likely to be indicative of the planet as a whole.

6.5.9 Composition of Surface Material

The X-Ray Fluorescence Experiment analyzed the elemental composition of the loose debris at the Viking landing site [6-37]. The experiment could not detect elements with atomic numbers less than 12 (Mg). The determination for a typical Mars sample appears below, and the assumed mineralogical composition is given in Tables 6-5 and 6-6 [6-38 through 6-40]. (Phosphorus is not listed because its signal is hidden by S and Si, although minor amounts may be present.)

The fine-grained debris probably consists mostly of Fe-rich clays with minor amounts of kieserite ($MgSO_4 \cdot H_2O$), calcite ($CaCO_3$), and rutile (TiO_2). The surface

TABLE 6-5. ELEMENTAL COMPOSITION OF THE VIKING 1 LANDER SITE [6-37]

Element	Percent by Mass
Mg	5.0 ± 2.5
Al	3.0 ± 0.9
Si	20.9 ± 2.5
S	3.1 ± 0.5
Cl	0.7 ± 0.3
K	<0.25
Ca	4.0 ± 0.8
Ti	0.51 ± 0.2
Fe	12.7 ± 2.0
L*	50.1 ± 4.3
X**	8.4 ± 7.8
Rb	<30 ppm
Sr	60 ± 30 ppm
Y	70 ± 30 ppm
Zr	<30 ppm

*L is the sum of all elements not directly determined.

**If the detected elements are all present as their common oxides (Cl excepted) then X is the sum of components not directly detected, including H_2O, NaO, CO_2, and NO_x.

TABLE 6-6. CHEMISTRY OF THE VIKING 1 LANDER SITE [6-39,6-40]

Compound	Percent Mass
SiO_2	44.7
Al_2O_3	5.7
Fe_2O_3	18.2
MgO	8.3
CaO	5.6
K_2O	<0.3
TiO_2	0.9
SO_3	7.7
Cl	0.7
SUM	91.8

material contains significant quantities of adsorbed volatiles. When heated to 500°C, the sample material released about 1 percent water by weight and from 50 to 100 ppm CO_2 [6-41]. Additionally, trace amounts of O_2 (less than 7×10^{-7} moles g^{-1}) and other gases were released upon humidification [6-42]. There may be significant amounts of CO_2 and H_2O adsorbed into the top regolith layers, perhaps as much as 400 g cm^{-2} adsorbed CO_2, which is equivalent to a surface pressure at equilibrium of over 100 mb [6-43].

The results of the Viking biological experiments support the suggestion that the martian top regolith contains highly oxidizing compounds [6-44]. The hypothesized peroxides and superoxides could be produced by the ultraviolet radiation which reaches the martian surface since there is no blocking ozone layer in the atmosphere.

6.5.10 Optical, Thermal, and Mechanical Soil Properties

Optical, thermal, and mechanical soil properties of the Mars top regolith are given in Table 6-7 while those for the Viking 1 landing site are compared in Table 6-8 with the Moon.

TABLE 6-7. PROPERTIES OF THE MARS TOP-REGOLITH*

Parameter	Nominal Value
Thermal Conductivity	2 to 20×10^{-5} cal sec^{-1} cm^{-1} K^{-1}
Specific Heat	0.15 to 0.19 cal g^{-1} K^{-1}
Emissivity	0.90 to 0.98
Thermal Inertia	100 to 600 $cm^2 s^{\frac{1}{2}} K/cal$: $(k \rho c)^{-\frac{1}{2}}$
Albedo	0.2 to 0.4
Bolometric Albedo	0.43 to 0.93*
Dielectric Constant	2.3 to 3.5
Bulk Density (porosity)	1 to 1.8 g cm^{-3}
Penetration Resistance	0.3 N cm^{-2} cm^{-1}
Cohesion	0.01 to 0.1 N cm^{-2}
Adhesion	10^{-4} to 10^{-3} N cm^{-2}
Coefficient of Sliding Friction	0.55 to 0.65
Density	3.933 g cm^{-3}

*Equatorial Regions [6-45].

TABLE 6-8. COMPARISON OF VIKING 1 LANDING SITE AND LUNAR SOIL PROPERTIES

Property*	Mars (Viking 1)		Lunar Depth	
	Sandy Flats	Rocky Flats	0 to 0.01 m	0.1 to 3 m
Bulk density (porosity) (g/cm^3)	1 to 1.6	1.8	1.0 to 1.3	1.5 to 2.1
Particle size (surface and near surface)				
10 to 100 μm (%)	60	30	30 to 60	
100 to 2000 μm (%)	10	30	30 to 35	
Angle of internal friction (deg)	20 to 40	40 to 45	35 to 50	
Penetration resistance ($dyne/cm^2/cm$)	3×10^4	6×10^5	3×10^5	
Cohesion ($dyne/cm^2$)	10^3 to 10^4		10^4	
Adhesion ($dyne/cm^2$)	10^1 to 10^2		10^2 to 10^3	
Coefficient of sliding friction	0.55 to 0.65		0.5 to 1	

*Soil properties deduced from Viking 1 data. Lunar soil is included for comparison and because the nominal engineering design soil model was based on the lunar soil [6-46].

The Viking Infra-Red Thermal Mapper experiment aboard the orbiters indicates a wide range of surface thermal properties and large atypical regions. Planetwide measurements of the infrared emission and reflection yielded information on the thermal inertia of the surface [6-45]. Temperatures observed during the Viking primary mission ranged from 130 to 290°K.

6.6 ATMOSPHERE

The general temperature structure of the atmosphere is shown in Figure 6-8.

6.6.1 The Lower Atmosphere, Temperature and Pressure

The mean temperature profile for the martian lower atmosphere at summer temperate latitudes, derived from data gathered during the Viking entries, is shown in Figure 6-9 [6-36].

Model atmospheres for "warm" and "cool" conditions, ±10°K from nominal, coupled with high and low surface pressures, are shown in Table 6-9 [6-36].

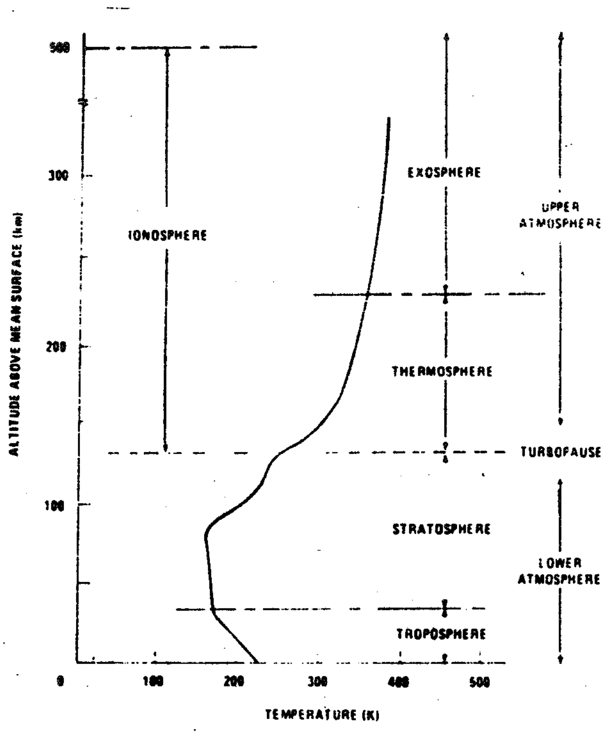

Figure 6-8. General temperature structure of the atmosphere of Mars.

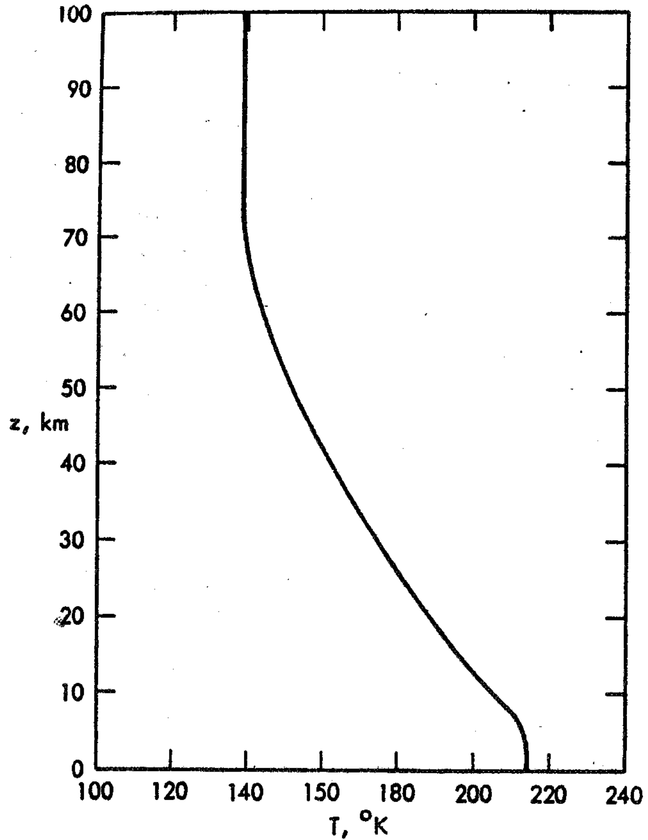

Figure 6-9. Nominal mean temperature profile for summer temperate latitudes (6-36).

TABLE 6-9. SUMMER, MID-LATITUDE, DAILY-MEAN ATMOSPHERE OF MARS (COOL AND WARM MODELS) (6-36)

	Cool, Low Pressure Model				Warm, High Pressure Model			
z, km	T, ^{o}K	p, mb	ρ, kg/m^{2}	p/p_o	T, ^{o}K	p, mb	ρ, kg/m^{3}	p/p_o
0	204	5.9	1.51×10^{-2}	1.000	224	7.8	1.82×10^{-2}	1.000
4	204	4.03	1.03	0.683	224	5.51	1.29	0.706
8	199	2.74	7.20×10^{-3}	0.464	219	4.09	9.77×10^{-3}	0.524
12	191	1.84	5.04	0.312	211	2.85	7.07	0.366
16	185	1.22	3.45	0.207	205	1.97	5.01	0.252
20	178	7.96×10^{-1}	2.34	0.135	198	1.34	3.54	0.172
24	173	5.13	1.55	8.70×10^{-2}	193	9.03×10^{-1}	2.45	0.116
28	168	3.27	1.02	5.54	188	6.03	1.68	7.73×10^{-2}
32	163	2.06	6.60×10^{-4}	3.49	183	3.99	1.14	5.11
36	158	1.28	4.23	2.17	178	2.61	7.67×10^{-4}	3.35
40	152	7.81×10^{-2}	2.69	1.32	172	1.69	5.13	2.16
44	148	4.70	1.66	7.96×10^{-3}	168	1.08	3.36	1.38
48	144	2.79	1.01	4.73	164	6.83×10^{-2}	2.18	8.75×10^{-3}
52	140	1.64	6.12×10^{-5}	2.78	160	4.28	1.40	5.48
56	137	9.49×10^{-3}	3.62	1.61	157	2.65	8.84×10^{-5}	3.40
60	134	5.44	2.12	9.22×10^{-4}	154	1.63	5.55	2.09
64	132	3.09	1.22	5.23	152	9.99×10^{-3}	3.44	1.28
68	130	1.74	7.01×10^{-6}	2.95	150	6.08	2.12	7.79×10^{-4}
72	129	9.76×10^{-4}	3.96	1.65	149	3.68	1.29	4.72
76	129	5.47	2.22	9.27×10^{-5}	149	2.23	7.83×10^{-6}	2.86
80	129	3.07	1.24	5.20	149	1.35	4.75	1.73
84	129	1.72	6.99×10^{-7}	2.92	149	8.21×10^{-4}	2.88	1.05
88	129	9.70×10^{-5}	3.93	1.64	149	4.99	1.75	6.39×10^{-5}
92	129	5.46	2.22	9.26×10^{-6}	149	3.03	1.07	3.89
96	129	3.08	1.25	5.22	149	1.85	6.49×10^{-7}	2.37
100	129	1.74	7.06×10^{-8}	2.95	149	1.13	3.96	1.44

To represent variations in the summertime atmosphere, temperature profiles were displaced by ±10°K from the nominal. This variation everywhere exceeds the maximum deviation of the Viking 1 and Viking 2 mean curves from the nominal by at least a factor of 2. The range ±10 deg about the nominal is chosen as a reasonable bound for warm and cool models and appears suitable down to the near-surface level and at the surface to near the end of the northern summer season.

The cool model has pressure falling most rapidly with altitude and, hence, is combined with a selected minimum value of surface pressure, 5.9 mb, to define a cool, low-pressure model. This model would tend to occur near 160-deg solar longitude at northern latitudes about 45 deg. By similar reasoning, the warm model is associated with a maximum level of surface pressure, 7.8 mb, to define a warm high-pressure model. The 7.8-mb maximum occurs in southern early summer around 280-deg solar longitude and might tend to occur around 25-deg south latitude where the solar incidence at noon is normal.

The selected combinations of surface pressure and temperature profile do not yield the greatest range in surface density which, in the models, ranges from 0.0151 to 0.0182 kg/m^3 or ±9.3 percent about the mean of 0.0166 kg/m^3. The maximum range of surface density is obtained by combining the cool temperature limit with the maximum surface pressure and vice versa. This yields surface (datum level) densities from 0.0137 to 0.0200 kg/m^3. (The lower limit might occur near solar longitude 160 deg at subsolar latitudes; the upper limit, at Ls = 280 deg, θ = 45 deg S.) However, the selected models do yield the maximum density range at high altitudes where entry vehicles must decelerate, showing a range of 5.6/1 at 100 km [6-36].

6.6.2 Lower Atmosphere Composition

The composition of the lower atmosphere as determined by mass spectrometers on the Viking landers is given in Table 6-10 while Table 6-11 gives isotopic ratios. The major constituent is CO_2. Its abundance varies during the martian year by 26 percent, slightly changing the mixing ratios of the other gases [6-47].

TABLE 6-10. COMPOSITION OF THE MARTIAN LOWER ATMOSPHERE [6-48]

Gas	Percent Volume
Carbon Dioxide (CO_2)	95.32 percent
Nitrogen (N_2)	2.7 percent
Argon (Ar)	1.6 percent
Oxygen (O_2)	0.13 percent
Carbon Monoxide (CO)	0.07 percent
Water Vapor (H_2O)	0.03 percent variable
Neon (Ne)	2.5 ppm
Krypton (Kr)	0.3 ppm
Xenon (Xe)	0.08 ppm

TABLE 6-11. ISOTOPE RATIOS IN ATMOSPHERIC GASES (6-36)

Ratio	Mars	Earth
$^{12}C/^{13}C$	90	89
$^{16}O/^{18}O$	500	499
$^{14}N/^{15}N$	165	277
$^{40}Ar/^{36}Ar$	3000	292
$^{129}Xe/^{132}Xe$	2.5	0.97

The traces of ozone detected by Mariner 9 are not enough to block solar ultraviolet radiation, though ozone may influence the atmospheric radiation balance [6-49]. A maximum of 57 μm STP over the polar regions during winter was reported [6-50]. Typical values range from 3 μm in summer to 16 μm in winter over the polar regions.

The average amount of atmospheric water vapor is 0.03 percent by volume, or approximately 10 precipitable microns. The water vapor concentration is closely linked to the temperature distribution: during most of the year and at most latitudes the atmosphere holds all the water possible (i.e., the relative humidity is 100 percent at night) [6-51].

The isotopic ratios in atmospheric gases, compared to terrestrial values, appear in Table 6-11. The anomalous nitrogen and argon ratios can be used to put constraints on the history of volatiles in the atmosphere of the planet [6-38,6-52,6-53, 6-54,6-55].

6.6.3 Meteorology

6.6.3.1 Meteorological Parameters and Length of Seasons

Tables 6-12 and 6-13 list global meteorological properties and compare the seasons in the northern and southern hemispheres. The most striking feature is the seasonal variation in atmospheric pressure due to condensation of CO_2.

6.6.3.2 Pressure Variations

Figure 6-10 gives the pressure at both lander sites for an entire martian year and clearly shows the asymmetry between the poles [6-56]. The north cap does not exchange as much mass as the south polar cap, primarily because of the eccentricity of the orbit (0.093). The near coincidence of the perihelion (aerocentric longitude, LS = 253 deg) and northern winter solstice (Ls = 270 deg) results in more extreme seasons in the southern hemisphere. Note that the Viking 2 site is nearly 1 km below the Viking 1 site, referred to the mean datum.

TABLE 6-12. METEOROLOGICAL PROPERTIES

Parameter	Nominal Value	Note or Range
Pressure	8 mb	7 to 9 mb
Temperature	215°K	130 to 290°K
Temperature Lapse Rate	2°K km^{-1}	
Adiabatic Lapse Rate	4.5°K km^{-1}	
Scale Height	11 km	
Tropopause Height	40 km	
Turbopause Height	120 km	
Wind Speed	0 to 50 m sec^{-1}	above boundary layer
Solar Radiation		
mean	590.0 W m^{-2}	based on the solar
perihelion	718.0	constant at 1 AU of
apehelion	493.0	1371 ± 5 W m^{-2}
Albedo		
average	0.2 to 0.4	
ice caps	0.7	
Solar UV Flux	10^4 erg cm^{-2} sec^{-1}	200-300 nm, top of atmosphere, subsolar point, perihelion.

TABLE 6-13. DURATIONS OF SEASONS ON MARS

Season		Length	
Northern Hemisphere	Southern Hemisphere	Days	Sols
spring	autumn	199	194
summer	winter	183	178
autumn	spring	147	143
winter	summer	158	154
		687	669

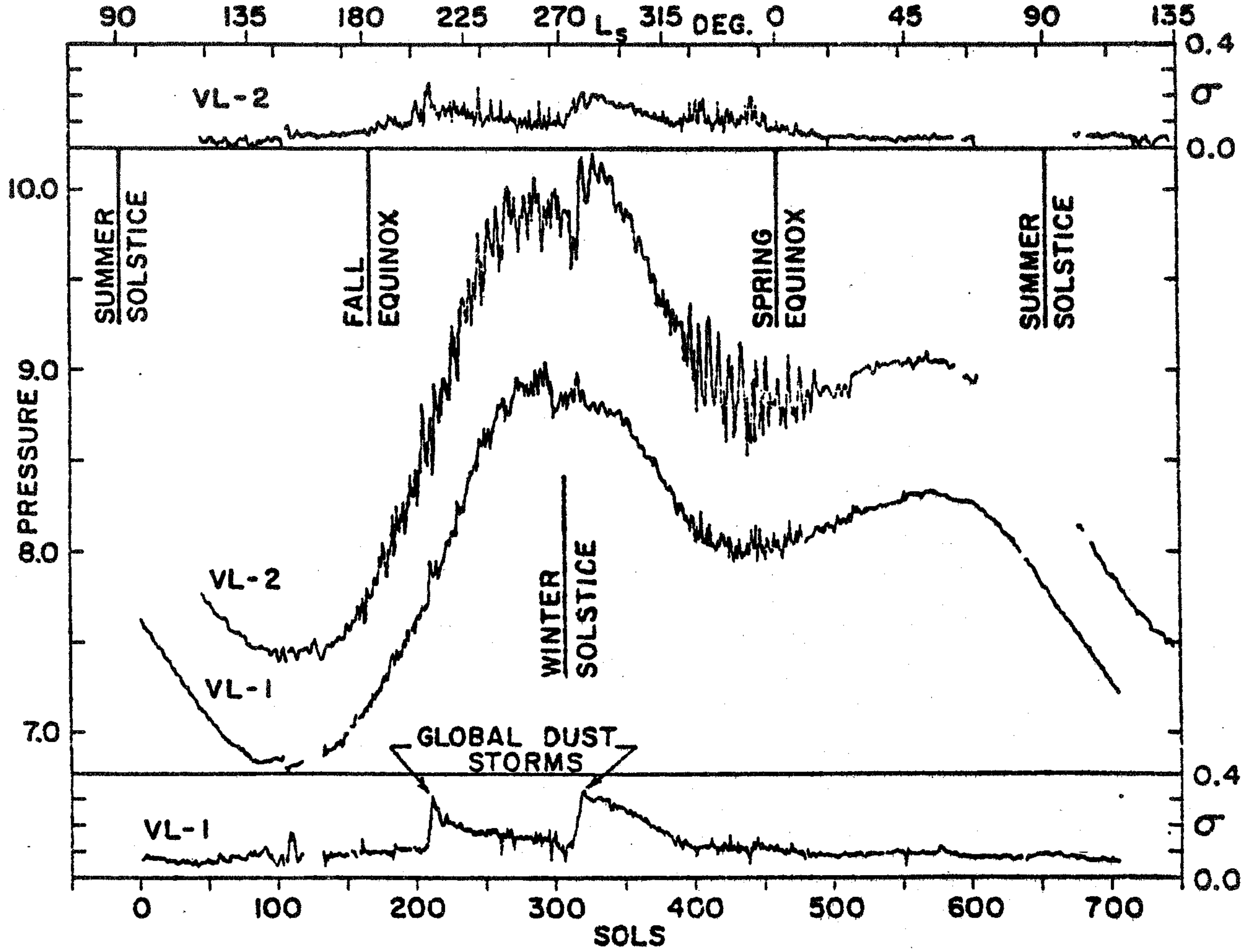

Figure 6-10. Surface pressure variation over one Mars year [6-56]. Center section: Daily mean pressures at the two landers for 700 sols. Upper and lower sections: Standard deviations of pressure within each sol. All pressures and standard deviations are in mb. The abscissa is time measured in sols. The scale labeled Ls is the aerocentric (refers to Mars orbit around Sun) longitude of the Sun. The dates of initiation of two global dust storms are marked. Gaps are due to lost data.

6.6.3.3 Diurnal Surface Temperatures

Large diurnal temperature variations were observed at both landing sites. Fig. 6-11a shows the air temperature for one sol (24.46 hr) at both Viking landing sites early in the mission during martian summer, as measured 1.6 m above the surface [6-57]. The Viking orbiter also measured surface temperatures over the entire planet which ranged from 130 to 290°K [6-45].

Minimum air temperature differs only slightly from minimum soil temperatures while maximum air temperatures are considerably lower than surface temperatures. Fig. 6-11b shows a typical diurnal temperature cycle for equatorial equinox conditions [6-58].

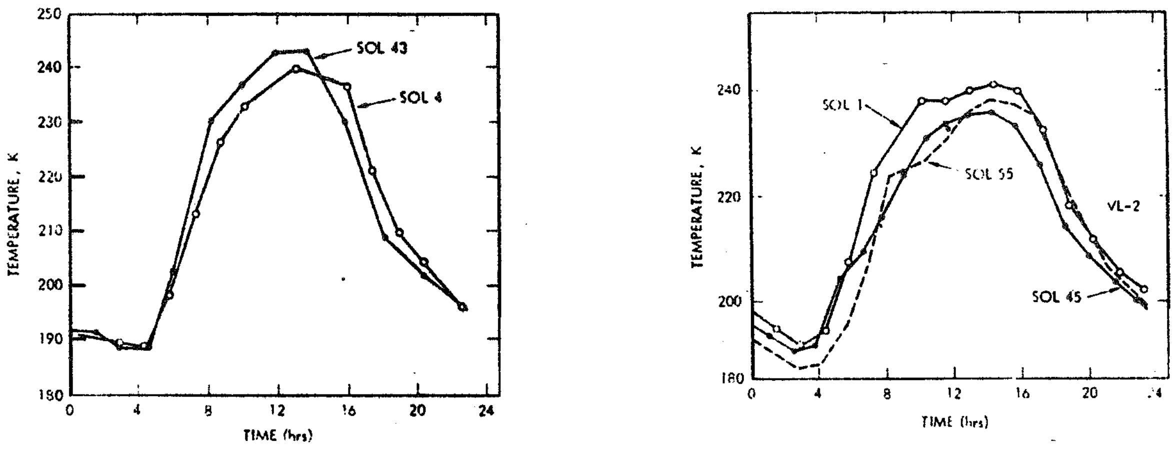

Figure 11a. Diurnal temperature variations at Viking sites [6-57].

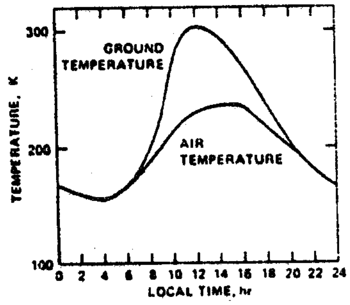

Figure 11b. Diurnal temperature variations for Mars air and surface; at the equator at equinox [6-58].

6.6.3.4 Winds, Aerosols, and Dust Storms

The winds at the Viking lander sites ranged from 2 to 7 m sec^{-1}, with strong diurnal and seasonal variation in both direction and magnitude. Winds above the boundary layer may be as high as 50 m sec^{-1} [6-57]. (The daily winds result from meteorological disturbances and are not directly due to the pole-to-pole transfer of CO_2.)

Dust storms have long been observed. They tend to occur near perihelion (Ls = 253 deg). Because of the eccentricity of the martian orbit, the insolation at perihelion is fully 45 percent stronger than at aphelion. Additionally, perihelion nearly coincides with southern summer solstice (Ls = 270 deg). The martian atmosphere tends to be in radiative equilibrium, and this intense period of summertime radiation coupled with topographic variations apparently triggers the global dust storms. Storms may last for several months. The opacity of the dust cloud in visible wavelengths may be quite high, reaching 5 optical depths in the visible [6-59].

The particles in the air follow the size distribution:

$$n(r) = Cr^2 \exp [-4r/r_m]$$

where n(r) is the number density of particles of radius r, and r_m, the mode radius, equals 0.4 microns [6-60]. The total column mass loading during a global storm is typically 10^{-3} g cm^{-2}. The single scattering properties of the particles are listed below, averaged over the solar spectrum [6-60].

Single Scattering Albedo ω	Average Scattering Asymmetry Parameter $\cos \theta$	Extinction Efficiency Q_{ext}
0.86	0.79	2.74

The slightly red color of the martian sky observed by the Viking cameras is due to this dust in the atmosphere; even on "clear" days the opacity exceeds 0.18 [6-61].

It is interesting to note that the two global dust storms observed, identified by orbital imaging, resulted in only minor redistribution and accumulation of debris at the lander sites [6-62]. Martian dust storms are not large walls of fast moving debris, as often imagined. While martian wind speeds may be typically ten times those of terrestrial winds, the density of the martian air at the surface is 120 times less. The drag of the martian winds is, in fact, comparable to that of typical terrestrial winds because wind drag is roughly proportional to air density times wind velocity squared. However, the dust storms and transport of dust into the polar regions are a major factor in martian climate.

6.6.3.5 Clouds

Clouds, frequently seen in orbiter photographs, can generally be divided into two types, dust and condensate ices (water and carbon dioxide).

Yellow clouds are generally associated with dust storms. The storms typically begin near perihelion and the yellow cloud may then quickly obscure the entire surface.

A wide variety of white condensate cloud types occur. They are composed primarily of water, but a few have been observed at altitudes high enough (i.e., 80 km) to imply CO_2 composition.

Large, well-developed spiral cloud formations seen by the Viking orbiters appeared to be at 65 to 81 deg N and at about 6 to 7 km altitude [6-63].

Topographic clouds are produced by air flow over craters, ridges, and mountains [6-64]. The clouds associated with the Tharsis summits are particularly striking, covering large areas and obscuring all but the peaks.

Frost and early morning fog layers are common [6-61]. They are often seen in orbiter pictures in the bottom of canyons and were detected at both lander sites during the summer. Hoods have been observed over both poles in late winter with the north polar hood being much larger in temporal and spatial extent.

6.6.3.6 The "Blue Clearing"

Astronomers have noted that the contrast of the martian surface decreases toward the blue end of the spectrum, and that occasionally a "clearing" occurs. Though this phenomenon is well documented, nothing that can be related to it was observed during spacecraft encounters. A discussion of recent ground-based observations appear in Reference 6-65.

6.7 UPPER ATMOSPHERE AND EXOSPHERE

The atmosphere is well mixed below 120 km. Above this altitude (the turbopause) composition varies according to the molecular weights of individual constituents. Carbon dioxide remains dominant up to at least 180 km.

The eddy diffusion coefficient at 120 km, as determined by height profiles of Ar and N_2, is 5×10^7 cm sec^{-1}.

The thermal structure of the upper atmosphere is complex and variable. The Viking 1 and 2 entries observed average temperatures near 200°K, which is considerably colder than the 300 to 350°K temperatures observed by Mariners 6, 7, and 9 [6-50,6-66].

The exosphere and the escape of gases are important factors in determining atmospheric evolution. The escape rate of H_2 is of the order of 10^8 cm^{-2} sec^{-1}, twice the escape rate of O_2. The estimated average of 10 precipitable microns of water vapor in the atmosphere could support this escape rate for only 10^4 years. Isotopic separation of oxygen and nitrogen may occur in the martian exosphere, which could account for the observed nitrogen isotopic ratios. The oxygen ratios reflect a large reservoir of exchangeable oxygen (6-52).

6.8 IONOSPHERE

The martian ionosphere extends upwards from 120 km; CO_2 is a dominant constituent, and free electrons are mainly produced by its photoionization. Mars does not have an E or F_2 ionosphere layer but does have an F_1 peak formed near unit optical depth for solar ultraviolet radiation in the wavelength range from 200 to 900 Å. Just below 130-km altitude the F_1 ion concentration reaches a peak of approximately 10^5 cm^{-3} of which 90 percent is O_2^+ and 10 percent is CO_2^+. At higher altitudes, O^+ ions were detected with a peak concentration near 225 km of less than 10^3 cm^{-3}. Viking 1 measured ion temperatures of approximately 150°K near the F_1 peak increasing to an apparent exospheric temperature of 210°K near 175 km. Above this altitude departures from thermal equilibrium with the neutral gas occur, and the ion temperature increases rapidly to over 1000°K at 250 km [6-67]. Figure 6-12 shows profiles of ion concentrations compared with theoretical chemical model results.

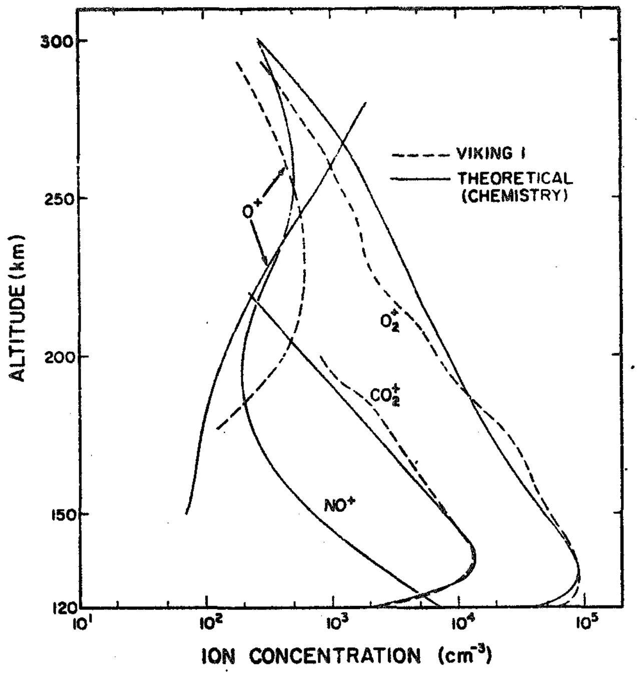

Figure 6-12. A comparison of the measured ion concentration from Viking 1 profiles and a theoretical model ionosphere in chemical equilibrium [6-67].

6.9 MAGNETOSPHERE

The interaction of Mars with the solar wind appears to require a magnetospheric component in addition to an atmospheric component. Intriligator and Smith [6-15] interpret spacecraft results as indicating a situation between "Venus-like" (effectively no intrinsic magnetic field, interaction directly with ionosphere) and "Earth-like" (interaction dominated by the intrinsic magnetic field).

6.10 SATELLITES

Asaph Hall discovered and named Mars' two natural satellites Phobos (fear) and Deimos (terror) in 1877. Their orbital elements and physical parameters are listed in Table 6-14 [6-68].

The orbit of Phobos is just outside the Roche limit of Mars and inside a stationary orbit (analogous to geostationary orbit). An observer on the surface of Mars would see Phobos rise in the west and cross the sky to set in the east in under four hours; the disc would subtend 12 min of arc (compared to 30 min for the Earth's Moon). This is almost half the apparent diameter of the Sun as seen from Mars and the penumbral shadow of Phobos sweeps across the martian surface on every orbit. As is characteristic of satellites within stationary orbit, the tidal drag on Phobos is decreasing its orbital distance from Mars and Phobos will strike the martian surface

TABLE 6-14. CHARACTERISTICS OF PHOBOS AND DEIMOS (6-68)

	Phobos	Deimos
Orbital Elements		
Semi-major axis	9378 km 2.76 R_{Mars}	23459 km 6.90 R_{Mars}
Eccentricity	0.015	0.00052
Inclination (deg)	1.02	1.82
Sidereal period	$7^h39^m13.85^s$	$30^h17^m54.87^s$
Physical Parameters		
Longest axis	13.5 km	7.5 km
Intermediate axis	10.7 km	6.0 km
Shortest axis	9.6 km	5.5 km
Rotation	synchronous	synchronous
Density	2.0 g cm^{-3}	1.9 g cm^{-3}
Mass	9.8×10^{18} g	2.0×10^{18} g
Albedo	0.05	0.06
Surface gravity	1 cm sec^{-2}	0.5 cm sec^{-2}

in less than 10^8 years [6-69 through 6-71]. It is possible that tidal forces will result in disruption first as Phobos crosses the Roche radius. The surface of Phobos is heavily cratered. The two largest craters, "Stickney" and "Hall," are 10 and 5 km in diameter, respectively [6-72].

The orbit of Deimos lies just outside the stationary altitude. Its surface is also heavily cratered. There is evidence of regoliths on both satellites to depths of at least 5 m and probably more [6-72, 6-73].

(Photos from the Viking Missions are available from NASA.)

6.11 SPACE IN THE VICINITY OF MARS

Mars' nearest celestial neighbor is the Earth-Moon system. Mars is near the asteroid belt, and interactions may have been an important factor in the evolution of the planet and its satellites.

6.12 THE SEARCH FOR LIFE ON MARS

In addition to the lander cameras, which would be expected to show any large life-forms, the Viking landers contained three experiments to search for indications of life.

a) The gas exchange experiment, designed to detect metabolization and related gaseous exchange products in the presence of a nutrient solution [6-42].

b) The labeled release experiment designed to detect the release of radioactivity from labeled carbon bound in a nutrient solution [6-74].

c) The pyrolitic release experiment which was based on the assumption that any martian life would be able to incorporate radioactivity-labeled atmospheric carbon in the presence of sunlight (i.e., by photosynthesis) [6-75].

All three experiments showed signs of activity, but probably of chemical not biological origin [6-44,6-76,6-77,6-78,6-79].

In addition, the Gas-Chromatograph/Mass Spectrometer (GCMS) failed to detect organic material at even very low concentrations, less than parts per billion for heavy organics and parts per million for lighter ones [6-41].

Although the results of the biology detection experiments were hardly encouraging, all the chemical elements necessary to support Earth-type life exist on Mars, and speculation about life there continues [6-14,6-74,6-80,6-81,6-82,6-83].

The properties of the martian environment that seem most unfavorable to life as we know it, are:

a) The scarcity of water and lack of liquid water at the surface

b) The cold temperatures and extreme temperature variations that occur both diurnally and seasonally

c) The solar ultraviolet radiation between 1900 and 3000 Å, which penetrates to the surface (Table 6-12, paragraph 6.6.3.1)

d) The presence of strong oxidants in the soil

e) The low surface atmospheric pressure

f) The low atmospheric concentration of N_2 and the apparent absence of any form of nitrogen in the top-regolith.

The issue will not be settled definitively until further studies are made, preferably through specimens returned to Earth or manned exploration.

6.13 SPACECRAFT MISSIONS TO MARS

Table 6-15 is a list of Mars missions.

TABLE 6-15. MARS MISSIONS

Mission	Origin	Launch Date	Outcome
Mars 1	USSR	November 1, 1962	Contact lost after 105 million kilometers
Mariner 3	USA	November 5, 1964	Failed (shroud malfunction)
Mariner 4	USA	November 28, 1964	Fly-by on July 14, 1965
Zond 2	USSR	November 30, 1964	Batteries failed on May 5, 1965
Mariner 6	USA	February 24, 1969	Fly-by on July 31, 1969
Mariner 7	USA	March 27, 1969	Fly-by on August 5, 1969
Mars 2	USSR	May 19, 1971	Capsule ejection on November 27, 1971
Mars 3	USSR	May 28, 1971	Capsule soft landing on December 2, 1971
Mariner 9	USA	May 30, 1971	Orbiter since November 13, 1971
Mars 4	USSR	July 21, 1973	Orbiter since February 10, 1974
Mars 5	USSR	July 25, 1973	Orbiter since February 12, 1974
Mars 6	USSR	August 5, 1973	Landed on March 12, 1974
Mars 7	USSR	August 9, 1973	Contact lost on March 9, 1974
Viking 1	USA	August 20, 1975	Landed on July 20, 1976
Viking 2	USA	September 9, 1975	Landed on September 3, 1976

REFERENCES

6-1. Glasstone, S.: The Book of Mars. NASA Special Publication, No. 179, 1969.

6-2. Mutch, T. A., Arvidson, E., Head, J. W., III, Jones, L., and Saunders, R. S.: The Geology of Mars. Princeton University Press, Princeton, New York, 1976.

6-3. J. Geophys. Res., vol. 82, Special Mars Issue, 1977.

6-4. J. Geophys. Res., vol. 84, Special Issue, 1979, pp. 7909-8519.

6-5. Mayo, A. P., Blackshear, W. T., Tolson, R. H., Michael, W. H., Kelly, G. M , Brenkle, J. P., and Komarek, T. A.: Lander Locations Mars Physical Ephemeris and Solar System Parameters, Determination from Viking Lander Tracking Data. T.A.M. Geophys. (EOS), vol. 58, 1977, p. 828.

6-6. American Ephemeris and Nautical Almanac, U. S. Naval Observatory, 1980.

6-7. Ward, W. R.: Present Obliquity Oscillations of Mars' Fourth-Order Accuracy in Orbital e and I. J. Geophys. Res., vol. 84, 1979, pp. 237-241.

6-8. Kaula, W. M.: Moment of Inertia of Mars. Geophys. Res. Lett., vol. 6, 1979, pp. 194-196.

6-9. Pritchard, E. B., Harrison, E. F., and Moore, F. W.: Options for Mars Exploration. Astronautics and Aeronautics, vol. 12, Feb. 1974, pp. 46-56.

6-10. Davies, M. E.: The Control Net of Mars: May 1977. J. Geophys. Res., vol. 83, 1978, p. 2311.

6-11. U. S. Geological Survey (USGS) Topographic Map of Mars. MAP I-961, Flagstaff, Arizona, 1976.

6-12. Snyder, C. W.: The Planet Mars as Seen at the End of the Viking Mission. J. Geophys. Res., vol. 84, 1979, pp. 8487-8519.

6-13. Christensen, E. J. and Balmino, G.: Development and Analysis of a Twelfth Degree and Order Gravity Model for Mars. J. Geophys. Res., vol. 84, 1979, pp. 7943-7945.

6-14. Gapcynski, J. P., Tolson, R. H., and Michael, W. H., Jr.: Mars Gravity Field: Combined Viking and Mariner 9 Results. J. Geophys. Res., vol. 82, 1977, pp. 4325-4326.

6-15. Intriligator, D. S. and Smith, E. J.: Mars in the Solar Wind. J. Geophys. Res., vol. 84, 1979, pp. 8427-8435.

6-16. Russell, C. T.: Planetary Magnetism. Rev. Geophys. Space Phys., vol. 18, 1980, pp. 77-106.

6-17. Johnson, D. H. and Toksoz, M. N.: Internal Structure and Properties of Mars. ICARUS, vol. 32, 1977, pp. 73-84.

6-18. Bills, B. G. and Ferrari, A. J.: Mars Topography, Harmonics and Geophysical Implications. J. Geophys. Res., vol. 83, 1978, pp. 3497-3508.

6-19. Wu, Sherman: Photogrammatic Portrayal of Mars Topography. J. Geophys. Res., vol. 84, 1979, pp. 7955-7959.

6-20. Wise, D. U., Golombek, M. P., and McGill, G. E.: Tectonic Evolution of Mars. J. Geophys. Res., vol. 84, 1979, pp. 7934-7939.

6-21. Carr, M. H.: The Morphology of the Martian Surface. Space Science Reviews, vol. 25, 1980, pp. 231-284.

6-22. Warner, J. L. and Minear, J.: Results of the Mars Sample Acquisition Study. JPL Publication 80-59, NASA, Pasadena, California, 1980.

6-23. Moore, H. J., Spitzer, C. R., Bradford, K. Z., Cates, P. M., Hutton, R. E., and Shorthill, R. W.: Sample Fields of the Viking Landers, Physical Properties, and Aeolian Processes. J. Geophys. Res., vol. 84, 1979, pp. 8365-8377.

6-24. Blasisus, K. R., Cutts, J. A., Guest, J. E., and Masursky, H.: Geology of the Valles Marineris: First Analysis of Imaging from the Viking 1 Orbiter Primary Mission. J. Geophys. Res., vol. 82, 1977, pp. 4067-4091.

6-25. Kieffer, H. H.: Mars South Polar Spring and Summer Temperatures: A Residual CO_2 Frost. J. Geophys. Res., vol. 84, 1979.

6-26. Sharp, R. D.: Ice on Mars? J. Glaciol., vol. 13, 1974, pp. 173-185.

6-27. Cutts, J. A., Briggs, G. A., Carr, M. H., Greeley, R., and Masursky, H.: North Polar Region of Mars: Imaging Results from Viking 2. Science, vol. 196, 1976, pp. 1329-1337.

6-28. Murray, B. C., Soderblom, L A., Cutts, J. A., Sharp, R. P., Milton, D. J., and Leighton, R. B.: Geological Framework of the South Polar Regions of Mars. ICARUS, vol. 17, 1972, pp. 328-345.

6-29. Sagan, C., Toon, O. B., and Gierasch, P. J.: Climatic Changes on Mars. Science, vol. 181, 1973, pp. 1045-1049.

6-30. Dzurisin, D. and Blasisus, K. R.: Topography of the Layered Deposits of Mars. J. Geophys. Res., vol. 80, 1975, pp. 3286-3306.

6-31. Murray, B. C. and Malin, M. C.: Polar Wandering on Mars? Science, vol. 1799, 1973, pp. 997-1000.

6-32. Cutts, James A.: Wind Erosion in the Martian Polar Regions. J. Geophys. Res., vol. 78, 1973, pp. 4211-4213.

6-33. Clark, B. R. and Mullin, R. P.: Martian Glaciation and the Flow of Solid CO_2. ICARUS, vol. 27, 1976, pp. 215-228.

6-34. Howard, A. D.: Origin of the Stepped Topography of the Martian Poles. ICARUS, vol. 34, 1978, pp. 581-599.

6-35. Carr, M. H. and Schaber, G. G.: Martian Permafrost Features. J. Geophys. Res., vol. 82, 1977, pp. 4039-4054.

6-36. Kliore, A. J. (ed.): The Mars Reference Atmosphere. COSPAR, 1978.

6-37. Clark, B. C., Baird, A. K., Rose, H. J., Jr., Toulmin, P., III, Christian, R. P., Kelliher, W. C., Castro, A. J., Rowe, C. D., Keil, K., and Huss, G. R.: The Viking X-Ray Fluorescence Experiment: Analytical Methods and Early Results. J. Geophys. Res., vol. 82, 1977, pp. 4577-4594.

6-38. Clark, B. C. and Baird, A. K.: Volatiles in the Martian Regolith. Geophys. Res. Lett., vol. 6, 1979, pp. 811-814.

6-39. Toulmin, P., III, Baird, A. K., Clark, B. C., Keil, K., and Rose, H. J., Jr.: Preliminary Results from the Viking X-Ray Fluorescence Experiment: The First Sample from Chryse Planitia, Mars. Science, vol. 194, 1976, pp. 81-84.

6-40. Toulmin, P., III, Baird, A. K., Clark, B. C., Keil, K., Rose, H. J., Jr., Christian, R. P., Evans, P. H., and Kelliher, W. C.: Geochemical and Mineralogical Interpretations of the Viking Inorganic Chemical Results. J. Geophys. Res., vol. 82, 1977, pp. 4625-4634.

6-41. Biemann, K., Oro, J., Toulmin, P., III, Orgel, L. E., Nier, A. O., Anderson, D. M., Simmonds, P. G., Flory, D., Diaz, A. V., Rushneck, D. R., Biller, J. E., and Lafleur, A. L.: The Search for Organic Substances and Inorganic Volatile Compounds in the Surface of Mars. J. Geophys. Res., vol. 82, 1977, pp. 4641-4658.

6-42. Oyama, I. and Berdahl, B. J.: The Viking Gas Exchange Experiment Results from Chryse and Utopia Surface Samples. J. Geophys. Res., vol. 82, 1977, pp. 4669-4676.

6-43. Fanale, F. P. and Cannon, W. A.: Mars: CO_2 Absorption and Capillary Condensation on Clays – Significance for Volatile Storage and Atmospheric History. J. Geophys. Res., vol. 84, 1979, pp. 8404-8414.

6-44. Mazur, P., Barghoorn, E. S., Halvorson, H. O., Jukes, T. H., Kaplan, I. R., and Margulis, L.: Biological Implications of the Viking Mission to Mars. Space Sci. Rev., vol. 22, 1978, pp. 3-34.

6-45. Kieffer, H. H., Chase, S. C., Miner, E. D., Pallucon, F. D., Munch, G., Neugebauer, G., and Martin, T. Z.: Infrared Thermal Mapping of Martian Surface and Atmosphere – 1st Results. Science, vol. 193, 1976, pp. 780-786.

6-46. Shorthill, R. W., Moore, H. J., Scott, R. F., Hutton, R. E., Liebes, S., Jr., and Spitzer, C. R.: The Soil of Mars (Viking I). Science, Oct. 1976, pp. 91-97.

6-47. Hess, S. L., Henry, R. M., and Tillman, J. E.: The Seasonal Variation of Atmospheric Pressure on Mars as Affected by the South Polar Cap. J. Geophys. Res., vol. 84, 1979, pp. 2923-29[illegible]

6-48. Owen, T., Biemann, K., Rushneck, D. R., Biller, J. E., Howarth, D. W., and Lafleur, A. L.: The Composition of the Atmosphere at the Surface of Mars. J. Geophys. Res., vol. 82, 1977, pp. 4635-4639.

6-49. Leovy, C. B., Briggs, G. A., and Smith, B. A.: Mars Atmosphere During Mariner 9 Extended Mission — Television Results. J. Geophys. Res., vol. 78, 1973, p. 4252.

6-50. Barth, C. A.: The Atmosphere of Mars. Ann. Rev. Earth Sci., vol. 2, 1974, pp. 333-367.

6-51. Davies, D. W.: The Relative Humidity of Mars' Atmosphere. J. Geophys. Res., vol. 84, 1979, pp. 8335-8340.

6-52. McElroy, M. B., Kong, T. Y., and Yung, Y. L.: Photochemistry and Evolution of Mars' Atmosphere: A Viking Perspective. J. Geophys. Res., vol. 82, 1977, pp. 4379-4388.

6-53. Anders, E. and Owen, T.: Mars and Earth: Origin and Abundance of Volatiles. Science, vol. 198, 1977, pp. 453-456.

6-54. Rasool, S. I., Hunten, D. M., and Kaula, W. M.: What the Exploration of Mars Tells Us About Earth. Physics Today, July 1977, pp. 23-32.

6-55. Pollack, J. B. and Black, D. C.: Implications of the Gas Compositional Measurements of Pioneer Venus for the Origin of Planetary Atmospheres. Science, vol. 205, 1979, pp. 56-59.

6-56. Hess, S. L., Ryan, J. A., Tillman, J. E., Henry, R. M., and Leovy, C. B.: The Annual Cycle of Pressure on Mars Measured by Viking Landers 1 and 2. Geophys. Res. Lett., vol. 7, 1980, pp. 197-200.

6-57. Hess, S. L., Henry. R. M., Leovy, C. B., Ryan, J. A., and Tillman, J. E.: Meteorological Results of the Surface of Mars: Viking 1 and 2. J. Geophys. Res., vol. 82, 1977, pp. 4559-4574.

6-58. Averner, M. M. and MacElroy, R. D.: On the Habitability of Mars: An Approach to Planetary Ecosynthesis. NASA Special Publication No. 414, 1976.

6-59. Hunt, G. E.: On the Opacity of Martian Dust Storms Derived by Viking IRTM Spectral Measurements. J. Geophys. Res., vol. 84, 1979, pp. 8301-8310.

6-60. Pollack, J. B., Colburn, D. S., Flasar, F. M., Kahn, R., Carlston, C. E., and Pidek, D.: Properties and Effects of Dust Particles Suspended in the Martian Atmosphere. J. Geophys. Res., vol. 84, 1979, pp. 2929-2945.

6-61. Pollack, J. B., Colburn, D., Kahn, R., Hunter, J., VanCamp, W., Carlston, C. E., and Wolf, M. R.: Properties of Aerosols in the Martian Atmosphere as Inferred from Viking Lander Imaging Data. J. Geophys. Res., vol. 82, 1977, pp. 4479-4496.

6-62. Guinness, E. A., Arvidson, R. E , Gehret, D. C., and Bolef, L. K.: Color Changes at the Viking Lander Sites Over the Course of a Mars Year. J. Geophys. Res., vol. 84, 1979, pp. 8355-8364.

6-63. Hunt, G. E. and James, P. B.: Martian Extratropical Cyclones. Nature, vol. 278, 1979, pp. 531-532.

6-64. Pickersgill, A. O. and Hunt, G. E.: The Formation of Martian Lee Waves Generated by a Crater. J. Geophys. Res., vol. 84, 1979, pp. 8317-8331.

6-65. Thompson, D. T.: A New Look at the Martian Violet Haze Problem: II Blue Clearing in 1969. ICARUS, vol. 18, 1973, pp. 164-170.

6-66. Nier, A. O. and McElroy, M. B.: Composition and Structure of Mars' Upper Atmosphere: Results from the Neutral Mass Spectrometers on Viking 1 and 2. J. Geophys. Res., vol. 82, 1977, pp. 4341-4349.

6-67. Hanson, W. B., Sanatani, S., and Zuccaro, D. R.: The Martian Ionosphere as Observed by the Viking Retarding Potential Analyzers. J. Geophys. Res., vol. 82, 1977, pp. 4351-4363.

6-68. Veverka, J. and Burns, J. A.: The Moons of Mars. Ann. Rev. Earth Planet. Sci., vol. 8, 1980, pp. 527-558.

6-69. Sinclair, A. T.: The Orbits of the Satellites of Mars. Vistas in Astronomy, vol. 22, 1978, pp. 133-140.

6-70. Burns, J. A.: The Dynamical Evolution and Origin of the Martian Moons. Vistas in Astronomy, vol. 22, 1978, pp. 193-210.

6-71. Burns, J. A.: Dynamical Characteristics of Phobos and Deimos. Rev. of Geophys. and Space Phys., vol. 10, 1972, pp. 463-483.

6-72. Veverka, J.: The Surfaces of Phobos and Diemos. Vistas in Astronomy, vol. 22, 1978, pp. 163-192.

6-73. Toon, D. B., Pollack, J. B., and Sagan, C.: Physical Properties of the Particles Composing the Martian Dust Storm of 1971-1972. ICARUS, vol. 30, 1977, pp. 663-665.

6-74. Levin, G. V. and Straat, P. A.: Recent Results from the Viking Labeled Release Experiment on Mars. J. Geophys. Res., vol. 82, 1977, pp. 4663-4667.

6-75. Horowitz, N. H. and Hobby, G. L.: Viking on Mars: The Carbon Assimilation Experiments. J. Geophys. Res., vol. 82, 1977, pp. 4659-4662.

6-76. Horowitz, N. H.: The Search for Life on Mars. Scientific American, November, 1977, pp. 52-61.

6-77. Klein, H. P.: The Viking Biological Investigation: General Aspects. J. Geophys. Res., vol. 82, 1977, pp. 4677-4680.

6-78. Klein, H. P.: The Viking Biological Experiments on Mars. ICARUS, vol. 34, 1978, pp. 666-674.

6-79. Margulis, L., Mazur, P., Barghoorn, E. S., Halvorson, H. O., Jukes, T. H., and Kaplan, I. R.: The Viking Mission: Implications for Life on Mars. J. Mol. Evol., vol. 14, 1979, pp. 223-232.

6-80. Friedman, E. I. and Ocampo, R.: Endolithic Blue-Green Algae in the Dry Valleys: Primary Producers in the Antarctic Desert Ecosystem. Science, vol. 193, 1976, pp. 1274-1249.

6-81. Clark, B. C.: Solar-Driven Chemical Energy Source for a Martian Biota. Origins of Life, vol. 9, 1979, pp. 241-249.

6-82. Foster, T. L., Winans, L., Casey, R. C., and Kirschner, L. E.: Response of Terrestrial Microorganisms to a Simulated Martian Environment. App. and Environ. Microbiol., vol. 35, 1978, pp. 730-737.

6-83. Kuhn, W. R., Rogers, S. R., and MacElroy, R. D.: The Response of Selected Terrestrial Organisms to the Martian Environment: A Modeling Study. ICARUS, vol. 37, 1979, pp. 336-346.

APPENDIX A. NEUTRAL ATMOSPHERE MODELS

A.1 DENSITY VARIATIONS AND MODELS

Since the advent of the first orbiting satellite in 1957, significant advances have been made in our knowledge of the Earth's upper atmosphere. The accepted model of the Earth's upper atmosphere at that time was one in which the temperature, pressure, density, and composition varied only with height. Predictions of future sightings (orbital positions) of the first satellites using this invariant atmosphere soon showed that the model was in error. Subsequently, several periodic variations in the density, temperature, and composition of the upper atmosphere have been identified. They are classified as:

a) Variations with the solar cycle approximately 11 years

b) Variations with the daily change in activity on the solar disc

c) The diurnal variation

d) Variations with geomagnetic activity

e) The semiannual variation

f) Seasonal-latitudinal variations of the low thermosphere

g) Seasonal-latitudinal variations of helium at all altitudes

h) Rapid density fluctuations probably connected with tidal and gravity waves.

The first seven have some regularity and can be modeled with varying degrees of accuracy. Since temperature plays a minor role in comparison with density, current models have been developed to represent, insofar as practical and possible, the variability of the ambient mass density rather than the temperature. The models are based on temperature profiles (Fig. A-1) [A-1] which have been adjusted so as to produce the density values derived from the analyses of satellite orbital decay data.

A.1.1 Variations with Solar Activity

The ultraviolet solar radiation that heats and causes compositional changes (Fig. A-2) [A-1] in the Earth's upper atmosphere consists of two components, one related to active regions on the solar disc and the other to the disc itself. The active-region component varies from day-to-day while the disc component varies more slowly, presumably with the longer periodicities in the solar activity; i.e., the approximately 11-year solar cycle. The atmosphere has been observed to react in a different manner to each of these two components. Jacchia and Slowey have found that the disc component of the solar radiation is, for all practical purposes, linearly related to the 10.7-cm solar flux smoothed over six solar rotations (162 days).

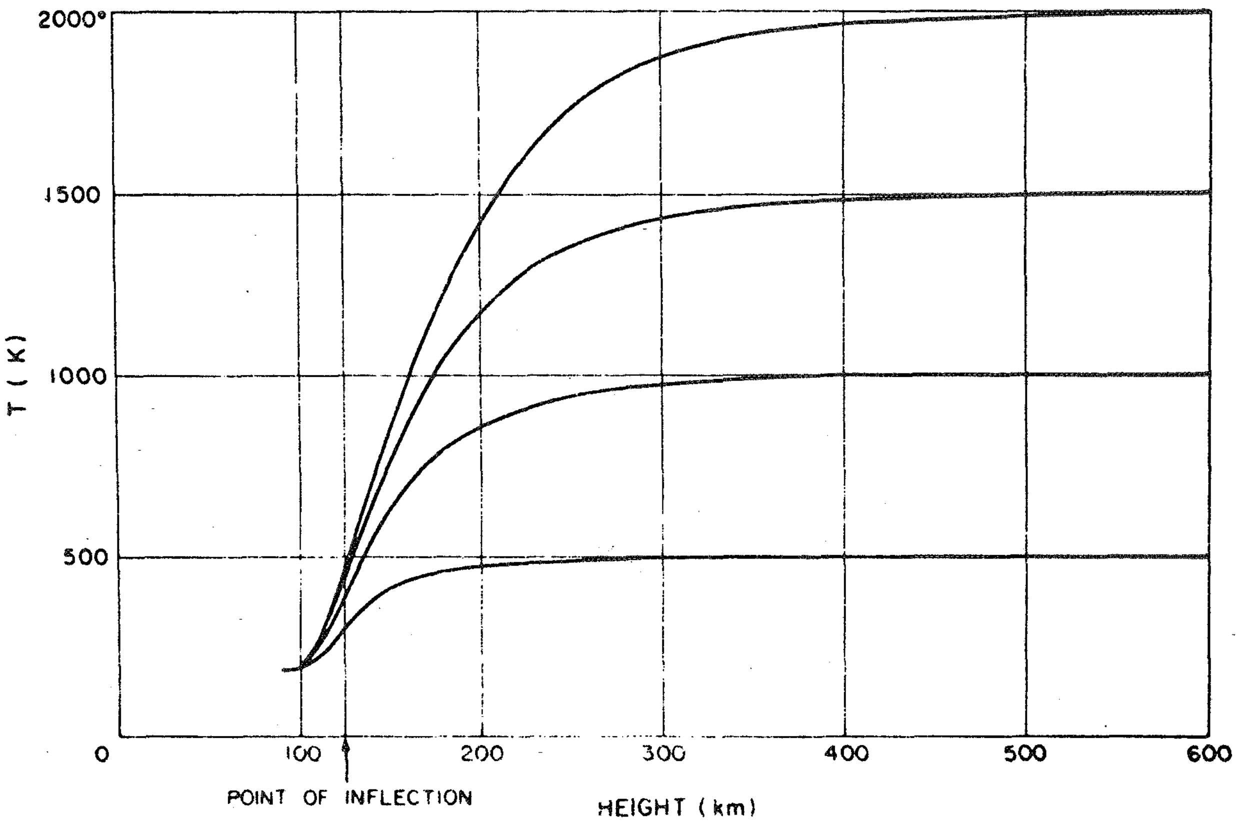

Figure A-1. Four temperature profiles from the present models [A-1].

The effect of solar activity on atmospheric density is shown in Figures A-3 and A-4 after Jacchia [A-1]. When the short-period oscillations which are caused by the diurnal variation are removed, there is essentially an 11-year variation that parallels the smoothed 10.7-cm solar flux data.

Figure A-5, after Jacchia [A-1], shows some of the variations in greater detail. The variations with a 27-day period are caused by the Sun's rotation – the active-region component. The semiannual variation can also be seen.

A.1.2 The Diurnal Variation

Analyses of satellite orbital decay histories have shown that upper atmospheric densities reach a maximum around 2 p.m. local solar time at a latitude approximately equal to that of the subsolar point while the minimum occurs between 3 and 4 a.m. at about the same latitude in the opposite hemisphere. Consistency between temperature and density cannot be achieved on a diurnal basis in a static model; therefore, the temperature profile has been used as a parameter so that observed density values can be reproduced by the models. The temperature distribution needed to achieve this required reproduction of the observed density values is depicted on a global scale in Figure A-6 [A-1]. Even though the global temperature distribution is an artifact developed solely for use in the density and composition models, some experimental results are in good agreement [A-2 through A-5]. Thomson-scatter temperature measurements [A-6 through A-8], as shown in Figure A-7 [A-1], generally

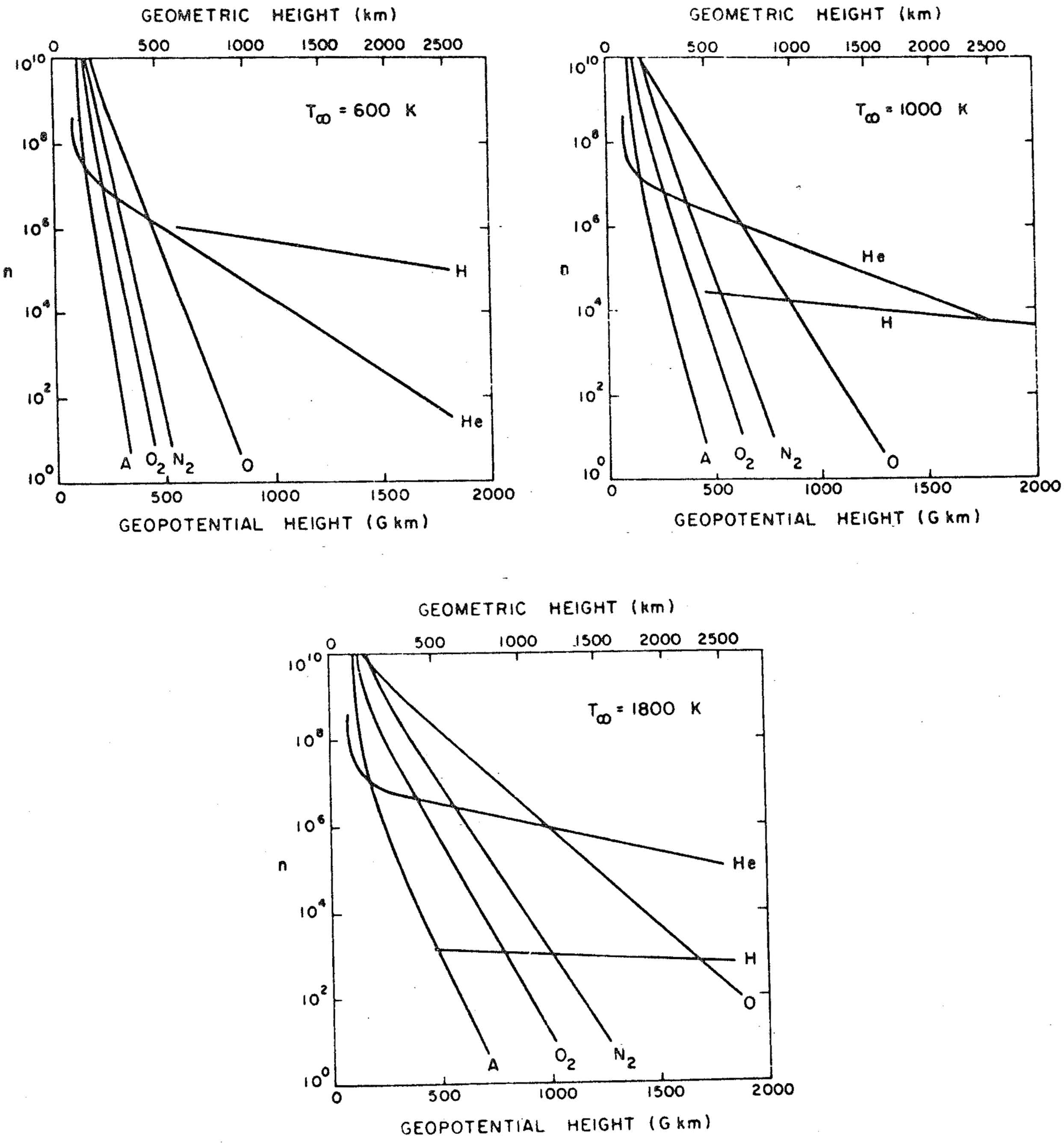

Figure A-2. Atmospheric composition for three values of the exospheric temperature [A-1]. (Number densities (n) are plotted against geopotential height. The corresponding geometric heights are marked at the top of the diagrams.)

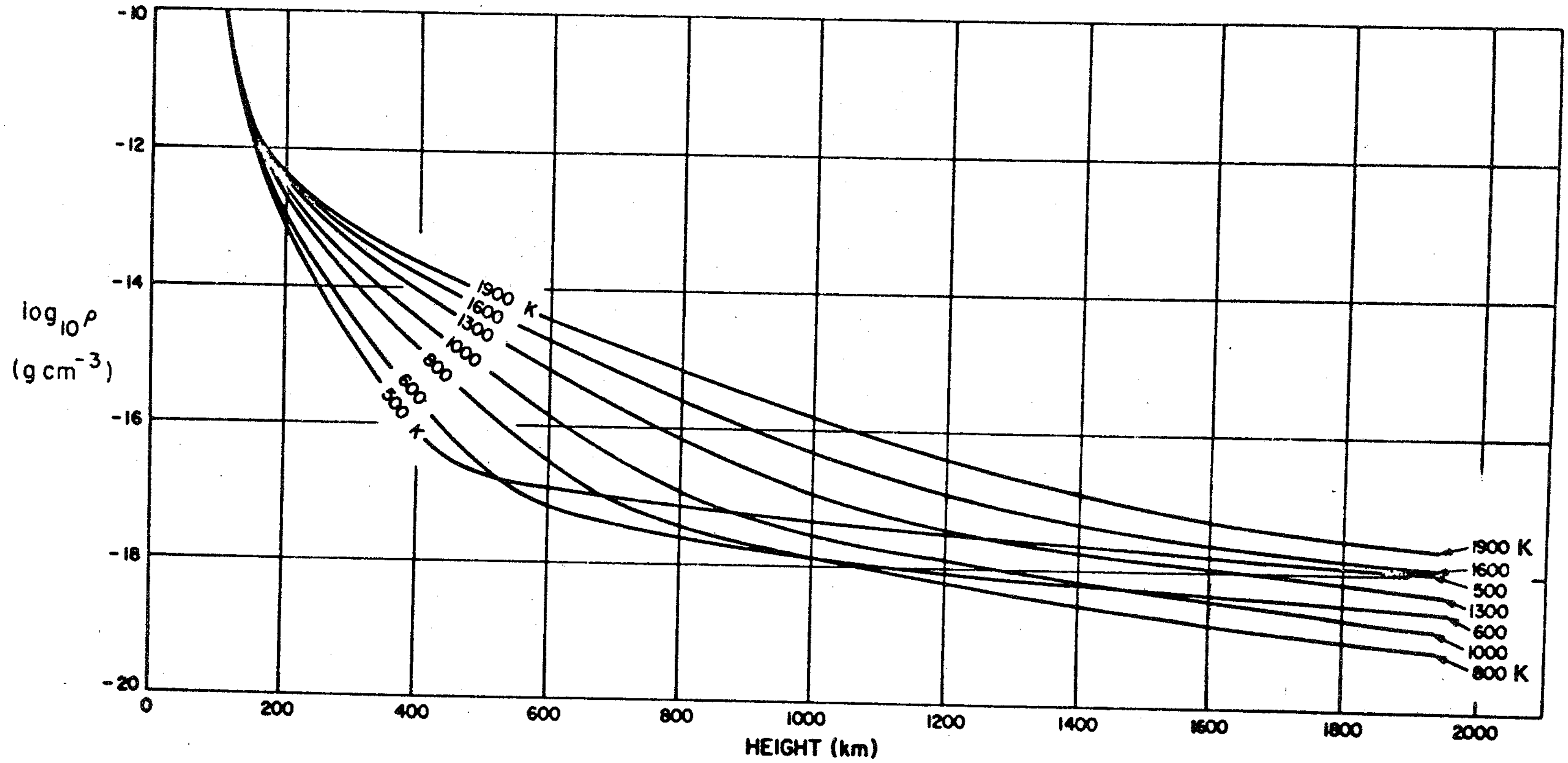

Figure A-3. Density profiles for seven values of the exospheric temperature [A-1].

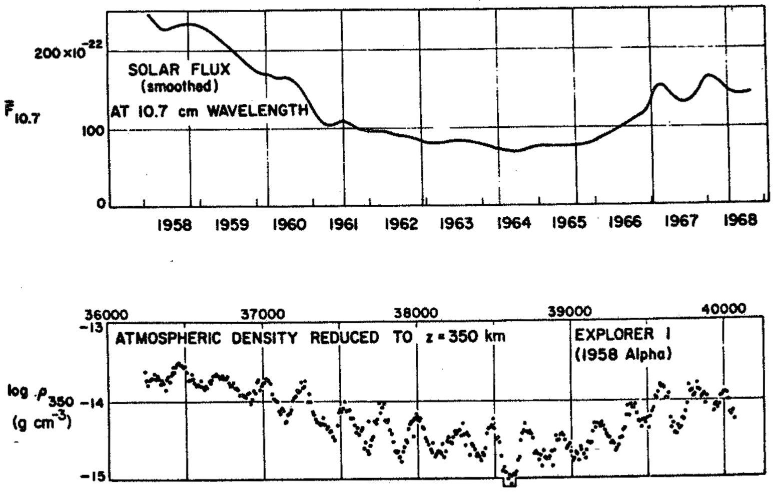

Figure A-4. Ten-day means of the densities obtained from the drag of the Explorer 1 satellite compared with variations in the 10.7-cm solar flux [A-1]. [M.J.D. is the Modified Julian Day (J.D. minus 2 400 000.5).]

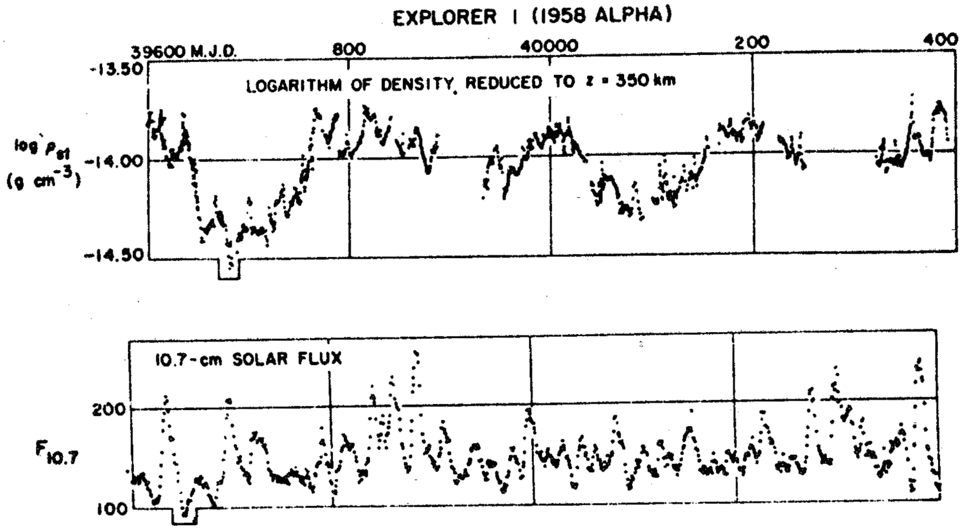

Figure A-5. Densities obtained from the drag of the Explorer 1 satellite compared with variations in the 10.7-cm solar flux.

EXOSPHERIC TEMPERATURE DISTRIBUTION AT THE EQUINOXES

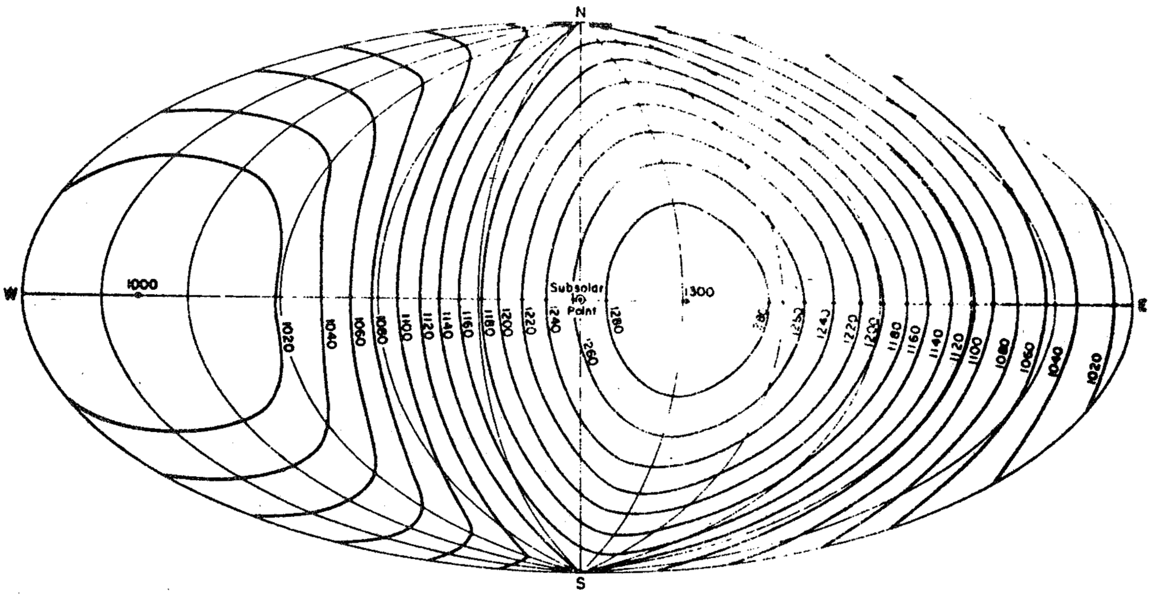

EXOSPHERIC TEMPERATURE DISTRIBUTION AT NORTHERN SUMMER SOLSTICE

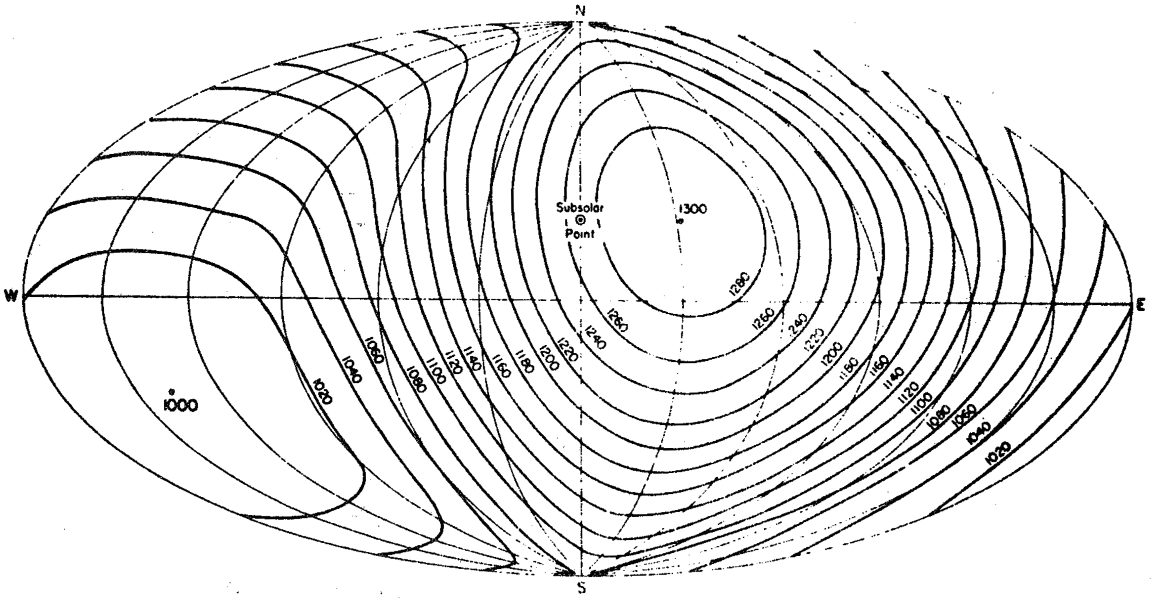

Figure A-6. Exospheric isotherms (K) above the globe, for the case when the minimum temperature is 1000 K [A-1].

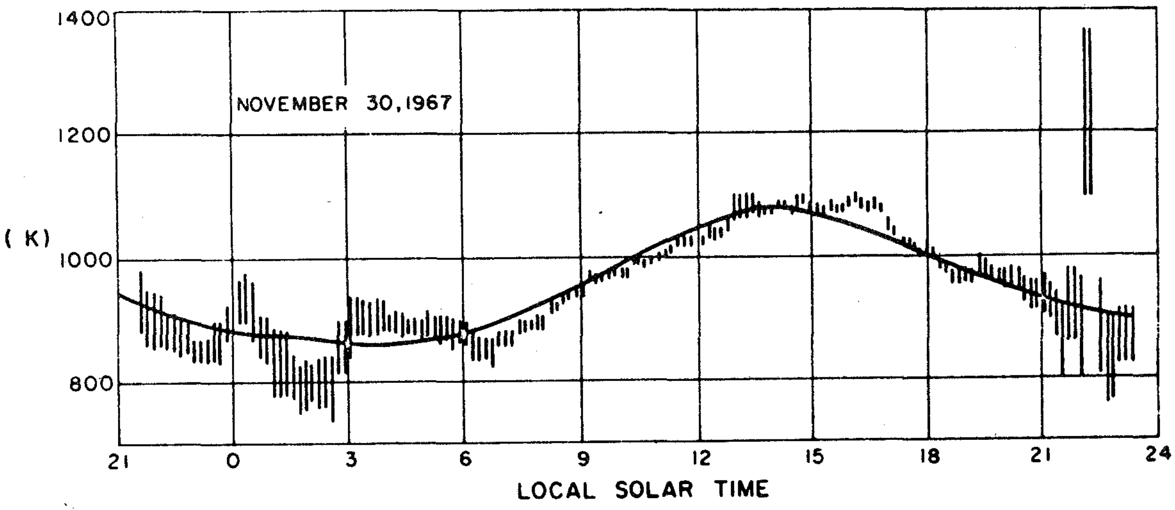

Figure A-7. Atmospheric temperatures obtained on November 30, 1967, by Carru and Waldteufel [A-7] by use of Thomson-scatter techniques, compared with temperatures predicted by the present models for a height of 300 km (solid line).

show that the temperature maximum occurs between 3 and 5 p.m. rather that near 2 p.m. This controversy has not been resolved at this time; however, it appears as if there is a phase lag between the density maximum and the temperature maximum which cannot be included in the current atmospheric models.

A.1.3 The Semiannual Variation

No satisfactory explanation has been found for this variation. It was initially assumed that this density variation could be linked with a temperature variation; however, data from analyses of more recently orbited satellites showed that the original assumption was in error. The amplitude of this density variation is strongly height-dependent and variable from year-to-year, with a primary minimum in July and principal maximum in October; however, it does not appear to be related to solar activity. Figure A-8 [A-1] shows the semiannual variation as derived from the orbital decay analysis of the Explorer 32.

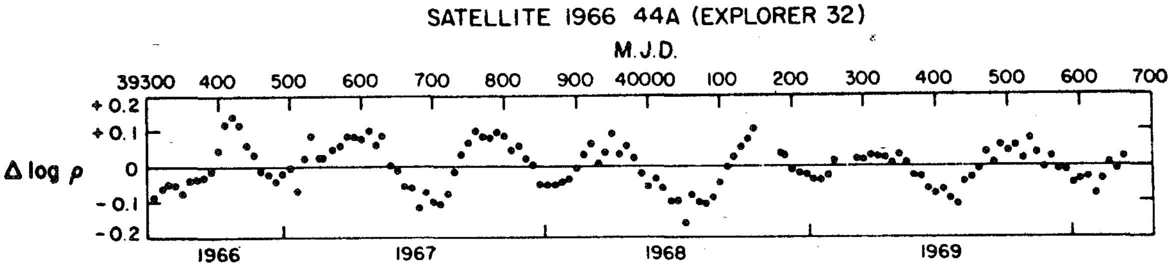

Figure A-8. The semiannual density variation as derived from drag analysis on Satellite 1966 44 A (Explorer 32). [All other variations have been suppressed by using the appropriate equations. M.J.D. is the Modified Julian Day (J.D. minus 2 400 000.5).]

A.1.4 Variations with Geomagnetic Activity

Analyses of orbital decay histories can give only a blurred picture of the complex reaction of the upper atmosphere to geomagnetic disturbances (Fig. A-9) [A-1]. Blamont and Luton [A-9] and DeVries [A-10] have shown that the upper atmosphere first reacts in the auroral zones with the energy subsequently propagating toward the equator apparently in the form of wave-like perturbations. It appears as if the atmosphere reacts with a zero time delay in the auroral zones with the geomagnetic storm effects showing up in the equatorial zone about 6 to 9 hr later. It is very difficult to adequately include this effect in a static model. The current models calculate the density variations on the basis of a global increase in exospheric temperature. Observations [A-9, A-10] have shown that this is not the case; however, for satellite lifetime prediction calculations, an assumed global temperature increase is acceptable. For some calculations, such as control dynamics analyses, control moment gyro analyses and aerodynamic torques, instantaneous temperature (and therefore density), increases for short time periods, and specific locations may be required. These studies may require special applications of the models.

A.1.5 Seasonal-Latitudinal Variations of the Lower Thermosphere

Presently accepted models assume constant temperature and density values at 90 km to prevent the models from becoming too complex even though large temperature and somewhat smaller density variations are known to exist. Current models therefore are constructed with a seasonal-latitudinal density variation which varies in the vertical from 0 at 90 km to a maximum at 110 and back 0 at 170 km. In the horizontal, the maximum occurs on December 27 at the North Pole and on June 25 at the South Pole. These variations are included as additions to the mass densities calculated as a function of the exospheric temperature used in the model. These variations are small and because they occur solely below 170-km altitude they will have little effect on orbital lifetime prediction calculations.

A.1.6 Seasonal-Latitudinal Variations of Helium

Experimental results have shown a strong increase of helium above the winter pole. The mechanism for this migration is unclear; however, empirical equations which describe the phenomenon are included in the models. These variations influence the computed densities only at heights above approximately 600 km (Fig. A-10).

A.1.7 Density Waves

Ambient density waves have been detected throughout the upper atmosphere in the height range from 140 to at least 510 km [A-4, A-10]. In addition, traveling ionospheric disturbances (TIDs) have long been thought of as manifestations of internal gravity waves. The waves appear to be more prevalent at the higher latitudes near the auroral zone; however, TIDs have been observed at all latitudes. Their vertical wavelengths apparently increase with altitude. Density increases on the order of 100 percent have been observed to occur over short distances [A-10]. The waves apparently propagate from either south to north or north to south with maximum horizontal wavelengths on the order of 500 to 700 km. Although current models do not include variations associated with internally propagating waves, users should be cautioned that they have been observed.

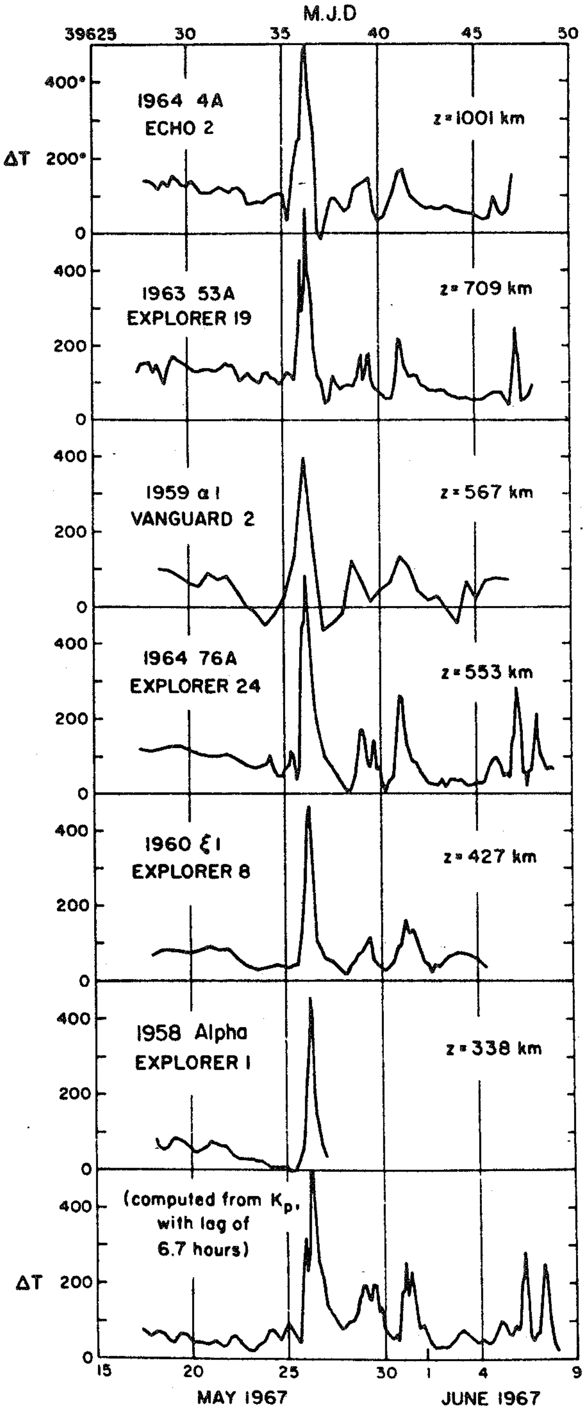

Figure A-9. The geomagnetic effect as derived from the drag of six satellites in May and June 1967. [The plotted ΔTs are temperature residuals from the models when all variations except the geomagnetic effect have been taken into account. M.J.D. is the Modified Julian Day (J.D. minus 2 400 000.5).]

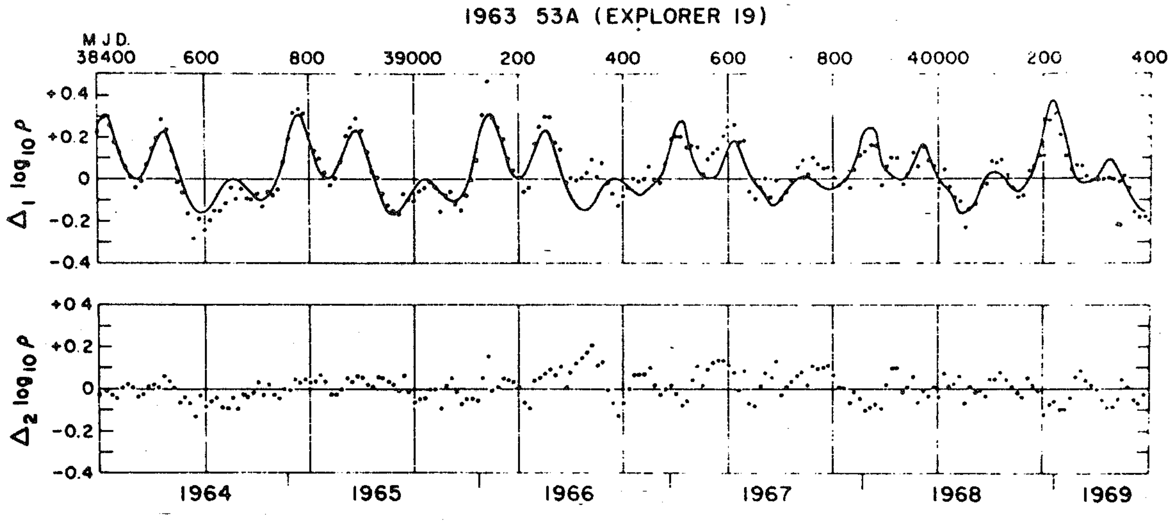

Figure A-10. Observed and computed density variations caused by the helium migration, as derived from the drag on Satellite 1963 53A (Explorer 19). [The data points in Δ_1 log ρ are density residuals from the model when all variations except the helium variations are suppressed. Δ_2 log ρ is the difference O-C in Δ_1 log ρ. M.J.D. is the Modified Julian Day (J.D. minus 2 400 000.5).]

A.2 APPLICATIONS

Requirements exist for models of the Earth's neutral upper atmosphere which will:

a) When used in lifetime prediction calculations, make predictions of lifetimes for satellites with orbital altitudes between approximately 180 and 2500 km within reasonable limits.

b) Contain the short period fluctuations observed in upper atmospheric density which may influence the design and operation of reaction control systems (RCS), thrust augmented control systems (TACS), control moment gyroscopes (CMG), rendezvous and docking systems, etc.

c) Provide continuous values of atmospheric parameters from orbital altitudes down to about 25-km altitude for use in evaluating thermal protection systems (TPS), control and guidance systems, etc., during reentry of space vehicle (e.g., the Shuttle), and in accomplishing orbital debris analyses.

d) Provide data on the composition and thermal structure of the upper atmosphere and its temporal and spatial variability for use in interpreting and analyzing results of scientific and technical investigations; e.g., contamination surrounding the Spacelab.

e) Provide data on the variability of the neutral atmosphere at mesopause heights for use in aerobraking maneuver studies.

A.3 CRITERIA

a) The Global Reference Atmosphere (A-13, A-14) model will be used in conjunction with the MSFC Lifetime Prediction Computer Routine for calculating orbital lifetime. This model is a combination of the 4-D Model Atmosphere, the Groves Model, and the Jacchia 1970 (A-11) Atmosphere model. It provides continuous density, temperature, and composition data from the surface to 2500 km for analyses requiring these data. Copies of the computer program for this model and a computerized simplified version of the Jacchia 1970 atmosphere model are available upon request from the Atmospheric Sciences Division, Marshall Space Flight Center, Alabama 35812.

b) Personnel performing analyses requiring knowledge of any small-scale, short-time period fluctuations in atmospheric parameters such as those perturbations associated with internally propagating waves should contact the Atmospheric Sciences Division, Marshall Space Flight Center, Alabama 35812.

☆U.S. GOVERNMENT PRINTING OFFICE: 1983 639 008 25

REFERENCES

A-1. Jacchia, L. G.: Revised Static Models of the Thermosphere and Exosphere with Empirical Temperature Profiles. Smithsonian Astrophysical Obs., Special Report 332, May 5, 1972.

A-2. Taeusch, D. R., Niemann, H. B., Carignan, G. R., Smith, R. E., and Ballance, J. O.: Space Research 8. A. P. Mitra, L. G. Jacchia, and W. S. Newman, eds., North Holland Publishing Co., Amsterdam, 1968, pp. 930-939.

A-3. Reber, C. A. and Nicolet, M.: Planet. Space Science, vol. 13, 1965, pp. 617-646.

A-4. Newton, G. P.: Journal of Geophysical Research, vol. 74, 1969, pp. 6409-6414.

A-5. Hall, L. A., Chagnon, G. W., and Hinteregger, H. E.: Journal of Geophysical Research, vol. 74, 1967, pp. 3425-3427.

A-6. Carru, H., Petit, M., and Waldteufel, P.: Planet. Space Science, vol. 15, 1967, pp. 944-945.

A-7. Carru, H. and Waldteufel, P.: Ann de Geophys, vol. 25, 1969, pp. 485-494.

A-8. McClure, J.P.: Journal of Geophysical Research, vol. 74, 1969, pp. 279-291.

A-9. Blamont, J. E. and Luton, J. M.: Space Research, vol. 11, Akademie-Verlag, Berlin, 1971.

A-10. DeVries, L. L.: Experimental Evidence in Support of Joule Heating Associated with Geomagnetic Activity. NASA TM X-64568, MSFC, February 10, 1971.

A-11. Jacchia, L. G.: Smithsonian Astrophysical Observatory Special Report No. 313, 1970, p. 87.

A-12. Groves, G. V.: Environmental Research Papers, No. 368, AFCRL-71-0410, Bedford, Mass., 1971.

TECHNICAL REPORT STANDARD TITLE PAGE

1. REPORT NO.
NASA TM-82478

2. GOVERNMENT ACCESSION NO.

3. RECIPIENT'S CATALOG NO.

4. TITLE AND SUBTITLE
Space and Planetary Environment Criteria Guidelines for Use in Space Vehicle Development, 1982 Revision (Volume 1)

5. REPORT DATE
January 1983

6. PERFORMING ORGANIZATION CODE

7. AUTHOR(S)
Compiled by Robert E. Smith and George S. West

8. PERFORMING ORGANIZATION REPORT #

9. PERFORMING ORGANIZATION NAME AND ADDRESS

George C. Marshall Space Flight Center
Marshall Space Flight Center, Alabama 35812

10. WORK UNIT NO.
M-397

11. CONTRACT OR GRANT NO.

13. TYPE OF REPORT & PERIOD COVERED
Technical Memorandum

12. SPONSORING AGENCY NAME AND ADDRESS

National Aeronautics and Space Administration
Washington, DC 20546

14. SPONSORING AGENCY CODE

15. SUPPLEMENTARY NOTES
This document was prepared for the most part by various staff members of USRA (Universities Space Research Association) and their associated scientists and scientific sources.

16. ABSTRACT

This document provides guidelines on space and planetary environment criteria for use in space vehicle development. Information is incorporated in the disciplinary areas of atmospheric and ionospheric properties, radiation, geomagnetic field, astrodynamic constants, and meteoroids for the Earth's atmosphere above 90 km, interplanetary space, and the atmosphere and surfaces (when available) of the Moon and the planets (other than Earth) of this solar system. Chapters on the Sun, Terrestrial Space, the Moon, Mercury, Venus, and Mars constitute Volume 1 (NASA TM-82478). Volume 2 (NASA TM-82501) contains chapters on Jupiter, Saturn, Uranus, Neptune, Pluto, Comets, Asteroids, and Interplanetary Dust.

These documents (Volumes 1 and 2) are recommended as tools for use in the development of space vehicles. However, an environment specialist should be consulted in critical design interface applications for the most current information and scientific interpretation.

NASA TM-82473 entitled, "Terrestrial Environment (Climatic) Cirteria Guidelines for Use in Aerospace Vehicle Development, 1982 Revision," provides natural environmental information for altitudes below 90 km.

There is no intent to automatically change any references to previous documents in contract Scopes of Work by the issurance and acquisition of either NASA TM-82473, NASA TM-82478, or NASA TM-82501.

17. KEY WORDS
Environment criteria
Space environment
Solar radiation
Atmospheric models; upper atmosphere
Astrodynamic constants
Planetary environments

18. DISTRIBUTION STATEMENT
Unclassified - Unlimited

Subject Category 15

19. SECURITY CLASSIF. (of this report)
Unclassified

20. SECURITY CLASSIF. (of this page)
Unclassified

21. NO. OF PAGES
243

22. PRICE
A11

MSFC - Form 3292 (May 1969)

For sale by National Technical Information Service, Springfield, Virginia 22161